Long period (LP) seismic signals on Mt. Etna volcano (Italy) : moment tensor inversion and uncertainties in the source model interpretation

Claudio Trovato

UNIVERSITÉ D'ORLÉANS

ÉCOLE DOCTORALE
ENERGIE, MATERIAUX, SCIENCES DE LA TERRE ET DE L'UNIVERS

LABORATOIRES

BRGM (Bureau de Recherches Géologiques et Minières)

et ISTO (Institut des Sciences de la Terre d'Orléans)

THÈSE présentée par :

Claudio TROVATO

soutenue le : **15 Décembre 2015**

pour obtenir le grade de : **Docteur de l'Université d'Orléans**

Discipline/Spécialité : Géophysique/Volcano Sismologie

Séismes à Longue Période (LP) sur le Mt. Etna (Italie): inversion du tenseur des moments et incertitudes liées à leur interprétation

THÈSE dirigée par :
Claudio TROVATO   Thésard, BRGM/ISTO

RAPPORTEURS :
François BEAUDUCEL   Physicien, IPGP
Eugenio PRIVITERA   Directeur de Recherche, INGV
_____

MEMBRES DU JURY *:*

Hideo AOCHI   Ingénieur, BRGM, Directeur de thèse
Francois BEAUDUCEL   Physicien, IPGP, rapporteur
Michael PICHAVANT   Directeur de Recherche, ISTO, Président du jury
Eugenio PRIVITERA   Directeur de Recherche, INGV, rapporteur
Bruno SCAILLET   Directeur de Recherche, ISTO, Co-directeur de thèse
Martin VALLEE   Physicien-Adjoint, IPGP, examinateur

Claudio TROVATO

Séismes à Longue Période (LP) sur le Mt. Etna (Italie): inversion du tenseur des moments et incertitudes liées à leur interprétation

Résumé : Les séismes de type longue période (LP) sont aujourd'hui enregistrés sur la plupart des volcans dans le monde entier. Malgré cela, le mécanisme à leur source n'est encore que très peu compris. A l'heure actuelle les modèles proposés pour expliquer leur origine sont : 1) la résonance d'une fracture remplie de gaz ou de fluides excités par des instabilités dans l'écoulement des fluides ou par la rupture fragile du magma ; 2) la fracturation lente des sédiments peu consolidés à la surface des volcans, dans des conditions de transition entre le ductile et le fragile. L'outil le plus utilisé pour comprendre leur nature est aujourd'hui l'inversion du tenseur des moments. Au cours des dernières années, les inversions du tenseur des moments se concentraient principalement sur la compréhension du mécanisme physique à l'origine des séismes LP qui souvent supposaient des milieux géologiques très simples, voire homogènes. Des études récentes ont montré l'influence des sédiments peu consolidés à la surface des volcans sur la propagation des ondes à basse fréquence et en conséquence, sur l'inversion du tenseur des moments quand ils ne sont pas pris en compte dans le processus d'inversion. Le but de cette thèse est de mieux comprendre les processus physiques qui génèrent les séismes LP et de quantifier les incertitudes liées à leur interprétation.

La première partie de cette thèse introduit les notions du tenseur des moments et décrit toutes les techniques utilisées pour sa décomposition permettant d'interpréter le mécanisme de source des séismes LP. Ensuite, je décris quelques sources sismiques simples et j'essaye de relier le tenseur des moments à des grandeurs physiques facilement interprétables, comme la pression ou le changement de volume à la source. Une fois les outils principaux pour la compréhension des séismes LP décrits, je me concentre sur la sismicité enregistrée sur le volcan Mt. Etna, Italie.

Le Mt. Etna est l'un des volcans les plus actifs et étudiés au monde. Il montre une intense activité sismique, jusqu'à des centaines de séismes LP enregistrés par jour. J'utilise un code numérique pour la simulation de la propagation des ondes et je construis quatre modèles géologiques du Mt. Etna avec une complexité structurelle croissante. Le quatrième modèle (S4) est construit dans le but de reproduire le plus fidèlement possible, le contexte géologique du Mt. Etna. Puis, le modèle S4 est utilisé pour produire des données synthétiques avec comme processus de source une fracture verticale située à différentes profondeurs. Ensuite, j'effectue l'inversion du tenseur des moments pour cette source, en utilisant des fonctions de Green, calculées dans les trois autres modèles géologiques simplifiés. Les résultats montrent qu'introduire trop de complexités irréelles dans le modèle géologique peut amener à de mauvaises interprétations du mécanisme à la source. Mais il en est de même pour l'utilisation de modèles trop simples, qui ne prennent pas en compte certaines caractéristiques géologiques importantes, comme les sédiments peu consolidés à la surface.

Dans le dernier chapitre, les informations obtenues lors des tests synthétiques sont appliquées à des séismes LP enregistrés sur le Mt. Etna. En premier lieu, la capacité du réseau de stations déployées par l'INGV (Instituto Nazionale di Geofisica e Vulcanologia) à reproduire la solution est testée. Le test synthétique montre que le réseau de stations est capable de reproduire le mécanisme de source avec précision mais dans le cas de fractures verticales, elles peuvent être interprétées à tord par des fractures horizontales. L'inversion du tenseur des moments est appliquée à trois ensembles de données enregistrées pendant différents états d'activité du volcan. Les résultats montrent que le modèle classique de résonance d'une fracture, remplie des gaz/fluides, ne peut pas expliquer entièrement les solutions obtenues. Par conséquent, je propose plusieurs modèles de source qui pourraient expliquer les séismes LP enregistrés. Je conclus en donnant des perspectives pour les futures études de la sismicité LP sur les volcans, avec un regard spécial au Mt. Etna.

Long Period (LP) seismic signals on Mt. Etna volcano (Italy): moment tensor inversion and uncertainties in the source model interpretation

Abstract: Long-period (LP) seismic events are abundantly recorded during rest and unrest periods at many volcanoes worldwide. However, their source mechanism is still poorly understood. Models which have been proposed so far to explain their origin are: 1) the resonance of a fluid-filled cavity triggered by fluid instabilities or the brittle failure of magma; 2) slow-rupture earthquakes occurring in the low consolidated materials composing the shallow portion of the volcanic edifice. Nowadays the main tool used to get insights into their nature is moment tensor (MT) inversion. MT inversions carried out in the past years focused mainly on the understanding of the physical origin of LP events and often supposed a relative simple geological structure of the medium. Recent studies highlighted the strong influence of shallow unconsolidated materials on the retrieved MT solutions and the importance of considering geological inhomogeneity in the inversion process. The principal aim of this thesis is to gain a better understanding of the source processes that generate LP events and to quantify the uncertainties related to the MT inversion process.

I first give an exhaustive review of the MT inversion and all the decomposition techniques which can lead to accurate interpretations of the LP events. I further develop the source description and try to relate the MT solution to directly construable physical quantities such as the pressure and the volume variation occurring at the source. Once the MT inversion and its decomposition are well established I focus on the LP seismicity recorded at Mt. Etna volcano (Italy).

Mt. Etna volcano is one of the most active and studied volcanoes in the world and shows an intense seismic activity with many LP events recorded almost continuously. I take advantage of a numerical code for wave's propagation (EFISPEC3D) and I build four structural models of Mt. Etna with increased geological complexity. For the fourth model (*S4*), I use the best geological and geophysical information in my possession to reproduce as closely as possible the real structural model of Mt. Etna. Model *S4* is used to reproduce the synthetic case of a vertical tensile crack embedded at different depths below the summit craters. Further, I perform MT inversion with Green's functions computed in the three others structural models. The results show the importance of including (when present) the unconsolidated surface materials in the Green's functions computation. On the opposite, complex models of the volcano which do not corresponds to reality can lead to significant errors and to the misinterpretation of the source solution.

Then I apply the lessons learned through the synthetic test to the MT inversion of some real events recorded on Mt Etna in 2009, 2010 and 2013. First, the ability of the MT tensor inversion in retrieving the correct solution is checked again for the permanent station network deployed by INGV (Instituto Nazionale di Geofisica e Vulcanologia). The synthetic test highlights that the station network is able to correctly retrieve the original source mechanism. However, the limited number of summit stations could negatively influence the retrieved source mechanism in case of vertical tensile crack sources. I work on the three sets of LP events recorded during different states of the volcanic activity. MT inversion is performed for the three sets of events and the solutions are interpreted independently. The results of my analyses suggest that the classic LP's model of the resonance of a fluid-filled cavity hardly matches with the retrieved MT solutions, and therefore support an alternative source model of slow rupture of the weak shallow unconsolidated volcanic materials. I finish by giving some perspectives of the future trends in the field of volcano seismology.

Keywords: *moment tensor inversion; long period events; synthetic test; Mt. Etna; velocity structure; Green's functions; volcano; seismology;*

Table of Contents

Chapter 2

Chapter 5

MT inversion of LP signals on Mt. Etna volcano 130

Chapter 6

List of Figures

analytical solution of Mogi, (1958) for the static vertical displacement recorded at the surface is reported as an example. The key point is how to express the M_0 at source in function of the ΔP imposed at the sphere wall.

List of Tables

Résumé en français

Chapitre 1

Le premier chapitre introduit EFISPEC3D (De Martin, 2010, 2011), un code de calcul numérique pour la modélisation de la propagation des ondes sismiques. Je fais d'abord un résumé de la théorie de la propagation des ondes en milieu élastique et des principes d'utilisation du code. EFISPEC3D étant conçu pour la modélisation des séismes en milieu tectonique, le code a dû être modifié et testé pour vérifier sa capacité à modéliser correctement la propagation d'ondes en milieu volcanique. Je décris ensuite les équations permettant la modélisation des sources volcaniques et leur implémentation dans EFISPEC3D. J'effectue un premier test synthétique pour vérifier leur implémentation correcte et je compare mes résultats avec un code aux éléments finis. Enfin, j'effectue un dernier test synthétique pour vérifier la modélisation correcte d'une topographie complexe, comme attendue en contexte volcanique. Les tests donnant des résultats satisfaisants, EFISPEC3D sera utilisé pour modéliser les ondes séismiques en milieu volcanique tout au long de la thèse.

Chapitre 2

Le deuxième chapitre est consacré aux séismes longue période (LP), objets de cette étude. Dans une première partie je décris les différents types de séismes volcaniques, puis je porte mon attention vers les séismes LP. Les séismes LP sont caractérisés par un contenu basse fréquence (0.1 - 2 Hz) et ne montrent pas de claires arrivées des ondes -P et -S. Il est donc impossible de les analyser comme de classiques séismes tectoniques. Ils sont souvent interprétés comme étant générés par l'interaction entre gaz/fluides et les roches environnantes. Plus précisément, une perturbation dans le fluide pourrait générer une onde de surface se propageant à l'interface entre le fluide et la roche. La fréquence propre de résonance de la fracture atteinte, des ondes à longue période se propageraient dans le milieu. Le mécanisme engendrant cette résonance n'est pas encore bien compris aujourd'hui. Un nouveau modèle récent suppose que les séismes LP sont générés par la

déformation à la limite ductile/fragile des sédiments peu consolidés à la surface des volcans.

Une fois rappelés les principaux modèles utilisés pour expliquer les séismes LP, je décris la technique de l'inversion du tenseur des moments, qui est la plus utilisée pour essayer de comprendre leur mécanisme à la source. Je décris ensuite toutes les méthodes de décomposition du tenseur des moments. Enfin, j'essaye de relier le tenseur des moments à des grandeurs physiques, comme la pression et le changement volumique de la source lors de l'interaction des gaz/fluides avec les roches. Ceci est fait en confrontant différentes approches issues de la littérature avec une solution analytique, le modèle de Mogi (1958).

Chapitre 3

Dans le troisième chapitre, je décris le contexte géologique du volcan de cette étude, le Mt. Etna en Italie. Je commence par une introduction sur l'histoire géologique du volcan suivie par le contexte tectonique dans lequel le volcan s'inscrit et je poursuis par une description de la morphologie actuelle des cratères sommitaux. Le chapitre se termine par une présentation exhaustive des récents travaux effectués sur l'Etna pour l'interprétation des séismes LP.

Chapitre 4

Dans le quatrième chapitre, je reproduis un travail original soumis à Geophysical Journal International (GJI).

L'étude porte sur l'analyse de l'influence du modèle de vitesse sur les résultats de l'inversion du tenseur des moments des séismes LP. L'analyse est effectuée grâce à des tests synthétiques basés sur quatre modèles de vitesse du volcan avec complexité croissante. Ensuite, je calcule la réponse du milieu à une fonction impulsive (fonctions de Green) pour les trois modèles les plus simples. Le quatrième modèle, et le plus complexe, est utilisé pour créer des données synthétiques pour des sources volcaniques (LP avec une variation volumique). J'utilise ensuite les fonctions de Green pour le problème inverse. Le but est de vérifier quantitativement si des modèles de vitesse plus complexes

donnent de meilleures solutions après inversion du mécanisme de la source. Le test synthétique montre qu'ajouter des complexités, qui ne sont pas forcément réelles, complique la solution. À l'inverse, des modèles de vitesse trop simples (homogènes) ne sont pas fiables non plus. Les résultats montrent que les basses vitesses sismiques rencontrées dans les sédiments peu consolidés à la surface peuvent fortement influencer le processus d'inversion. Donc, connaissant leur présence, une couche en surface à basse vitesse devrait toujours être inclue dans les calculs du modèle géologique avant inversion. Parmi les autres considérations que je peux faire : i) plus les sources sont superficielles, plus des erreurs sont introduites dans le processus d'inversion dues aux inhomogénéités structurelles ; ii) les solutions qui montrent les meilleurs ajustements entre les signaux observés et les signaux calculés ne correspondent pas à la meilleure solution ; iii) des composantes non voulues (comme des composantes de cisaillements) sont introduites dans la solution lorsque le modèle de vitesse ne correspond pas à la réalité.

Chapitre 5

Dans ce dernière chapitre, j'utilise les informations acquises grâce aux tests synthétiques du chapitre précédent et j'effectue l'inversion du tenseur des moments pour des séismes à longue période enregistrés sur le volcan Etna, pendant différents états d'activité du volcan. Je choisis des événements enregistrés pendant une effusion de lave, des événements enregistrés pendant une période où le volcan expérimente principalement un comportement explosif et un événement relié directement à une grande explosion du cratère Bocca Nuova, associée à une forte manifestation en surface. J'effectue d'abord des tests synthétiques comme dans le chapitre précédent, pour tester la capacité du réseau de stations utilisé à reproduire la solution initiale du mécanisme de source. Ensuite, j'analyse les évènements réels avec les techniques expliquées dans le deuxième chapitre et je donne une interprétation du mécanisme de source possible pour chacun des ensembles de données, indépendamment. Les résultats montrent que le modèle classique de résonance d'une fracture remplie de gaz ou de fluides ne peut pas expliquer entièrement la nature des signaux analysés et je suggère que d'autres modèles de source doivent être explorés.

Conclusions

Dans ce travail de thèse j'ai exploré l'une des principales méthodes pour l'étude de séismes à longue période, l'inversion du tenseur des moments. Grâce aux tests synthétiques, les incertitudes reliées au modèle de vitesse du volcan choisi peuvent être minimisées. L'impossibilité de modéliser parfaitement le contexte géologique du volcan introduit toujours des erreurs dans la solution que les tests synthétiques peuvent aider à discriminer. Tandis que les modèles de vitesse peuvent être affinés, l'application au cas réel du Mt. Etna montre que le modèle de source souvent utilisé pour expliquer les séismes à longue période n'est pas complètement adapté au cas considéré. Je suggère donc des modèles de source alternatifs proposés récemment en littérature. Je conclus en proposant des perspectives pour l'étude des séismes à longue période ainsi que des suggestions pour les tendances futures dans le domaine de la sismologie volcanique.

Remerciements

Voici rendu au terminus. Tutte le persone che ho incontrato in questi tre anni meriterebbero una parola, un saluto, un ringraziamento. Mi avete sempre dato l'incoraggiamento o il buon umore di cui avevo bisogno e tante delle difficoltà di questa tesi le ho superate soprattutto grazie a voi.

Merci Hideo de m'avoir accuelli et suivi tous ces trois ans et merci Florent pour tous les discussions sur le code et les milieres des questions que je t'ai posé. Merci à l'equipe et à tous les collegues au BRGM. Merci Bruno pour votre point de vue toujours me ramenant un peu vers la géologie.

Thank you Ivan, you gave me a lot of motivation (and a lot of help) with the codes, the ideas, the tests and also with our discussions in front of a pint(s). Thank you all the Nemoh friends, it was such a good time with you, each time. I'm looking forward for this last NEMOH conference, it will be the right goodbye. And thank you Paolo, papaNemoh, ti dobbiamo molto, ti devo molto.

Grazie Andrea, per tutto, per avermi mostrato l'osservatorio, avermi scorrazzato in auto, per le cene, per la scienza, per essere sempre stato paziente ed avermi dato mille consigli.

E grazie a voi, senza spiegarvene il motivo, già sapete – Tonno, Guillaume, Cristophe, Luca, Pierangelo, Marcello, Andre, Giova, Gush, Xtu, Paco, Eno, Richie, Spin, Gush, Reca, Tere, Cugi, Isa, i coinquilini e tutti, ma proprio tutti.

Ed infine, grazie a te Amelie, per essermi stata accanto in tutti questi mesi, per avermi pienamente supportato nonostante la tesi rubasse sempre troppo tempo a noi due. Voici la tant attendue fin, vivement le voyage, vivement le libre esprit des prochains mois et vivement les aventures qu'on vivra ensemble !

Grazie a voi mamma e papà per avermi sempre supportato ed avermi permesso di raggiungere quest'ennesimo traguardo. Sono felice di condividerlo con te papà.

Grazie mamma, ci hai lasciati improvvisamente, quasi a traguardo raggiunto, col sorriso che sempre ti contraddistingueva, spero tu possa aver gettato un occhio, da lassù. Ti porterò sempre nel cuore.

Grazie a tutti, merci à tous, thank you all !

Introduction

Volcanology is a multidisciplinary science, bringing together different fields such as geology, geochemistry and geophysics. Small and Naumann, (2001) estimated that almost 9% of the 1990's world population lived within 100 km of any of historically active volcanoes. Thus, the main aim of volcanology is to understand the complex behavior of volcanoes in order to forecast eruptions and to quantify the vulnerability of the populations exposed in front of the natural hazard related to volcanoes.

Among the different areas, volcano seismology is a science about seismic signals originating on volcanoes and associated to volcanic activity. Zobin, (2012) clearly defined the field of volcano seismology as: "*The study of the origin of these (seismic) signals, their spatial-temporal distributions, their relationships with volcanic processes and using them as an instrument to investigate the volcano deep structure and to predict a volcanic eruption together create the subject of volcanic seismology*". Since some pioneering works at the beginning of the 20th century (Zobin, 2012, and references therein) it became clear that volcanoes show a variety of seismic signals which often differ from classical tectonic earthquakes. In the late 1960s and early 1970s the appearance of portable instruments opened new horizons in the field of volcano seismology, but It was in the 1980s when broadband instruments highlighted the occurrence of different volcanic signals and their importance in the framework of early warning (Wassermann, 2011). The emergence of portable broadband seismic instrumentations was accompanied by the development of new analysis techniques which highlighted the role played by magmatic and hydrothermal fluids in the generation of seismic waves. In particular, seismic events with low (long period, LP) and very low (very long period, VLP) frequency contents are thought to be related with the dynamics of magmatic and hydrothermal fluids inside volcanoes (Chouet, 1996).

Among the different signals, LP events have been often observed preceding or accompanying volcanic eruptions (e.g. Aiuppa et al., 2010; Budi-Santoso et al., 2013; Fehler, 1982; Jousset et al., 2013; Matoza et al., 2009; Neuberg et al., 2000; Varley et al.,

2010). LP events are generally thought to be associated with the resonance of fluid-filled conduits (Chouet, 1986, 1988). However, a physical, united model explaining the mechanism which could trigger such a resonance is still missing. Many attempts have been done in the recent years to explain the excitation mechanism of LP events, for instance (Chouet and Matoza, 2013): a) sudden pressure drop in a fracture with discharge of the fluid from the resonator, thus generating the LP waveforms (e.g. Chouet, 1992; Kumagai et al., 2005; Nakano et al., 2003); b) dome growth (Morgan et al., 2008; Neuberg et al., 2000); c) brittle failure of melt in the conduit (Goto, 1999; Neuberg et al., 2006); d) magmatic fragmentation, degassing and explosions (Chouet and Matoza, 2013 and references therein); e) self-sustaining oscillations within magma flow channels (Julian, 1994). Recently, Bean et al., (2014) developed the work of Harrington and Brodsky, (2007) and proposed a new model for explaining shallow volcanic LP seismicity. In their model the LP source is interpreted in terms of low-stress fracturing instead of fluid-driven mechanisms. In this context LP seismicity would represent a marker of the deformation of the upper portion of the volcanic edifice.

The main difficulties encountered in the understanding of the LP events come from their intrinsic nature. LP events usually show no P-wave and S-wave arrivals and a very emergent signal onset, thus avoiding the use of classical seismology location techniques. Moreover, volcanoes are characterized by very complex geology and strong topographic gradients which heavily affect ray path trajectories. These considerations taken together have led to the development of new advanced techniques able to tackle the complicate behavior of LP events.

The source mechanism of LP events is quantitatively estimated via full-waveforms moment tensor (MT) inversion. MT inversions are usually conducted under the point - source assumption and many authors have successfully applied this technique to LP signals observed on many volcanoes in the world (e.g. Davi et al., 2010; De Barros et al., 2011; Jousset et al., 2004, 2013; Kumagai, 2002a; Kumagai et al., 2005; Lokmer et al., 2007; Nakano, 2005; Nakano et al., 2003). MT representation is a powerful tool because it is not restricted to classic shear faulting, but can express both tensile and rotational components occurring at the source. Coupled with single forces, MT inversion is also able to take in account of mass (fluid/gas, magma) movements which are intuitively expected

in volcanic environments.

In this thesis I focus my attention on the designing of a MT inversion and on the uncertainties related to the understanding of the source mechanism of volcanic LP seismicity. In the first chapter I recall the fundamentals of the equation of motion with a special regard to numerical modelling and the verification tests which will be utilized during the whole work of this thesis.

In the 2nd chapter I give a brief review of the different types of volcano seismic signals and then summarize all the source models proposed in the past years for explaining the LP seismicity. Further, I provide a complete description of the MT inversion technique, the decomposition of the MT and the principal tools used to get insights into the source process. The MT inversion solution is not directly related to any real physical mechanism. Thus I develop a classical seismological problem (Mogi, 1958) and I try to relate the MT to the volume variation of an equivalent sphere or crack source. Mogi, (1958) proposed an analytical solution to relate the pressure variation of a sphere embedded in a homogeneous half-space to the static deformation recorded at the surface. Many approaches are present in literature to relate the MT to a certain value of pressure. The different approaches are tested numerically and compared with the Mogi, (1958) analytical solution.

Once the MT inversion and its decomposition are well established, I focus my attention (chapter 4) on the uncertainties derived by the choice of a particular velocity model on the retrieved MT solutions. For this purpose, I build four different velocity models of Mt. Etna volcano (Italy) with increased geological complexity and I perform synthetic tests. Mt. Etna is one of the most studied volcanoes in the world, thus several many descriptions of the geological and tectonic context are available. Hence, I rely on geological (Branca et al., 2009, 2011a; Romano et al., 1979) and geophysical (Cauchie and Saccorotti, 2013; Chiarabba et al., 2000; Cristiano et al., 2010; Patane et al., 2002) descriptions of the volcano in order to reproduce as well as possible the structural complexity of Mt. Etna. The synthetic tests allow for testing many different issues related to the MT inversion process, in particular: 1) role of the shallow unconsolidated materials; 2) reliability of the solutions and considerations on the "best fit" (between observed and retrieved data) approach; 3) number of receivers and their distribution; 4) complexity of

the velocity model and reliability of the source mechanism interpretation.

The work presented in chapter 4 (influence of the velocity structure on the MT inversion) corresponds to a paper submitted to Geophysical Journal International (GJI).

The lessons learned toward the synthetic tests are then applied (chapter 5) to different LP events recorded on Mt. Etna volcano. I take three sets of LP signals recorded during different states of activity of the volcano. The events are studied through MT inversion and each set of events is interpreted independently. The uncertainties highlighted during the synthetic tests are encountered again in this chapter, but I try to interpret the obtained solutions even under limited information.

I conclude giving some perspectives for the future trends in the field of volcano seismology.

Chapter 1

Implementation of volcanic sources in EFISPEC3D

In this chapter I provide the basic theory of the elastodynamics and seismology behind a Spectral Element Method (code EFISPEC3D@BRGM; De Martin, 2010, 2011). Then I describe the practical aspects of its utilization for this thesis purposes by showing some classical problems. I present two verification tests comparing my results with the calculations brought by finite difference simulations. First, I verify the correct implementation of the three fundamental modes of the volcanic sources (isotropic, cylinder, opening crack) in the EFISPEC3D. Hence, I carry out a numerical test on the waves propagation under a synthetic Gaussian hill reproducing and comparing the results with the test case brought by Ohminato and Chouet, (1997).

1.1 Introduction

The analytical and semi-analytical solutions of the elastic deformation and the elastic wave equations for some simple problems, including seismic sources, can be found in literature since more than 100 years (Aki and Richards, 2002; Lamb, 1904). However, such solutions are generally limited to simple structures, such as homogeneous mediums or 1D stratified layers with flat free surface. On the other hand, many numerical techniques have been developed and applied since 1970s to treat the wave propagation problems in a complex 3D heterogeneous medium. The most widely used numerical approaches are based on two different techniques: finite difference (FD) and finite element (FE) methods. In this work I focus my attention on a particular class of FE methods, the Spectral Element Method (SEM). For comparison,

- the <u>Finite Difference Method</u> (FDM) (Virieux, 1986) is the most popular method solving step by step the differential equations. The structural grids are usually used. The implementation is easy but there are problems on numerical dispersion and on treating boundary conditions;

- the <u>Pseudo-Spectral Method</u> (Carcione and Wang, 1993), which solves the differential equations by decomposing space variables using a chosen set of test and trial functions (in a certain space of the model) in order to obtain smooth solutions. It is thus difficult to implement boundary conditions and problems can arise in the treatment of strong heterogeneities;

- the <u>Finite Elements Method</u> (FEM) (Zienkiewicz, 1989a, 1989b) which solves the differential equations by constructing a global system of equations over the model domain and finding the solutions based upon low-order approximations polynomials. This method is very powerful to treat complex equations and geometries, but includes a numerical dispersion in the case few nodes per minimal wavelength are present;

- the <u>Spectral Elements method</u> (SEM) (De Martin, 2010; Festa, 2004; Komatisch, 1999, 2007; Priolo, 1994): basically a finite element method, but locally in an element the solution is decomposed by basic spectral functions and solved explicitly. This can be seen as a subclass of FEM and combines the advantages of FEM and the flexibility and the accuracy of spectral methods.

The Spectral Element Method was introduced the first time almost 30 years ago in the context of computational fluid dynamics (Patera, 1984; Yoon, 1996). Since the late 1990s this method has been adopted to solve for the elastic wave equation (Azaïez et al., 1993; De Martin, 2010; Festa, 2004; Komatisch, 1999; Komatitsch, 1996; Schuberth, 2003). Compared to the classical FEM, the higher degree polynomials used for the approximation of the solution allow for an increased numerical stability (Komatitsch, 1996). Like the FEM, meshing is flexible, allowing taking in account complex topographies and curved interfaces.   This is very important in seismology and especially in volcano/seismology where surface heterogeneities strongly influence the recorded waveforms.

In this first section I present the basics of elastic wave propagation as well as the source description particular to the volcanic context. Then I will show some numerical tests using the code EFISPEC3D for validating its use in modeling wave propagation in a volcanic context.

1.2 Wave Propagation in an Elastic Medium

I briefly review the basic formulation of the elastic wave propagation. The notations are principally based on the classical textbook of Aki and Richards, (2002). In any material, strain is defined in a Cartesian coordinate system (x_1, x_2, x_3) by the derivatives of the displacement field as

$$\epsilon_{ij} = \frac{1}{2} \left(u_{i,j} + u_{j,i} \right)$$

where ϵ_{ij} is the *ij*-th component of the strain tensor and u_i is the *i*-th component of displacement. A comma between subscripts is used for a spatial derivative (e.g. $u_{i,j} = \partial u_i / \partial x_j$). Traction is the force across any plane in the medium so that it is written as

$$T_i = \tau_{ij} n_j$$

(2)

where T_i is the *i*-th component of the traction vector acting on the plane for which n_j is the *j*-th component of the normal vector.

For any volume (*V*) with its surface (*S*) in the medium, the equilibrium for the momentum rate and applied forces (traction and body force) is:

$$\frac{\partial}{\partial t} \iiint_V \rho \frac{\partial \boldsymbol{u}}{\partial t} \, dV = \iiint_V \boldsymbol{f} \, dV + \iint_S \boldsymbol{T}(\boldsymbol{n}) dS$$

(3)

where ρ is the bulk density of the medium and $\boldsymbol{f}$ represents the body force.

By applying the Gauss's divergence theorem, I rewrite the surface integration by volume integration:

$$\iint_S T_i \, dS = \iint_S \tau_{ij} n_j \, dS = \iiint_V \tau_{ij,j} \, dV$$

(4)

Thus I get

$$\iiint_V \left(\rho \ddot{u}_i - f_i - \tau_{ij,j} \right) dV = 0$$

(5)

where $\ddot{u}_i$ is the *i*-th component of the second time-derivative of the displacement, namely

acceleration. Equation (5) should be satisfied for any volume V, hence I obtain the equation of motion:

$$p\ddot{u}_i = f_i + \tau_{ij,j}$$

(6)

In linear elastic medium, the constitutive relation between stress and strain is generalized by Hooke's law as

$$\tau_{ij} = c_{ijkl}\epsilon_{kl}$$

(7)

where c_{ijkl} are material constants (elastic coefficients) of fourth-order tensor ($3^4 = 81$ constants). In an isotropic medium, the number of independent coefficients reduces only to two

$$c_{ijkl} = \lambda\delta_{ij}\delta_{kl} + \mu(\delta_{ij}\delta_{kl} + \delta_{il}\delta_{jk})$$

(8)

where λ and μ are known as the Lamé moduli and δ_{ij} is a Kronecker's delta function. The constitutive relation (7) becomes

$$\tau_{ij} = \lambda\delta_{ij}\epsilon_{kk} + 2\mu\epsilon_{ij}$$

(9)

and the equation of motion in Equation (6) becomes

$$\rho\ddot{u}_i = f_i + (\lambda + \mu)u_{j,ji} + \mu u_{i,jj}$$

(10)

As stated before, both Lamé's coefficients are enough to define the physical properties of an elastic linear medium, but they are not directly related to any physical parameter easily measurable. To define Lamé's coefficients in a numerical simulation I

take advantage of the definition of the compressional and transversal speed of waves in the considered medium plus the material density as

$$V_p = \sqrt{\frac{\lambda + 2\mu}{\rho}}$$

(11)

$$V_s = \sqrt{\frac{\mu}{\rho}}$$

(12)

where V_p and V_s are the compressional and transversal wave velocities respectively and ρ is the material density.

In order to obtain a unique solution by integration of the elastodynamic equation (10) in the reference domain, initial and boundary conditions have to be specified (Festa, 2004; Komatitsch, 1997). Seismic waves naturally propagate in infinite mediums, but in a numerical calculation the medium is naturally limited due to the memory capacity of the machine used for computation. I can distinguish between a physical boarder (the free surface) and numerical boarders which delimitate the medium artificially and where I have to define absorbing boundary conditions (Komatitsch, 1997). In EFISPEC3D absorbing boundaries are treated with Classical P1 paraxial approximation (Stacey, 1988) to prevent reflections and to guarantee stability in the numerical simulations.

1.3 Source description

Initial conditions concern the knowledge of the displacement at the initial time (τ) everywhere in the domain of study. An excitation source can be introduced in the medium by a punctual force or by a system of forces where compressional and rotational moments act simultaneously (Komatitsch, 1997). The temporal dependence of the source can be represented by any signal characterized by a limited frequency band. In this study the source time function used in each simulation will vary following the purposes of each section, a better description of each source time function used will be given along the

text. Here I present the classic theory beyond the source implementation and the special formulation for volcanic sources.

According to the representation theorem of the elasticity (e.g. Aki and Richards, 2002), the displacement field u_n at any point x at time t in the medium is written as

$$u_n(\mathbf{x},t) = \int_{-\infty}^{\infty} d\tau \iint_{\Sigma} [u_i(\xi,\tau)] c_{ijpq} v_j \frac{\partial}{\partial \xi_q} G_{np}(\mathbf{x}, t-\tau \,; \xi\,,0)\, d\,\Sigma$$

(13)

where $[u_i]$ is the displacement discontinuity between upper and lower interfaces of the surface Σ in the source region, v_j is the normal vector of the interface (from lower to upper), ξ is a position on the surface Σ, G_{np} represents the Green function and c_{ijpq} is the elastic coefficient like outlined in Equation (8). Thus, the source terms are grouped in the form of a tensor

$$m_{pq} = [u_i]\, v_j c_{ijpq}$$

(14)

or

$$M_{pq} = \int_{\Sigma} [u_i]\, v_j c_{ijpq} d\Sigma.$$

(15)

The former is called moment tensor density (N/m) and the latter is moment tensor (Nm). The convolution is then often written simply

$$u_n = M_{pq} * \frac{\partial G_{np}}{\partial \xi_q}$$

(16)

The above formulation is valid not only for shear faulting but also for tensile faulting. The code EFISPEC3D was initially developed for simulating regional earthquakes, namely implemented only with the formulation of shear faulting (double-couple sources) (De

Martin, 2010, 2011). Now I further implement different types of sources.

1.3.1 Volume change

In the volcanic context, it is supposed that earthquakes are due not only to tectonic faulting processes, but also to some volume changes or material movement. Such processes are considered as some tensile response of the volcanic conduit to magma injection and gas movements, deflation/inflation of fluid/filled cracks and explosions. Traditionally, three basic geometries, cracks, pipes or spheres, are often used. These geometries are represented in the form of non-double couple moment tensors and based on the point source assumption. The moment tensor is represented by a 3 x 3 matrix where the diagonal components are the so-called dipoles and represent a tensile movement, while the six others components correspond to double couple forces and represent the deviatory (shear) part of the process (Figure 1). Each moment tensor can be understood by a couple force composed by two forces acting in the opposite direction. In the following, I briefly present the formulation of the moment tensor components for three fundamental models (Figure 2) often used in volcanology.
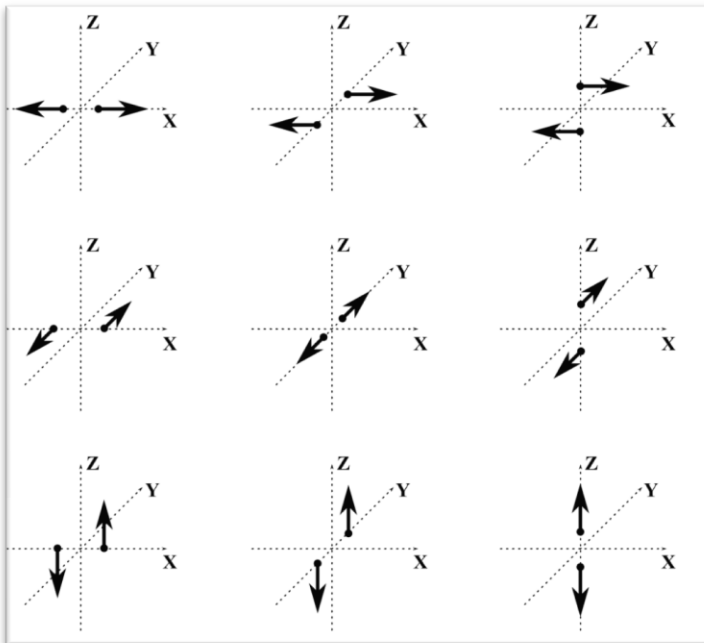
Figure 1 - Illustration of the nine force couples contained in the moment tensor after (Krieger, 2011). On the top, Mxx, Mxy, Mxz from left to right. Then Myx, Myy, Myz in the middle and Mzx, Mzy and Mzz at the bottom.

1.3.2 Explosion source

An isotropic volume change (Figure 2c) of a small sphere is expected to only have the isotropic diagonal components in the moment tensor. Approximated at a point an isotropic source can be expressed as

$$m_{xx} = m_{yy} = m_{zz} = m_0$$
$$m_{xy} = m_{xz} = m_{yz} = 0 \tag{17}$$

this formulation is obtained from Eshelby, (1957), or I can also evaluate Equation (13).
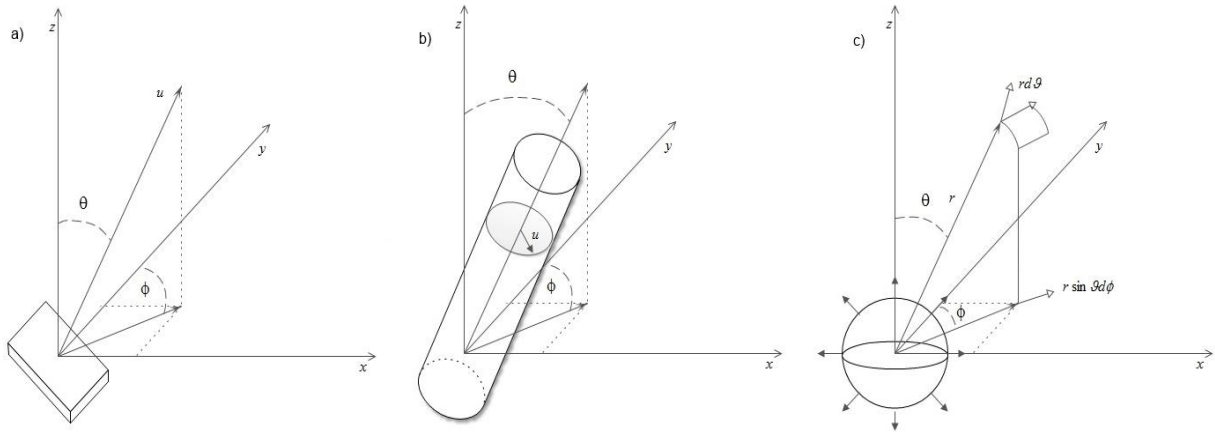
Figure 2 - *Definition of source coordinates and geometry for three fundamental models. a) Tensile crack opening in the direction v = u and defined by the angles φ and θ; b) radial expansion of a pipe; c) radial expansion of a sphere.*

Supposing a sphere of radius *r*, on which normal displacement is applied isotropically, the displacement and normal vector have the following vector components in standard spherical coordinates (φ, θ)

$$\boldsymbol{u}, \boldsymbol{v} = \begin{pmatrix} \sin\theta\sin\varphi \\ \sin\theta\sin\varphi \\ \cos\theta \end{pmatrix} \tag{18}$$

where φ and θ take $(0, 2\pi)$ and $(0, \pi)$ respectively. Considering $d\Sigma = \sin\theta\, d\theta\, d\varphi$ and the range of integral of Equation (15) only for a semi-sphere (e.g. θ takes $(0, \pi/2)$ instead of

$(0, \pi))$, I can write the moment tensor in the following:

$$M_{pq} = \int_0^{\pi/2} d\theta \int_0^{2\pi} d\varphi \, ([u_i] \, v_j \, c_{ijpq} \, r^2 \sin\theta) \tag{19}$$

Then for M_{xx}, I can evaluate, following Equation (8) for the elastic coefficients,

$$M_{xx} = \int_0^{\pi/2} d\theta \int_0^{2\pi} d\varphi \, ([u_i] \, v_j \, c_{ijxx} \, r^2 \sin\theta)$$

$$= \int_0^{\pi/2} d\theta \int_0^{2\pi} \left((\lambda[u_i]v_i + 2\mu[u_x]v_x) \, r^2 \sin\theta \right) d\varphi$$

$$= \int_0^{\pi/2} d\theta \int_0^{2\pi} d\varphi \, \lambda[u] \, r^2 \sin\theta + \int_0^{\pi/2} d\theta \int_0^{2\pi} d\varphi \, 2\mu\,[u] \, r^2 \sin\theta \, \sin^2\theta \, \sin^2\varphi$$

$$= 2\pi\lambda[u]r^2[-\cos\theta]_0^{\pi/2} + 2\mu[u]r^2 \left[\frac{1}{2}\varphi - \frac{1}{4}\sin 2\theta\right]_0^{2\pi} \left[\frac{1}{12}\cos 3\theta - \frac{3}{4}\cos\theta\right]_0^{\pi/2}$$

$$= 2\pi\lambda[u]r^2 + 2\mu[u]r^2[\pi]\left[-\frac{1}{12} + \frac{3}{4}\right]$$

$$= 2\pi\lambda[u]r^2 + 2\mu\pi[u]r^2\frac{2}{3} = 2\pi r^2\mu\,[u]\left(\frac{\lambda}{\mu} + \frac{2}{3}\right) \tag{20}$$

and

$$M_{xy} = \int_0^{\pi/2} d\theta \int_0^{2\pi} d\varphi \, ([u_i] \, v_j \, c_{ijxy} \, r^2 \sin\theta)$$

$$= \int_0^{\pi/2} d\theta \int_0^{2\pi} \mu([u_x]v_y + [u_y]v_x) \, r^2 \sin\theta \, d\varphi$$

$$= \int_0^{\pi/2} d\theta \int_0^{2\pi} 2\,\mu\,[u]\ r^2 \sin^3\theta\,\sin\varphi\,\cos\varphi\ d\varphi$$

$$= \mu\,[u]r^2 \left[\frac{1}{12}\cos 3\theta - \frac{3}{4}\,\theta\right]_0^{\pi/2} \left[\frac{\sin^2\varphi}{2}\right]_0^{2\pi} = 0 \tag{21}$$

Other components are written in the same manner. With respect to the original volume of this explosion source $V = \frac{4}{3}\pi r^2$, I describe the volume change as

$$\Delta V = 4\pi r^2 u \tag{22}$$

where $u = \frac{1}{2}[u]$. Thus, I can obtain

$$M_{pq} = \Delta V \begin{pmatrix} \lambda + \dfrac{2}{3}\mu & 0 & 0 \\ 0 & \lambda + \dfrac{2}{3}\mu & 0 \\ 0 & 0 & \lambda + \dfrac{2}{3}\mu \end{pmatrix} \tag{23}$$

1.3.3 Tensile Crack

Let us think a tensile crack whose geometry is defined by a normal vector (φ, θ), $(0 \le \varphi \le 2\pi)$ and $(0 \le \theta \le \pi/2)$, as shown in Figure 2a. In the case where a discontinuity takes place in the perpendicular direction to the crack plane (tensile mechanism), its direction is the same as the normal vector,

$$\boldsymbol{u}, \boldsymbol{v} = \begin{pmatrix} \sin\theta\,\sin\varphi \\ \sin\theta\,\cos\varphi \\ \cos\theta \end{pmatrix} \tag{24}$$

Following the definition of moment tensor M_{pq} of Equation (15) supposing a uniform tensile continuity on a small fault plane A and representing a seismic moment $M_0 \approx \mu A[u]$, I can write down in the following,

$$M_{xx} = \int_{\Sigma} [u_i]v_j c_{ijxx} \, d\Sigma = A\big(\lambda [u_i]v_j + \mu [u_x] v_x\big)$$

$$= A \left([u]\lambda + [u]2 \, sin^2\theta \, sin^2\varphi\right) = M_0 \left(\frac{\lambda}{\mu} + 2 \, sin^2\theta \, sin^2\varphi \right)$$

$$(25)$$

$$M_{xy} = \int_{\Sigma} [u_i]v_j c_{ijxy} \, d\Sigma = A\big(\lambda [u_i]v_j + \mu ([u_x] v_y + [u_y] v_x)\big)$$

$$= A[u]\mu \left(2sin^2\theta \, \sin\varphi \cos\varphi \right) = M_0 \left(2sin^2\theta \, \sin\varphi \cos\varphi \right)$$

$$(26)$$

$$M_{yz} = \int_{\Sigma} [u_i]v_j c_{ijyz} \, d\Sigma = A\big(\lambda [u_i]v_j + \mu ([u_y] v_z + [u_z] v_y)\big)$$

$$= A[u]\mu \left(2 \sin\theta \cos\varphi \cos\theta \right) = M_0 \left(2 \sin\theta \cos\varphi \cos\theta \right)$$

$$(27)$$

$$M_{xz} = \int_{\Sigma} [u_i]v_j c_{ijxz} \, d\Sigma = A\big(\lambda [u_i]v_j + \mu ([u_x] v_z + [u_z] v_x)\big)$$

$$= A[u]\mu \left(2 \sin\theta \sin\varphi \cos\theta \right) = M_0 \left(2 \sin\theta \sin\varphi \cos\theta \right)$$

$$(28)$$

$$M_{yy} = \int_{\Sigma} [u_i]v_j c_{ijyy} \, d\Sigma = A\big(\lambda [u_i]v_j + \mu [u_y] v_y\big)$$

$$= A \left([u]\lambda + [u]2 \, sin^2\theta \, cos^2\varphi\right) = M_0 \left(\frac{\lambda}{\mu} + 2 \, sin^2\theta \, cos^2\varphi \right)$$

$$(29)$$

$$M_{zz} = \int_{\Sigma} [u_i]v_j c_{ijzz}\, d\Sigma = A\big(\lambda\, [u_i]v_j + \mu\, [u_z]\, v_z\big)$$

$$= A\,([u]\lambda + [u]2\,cos^2\theta) = M_0\left(\frac{\lambda}{\mu} + 2\,cos^2\theta\right) \tag{30}$$

Thus, when taking $M_0 = \mu\Delta V$, I can write the entire moment tensor for a crack as,

$$M_{pq} = \mu\Delta V \begin{pmatrix} \lambda/\mu + 2\,sin^2\theta\,sin^2\varphi & 2sin^2\theta\,\sin\varphi\cos\varphi & 2\sin\theta\sin\varphi\cos\theta \\ 2sin^2\theta\,\sin\varphi\cos\varphi & \lambda/\mu + 2\,sin^2\theta\,cos^2\varphi & 2\sin\theta\cos\varphi\cos\theta \\ 2\sin\theta\sin\varphi\cos\theta & 2\sin\theta\cos\varphi\cos\theta & \lambda/\mu + 2\,cos^2\theta \end{pmatrix} \tag{31}$$

1.3.4 Pipe

The last mechanism I consider for representing a volcanic source is straight pipe geometry. Let us think a cylinder whose cross-section is expressed by the same geometry as the crack plane (Figure 2b). The axis of the cylinder is the same as the normal vector of Equation (15). A normal displacement u along the cylindrical boundary and the normal vector of the cylindrical boundary can be written as

$$\boldsymbol{u}, \boldsymbol{v} = \begin{pmatrix} u\cos\delta\cos\theta\sin\varphi - u\sin\delta\cos\varphi \\ u\cos\delta\,\cos\theta\cos\varphi + u\sin\delta\sin\varphi \\ -u\cos\delta\sin\theta \end{pmatrix} \tag{32}$$

where δ expresses the circumference of the pipe cross-section ($0 \le \delta \le \pi$). If I integrate over the circumference of the pipe δ for a unit pipe length, Equation (15) becomes

$$M_{pq} = \int_{\Sigma} [u_i]\, v_j c_{ijpq} d\Sigma = \int_{0}^{\pi}\big([u_i]\, v_j c_{ijpq}\big)r\, d\delta \tag{33}$$

and all the six independent components of the moment tensor can be written as

$$M_{xx} = \int_0^\pi r\, d\delta\big([u_i]\, v_j c_{ijxx}\big) = \int_0^\pi r\, d\delta \big(\lambda\, [u_i] v_j + \mu\, [u_x]\, v_x\big)$$

$$=$$

$$\int_0^\pi r\, d\delta \big(\lambda + 2\mu(cos^2\delta\ cos^2\theta\ sin^2\varphi\ +\ sin^2\delta\ cos^2\varphi - 2\cos\delta\sin\delta\sin\varphi\cos\varphi\cos\theta\big)$$

$$= [u]r\left(\lambda\, [\delta]_0^\pi + 2\mu\left(\left[\tfrac{1}{4}\sin 2\delta + \tfrac{1}{2}\,\delta\right]_0^\pi cos^2\theta\ sin^2\varphi + \left[\tfrac{1}{2}\,\delta - \tfrac{1}{4}\sin 2\delta\right]_0^\pi cos^2\varphi - \right.$$

$$2\ -\!sin\delta 0\pi - cos\delta 0\pi sin\varphi cos\varphi cos\theta$$

$$= [u]r\left(\lambda\pi + 2\mu\left(\tfrac{\pi}{2}cos^2\theta\ sin^2\varphi + \tfrac{\pi}{2}cos^2\varphi\right)\right)$$

$$= [u]r\,\pi\,\big(\lambda + \mu\,(1 - sin^2\theta\ sin^2\varphi)\big)$$

$$(34)$$

$$M_{xy} = \int_0^\pi r\, d\delta\big([u_i]\, v_j c_{ijxy}\big) = \int_0^\pi r\, d\delta\ \mu\ \big([u_x]v_y + [u_y]v_x\big)$$

$$= 2\,[u]\,r\,\mu\ \int_0^\pi d\delta\ \big(cos^2\delta\ cos^2\theta\ \cos\varphi\sin\varphi\ +\ O(\cos\delta\sin\delta) - O(\cos\delta\sin\delta) - $$

$$sin2\ \delta cos\varphi sin\varphi)$$

$$= 2[u]r\,\mu\left(\left[\tfrac{1}{4}\sin 2\delta + \tfrac{1}{2}\,\delta\right]_0^\pi cos^2\theta\ \cos\varphi\sin\varphi - \left[\tfrac{1}{2}\,\delta - \tfrac{1}{4}\sin 2\delta\right]_0^\pi \cos\varphi\sin\varphi\right)$$

$$= 2\,[u]r\,\mu\left(\tfrac{\pi}{2}cos^2\theta\ \cos\varphi\sin\varphi - \tfrac{\pi}{2}\cos\varphi\sin\varphi\right)$$

$$= -\,[u]r\,\pi\,\mu\,\big(sin^2\theta\ \cos\varphi\sin\varphi\,\big)$$

$$(35)$$

$$M_{yz} = \int_0^\pi r\, d\delta\big([u_i]\, v_j c_{ijyz}\big) = \int_0^\pi r\, d\delta\ \mu\ \big([u_z]v_y + [u_y]v_z\big)$$

$$= -2\,[u]\,r\,\mu \int_0^\pi d\delta\,(\cos^2\delta\,\cos\theta\,\sin\theta\,\cos\varphi \;+\; O(\cos\delta\,\sin\delta))$$

$$= -2[u]r\,\mu \left(\left[\tfrac{1}{4}\sin 2\delta + \tfrac{1}{2}\,\delta\right]_0^\pi \cos\theta\,\sin\theta\,\cos\varphi\right)$$

$$= -\,[u]r\,\mu\,(\cos\theta\,\sin\theta\,\cos\varphi)$$

<div align="right">(36)</div>

$$M_{xz} = \int_0^\pi r\,d\delta([u_i]\,v_j c_{ijyz}) = \int_0^\pi r\,d\delta\,\mu\,([u_x]z + [u_z]v_x)$$

$$= -2\,[u]\,r\,\mu \int_0^\pi d\delta\,(\cos^2\delta\,\cos\theta\,\sin\theta\,\sin\varphi \;-\; O(\cos\delta\,\sin\delta))$$

$$= -2[u]r\,\mu \left(\left[\tfrac{1}{4}\sin 2\delta + \tfrac{1}{2}\,\delta\right]_0^\pi \cos\theta\,\sin\theta\,\sin\varphi\right)$$

$$= -\,[u]r\,\mu\,(\cos\theta\,\sin\theta\,\sin\varphi)$$

<div align="right">(37)</div>

$$M_{yy} = \int_0^\pi r\,d\delta([u_i]\,v_j c_{ijyy}) = \int_0^\pi r\,d\delta\,\left(\lambda\,[u_i]v_j + \mu\,[u_y]\,v_y\right)$$

$$= \int_0^\pi r\,d\delta\,\left(\lambda + 2\mu(\cos^2\delta\,\cos^2\theta\,\cos^2\varphi + \sin^2\delta\,\sin^2\varphi - 2O(\sin\delta\,\cos\delta))\right)$$

$$= [u]r\,\left(\lambda\,[\delta]_0^\pi + 2\mu\left(\left[\tfrac{1}{4}\sin 2\delta + \tfrac{1}{2}\,\delta\right]_0^\pi \cos^2\theta\,\cos^2\varphi + \left[\tfrac{1}{2}\,\delta - \tfrac{1}{4}\sin 2\delta\right]_0^\pi \sin^2\varphi\right)\right)$$

$$= [u]r\,\left(\lambda\pi + 2\mu\left(\tfrac{\pi}{2}\cos^2\theta\,\cos^2\varphi + \tfrac{\pi}{2}\sin^2\varphi\right)\right)$$

$$= [u]r\,\pi\,\left(\lambda + \mu\,(1 - \sin^2\theta\,\cos^2\varphi)\right)$$

<div align="right">(38)</div>

$$M_{zz} = \int_0^\pi r\, d\delta \big([u_i]\, v_j c_{ijzz} \big) = \int_0^\pi r\, d\delta \left(\lambda\, [u_i] v_j + \mu\, [u_z]\, v_z \right)$$

$$= \int_0^\pi r\, d\delta \left(\lambda + 2\mu(cos^2\delta\ sin^2\theta\,) \right)$$

$$= [u] r \left(\lambda\, [\delta]_0^\pi + 2\mu \left(\left[\tfrac{1}{4} \sin 2\delta + \tfrac{1}{2}\, \delta \right]_0^\pi sin^2\,\theta \right) \right)$$

$$= [u] r\, \pi\, (\lambda + \mu\, sin^2\,\theta)$$

$$(39)$$

The volume change par unit length of a tube is given by

$$\Delta V = 2\pi r u = \pi r [u]$$

$$(40)$$

and the whole moment tensor is summarized as

$$M_{pq} =$$

$$\Delta V \begin{pmatrix} \lambda + \mu\,(1 - sin^2\,\theta\, sin^2\,\varphi) & -\mu\, sin^2\,\theta\, \cos\varphi\, \sin\varphi & -\mu\, \cos\theta\, \sin\theta\, \sin\varphi \\ -\mu\, sin^2\,\theta\, \cos\varphi\, \sin\varphi & \lambda + \mu\,(1 - sin^2\,\theta\, cos^2\,\varphi) & -\mu\, \cos\theta\, \sin\theta\, \cos\varphi \\ -\mu\, \cos\theta\, \sin\theta\, \sin\varphi & -\mu\, \cos\theta\, \sin\theta\, \cos\varphi & \lambda + \mu\, sin^2\,\theta \end{pmatrix} \quad (41)$$

In literature of volcanology different definitions are adopted for the geometrical reference system (Chouet, 1996; De Barros et al., 2011; Kumagai et al., 2010; Nakano, 2005) so that a careful attention is needed for the comparison.

1.4 Tests and comparisons

The EFISPEC3D code has been verified through different numerical tests on the wave propagation radiated from a shear faulting process (De Martin, 2010, 2011). In this section I show some numerical tests on the newly implemented volcanic sources for some

classical simple problems. The seismic signals recorded in and around a volcano show a large band of frequencies and this because their origin shows different physical processes, involving some volume change in the source area. I will first verify the implementation of the tensile sources presented in Section 1.3 by comparing my results with a finite difference simulation. I will then consider a classical problem in volcano-seismology brought by Ohminato and Chouet, (1997) to test the ability of EFISPEC3D in reproducing seismic signals in strong topography gradient environments (typical of volcanic contexts).

1.4.1 Test of tensile sources implementation

The mathematical implementation of the tensile sources described in section (1.3) will be tested by comparing our results for an oriented crack and an oriented pipe source with those obtained from a FDM code. I will proceed by describing the simulation input parameters followed by a graphical comparison of results. The parameters concerning the medium properties and source orientation have been taken constant for both simulations. The only change is in the chosen mechanism, and will be outlined.

1.4.1.1 Model setting

The model volume is 20 km x 20 km x 20 km with the flat ground surface at z = 0 km. I suppose a homogeneous half-space with Vp = 4000 m/s, Vs = 2000 m/s and density ρ = 2600 kg/m3. For all the simulations the source is located at 1000 m of depth, namely at (0, 0, -1000 m). I choose a source orientation with φ=30° and θ=80° for a tensile crack and a pipe (see Section 1.3). I assume a Ricker function as source time function (Equation (42), next section 1.4.2) with rise time of 0.66 s and time shift of 2 s and assume the maximum value of the seismic moment to be equivalent to Mw = 2.5. I record velocity time histories (in m/s) on the ground surface in nine points whose coordinates are in the following:

1.   -8000.0   2000.0   0.0

2. -6000.0   2000.0   0.0

3. -4000.0   2000.0   0.0

4. -2000.0   2000.0   0.0

5. 0.0   2000.0   0.0

6. 2000.0   2000.0   0.0

7. 4000.0   2000.0   0.0

8. 6000.0   2000.0   0.0

9. 8000.0   2000.0   0.0

I calculate for a total duration of 16 seconds with a time step increment of 0.001 s. To obtain enough numerical accuracy, I mesh the volume by hexahedral elements with a minimal edge of 153.22 m after refining the first shallow 1000 m below the free-surface. For the deeper part, the elements are coarser in order to fasten the speed of the simulation (maximal edge = 208 m). The total number of elements was 98304 and parallelizing the calculus on 16 CPUs the time taken for performing the computation was of 41 minutes on the local server (AMD Abu Dhabi at 1.6 GHz).

1.4.1.2 Results

Figure 3 and Figure 4 show the comparison of the results for a tensile crack and a pipe respectively. The results are compared with the calculations brought by a finite difference method under the same source and model parameters. The good agreement in amplitude and phases corresponding to the P- and S-waves at all the receivers for both source types assures that the implementation of the volcanic sources is correct. Some differences are found, for example, at station 5 at around t = 2 s, when P- and S-wave phases are not separated yet. A similar difference is observed at station 6 (U-D component). Those differences could be due to the intrinsic numerical dispersion of the numerical methods, but for the future applications of our interest, such difference will not be significant.
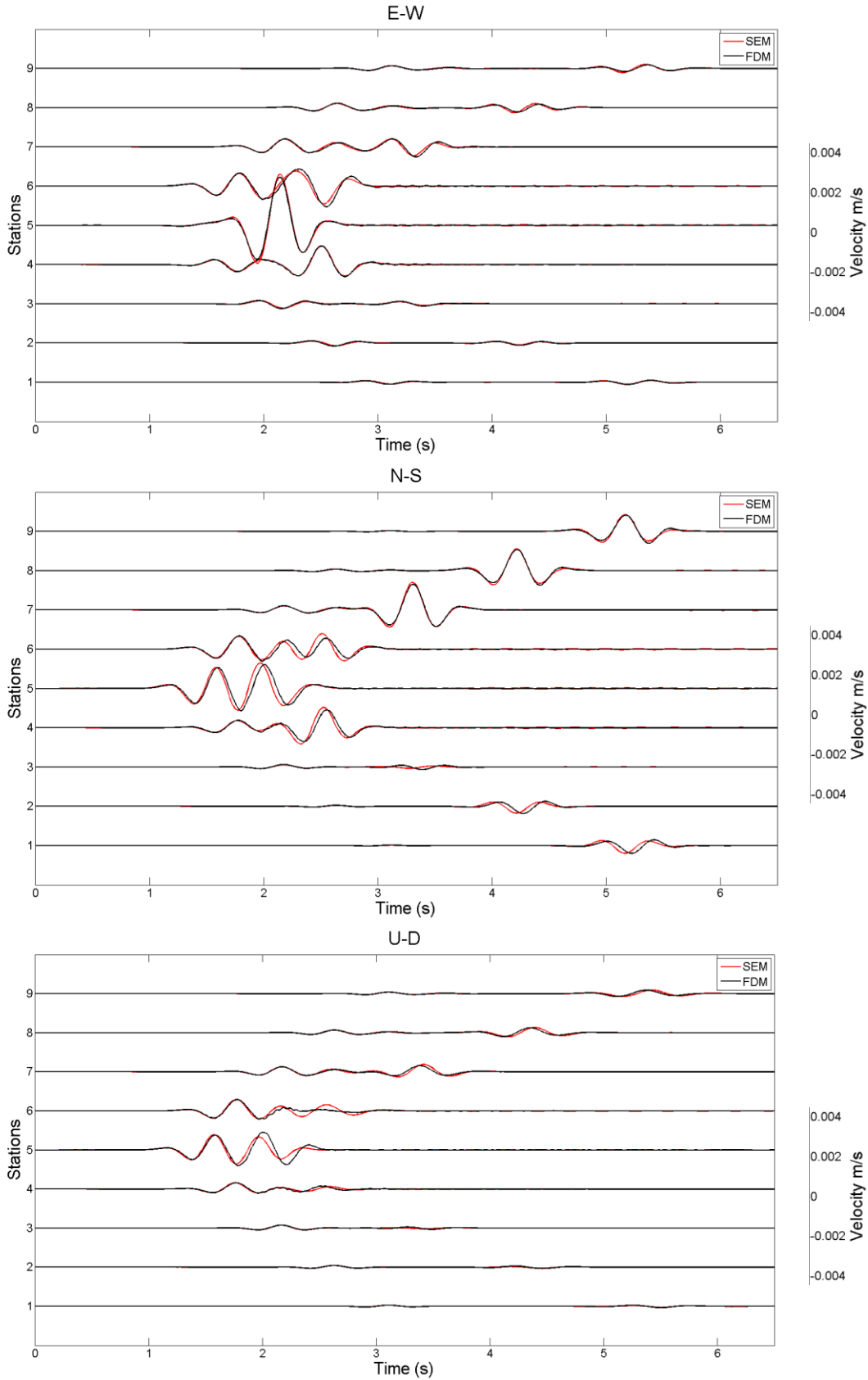
Figure 3 – Synthetic ground motion (three components velocity) for a tensile crack case at nine stations aligned by number. Red curves show the results of the SEM calculations, and black one show the FDM results.
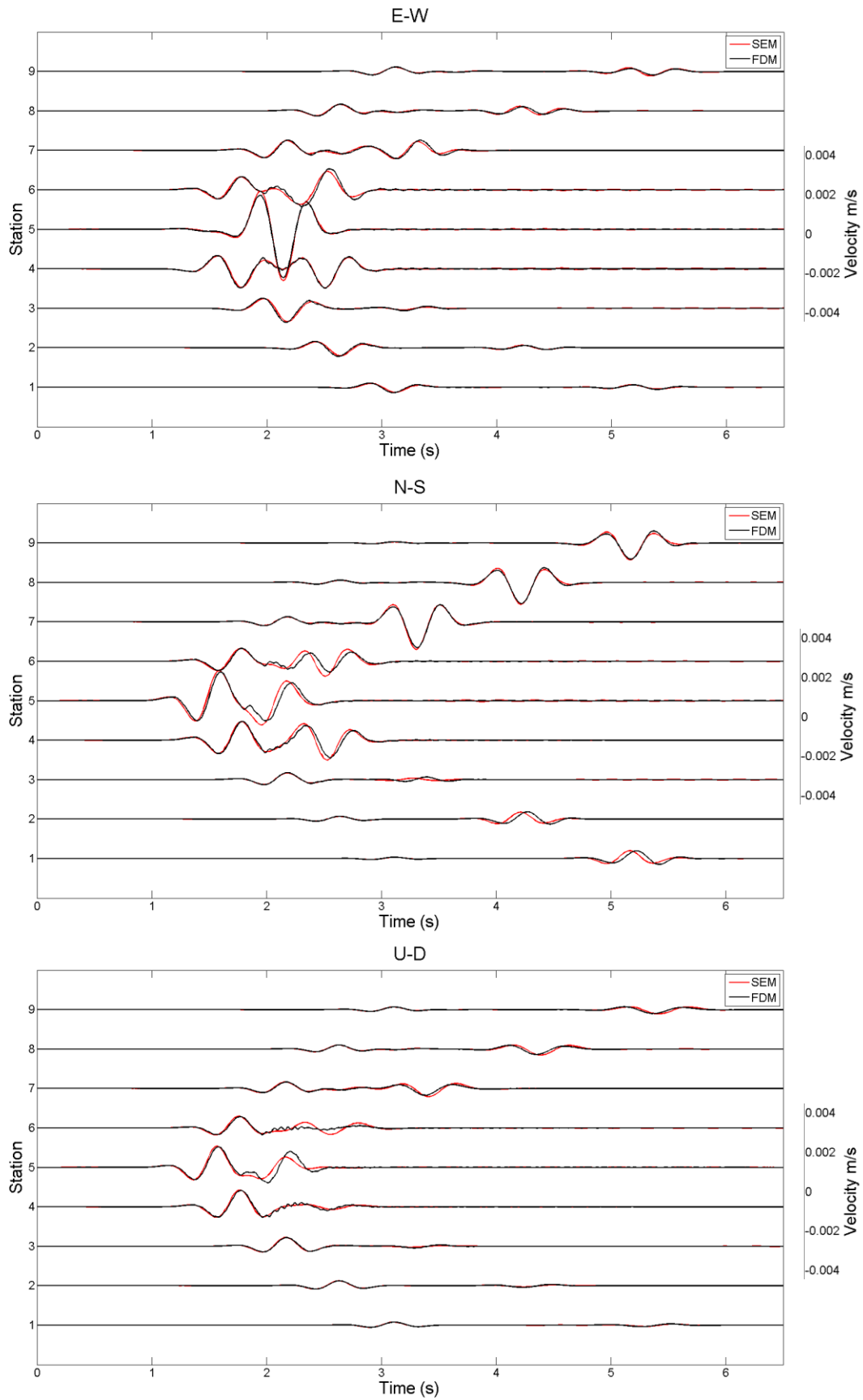
Figure 4 – Synthetic ground motion (three components velocity) for a pipe source for nine stations. SEM calculations in red and FDM in black.

1.4.2 Test of a Gaussian-Hill case

1.4.2.1 Model setting

I perform the second test by comparing my results with those of Ohminato and Chouet, (1997), who use a Finite-Difference-Method to carry out a wave propagation simulation in a 3D homogenous medium with a surface topography of Gaussian shape (Figure 5). The model space is (-3500 m, 3500 m) in the X-direction (EW), (-3500 m, 3500 m) in the Y-direction (NS) and (-4000 m, 1000 m) in the Z-direction (UD). The surface topography (z) is a Gaussian function with a height of 1000 m at the model center which becomes gradually z = 0 toward the far end of the model. The medium is supposed to be homogeneous with Vp = 3000 m/s, Vs = 1500 m/s and density ρ = 1200 Kg/m^3. An isotropic explosion source is assumed with a moment tensor of M_o = 7.96 10^{11} Nm. The source time function is given by the multiplication between the constant M_o and a Ricker function in the form

$$s(t) = 2\,a\ \frac{\pi^2 (t - ts)^2}{tp^2 - 0.5}\ e^{\pi^2 (t - ts)^2 / tp^2}$$

(42)

where *a* is the amplitude, *tp* is the time period and *ts* is the time shift, and it is assumed that *a* = 1, *tp* = 0.66 s and *ts* = 2 s. The focal depth is fixed at z = 427 m (-800 m , 0, 427 m) near the surface of the volcanic body slope. The seismograms are compared in the following six stations on the ground surface (x-, y- and z- coordinates)

1. (-2400 m, 1300 m, 0.58 m)
2. (-1600 m, 1300 m, 14.26 m)
3. (-800 m, 1300 m, 97.29 m)
4. (0.0 m, 1300 m,   184.51 m)
5. (800 m, 1300 m,   97.29 m)
6. (1600 m, 1300 m, 14.26 m)

I mesh the domain (Figure 5) with hexahedral elements with a minimal edge of 38.46 m. Refining is applied to the first 1000 m below the ground surface. The element edge becomes coarser at depth (maximal edge = 153 m). I calculate for a duration of 15 seconds with a time step increment of $5 \cdot 10^{-4}$ s. The total number of elements was 115072 and parallelizing the calculus on 16 CPUs the time taken for performing the computation was of 21 minutes on the local server (AMD Abu Dhabi at 1.6 GHz).

1.4.2.2 Results

The synthetic displacements computed for all the six stations with the code EFISPEC3D and those from Ohminato and Chouet, (1997) are compared in Figure 6. Amplitudes in my simulation are normalized in respect to station number 3, as the solutions presented in Ohminato and Chouet, (1997) were already normalized. The waves are affected due to the irregular topography, especially in the latter part of seismograms and in the wave field beyond the irregularity (Stations 5 and 6). The overall shape of the synthetics is globally similar, especially for the first wave packet (direct wave), and this verifies our numerical simulation. Some differences in amplitude and in phase are found in the second part of the seismograms, especially in Stations 5 and 6 where the influence of topography is strong. A further mesh refining is performed in order to assure the precision of my result (minimal edge of elements 18.5 m, total number of elements 787059, calculus parallelized on 64 CPUs performed in 9 hours and 38 minutes). Figure 6 and Figure 9 show the comparison between the two simulations (fine and coarse) performed by EFISPEC3D and Ohminato results. As the two simulations performed with EFISPEC3D show any difference (Figure 7 and Figure 8), I can consider that my solution is precise enough and well converged. It is thus considered that the difference between EFISPEC3D and Ohminato solution originates from the difference of the numerical implementation. As there is no analytical solution, it is impossible to verify further. However it is necessary to keep in mind that there might be some difference when using different numerical schemes.
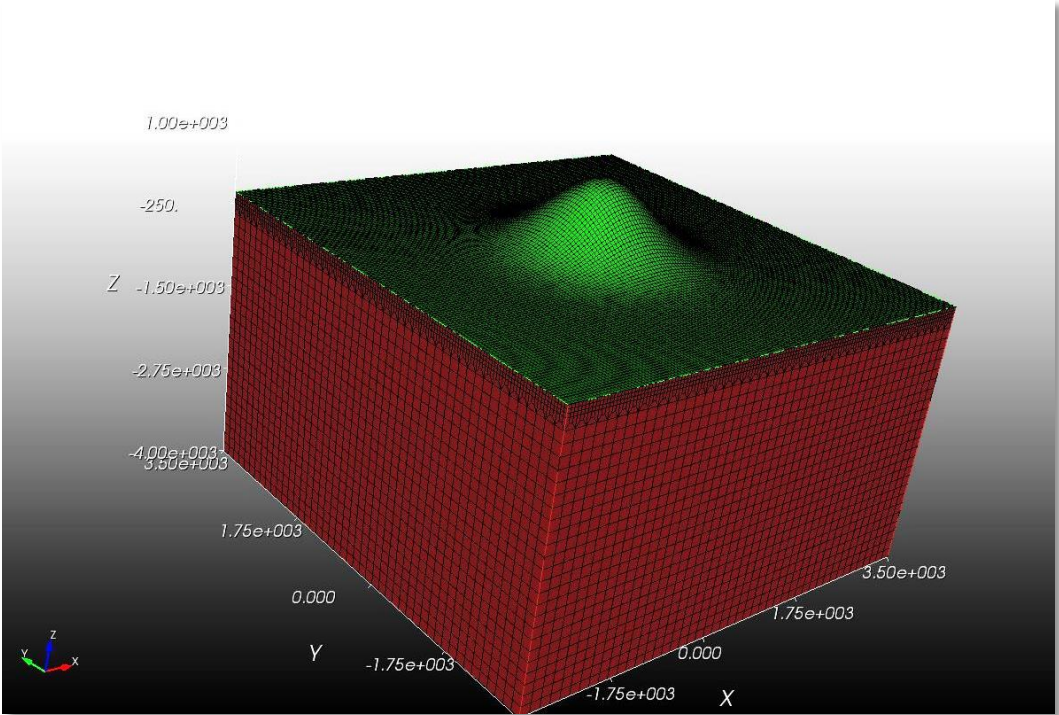
Figure 5 – Model volume meshed by Cubit with a Gaussian-shape hill.
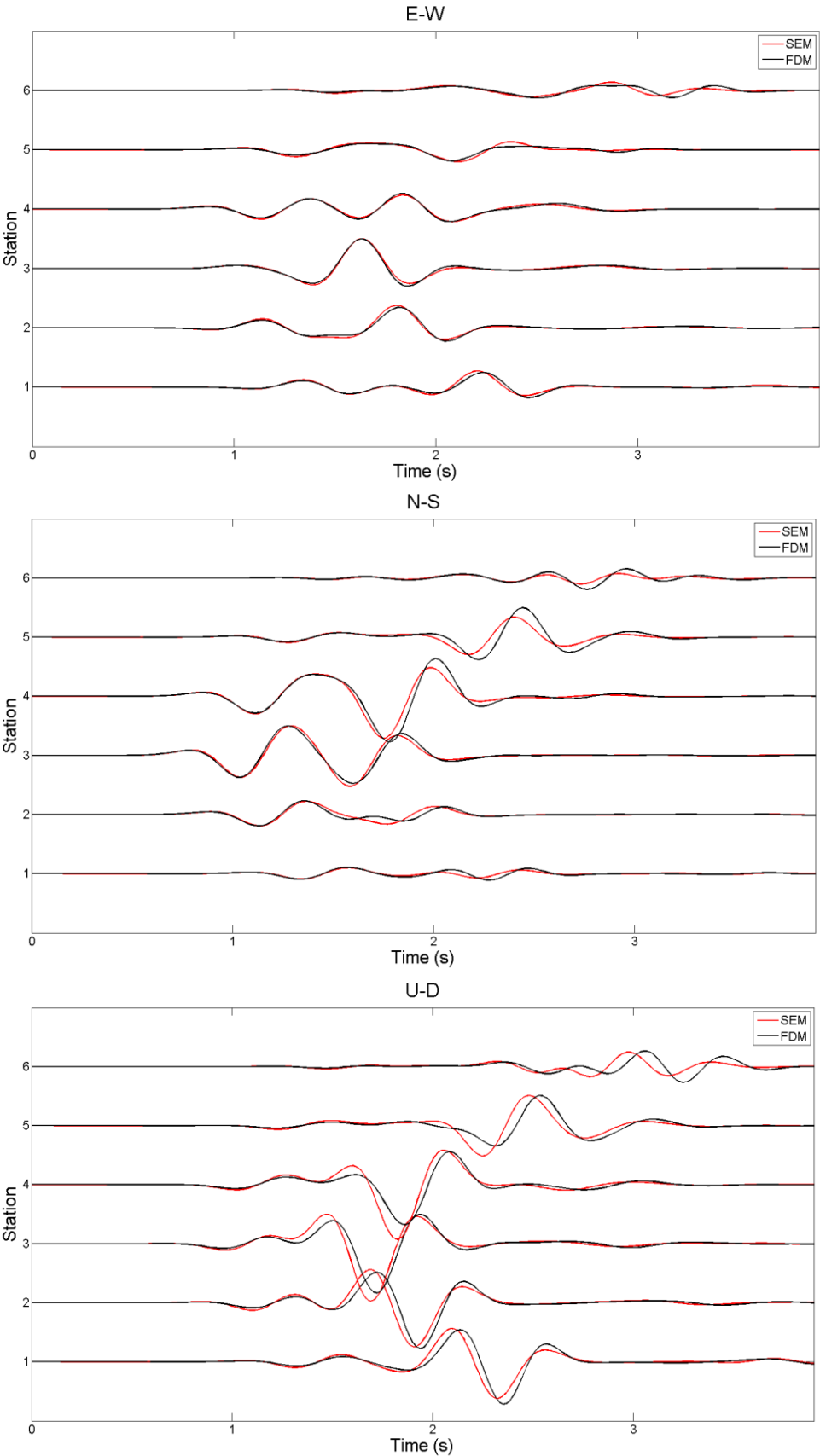
Figure 6 – Comparison of synthetic ground motions between the SEM (in red) and FDM (in black) simulations in a Gaussian hill topography.
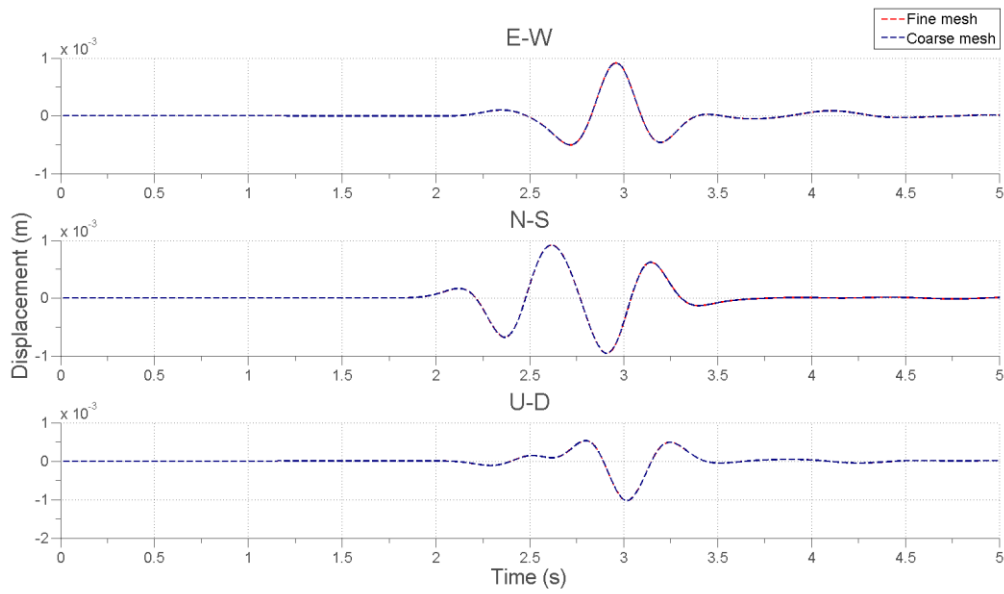
Figure 7 – Comparison of synthetics ground motion (displacement) for station number 3 in the Gaussian-Hill topography. The test has been performed with EFISPEC3D for both simulations with a fine (red dashed line) and a coarser (blue dashed line) meshing scheme.
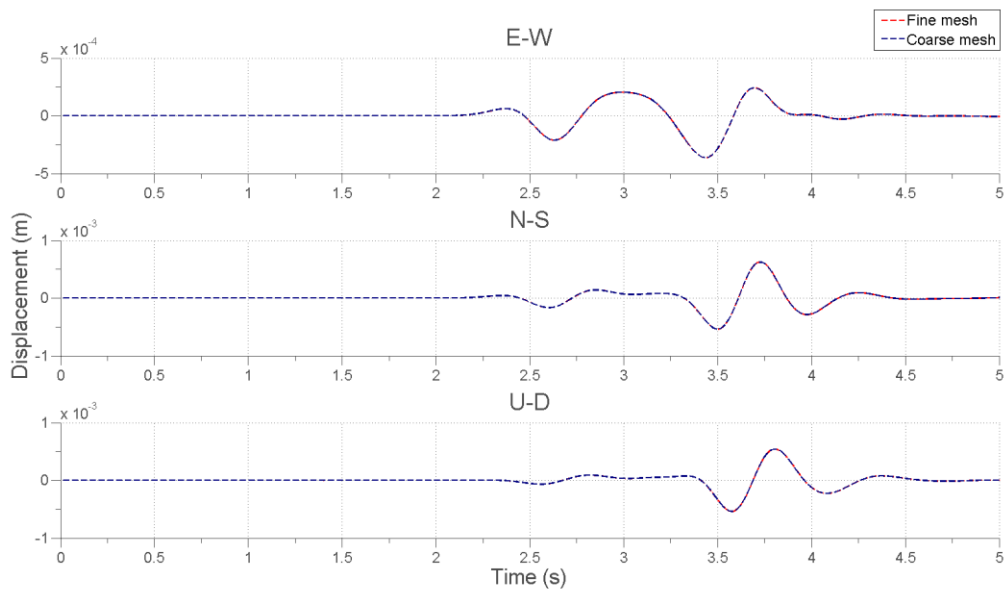
Figure 8 – Comparison of synthetics ground motion (displacement) for station number 5 in the Gaussian-Hill topography. The test has been performed with EFISPEC3D for both simulations with a fine (red dashed line) and a coarser (blue dashed line) meshing scheme.
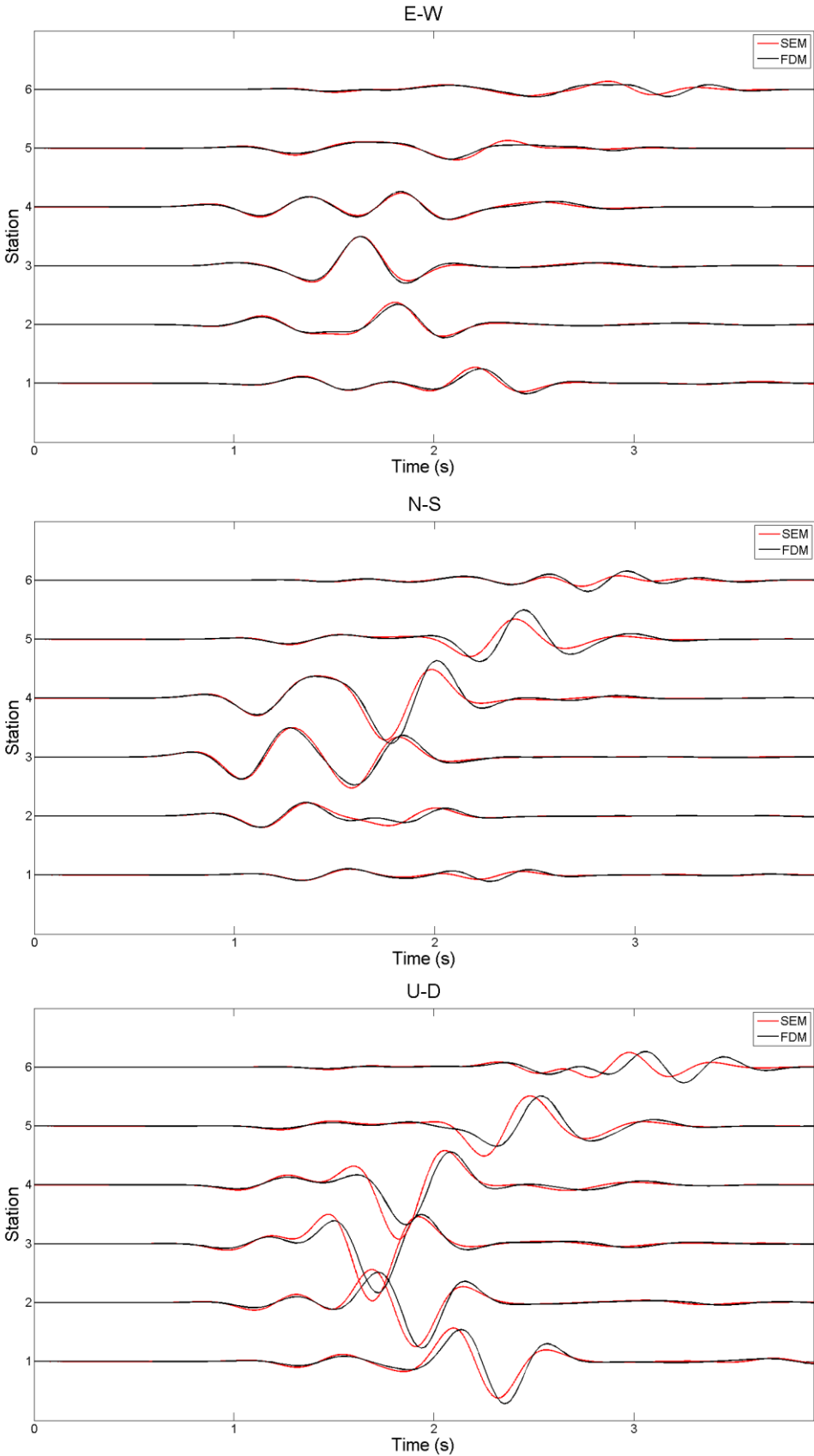
Figure 9 – Comparison of results between the SEM and FDM simulation like Figure 6 with a finer meshing scheme, the results are equivalents to the coarser meshing scheme.

Chapter 2

Source models and characterization of Long-Period events

In this chapter I provide a description of volcano seismicity observed on volcanoes with a special regard to long-period events. A review of the seismic signals recorded on volcanoes is given in the first part, follows a detailed description of long-period activity on volcanoes worldwide and the main accepted theories beyond their physical explanation. The third part is focused on the mathematical theory beyond moment tensor inversion, a recognized tool for describing the physical behavior of the source of long period events. I show the main tools used to determine the physical mechanism at the origin of the long-period activity. I end up by comparing numerical results with an analytical solution (the Mogi problem) for the determination of the volume of materials involved in the source process.

2.1 Volcano Seismicity

Volcanic eruptions are among the most severe natural hazards and it is since the beginning of 20th century that scientists made observation on the signals preceding or accompanying an eruption. It is since the 1960s and 1970s that the availability for more portable and sensitive instruments has led to modern volcano seismology, but it's only since the 1980s, with the widespread of broadband instruments, that scientists could start investigate deeply the physical mechanism beyond volcanic seismic signals generation. The main goal of volcano seismology is to understand the origin process of volcanic seismic signals. Seismic signals recorded on volcanoes represent the elastic response of the volcanic edifice to the action of forces related to either rock's failure, or to rapid pressure changes due to mass movements (gas, magma) occurring at depth (Chouet and Matoza, 2013 and references therein). Defining the source mechanism of these signals would improve our understanding of the volcanic activity leading to better early warning and hazard assessment.

Classical literature classifies volcanic seismic signals in four main classes of events (Chouet, 2003a; McNutt, 2005): *high frequency events*, *long-period events*, *very long-period events* and *tremor* (Figure 10)*.* Those terms simply describe the appearance and frequency content of the signal, but nowadays also imply a certain characteristically source mechanism.

2.2.1 High frequency events

High frequency (>5Hz) events (also called volcano tectonic events, VT) are generated by brittle fracture. The process beyond their generation is well understood as they share many similarities with classical regional earthquakes: shear failure caused by stress build up and resulting in slip on a fault on a plane. They are characterized by clear *P-waves* and *S-waves* arrivals and are studied towards focal mechanisms and stress tensor inversions. They often occur in swarms and can be related to uprising magma or relaxation phase of the volcanic edifice. Recently a new class of VT events, denominated VT-B, has been observed sharing some similarities with lower frequency events (Wassermann, 2011).

They are usually shallow, with slightly lower frequency (1-10 Hz) content and with emergent *P-waves.* They are of difficult interpretation and little is known about their real origin.
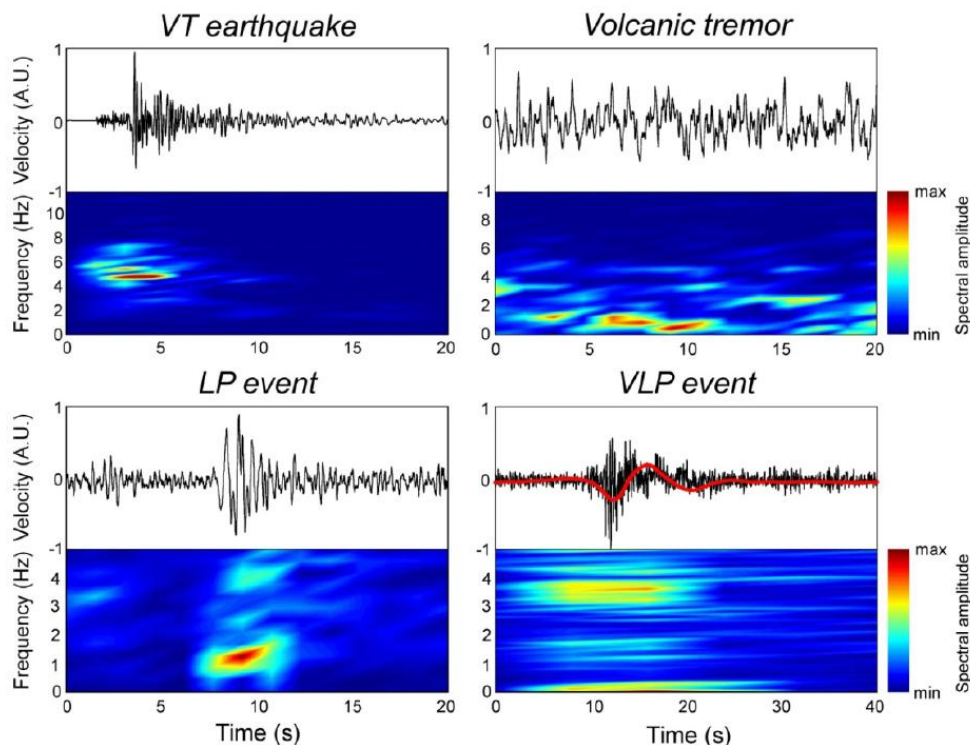
Figure 10 – Waveforms and spectrograms of VT earthquake, volcanic tremor, LP event and VLP event recorded on Mt. Etna. The tick red line plotted over the VLP waveform shows the signal low pass filtered below 0.15 Hz. Figure reproduced after Patanè, (2011)

2.1.2 Long-Period (LP) events

Long Period (LP) events are characterized by a narrow frequency band (usually comprised between 0.1 and 2 Hz) and show an emergent onset with no clear P-waves and S-waves arrivals. They show different shapes and vary a lot between different volcanoes worldwide (Figure 11). For instance only few events per year are recorded at Piton de la Fournaise (Zecevic et al., 2013) while on Etna (Saccorotti et al., 2007) and Turrialba (Eyre et al., 2013) hundreds of events can be recorded per day. In many cases their activity can be sustained over time, with the repetition of events which share similar waveforms (De Barros et al., 2011; Eyre et al., 2013). LP events are thought to be caused by fluid processes that are still not well understood. The main effort of the scientific community is to

quantify the quantity of gas or magma involved in their generation in order to get more insight on the behavior of the internal plumbing system of volcanoes where they occur. Nowadays many models have been proposed to explain their source mechanism. A more comprehensive review of the source processes of LP events is presented in the next section (2.2).
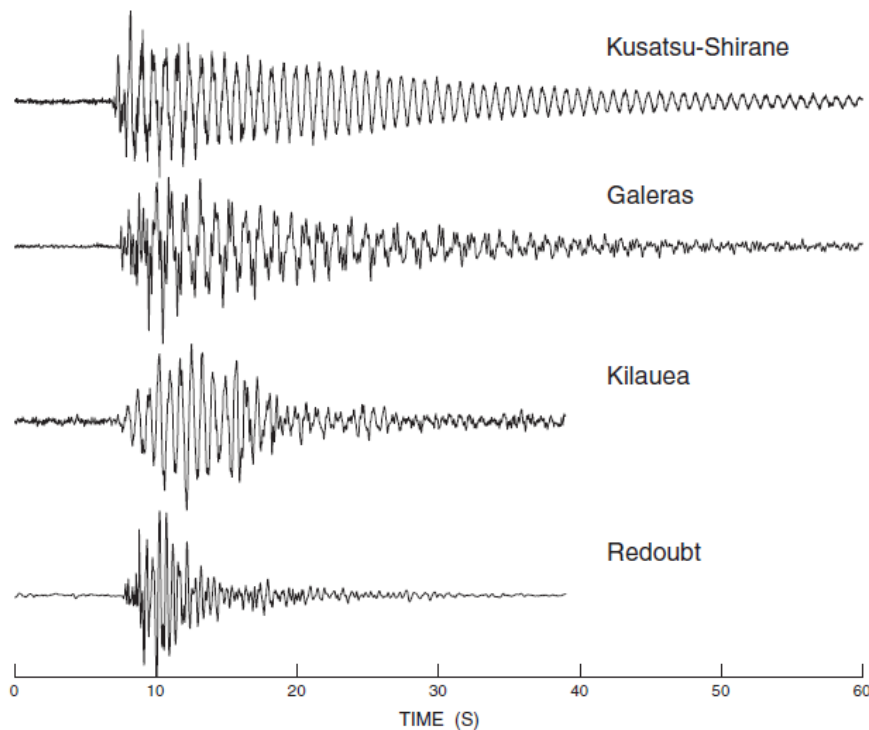
Figure 11 - Typical signatures for long-period signals at different volcanoes. From top to bottom is clear the different length of the harmonic coda. Figure reproduced after Chouet, (2003a)

2.1.3 Very-Long-Period (VLP) events

Very Long Period (VLP) events are characterized by very low frequency (0.01-0.1 Hz) content. They are often recorder in the very shallow part of the volcanic edifice (< 2 km) and due to their long wavelengths they suffer of little path distortion, which facilitates their analysis. Unlike LPs they are often interpreted as generated by inertial forces associated with perturbations in the flow of magma and gases through conduits (Chouet and Matoza, 2013). For instance, Chouet et al., (2005) interpreted VLP events recorded at Popocatépetl Volcano, Mexico, as originated by gas movements at the intersection of

two structures represented by a sill and a dike. A significant mass movement originated in the in the sill triggering a mass movement response in the dike. A similar structure was also imaged by Dawson, (2011) at Augustine Volcano, Alaska. VLP events were also recorded accompanying explosions during eruptions at Redbout Volcano, Alaska (Haney et al., 2013) and interpreted as a sill structure acting as magma storage at a depth of 1.4 km below the crater. A single sill structure was also inferred by Ohminato, (1998) for VLPs recorded at Kilauea Volcano, Hawaii, while VLPs recorded during explosions at Stromboli Volcano where interpreted by Chouet, (2003b) in terms of upward migration of gas slugs in the shallow conduit prior to eruptions.

2.1.4 Volcanic Tremor

Volcanic tremor is a sustained signal, lasting from several minutes to several days-months, observed during quiescent or eruptive stages (Konstantinou, 2003). It shows strong similarities in the frequency content (0.1 – 5 Hz) with LP events. The similarity in the spectral content leads to hypothesize its origin as an overlapping of a sequence of LP events (Chouet and Matoza, 2013 and references therein).

2.2   Source models for LP signals

As stated before, LP signals are of difficult interpretations and since their first observations many models have been proposed to explain their source mechanism and behavior.

2.2.1 The crack model

Since the late 1970s, when the first low frequency signals were recorded and analyzed on volcanoes, some authors started questioning about some oscillatory characteristics intrinsically present in the LP records. Aki, (1977) was the first author invoking a source model which involved fluids driven in a crack structure. He proposed a mechanism for volcanic tremor recorded at Kilauea, Hawaii, consisting in the vibration of

cracks caused by the opening of channels in response to excess magmatic pressure. Lately, in the 1980s in occasion of the eruption of Mt. St. Helen, Fehler, (1982) interpreted some LPs as originated from excitation of a fixed cavity situated under the active crater. Some models based on the resonance of a fluid filled cavity started to be proposed and investigated through numerical modeling for different geometries of the resonator: a pipe (Chouet, 1985), spheres (Crosson, 1985) and cracks (Chouet, 1986). The main feature of these models was the presence of the so called "crack wave", a very slow wave propagating along the crack boundary in the fluid. Ferrazzini and Aki, (1987) studied analytically the behavior of this wave arguing that reflections of this wave at the crack tips could be a reasonable source of radiations in case of finite cracks. They established that the crack wave velocity is slower than the acoustic velocity of the fluid at all wavelengths. Thus the resonance of the fluid reservoir depends on its geometry and on the physical properties of the fluid and the surrounding solid. Chouet, (1986) established that the excitation modes of a crack depend on the position of the pressure transient, the crack dimensions, the impedance contrast (between fluid and solid) and the crack stiffness. The crack stiffness is dependent on the bulk modulus of the fluid so that the involved fluid should play an important role on the oscillatory behavior of the resonator. The viscosity of the fluid decreases the amplitude of the main spectral peaks and reduces the duration of the radiated signals.

The crack model explains how the characteristics oscillations observed in LP signals could be produced, but the trigger mechanism is still unknown. Many volcanic processes could be involved such as: a) dome growth, as seen in Montserrat (Neuberg et al., 2000) or at Mount St. Helens (Morgan et al., 2008); b) hydrothermal processes from meteoric waters and heat source interaction (Eyre et al., 2013; Kumagai, 2002a; Syahbana et al., 2014); c) magmatic fragmentation, degassing and explosions (Chouet and Matoza, 2013, and references therein); d) brittle failure of the melt itself in the conduit (Goto, 1999; Neuberg et al., 2006); e) self-sustained oscillation within magma flow channels (Julian, 1994). Chouet and Matoza, (2013) gave an exhaustive description of the state of the art of all the possible trigger mechanisms for LP events. I refer to their paper and give a general overview of all the possible (and still in debate) source models.

2.2.2 Self-sustained oscillations

Julian, (1994) proposed a model for the generation of tremor based on the coupling between fluid and solid. In his model an increase in the flow speed leads to a decrease in fluid pressure by the Bernulli effect. The result is that the walls of the channel move inward constricting the flow which increases its pressure and the channel walls open again. Balmforth et al., (2005) extended Julian's study to include the dynamic behavior of the fluid and the elasticity of the surrounding walls. They concluded that magma itself is unlikely to generate flow-induced oscillation, but that rapid flow through fractured rocks of fluids exsolved from magma may. They obtained a critical value for flow speed required for the generation of this so called "roll wave instability". Rust et al., (2008) investigated the conditions for roll wave instability and concluded that roll waves are unlikely in geological context because they require high flow and speeds, but they also pointed out that could occur in the flow of hot, high pressure fluids such as H_2O- and CO_2- rich fluids.

2.2.3 Magmatic-hydrothermal interactions

Magmatic-hydrothermal fluids interactions are one of the first trigger mechanisms proposed for LP events generation (Chouet, 1985). LP seismicity could be generated via boiling and depressurization of ground water (Leet, 1988; Matoza and Chouet, 2010), cyclic collapse and recharge of pressurized hydrothermal cracks (Arciniega-Ceballos et al., 2012; Matoza and Chouet, 2010; Matoza et al., 2009; Nakano, 2005; Ohminato et al., 2006; Waite et al., 2008) or unsteady chocking of a supersonic flow of magmatic steam (Chouet et al., 1994; Morrissey and Chouet, 1997). An example of intensive study of the magmatic-hydrothermal interactions comes from the Kusatso-Shirane Volcano, Japan. This andesitic stratovolcano is surrounded by one of the major hot-spring regions in Japan and LP events have frequently been observed (Fujita et al., 1995; Hamada et al., 1976). The first LP analyses performed (Kumagai, 2002a; Nakano et al., 1998) pointed to the resonance of a crack filled with hydrothermal fluids. Nakano et al., (1998) used the Sompi method (Hori et al., 1989; Kumazawa et al., 1990) to determine the complex frequencies. Thus they

were able to recover a coefficient Q which is function of the resonator geometry and the density of the fluid. Hence Kumagai, (2002a) analyzed a sequence of 35 events recorded on Kusatso-Shirane and was able to infer possible changes in the fluid composition in the LP resonator. Lately Nakano et al., (2003) performed waveform inversion pointing to the existence of a sub-horizontal crack repeatedly excited at ~300 m depth. They proposed a conceptual model for LP generation (Figure 12) based on the increasing of the steam pressure inside the crack due to the underlying magmatic body. A rapid release of this pressure would cause depressurization of the fluid filled crack, triggering its resonance
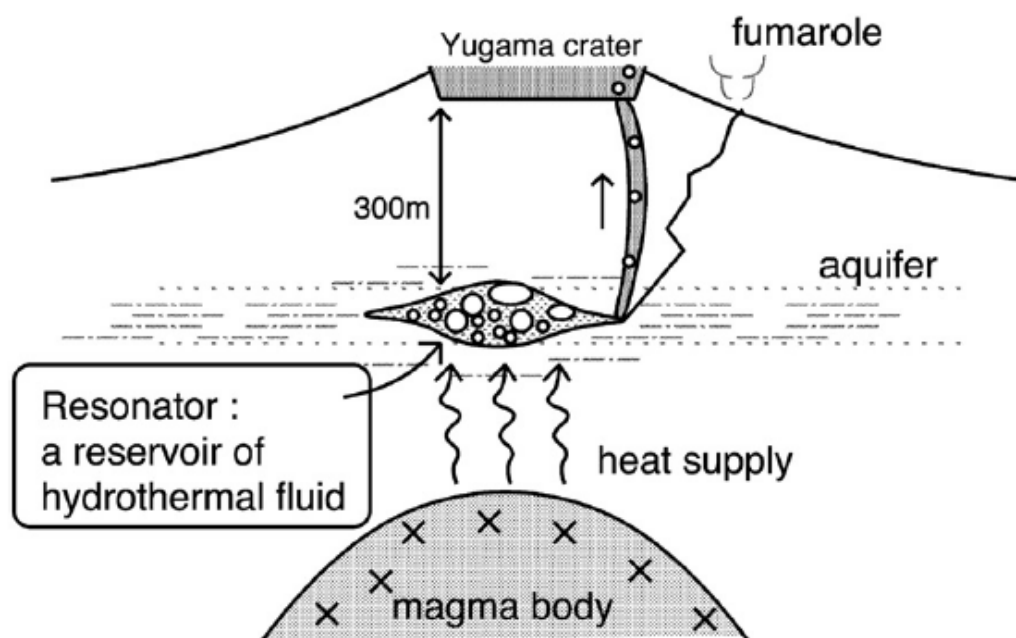
Figure 12 – Schematic view of the source process of LP events at Kusatsu-Shirane Volcano as imagined by Nakano et al., (2003) after waveform inversion. Figure reproduced after Chouet and Matoza, (2013)

which generates harmonics, slowly decaying LP codas. Similar observations linking LP events to magmatic-hydrothermal interactions have been done on a variety of volcanoes including, Kilauea (Almendros et al., 2002; Kumagai et al., 2005; Saccorotti et al., 2001), Redoubt (Chouet et al., 1994; Morrissey and Chouet, 1997; Stephens and Chouet, 2001), Mount St. Helens (Matoza and Chouet, 2010; Matoza et al., 2009; Waite et al., 2008), Popocateptl (Arciniega-Ceballos et al., 2012), Satsuma-Iwokima (Ohminato, 2006), Ontake (Nakamichi et al., 2009), Aso Volcano (Kaneshima et al., 1996; Kawakatsu et al., 2000), Campi Flegrei (D'Auria et al., 2011) and Vulcano (Alparone et al., 2010).

2.2.4 Magmatic degassing

Magmatic degassing has been recognized as trigger mechanism of LP events at many volcanoes worldwide. During the 1991-1992 eruptive crisis at Galeras Volcano, Colombia, Cruz and Chouet, (1997) recognized a correlation between the explosive pulses and the occurrence of LP events and identified a possible crack source mechanism. Davi et al., (2010, 2012) analyzed towards moment tensor inversion some LP signals recorded on Arenal Volcano. Despite the poor network coverage they were able to recover a moment tensor with dominant isotropic components, as would be expected for an isotropic explosion source. Long-period activity is also connected to explosions at Colima Volcano, Mexico (Varley et al., 2010; Zobin et al., 2008) and related to degassing processes at Stromboli and Kilauea volcanoes (Chouet, 2003b; Chouet and Dawson, 2011; Ohminato et al., 1998). In these cases a common interpretation is based on the oscillation of the terminal part of the conduit system induced either by the chocking of the flow or the explosive jet recoil. Palo et al., (2009) imaged for Colima Vulcano a pressure step occurring at depth in the conduit which excites the conduit itself to resonance followed by an upward migration of the source. Another common models relate the decompression-induced degassing and the volatile growth to the increasing pressure in the ascending magma as observed at Tungurahua Volcano (Molina et al., 2008) and at Montserrat (Rowe et al., 2004). The models proposed for magmatic degassing and magmatic-hydrothermal interactions are very similar and contemporary analysis of other geophysical or geochemical signals could help understanding the source mechanism.

2.2.5 Brittle failure of melt

Experimental and numerical studies have recently showed that highly viscous melts can exhibit solid–like brittle behavior (Alidibirov and Dingwell, 1996; Dingwell, 1996; Ichihara and Rubin, 2010; Webb and Dingwell, 1990) in conditions realizable in magma conduits (Collier and Neuberg, 2006; Gonnermann and Manga, 2007; Hale, 2007; Papale, 1999; Thomas and Neuberg, 2012). The process is related to non-Newtonian behavior of

different melt compositions which could experience a transition from viscous-fluid-like to solid-like mechanical behavior (Webb and Dingwell, 1990). Field observations in Iceland (Tuffen and Dingwell, 2005; Tuffen et al., 2003) revealed veins formed in young rhyolitic conduits filled of fragments of magma and broken phenocrystals interpreted as linked to faulting and volcano seismicity. Hybrid-volcanic events (mixed Low/High frequency content) could be generated by such a process. The brittle behavior of part of melt and crystals could result in shear-failure and trigger the resonance of the fluid filled crack generating the LP signal (Neuberg et al., 2006) and so the hybrid event.

Brittle failure of melt for generating LP/hybrid events is a newly topic of increased interest. Its better understanding could provide links between seismicity, extrusion dynamics, magma movement in conduits and also link to ground deformation and tilt (Green and Neuberg, 2006; Neuberg et al., 2006; Voight et al., 1999).

2.2.6 Solid lava dome extrusion

This model for the generation of shallow volcanic seismic events doesn't take in account for a classical fluid filled resonator, but it is referred to a completely different process invoked to explain shallow volcanic seismicity. The eruption of Mount St. Helens in 2004-2008 was characterized by a very regular shallow seismicity with slowly evolving waveforms (Morgan et al., 2008) and for their regular nature these events were termed *drumbeats* (Morgan et al., 2008)*.* Iverson, (2008) and Iverson et al., (2006) proposed a mechanical model for those *drumbeats* events generation. They supposed the existence of a solid plug pulled upward by a constant flux of molten (bubbly) magma at depth in the conduit (Figure 13). Each seismic event would correspond to stick-slip motion of the lava plug. This stick-slip motion would occur on the margins of the lava plug where extrusion is resisted by friction forces. Power and Lalla, (2010) recognized this drumbeats style seismicity in occasion of the 1986 dome building phase and 2006 effusive phase of Augustine, Alaska, but they did not relate this seismicity to be directly caused by the emplacement of lava dome at the volcano's summit.
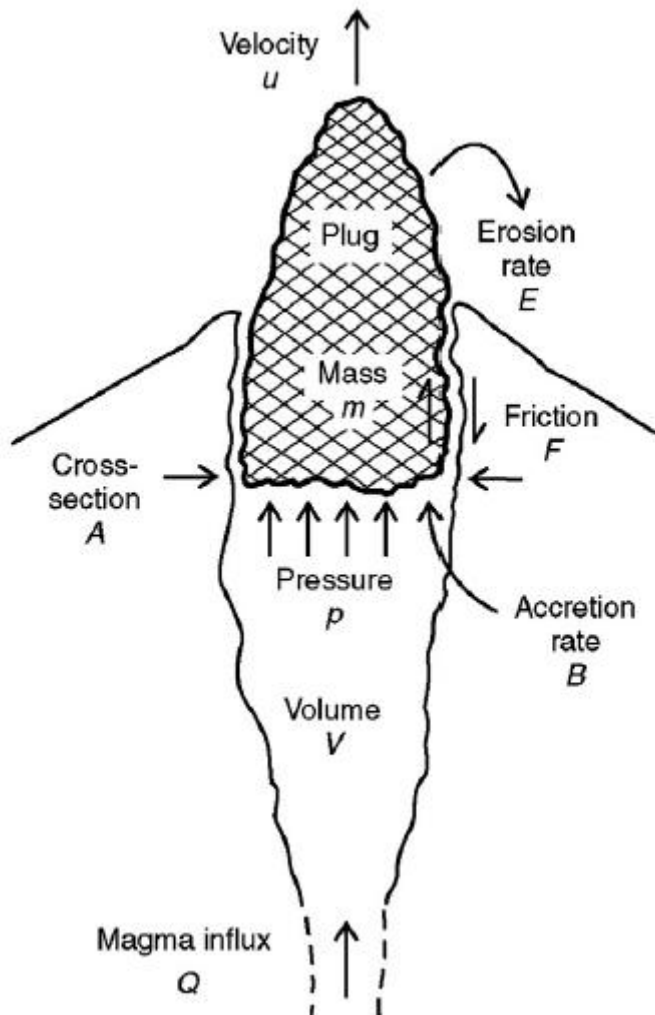
Figure 13 – Cartoon illustrating the conceptual stick-slip model of Iverson, (2008) and Iverson et al., (2006). A constant flux of magma pushes on a rigid plug of solidified magma at the top of the conduit. Earthquakes result from increment slip along the plug margins. Figure reproduced after Chouet and Matoza, (2013) and Iverson et al., (2006).

2.2.7 Slow-rupture earthquakes

Recently, Bean et al., (2014) proposed a new model for explaining shallow LP seismicity. They analyzed the pulse-like nature of some LP events recorded on volcanoes. For instance, in occasion of the 2008-2009 eruption of Mt. Etna (De Barros et al., 2009, 2011), they recognized that, while summit stations recorded pulse-like low-frequency signals, the same records on further stations appeared as classical resonating LP signals. They attributed the apparent resonance of these low-frequency seismic events caused by propagation effects and not being source related. They supported this new theory with

some laboratory experiments where they recognized that the corner frequency of LP events does not scale with events size (supposing that fixed crack geometry and stiffness are necessary conditions for resonance). They showed an example from 2004 field campaign on Mt. Etna where the corner frequency of events scales with moment magnitude and attributed those events as caused by dry failure. Their model hypothesizes that these LP events are consequence of failure in materials close to the brittle-ductile transition. The brittle-ductile transition in shallow volcanic material is not supposed to be related to high temperature and pressure, but to the low friction angles of the unconsolidated shallow volcanic deposits.

2.3 Source characterization

2.3.1 Representation Theorem

As seen in the previous section, seismic waves in a volcano can be set up by sources external to the edifice such as eruptions, explosions, pyroclastic flows, landslides and by internal sources such as shear failures, opening of pathways associated to fluid transport and tractions on conduit surfaces due to viscous fluid flow (Chouet, 1996). In order to represent all this possible effects on the displacement field recorded at a point $\mathbf{x}$ at a time t in the medium, I expand the representation theorem of Equation (13) including body forces (Ohminato et al., 1998), according to Aki and Richards, (2002)

$$
\begin{aligned}
u_n(\mathbf{x}, t) = &\int_{-\infty}^{\infty} d\tau \iiint_V f_p(\eta, \tau) G_{np}(\boldsymbol{x}, t - \tau; \eta, 0) dV(\eta) \\
&+ \int_{-\infty}^{\infty} d\tau \iint_\Sigma \left\{ \left[[u_i(\xi, \tau)] c_{ijpq} v_j \frac{\partial}{\partial \xi_q} G_{np}(\boldsymbol{x}, t - \tau; \xi, 0) \right] \right. \\
&\left. - \left[G_{np}(\boldsymbol{x}, t - \tau; \xi, 0) T_p(\boldsymbol{u}(\xi, \tau), \boldsymbol{v}) \right] \right\} d\Sigma
\end{aligned}
$$

(43)

where the new terms are: $f_p(\eta, \tau)$, a force applied in the *p*-direction at a point $\boldsymbol{\eta}$ within V at time τ and $T_p(\boldsymbol{u}(\xi, \tau), \boldsymbol{v})$, the stress discontinuity at ξ at time τ. Equation (43) states

that the displacement $\boldsymbol{u}$ at a point $\boldsymbol{x}$ is made up from the sum of the contributions due to body forces f throughout V, displacement $\boldsymbol{u}$ on ξ, and tractions $T(\boldsymbol{u}, \boldsymbol{v})$. For long waves (wavelengths much longer than the dimension of the source volume), the whole source can be considered as a point source and the force system equivalent to this source is localized at a point at the center of the source volume (Chouet, 1996). In the first chapter I developed the expression for the displacement $\boldsymbol{u}$ due to a displacement discontinuity over the surface Σ at the source (Equation (16)). Assuming an isotropic medium, the contribution from traction discontinuities has the dimension of a force and can be expressed as (integrating over Σ)

$$F_p^{[T]} = - \iint_{\Sigma} [T_p] d\Sigma$$

(44)

so that the contribution to $\boldsymbol{u}$ from the traction discontinuity is given by the convolution $F_p^{[T]} * G_{np}$. Similarly, integrating the body force over the volume V I obtain the contribution from the point force as the convolution $F_p * G_{np}$. The contributions from $F_p^{[T]}$ and F_p are assumed to originate from different processes, but they can be grouped in a single term (Chouet, 1996). Thus the representation theorem for point sources can be written as

$$u_n(\boldsymbol{x}, t) = M_{pq} * G_{np,q}(\boldsymbol{x}, t) + F_p(t) * G_{np}(\boldsymbol{x}, t) \qquad n, p = 1, 2, 3$$

(45)

which expresses the nth-component of displacement in terms of nine unknowns, namely, the three components of the force $\boldsymbol{F}$ and the six independent components of the moment tensor $\boldsymbol{M}$ (Aki and Richards, 2002; Chouet, 1996).

2.3.2 Green's functions

In the representation theorem (Equation (45)) the force and the moment terms are convoluted with $\boldsymbol{G}_{np}$ and $\boldsymbol{G}_{np,q}$ which represent the nth-component of the corresponding medium responses (Green's functions) and their derivatives, respectively. Green's

functions are computed taking advantage of the reciprocity theorem (Aki and Richards, 2002; Auger et al., 2006)

$$G_{np}(r;s) = G_{pn}(s;r) \tag{46}$$

where I omit the *t* (time) term and $G_{np}(r;s)$ expresses the nth-component at *r* (receiver) due to an unit impulse applied in the *p*-direction at *s* (source). For the moment components I'm looking for the spatial derivative that is

$$
\begin{aligned}
G_{np,q}(r;s) &= \frac{\partial G_{np}(r;s)}{\partial s_q} \\
&= \lim_{\Delta s_q \to 0} \frac{G_{np}(r;s + \Delta s_q) - G_{np}(r;s)}{\Delta s_q} \\
&= \lim_{\Delta s_q \to 0} \frac{G_{pn}(s + \Delta s_q; r) - G_{pn}(s;r)}{\Delta s_q} \\
&= \frac{\partial G_{pn}(s;r)}{\partial s_q}
\end{aligned}
\tag{47}
$$

Using the expressions outlined above (Equation (46) and (47)), the three components of displacement can be calculated at each source node for an impulsive force applied in the *x*, *y* and *z* directions at each receiver of the network (Auger et al., 2006). Thus, for many sources, the number of computations reduces at three times the number of receivers.

2.3.3 Moment Tensor Inversion

The source mechanism for LP events is usually determined by full moment tensor inversion (e.g. Auger et al., 2006; De Barros et al., 2011; Chouet, 2003; Eyre et al., 2013; Kumagai, 2002b; Ohminato, 1998). Here I show the main equations needed to solve a moment tensor inversion for determining the source characteristics.

In the frequency domain convolution becomes multiplication, thus the representation theorem (Equation (45)) can be written as (Menke, 1989)

$$u_n(\boldsymbol{x}, \omega) = M_{pq}(\omega) G_{np,q}(\boldsymbol{x}, \omega) + F_p(\omega)\, G_{np}(\boldsymbol{x}, \omega)$$

(48)

This equation is solved separately for each frequency and results are then transformed again in time domain using an inverse Fourier transform. If I write Equation (48) in matrix form

$$\boldsymbol{u} = \boldsymbol{Gm}$$

(49)

where **u** is the data matrix, **G** contains the Green's functions and **m** is the moment tensor and single forces components. If N is the number of seismograms used in the inversion, Equation (49) can be written in explicit form as (Dahm, 2014; Davi et al., 2010)

$$
\begin{bmatrix} u_1 \\ u_2 \\ u_3 \\ \vdots \\ \vdots \\ u_N \end{bmatrix}
=
\begin{bmatrix}
g_{11,1} & g_{12,2} & g_{13,3} & g_{11,2} & g_{11,3} & g_{12,3} & g_{11} & g_{12} & g_{13} \\
g_{21,1} & g_{22,2} & g_{23,3} & g_{21,2} & g_{21,3} & g_{22,3} & g_{21} & g_{22} & g_{23} \\
g_{31,1} & g_{32,2} & g_{33,3} & g_{31,2} & g_{31,3} & g_{32,3} & g_{31} & g_{32} & g_{33} \\
\vdots & \vdots & \vdots & \vdots & \vdots & \vdots & \vdots & \vdots & \vdots \\
\vdots & \vdots & \vdots & \vdots & \vdots & \vdots & \vdots & \vdots & \vdots \\
g_{N1,1} & g_{N2,2} & g_{N3,3} & g_{N1,2} & g_{N1,3} & g_{N2,3} & g_{N1} & g_{N2} & g_{N3}
\end{bmatrix}
\cdot
\begin{bmatrix} M_{11} \\ M_{22} \\ M_{33} \\ M_{12} \\ M_{13} \\ M_{23} \\ F_1 \\ F_2 \\ F_3 \end{bmatrix}
$$

(50)

The quality of the inversion process is then tested by comparing original and calculated data by evaluating the misfit (R) function as

$$R = \frac{(\boldsymbol{u} - \boldsymbol{Gm})^T \boldsymbol{W}\, (\boldsymbol{u} - \boldsymbol{Gm})}{\boldsymbol{u}^T \boldsymbol{Wu}}$$

(51)

where **W** is a diagonal matrix of the weights of the quality of waveforms. The lowest value of misfit R indicates the best solution for **m**. **m** is solved by least squares solution as (Menke, 1989)

$$\boldsymbol{m}^{est} = (\boldsymbol{G}^T \boldsymbol{WG})^{-1} \boldsymbol{G}^T \boldsymbol{Wu}$$

(52)

where superscript T denotes transpose matrix and **m**^{est} is the estimated moment tensor

matrix. As I don't make any a priori assumptions about the mechanism, the solution is unconstrained and I can solve independently for six moment tensor components (MT-only) or moment tensor plus three forces (MT+F).

   In case of a crack or a pipe I will extract also information about the orientation of the physical source responsible for the recorded signals. I will use the constrained inversion description proposed by Lokmer et al., (2007)

$$\boldsymbol{d} = \boldsymbol{G}\, M_0\, \boldsymbol{f}(^{\lambda}\!/_{\mu}\,,\phi,\theta)$$

(53)

where f is a column vector containing the six functions of Lame's constants. I will take constant values for the source medium properties (λ and μ) and invert the signals for two spherical angles ϕ (strike) and θ (dip). $\boldsymbol{f}$ is independent from frequency so the inversion reduces to the search for a unique parameter $M_0(\omega)$ in the frequency domain. I will perform constrained inversion for three different source mechanisms (explosion, crack and pipe) following the description proposed in Equations (23),   (31) and (41) respectively.

2.3.4 Single Forces

   The second term (**F**) of the representation theorem (Equation (45)) is related to three components of single forces (SFs) and is often included in moment tensor (MT) inversions (Ohminato et al., 1998). The recovered SFs often have a large amplitude (De Barros et al., 2011; Ohminato, 2006) and so their contribution to the solution has been questioned by different authors. Theoretical considerations (Takei and Kumazawa, 1994) and laboratory experiments (James et al., 2004) showed that SFs can be generated by mass transfer or by viscous fluid movement in the volcano and are often interpreted as magma upwelling in the conduits (Chouet, 2003b; Ohminato, 2006). However, recent interpretations point out that uncertainties in both velocity structure and source location can lead to the reconstructions of spurious SFs (Bean et al., 2008; Chouet, 2003b; De Barros et al., 2011, 2013; Ohminato et al., 1998). De Barros et al., (2013) investigated the role of SFs on the retrieved solution in a synthetic test for different MT inversion

scenarios. They stated that spurious SFs are likely to be recovered when the velocity model is incorrect. Higher errors arise when a (realistic) shallow low-velocity layer is not included in the velocity model and spurious SFs can also be recovered to accommodate converted waves generated at layer interfaces.

More generally, SFs are of difficult interpretation and their role in volcanic conduits is still in debate. Even with a high resolution network of stations just above a shallow LP source their presence can be unambiguously interpreted. Thus, in my MT inversions, I will tend to interpret SFs as accommodating errors in the velocity model and in source location (De Barros et al., 2013).

2.3.5 Singular Value Decomposition

Once the unconstrained inversion performed, I end up with nine (three forces + six moments) functions in time representing the time history of my source process. The six moment tensor functions contain information about the type of source mechanism (tensile, double-couple, CLVD, see next section) and its orientation angles. In order to extract such information I suppose that the source mechanism is simple enough that the geometry of the source can be separated from its time variation, so that the moment tensor can be written in the simple form (Madariaga, 2007)

$$\boldsymbol{M}_0(t) = \boldsymbol{M}s(t) \tag{54}$$

where $\boldsymbol{M}$ is a time-invariant tensor that describes the geometry of the source (as outlined in Equations (23), (31) and (41) and $s(t)$ is the time variation of the moment. The aim is to obtain a 3x3 matrix of constant values (the moment tensor) and then perform an eigenvalues/eigenvectors decomposition to get information about the source orientation and the mechanism type. In order to get $\boldsymbol{M}$ I can apply two methods: a) the first, proposed by Chouet, (2003), consists in taking the maximum peak-to-through amplitude of each individual moment function; b) the second, proposed by Vasco, (1989), consists in performing a singular value decomposition (hereafter "SVD") of the moment functions. The two methods show results which are roughly equivalents, however, the first method lack information about the truthfulness of the assumption that a single source time

function is enough to describe the source behavior. Hence, I choose to use the SVD method, here a brief review.

Factors such as source complexity, noise and lateral heterogeneities all introduces nonuniqueness in the source time function (hereafter "STF"). The technique of principal component analysis (through SVD) is used to factor the moment tensor into a set of orthogonal STFs (Vasco, 1989). SVD is applied to the data matrix **M** (Joreskog et al., 1976; Menke, 1989; Savage, 1988; Vasco, 1989) which is decomposed in three matrices

$$\boldsymbol{M} = \boldsymbol{U}\Lambda\boldsymbol{V}^{T} \tag{55}$$

where Λ (*n x m*) is a matrix of function weights and **U** (*n x n*) and **V** (*m x m*) are matrices related to the eigendecomposition of **M**, as **U** are the eigenvectors of **MM**$^{\mathsf{T}}$ and **V** are the eigenvectors of **M**$^{\mathsf{T}}$**M**. For uniqueness, orthogonality conditions are imposed

$$\begin{aligned} \boldsymbol{U}\boldsymbol{U}^{T} &= \boldsymbol{I} \\ \boldsymbol{V}\boldsymbol{V}^{T} &= \boldsymbol{I} \end{aligned} \tag{56}$$

where **I** is the identity matrix and has dimensions *n x n* and *m x m* in the first and the second case, respectively (Menke, 1989; Savage, 1988). For my purposes, the product $\Lambda\mathbf{V}^{\mathsf{T}}$ represents the source-time basis functions, the diagonal of Λ contains the basis coefficients for the basis functions (i.e. how much each function contributes to the main solution) and **U**Λ are the coefficients of each tensor related to each basis function (i.e. six values corresponding to one single basis function times the number of basis functions). In order to better understand the behavior of the SVD I show here, as an example, a test performed on a simple tensile crack.

I follow Equation (31) and compute the moment tensor for a vertical crack defined by directions ϕ=45° and θ=90° and Lamé's parameters computed for *Vp* = 3221 m/s, *Vs* = *1860* m/s and density ρ = 2335 kg/m^3 following Equations (11) and (12). The volume variation ($\mu\Delta V$) in time is represented by a Ricker function (Equation (42)) normalized by its maximal amplitude variation and multiplied by M_w (moment magnitude), with

$$M_w = 10^{(1.5M_L + 9.1)} \tag{57}$$

and

$$s(t) = \mu \varDelta V M_w \tag{58}$$

where M_L is the Ricker Magnitude ($M_L=1$ in this case). Applying Equation (54) I obtain six independent moment functions which describe the point source equivalent for the vertical tensile crack described above (Figure 14). I then compute the SVD on the moment
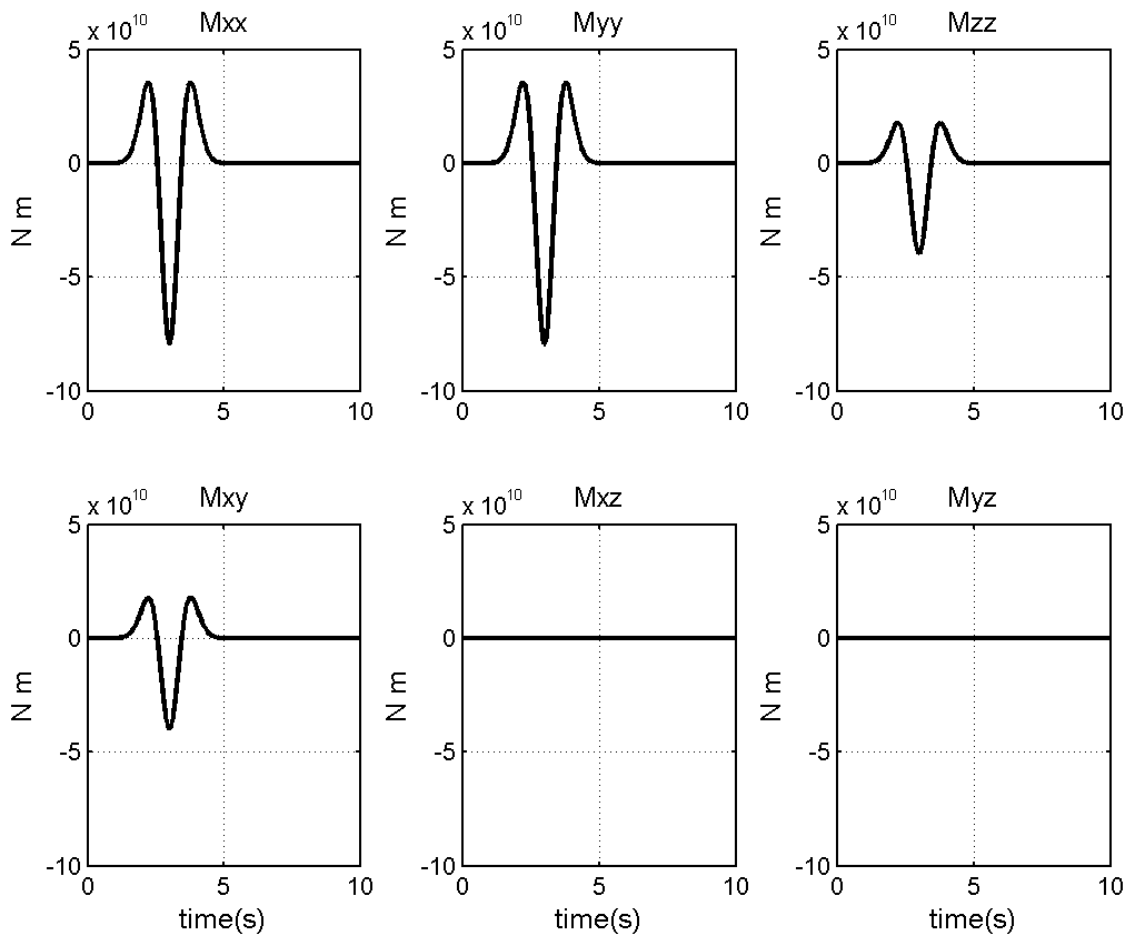
Figure 14 – Six moment tensor functions for the test case of a vertical, 45° oriented, tensile crack.
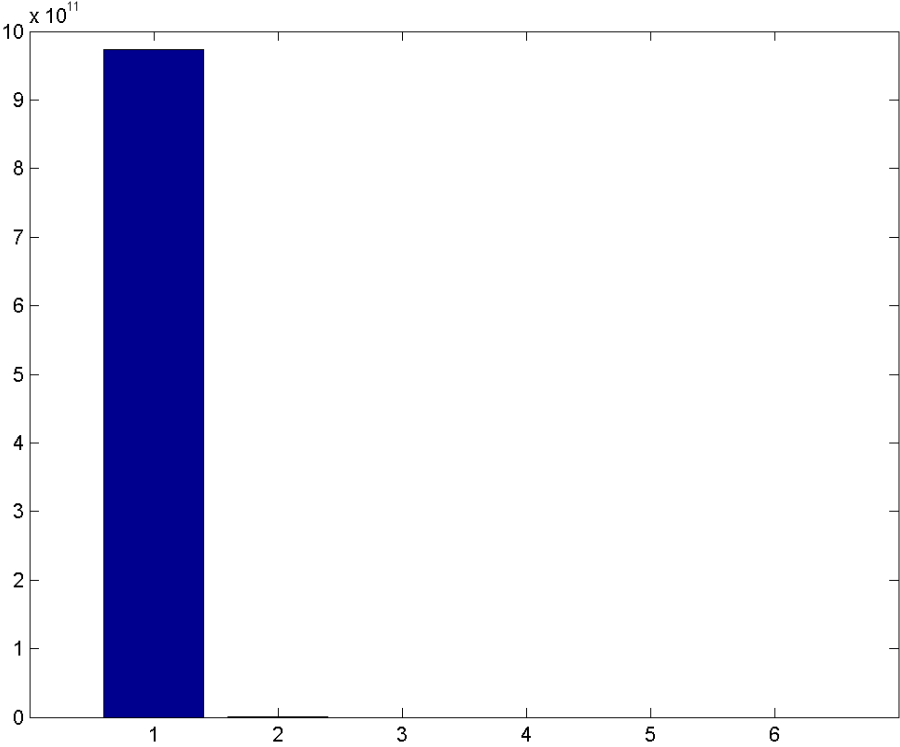
*Figure 15 – Histogram representing the six **Λ** function weights after performing SVD on the moment functions of Figure 14.*
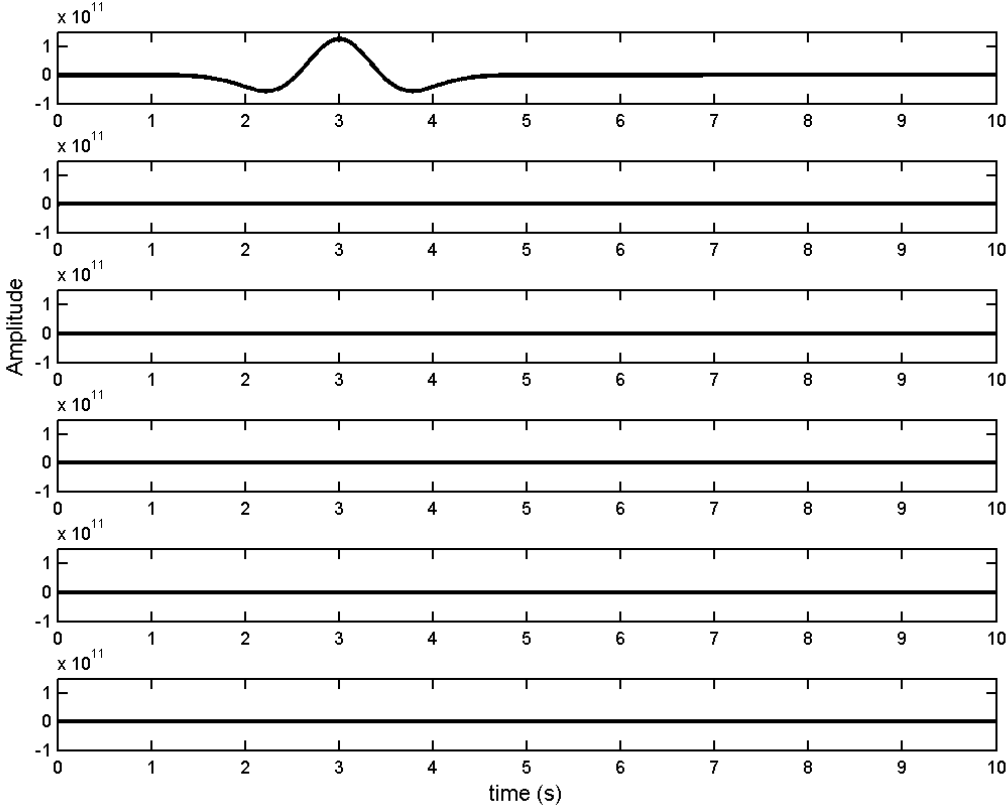
*Figure 16 – Six basis functions (**Λ**v^T) after SVD decomposition of the vertical crack of **Figure 14**. The first basis function at the top shows the highest amplitude and can be considered as contributing alone to the solution.*

functions and obtain the six Λ coefficients. I consider that my entire source mechanism can be fully described by a singular STF when the first value of Λ is at least double of the second (Lokmer et al., 2007). In this special case, the first value is way higher than the second (Figure 15), it means that the first basis function $\Lambda \mathbf{V}^{\mathsf{T}}$ (Figure 16) can fully explain the moment tensor time evolution. I end up performing an eigenvalues/eigenvectors decomposition on the first column of $\mathbf{U}\Lambda$ and, as anticipated, I obtain normal vectors orientation of $\phi=45°$ and $\theta=90°$ and eigenvalues ratio of (1:1:3) as expected for a tensile crack source.

2.3.6 ISO, DC and CLVD decomposition

The moment tensor as obtained from the MT inversion and the SVD has not a direct physical explanation thus, to make it easier to understand and interpret, it is decomposed into elementary force system. First, I express the moment tensor in its principal axis coordinate system by performing a diagonalization (Dufumier and Rivera, 1997). Three values are required to express the orientation of this system, and three other values specify the moments of three orthogonal dipoles oriented parallel to the coordinate axes (Julian et al., 1998). Thus the matrix **M**, after diagonalization, is decomposed into an isotropic force system ($\mathbf{M}_{\mathrm{ISO}}$) and a deviatoric remainder ($\mathbf{M}^{*}$). $\mathbf{M}^{*}$, in turn, is divided in compensated linear vector dipole ($\mathbf{M}_{\mathrm{CLVD}}$) and double-couple ($\mathbf{M}_{\mathrm{DC}}$) components as (Jost and Herrmann, 1989; Knopoff and Randall, 1970)

$$\boldsymbol{M} = \boldsymbol{M}_{ISO} + \boldsymbol{M}_{CLVD} + \boldsymbol{M}_{DC} \tag{59}$$

where

$$\boldsymbol{M}_{ISO} = \frac{1}{3} tr(\boldsymbol{M}) \begin{bmatrix} 1 & 0 & 0 \\ 0 & 1 & 0 \\ 0 & 0 & 1 \end{bmatrix}$$

$$\boldsymbol{M}_{CLVD} = |\varepsilon| M^{*}_{|max|} \begin{bmatrix} -1 & 0 & 0 \\ 0 & -1 & 0 \\ 0 & 0 & 2 \end{bmatrix}$$

$$\boldsymbol{M}_{DC} = (1 - 2|\varepsilon|)M^*_{|max|} \begin{bmatrix} -1 & 0 & 0 \\ 0 & 0 & 0 \\ 0 & 0 & -1 \end{bmatrix}$$

Parameter ε measures the size of CLVD relative to DC (Julian et al., 1998) and is defined as

$$\varepsilon = -\frac{M^*_{|min|}}{\left|M^*_{|max|}\right|} \tag{60}$$

where $M^*_{|max|}$ and $M^*_{|min|}$ are the eigenvalues of deviatoric moment $\boldsymbol{M}^*$ with the maximum and minimum absolute values, respectively. In principle, ε could range between -0.5 and 0.5, and should be zero for a perfect double-couple. In order to compute the percentage of each component relative to the others I use the formulas proposed by Vavryčuk, (2001) as

$$c^{ISO} = \frac{1}{3}\frac{tr(\boldsymbol{M})}{\left|M_{|max|}\right|}100\% \tag{61}$$

$$c^{CLVD} = 2\varepsilon(100\% - |c^{ISO}|) \tag{62}$$

$$c^{DC} = 100\% - |c^{ISO}| - |c^{CLVD}| \tag{63}$$

where $M_{|max|}$ denotes the eigenvalue of $\boldsymbol{M}$, which has the maximum absolute value. The DC percentage is always positive, the ISO and CLVD percentages are positive for tensile sources, but negative for compressive sources. The sum of their absolute values is 100%. The decomposition of the moment tensor can give indications on the nature of the source of the seismic events. Different ratios of c^{ISO}, c^{CLVD} and c^{DC} can give rise to many different interpretations (Vavryčuk, 2015). For instance (refer to Figure 17 for wave radiation patterns examples of each source mechanism):

1) *full isotropic source* ($c^{ISO} = \pm1$) can be interpreted as an explosion;
2) *shear faulting* has full double couple components ($c^{DC} = 1$);

3) ***pure CLVD*** ($c^{CLVD} = 1$) sources have a double-strength force couple along one axis, and unit-strength force couples in the direction of the two perpendicular directions (Lay and Wallace, 1995). CLVD sources have been related to tensile microseismic events that occur in hydraulic fracturing context (Nolen-Hoeksema and Ruff, 2001);

4) ***mixed shear-tensile*** dislocation is also a possible scenario (Vavryčuk, 2001, 2015) where both shear and tensile faulting are combined and is characterized by non-zero c^{ISO}, c^{CLVD} and c^{DC} components.
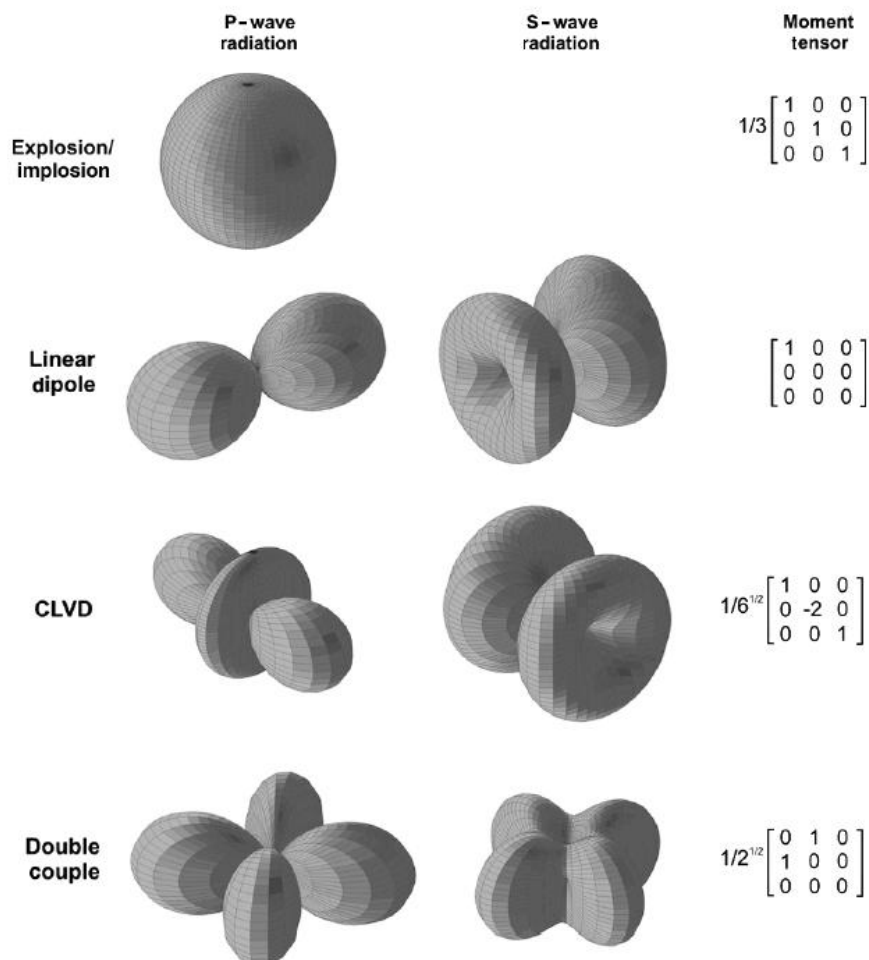
Figure 17 – P-wave and S-wave radiation patterns and representative moment tensors for four different seismic source types. CLVD denotes compensated linear vector dipole. Figure reproduced after (Eaton and Forouhideh, 2011).

Vavryčuk, (2001) developed a method to get insights into a tensile earthquake mechanism. A tensile earthquake could be imagined as tensile faulting combined to a

small amount of shear faulting. It can be described using a slip vector which is not strictly oriented in the same plane as the fault plane, i.e. it deviates from the fault plane producing some kind of tensile opening or closing of the fracture. Thus, the slip vector ($[\vec{u}]$) forms an angle (α) with the fault plane (Σ) as (Figure 18)

$$\alpha = sin^{-1}\left(3\frac{M^*_{max} + M^*_{min}}{|M^*_{max}| + |M^*_{min}|}\right) \tag{64}$$

The angle between the normal to the fault and the tension ($\vec{T}$) axis is

$$\beta = 45° - \alpha/2 \tag{65}$$
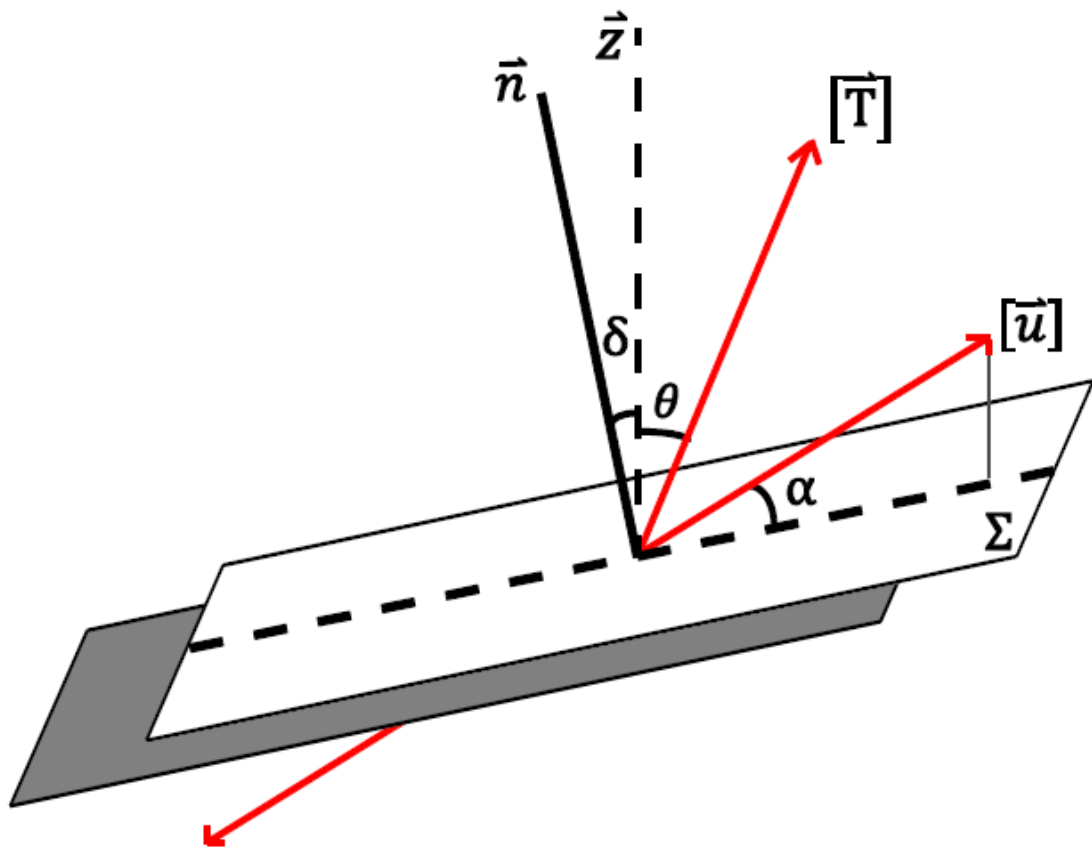
Figure 18 – Mixed tensile/shear faulting earthquakes angles definition. Figure reproduced after Eyre et al., 2015.

The angle (θ) between the tension axis and the vertical is computed using the eigenvectors of the moment tensor solution. Thus the orientation of the fault plane from

the vertical is computed as

$$\delta = \theta - \beta \tag{66}$$

Vavryčuk, (2001) also proposed a simple relationship to compute the λ/μ ratio (κ) of the medium surrounding the source region as function of c^{CLVD} and c^{ISO} as

$$\kappa = \frac{4}{3}\left(\frac{c^{ISO}}{c^{CLVD}} - \frac{1}{2}\right) \tag{67}$$

In the next section I will give some indications on how to interpret the results after the moment tensor decomposition. Special attention is given to the determination of the volume involved in the source process with a brief discussion of the Mogi, (1958) problem.

2.4 The Mogi Problem

Trying to relate the moment tensor decomposition to a real physical mechanism is not straightforward. Things become harder when a single component is not predominant on the others. As I am dealing with shallow long-period signals recorded on volcanoes I assume that the source process is related to mass movements and triggered resonance phenomena occurring in a fracture (e.g. De Barros et al., 2011; Chouet, 1996; Chouet and Matoza, 2013; Gilbert and Lane, 2008; Madariaga, 2007). Both processes could take place in a complicate interconnected system of fractures of different dimensions which are traversed by a mixture of melt rocks or water and gases (e.g. Kumagai and Chouet, 2000; Kumagai et al., 2005; Ohminato, 1998). The movement of this mixture is supposed to be triggered by pressure variations (Nakano et al., 2003). Thus, part of the displacement of the crack walls could result in a static permanent displacement that can be connected to the isotropic (M^{ISO}) part of the moment tensor. The simplest case I can consider is a spherical source without deviatoric ($\mathbf{M}^*$) components. I want to find the connection between a real system of forces, which could be the ΔP (pressure) exercised uniformly on the wall surface of the sphere, and the equivalent moment tensor magnitude. The aim is

to compute the volume variation of the hypothetical sphere to quantify the amount of gas/liquid involved in the process.

Mogi, (1958) proposed an analytical formula to compute the static permanent displacement at the surface due to an explosion source at a certain depth. He assumed that the Earth's crust is an ideal semi-infinite elastic body and that the deformation at the surface is caused by the spherical source with hydro-static pressure change.   The analytical formulas in his compact form are:

$$\Delta d = \frac{3a^3 P}{4\mu} \frac{d}{(f^2 + d^2)^{3/2}} \tag{68}$$

$$\Delta h = \frac{3a^3 P}{4\mu} \frac{f}{(f^2 + d^2)^{3/2}} \tag{69}$$

where Δd and Δh are the radial and vertical displacement at the surface, a is the radius of the sphere with the hydrostatic pressure, P is the hydro-static pressure variation, f is depth of the center of the sphere, d is radial distance on the surface from the center and μ is a Lame's constant. Mogi, (1958) validated his formula by obtaining good correspondence between his computed values for ground deformation and field data collected on some Japanese volcanoes in the first half of 20th century. The good correspondence was obtained for $a \ll f$, it means a sphere of small radius embedded at a considerable depth. Even if the analytical solution has been designed for long-period deformations, I can apply the same to the sudden elastic displacement induced by a seismic source.

2.4.1 Moment magnitude for an explosion

The deformation of the volcanic edifice is treated like an elastic response of the volcano to an excess magmatic pressure at depth (Anderson, 1937; Battaglia et al., 2003; Bonafede et al., 1986; Delaney and McTigue, 1994; Gudmundsson, 2006; McTigue, 1987; Mogi, 1958). The parameters which control this static displacement are the ΔP, the radius of the sphere a and its depth f (Figure 19). The process producing this static permanent

displacement at the free surface is directly related to the volume variation of the walls of
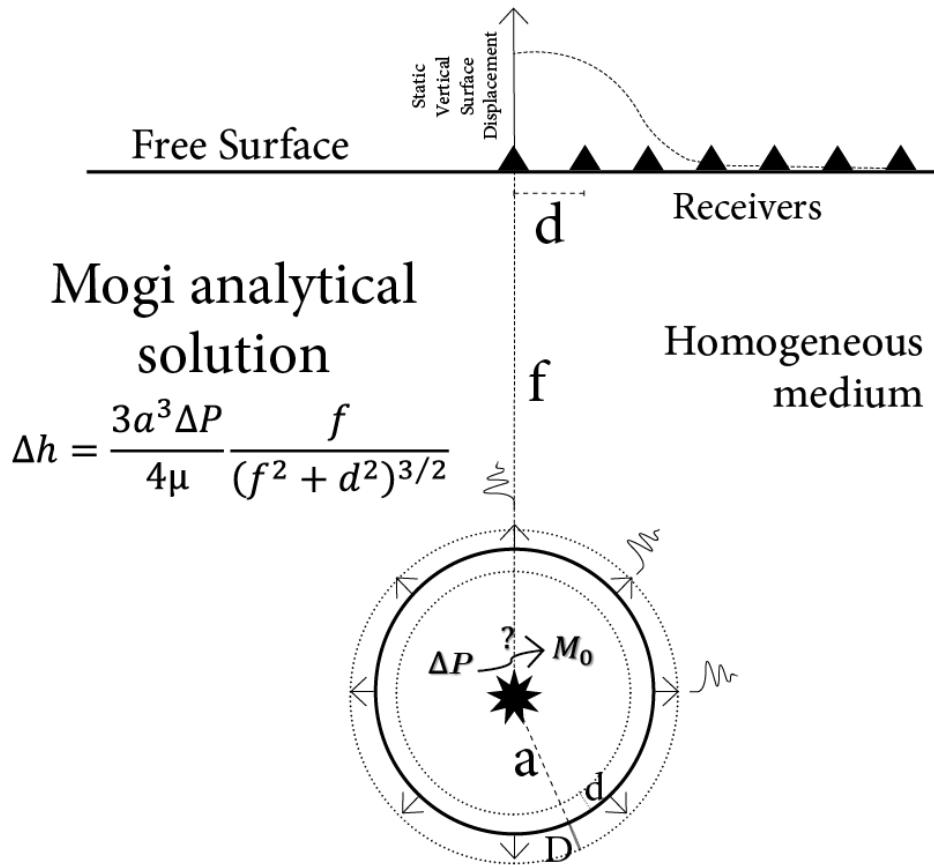
*Figure 19 – Schematic representation of the Mogi problem. A **ΔP** is imposed on the sphere wall at depth and a static vertical displacement is recorded at the surface. **a** is the radius of the sphere, **f** the sphere depth, **D** and **d** represent the external and internal displacement of the wall's sphere respectively. The analytical solution of Mogi, (1958) for the static vertical displacement recorded at the surface is reported as an example. The key point is how to express the **M₀** at source in function of the **ΔP** imposed at the sphere wall.*

the sphere. Two main approaches are present in literature to relate the volume expansion of a sphere and the isotropic moment of the signals recorded at the free surface: the first derived by Eshelby, (1957)

$$M_0 = \left(\lambda + \frac{2}{3}\mu\right)\Delta V \tag{70}$$

and the second proposed by Muller, (1973)

$$M_0 = (\lambda + 2\mu)\delta V \tag{71}$$

in both equations M_0 is the isotropic moment, λ and μ are the Lame's parameters of the homogenous isotropic elastic medium and ΔV and δV are the tensile expansion of the external wall of the sphere induced by the explosion. ΔV and δV are referred to the same process but I use a different notation following the work of Richards, (2005) who states that their use is similar but they are referred to the computation of two slightly different volume variations. The works of Muller, (2001) and Richards, (2005) are complementary and both threat the issue of which of the two Equations (70) or (71) better quantify the energy released (by meaning of the volume variation) by an explosive source at depth. For Richards, (2005) Equation (70) is related to the volume variation in case the source has no confining hydrostatic pressure (the so called "*unconfined volume change*"), so it's free to expand without constraints, while equation (71) should reflect the real case where the hydrostatic pressure at depth of the sphere is considered and the volume expansion is limited by the surroundings. For Muller, (2001) the two equations simply reflect two extreme cases of volume variation related to the shape of the source. Equation (70) should correspond to a crack (a volume with one dimension much smaller than the two others) while equation (71) should correspond to a sphere. The two computed values for ΔV and δV should simply give a range of possible volume variations for different source shapes. The best solution for the computation of the moment magnitude of our problem should be Equation (71) because I'm looking for the moment magnitude of a sphere embedded at a certain depth, so confined by a certain hydrostatic pressure. I will test both two approaches in order to find the best solution.

2.4.2 Volume Variation

The main issue is to relate the volume variation to the ΔP imposed on the wall of the sphere. Different approaches are present in literature to relate the ΔP to the radius expansion D (say from a to $a + D$) (Aki and Richards, 2002; Gottsmann, 2006; Masterlark, 2007; Muller, 2001; Wielandt, 2001). Among all the different approaches I will focus on the solutions proposed by Aki and Richards, (2002) and Muller, (2001). Both two approaches

of equations (70) and (71) will be used to compute the isotropic moment (M_0). I obtain the volume variation by the displacement of the sphere's wall using the formula (Aki and Richards, 2002)

$$\Delta V = 4\pi a^2 D$$

(72)

where *D* is the external displacement of the external wall.

2.4.2.1 Aky & Richards (2002)

The first solution comes from Aki and Richards, (2002). In chapter 3 they propose some problems connected to the quantification of the radial displacement of the external wall of a sphere. Following their equations the pressure variation can be related to the external displacement by

$$D = \frac{\Delta P\ a}{4\ \mu}$$

(73)

This solution applies in the case the expansion is able to attain his "*stress-free*" value, it means that the effects of the confining pressure of the medium are not taken in account. Hereafter, I refer to this solution as "*Aki & Richards I*".

A second solution from Aki and Richards, (2002) takes in account for the confinement of the source region. They propose to compute a constant of proportionality

$$A = \frac{\Delta P}{3\lambda + 2\mu}$$

(74)

such that the static radial displacement of the sphere wall is

$$D = Aa$$

(75)

Like expected the second solution leads to lower volume expansion values. Hereafter, I refer to this solution as *"Aki & Richards II"*.

2.4.2.2 Muller (2001)

In the approach followed by Muller, (2001) the author makes a distinction between an internal and an external displacement. He imagines that the wall of the sphere, after the application of ΔP, moves before outward (D) and then inward (d), the sum of the two displacement is $D_0 = D + d$ (Figure 19). To compute such displacements he introduces a second constant of proportionality

$$B = \frac{\Delta P \; a^3}{4 \; \mu}$$

(76)

then he computes the total displacement

$$D_0 = \left(\frac{B}{a^2}\right) - Aa$$

(77)

and the external displacement

$$D = \frac{\left(\lambda + \frac{2\mu}{3}\right) D_0}{\lambda + 2\mu}$$

(78)

Following the definition proposed by the author, the isotropic moment is computed by means of Equation (70) using the D_0 value for the total displacement (internal + external), and by means of Equation (71) using the D value for the external displacement.

2.4.3 Comparison and results

I will now test the different approaches solutions computed with EFISPEC3D and compare the results with the analytical solution of Mogi in order to validate the best approximation. Geometry and model parameters are as follow. The modeled medium is a

cube (x 50 km, y 50 km, z 50km). The large size becomes from the intent to avoid artificial reflections from the boundaries. I choose a homogenous medium with Vp = 3464.1 m/s, Vs = 2000 m/s and density ρ = 2600 Kg/m^3 in order to obtain Lame's parameters λ = μ as often assumed in classic seismological problems. The source is an explosive source (sphere source) embedded at depth. I test two different cases (one with the source at 1000 m depth, the second with the source at 2000 m depth). According to definition given by Mogi, (1958) the sphere source radius is much smaller compared to the source
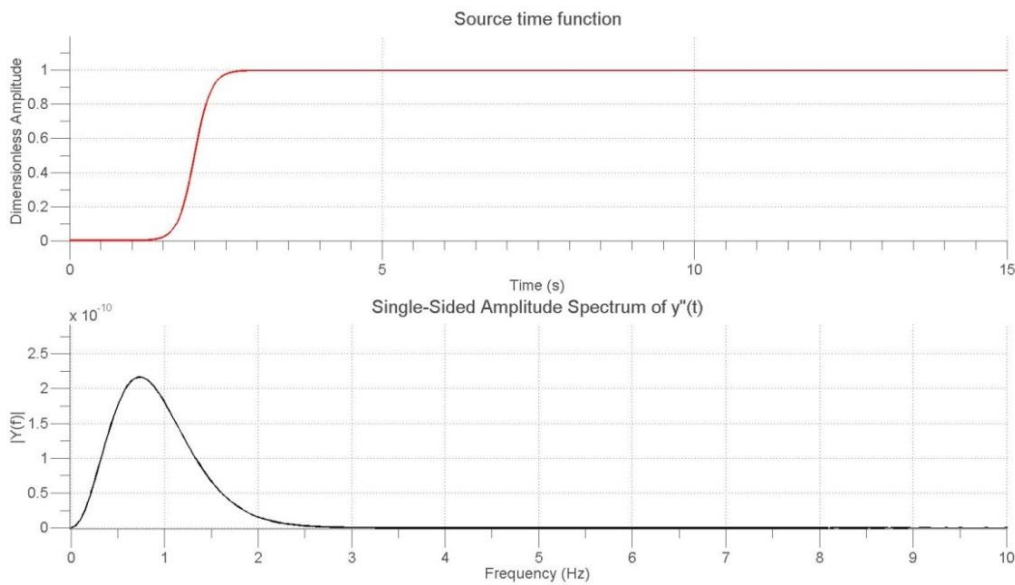
Figure 20 – Step source time function used to simulate the static permanent displacement of the sphere wall numerically (top). The spectrum of the STF (bottom) with a frequency content lower than 3 Hz.

Table 1 – Geometric configuration for different test cases

Configuration	Source depth (km)	Sphere radius (m)	ΔP (MPa)
1	1	100	1
2	1	100	0.1
3	1	10	1
4	2	100	1

depth. I test two different configurations, radius *a* = 100 m and *a* = 10 m. The source time function (STF) is a hyperbolic tangent function with a final static non-zero value in order to simulate the static permanent displacement (Figure 20). The frequency content of the second derivative of the STF is zero above 3 Htz in order to guarantee numerical stability in the simulations. I place 43 receivers along the *x*-axis (from x = 0 m to x = 9500 m) in

Table 2 - Values of M_{ISO} and ΔV for the geometric configuration 1 of Table 1 for each of the considered approaches to convert the ΔP in moment magnitude.

Configuration (1)	$M_0 \times 10^{12}$ (Nm)	ΔV (m^3)
Aki & Richards I (2002)	5,23	301,9
Aki & Richards II (2002)	4,18	241,5
Muller (2001)	1,05	33 - 60
Aki & Richards I (2002) – case Muller (1973)	9,42	301,9
Aki & Richards II (2002) – case Muller (1973)	7,54	241,5

Table 3 – Same as Table 2 but for geometrical configuration 2.

Configuration (2)	$M_0 \times 10^{11}$ (Nm)	ΔV (m^3)
Aki & Richards I (2002)	5,23	30.2
Aki & Richards II (2002)	4,18	24.1
Muller (2001)	1,05	1.3 – 3.3
Aki & Richards I (2002) – case Muller (1973)	9,42	30.2
Aki & Richards II (2002) – case Muller (1973)	7,54	24.1

Table 4 - Same as Table 2 but for geometrical configuration 3.

Configuration (3)	$M_0 \times 10^{9}$ (Nm)	ΔV (m^3)
Aki & Richards I (2002)	5,23	0.3
Aki & Richards II (2002)	4,18	0.24
Muller (2001)	1,05	0.03 – 0.06
Aki & Richards I (2002) – case Muller (1973)	9,42	0.3
Aki & Richards II (2002) – case Muller (1973)	7,54	0.24
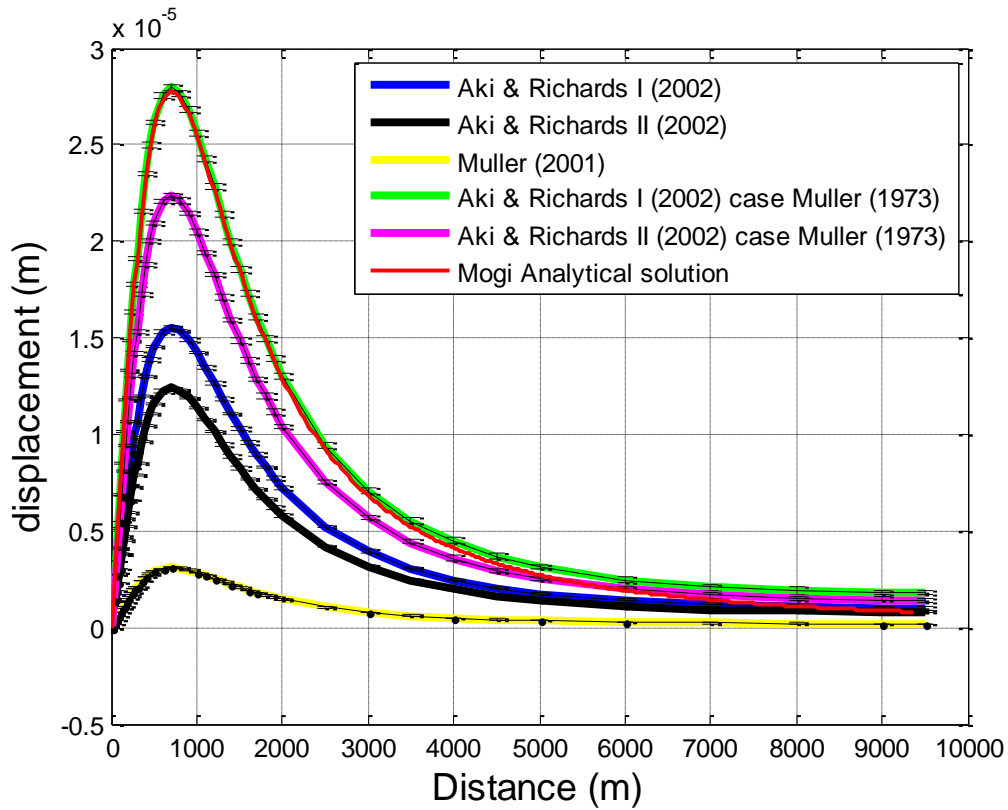
Figure 21 – Horizontal static displacement recorded at the surface for the different values of M_o. The analytical solution of Mogi is the red line. Perfect correspondence is obtained with the value of ΔV computed with the "Aki & Richard I" method and the equation M_o obtained with Equation (71) (Muller, 1973). Error bars appear on the numerical simulations.
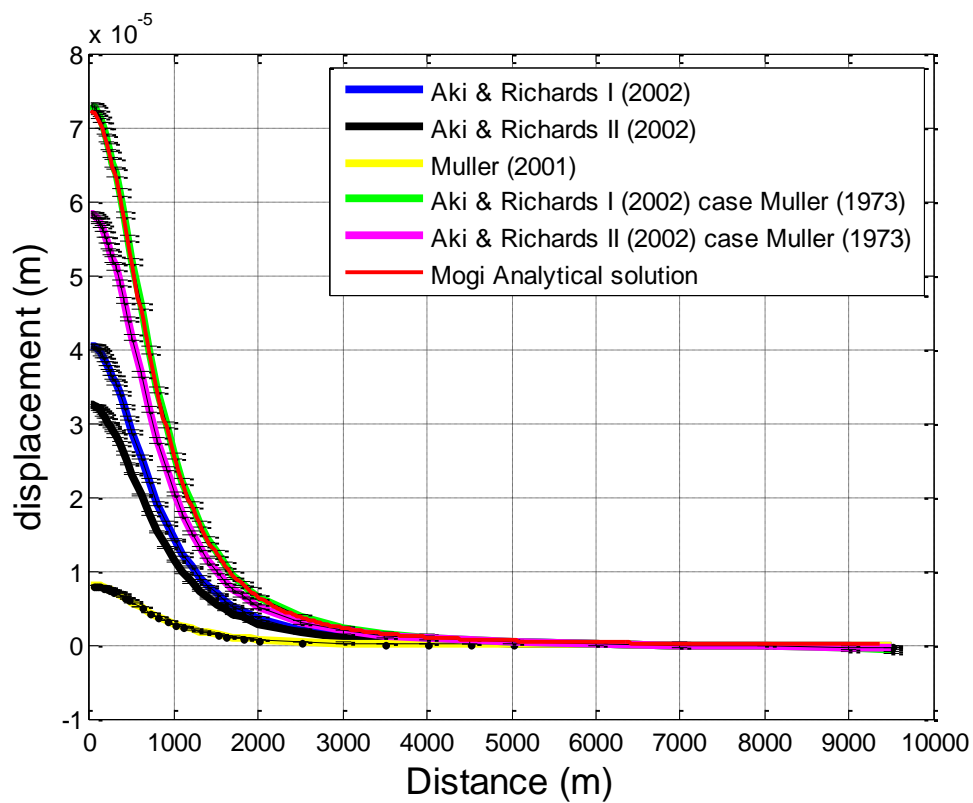
Figure 22 – Same as Figure 21 but for the vertical static displacement.

order to measure the final static permanent displacement on the vertical and radial components (when the final static value is reached, I choose to take values at 5 s later than the first S-Waves arrivals). I test two pressure values $\Delta P_1 = 1$ MPa and $\Delta P_2 = 0.1$ MPa. I run a simulation for each of the five M_0 computed above, and I repeat the simulations for each geometric configuration listed in Table 1 . The computed M_0 values for each geometric configuration are reported in Table 2, Table 3 and Table 4. As In the calculus for the computation of M_0 from the ΔP there is no relation to the sphere depth, the values of M_0 and ΔV computed for *configuration 4* are the same as in *configuration 1*. With *configuration 4* I want to test how the sphere depth, and so the intrinsic attenuation of the synthetic signals in the medium, can influence the solution.

Results for *configuration 1* (Figure 21 and Figure 22) show perfect matching between the analytical and numerical solutions for the *ΔV* computed with the *Aki & Richard I* case (Equations (72) and (73)). *Configuration 2, configuration 3* and *configuration 4* solutions show analog coherent results (not showed here) thus the interpretation is conducted on *configuration 1* solution. The M_0 (Aki & Richards I, case Muller 1973, in Figure 21 and Figure 22) at the source which shows perfect match with the analytical solution is computed by means of Equation (71) (Muller, 1973) which should take in account for the confining pressure. Some confusion arises as the corresponding *ΔV*, computed following the solution of *Aki & Richards I,* should correspond to a volume variation in case the source has no confining hydrostatic pressure. Moreover, the analytical solution proposed by Mogi, (1958) takes in account for the confining pressure. The *ΔV* variation at the source is only related to the ΔP imposed on the sphere's wall. Thus for the *Aki & Richards I* case the volume variation $\Delta V = \sim 300 m^3$ (*configuration 1*) is equivalent (Table 2) for both M_0 computed with Equation (70) or (71). In order to match the analytical solution numerically, I need a higher M_0 value. As stated by Muller, (2001), the choice of Equation (70) or (71) for computing the *ΔV* could depend on the hypothesized source mechanism geometry, i.e. a spherical source for Equation (71) or a crack (a source with dimension much smaller than the others) for Equation (70). Both two equations could reflect a range of possible *ΔV*. For my purposes, I'm interested in determining an order of magnitude for the volume of fluid or gas involved in the tensile source mechanism. As doubts remain on which equation better reflects reality, the $\boldsymbol{M}^{ISO}$ (Equation (59)) will be

interpreted as representing the tensile component of my source process and a quantification of the possible range of volume material involved will be extrapolated using both Equations (70) and (71). The CLVD percentage coming from the decomposition of the deviatoric moment complicates the understanding of the solution. A pure CLVD source does not correspond directly to any simple physical mechanism, but in combination with the ISO component can be thought as a product of the tensile faulting (Vavryčuk, 2015). Thus, mechanism orientation will be determined either on the whole moment tensor **M** or on the deviatoric component (M^*) following the interpretation of the source mechanism, i.e. in case of a predominant isotropic component (M^{ISO}) the orientation of the source will be extrapolated from the deviatoric component (M^*) decomposition.

2.4.4 Conclusion of the Mogi problem

The MT solution after MT inversion is of difficult interpretation. Hence I have investigated how the pressure exerted at the walls of a simple spherical source embedded at a certain depth can be related to the MT solution.

After defining the dimension of the sphere, the pressure value imposed on the sphere's wall has to be related to the volume variation of the sphere itself. Different approaches have been proposed in the literature to relate the volume variation and the pressure exerted at the sphere's wall (Aki and Richards, 2002; Muller, 2001). Once the volume variation computed, the moment magnitude (M_o) can be obtained by means of two different approaches (Eshelby, 1957; Muller, 1973). The retrieved moment magnitudes are used to perform some numerical simulations of the equivalent static displacement recorded at the free surface and compared to the analytical solution proposed by Mogi, (1958). The results show that perfect match is obtained for the M_o computation (Muller, 1973) which takes in account for the hydrostatic pressure at the source, but the corresponding $\varDelta V$ from the pressure (Aki and Richards, 2002) does not. Confusion arises, but Muller, (2001) suggested that the two approaches for computing M_o could correspond to two different source geometries, i.e. a sphere or a crack.

The results of the numerical test suggest that even if MT solution is perfectly

retrieved, the interpretation of the source mechanism is not unique. The volume of the fluid/gas involved in the source process will thus be computed using both two M_o equations (Eshelby, 1957; Muller, 1973) and interpreted as a range of possible volume variations.

Chapter 3

Mt. Etna Volcano

In this chapter I will give a brief description of the geological context of Mt. Etna. I will then focus my attention on Long Period seismic signals recorded on the volcano making a brief review of the previous studies on their detection and understanding.

3.1 Geological context

Mount Etna Volcano is located on the island of Sicily (Italy) and is the tallest volcano (3330 m a.s.l. Bousquet, 2004) in Europe. Certain authors refer to it as *"Mongibello" (Mons Gibel),* from Latin *mons* (mountain) and the Arab *jebel* (mountain) as to highlight its majesty. In recent times the name *Mongibello* is often used to refer to the summit craters and can be found in some publication at the place of *Mt. Etna.* It is the most active volcano of Europe and, after Kilauea on Hawaii, possibly the second most active volcano on Earth. It is almost continuously active since human records are present (2700 years ago), and it has shown incredible versatility in terms of eruptive styles. In the last 15000 years it has shown explosive activity (since 12 ka ago, Coltelli et al., 2000), which culminated in the 122 BC largest explosive episode, a plinian eruption of basaltic magma (Coltelli et al., 1998) and frequent effusive activity from the summit craters and flank eruptions (Branca et al., 2011a). Since the second half of the 17th century the eruptive activity was characterized by both explosive activity at the summit craters, from strombolian to lava fountains, and the occurrence of flank eruption almost purely effusive (Branca and Carlo, 2005). Etna has approximately 350 craters and minor vents on its flanks, each of which erupted only once.

3.1.2 Geodynamic setting

The tectonic context which gives origin to Mt. Etna is still not completely understood. Mt. Etna lies between the Appeninic-Maghrebian chain and the Catania-Gela foredeep (Bousquet, 2004). While out, in the Ionian Sea, the African plate (constituted by oceanic lithosphere) is subducting underneath the Calabrian arc, on the island itself the convergence due to subduction is blocked and the region is in a collisional regime. The result is mountain building going on in the Peloritani, Nebrodi and Madonie chains in the northern part of Sicily (Figure 23). Mt. Etna lies south, on the external boundary of this segment of the Alpine chain in the intersection zone of the major fault systems of eastern Sicily. Mt. Etna is bounded to the north by the Monte Kumeta-Alcantara faults and to the east by the Aeolian-Maltes fault (Bousquet, 2004). The Aeolian-Maltese fault divides the

calc-alkalin volcanism of the Aeolian Islands, which is in a subduction regime, to the collision regime of the Appeninic-Maghrebian chain. Thus, Mt. Etna lies in a quite
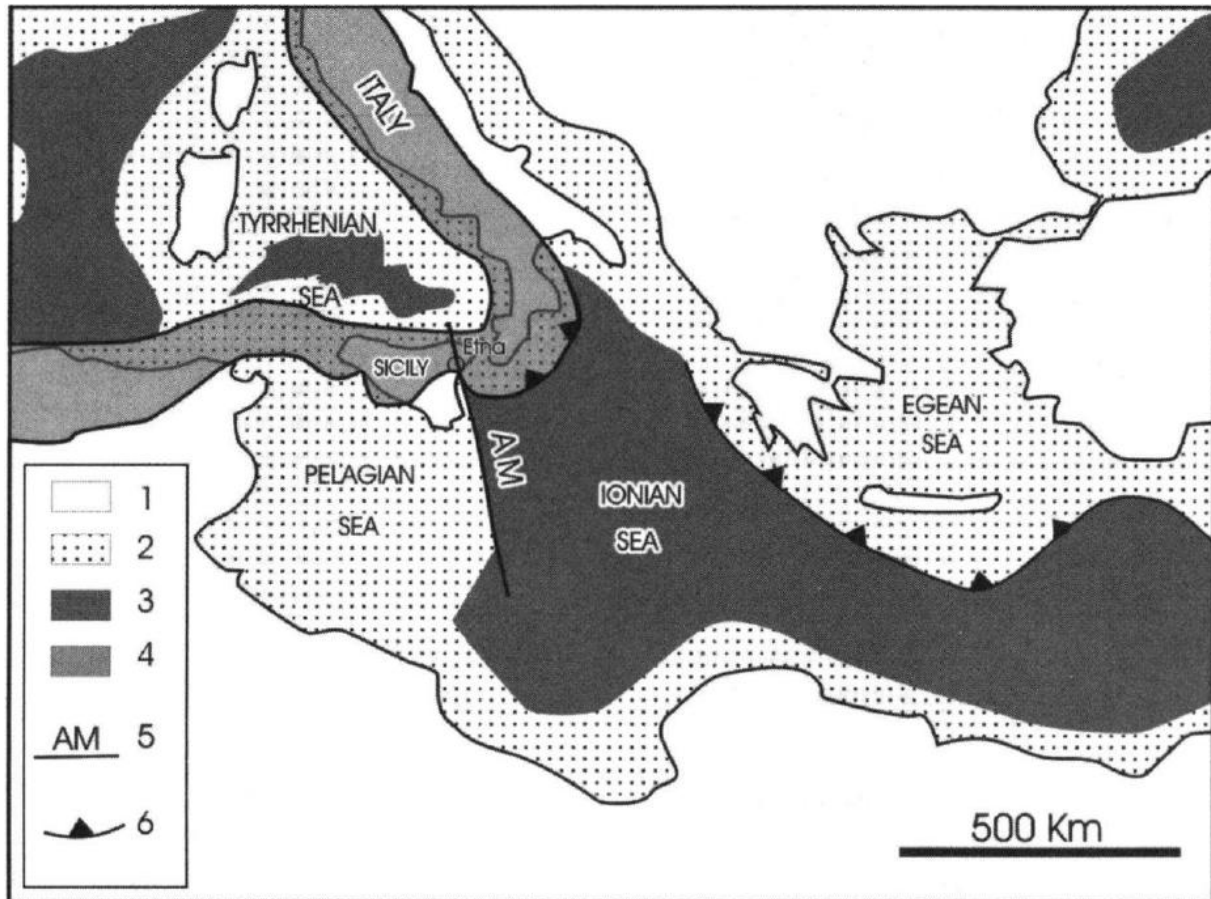
Figure 23 – Mt. Etna region in the geodynamic framework of the central Mediterranean (reproduced after Bousquet, 2004). 1, Continent; 2, continental margin and thin continental crus; 3, oceanic crust; 4, Appenin-Maghrebian chain; 5, Aeolian-Maltes transform fault system; 6, active subduction front.

unconventional place for a volcano. Gvirtzman and Nur, (1999) proposed that Mt. Etna has formed as a consequence of rollback of the Ionian slab underneath the Calabrian arc. The rollback mechanism could be explained as the Ionian slab slowly moving away (sout-east) from the subduction zone due to the weight of the subducting plate. This leads to the opening of a gap between the Ionian lithosphere and the African plate, gap which is filled by viscous material coming from the asthenosphere (Gvirtzman and Nur, 1999). Schellart, (2010), through fluid dynamic laboratory experiments, concluded that the volcanism on Mt. Etna is likely due to this slab rollback process where the upwelling of upper-mantle flow causes decompression and melting of the upper mantle itself
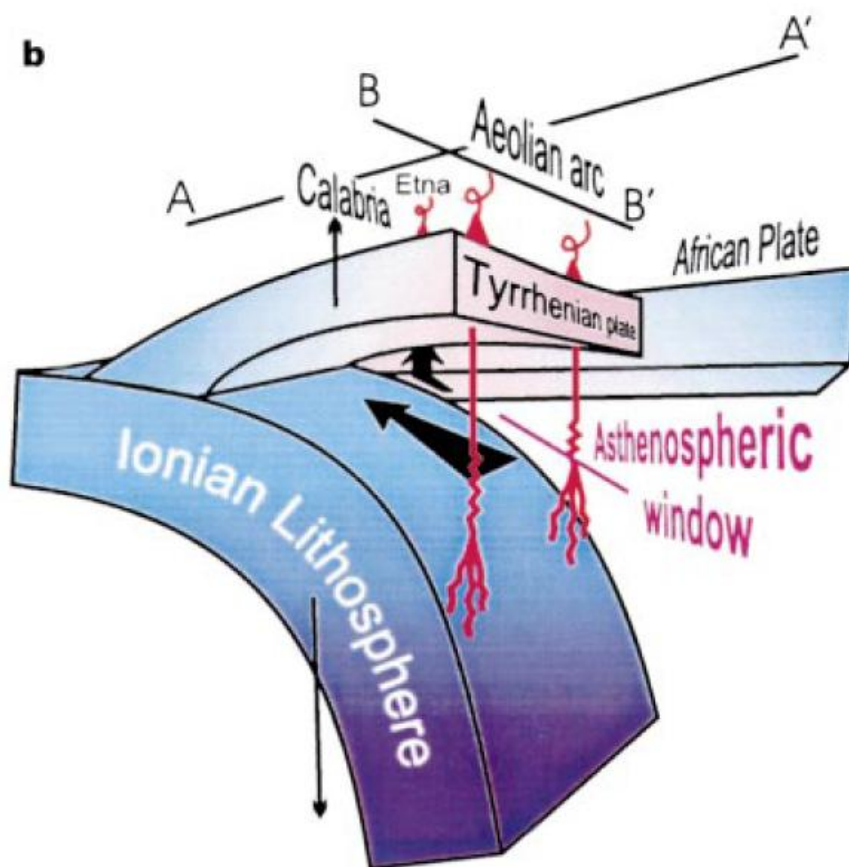
Figure 24 – Three dimensional sketch of the south-tyrrhenian subduction zone. The asthenospheric material penetrates along the plate contact between the Ionian Lithosphere and the African Plate. Black arrows represent local patterns of mantle flow; red lines represent magma rising from the top of the slab (close-up red lines are referred to the Aeolian volcanic arc). Reproduced after Gvirtzman and Nur, (1999).

(Figure 24) explaining the source of the volcanism of the region. Despite the complex geodynamic setting giving arise to the volcanism of the southern part of Italy, whose deep investigation is not the main aim of this work, the mechanism feeding Mt. Etna is very efficient.

3.1.2 Geological history

Geological history of Mt. Etna is quite recent, eruptive activity began in the middle of Pleistocene approximately 500,000 years ago (Branca et al., 2008). The geological evolution is subdivided in four main phases: (1) *the Basal Tholeiitic phase,* (2) *the Timpe phase,* (3) *the Valle del Bove centers phase* and (4) *the stratovolcano phase* (Branca et al.,

2011a, 2004, 2008).

The (1) *Basal Tholeiitic phase* groups the earliest volcanic products erupted in the Etna region. The first subaerial products were erupted about 330 ka ago (Branca et al., 2011b) along the coast of the Ionian Sea immediately to the north of Catania, leading to the Aci Castello formation formed by pillow lava and hyaloclastic breccia (Corsaro and Cristofolini, 2000, Figure 25a). To the south of the actual volcanic edifice, scattered fissure-type eruption generated thin lava flows succession that invaded
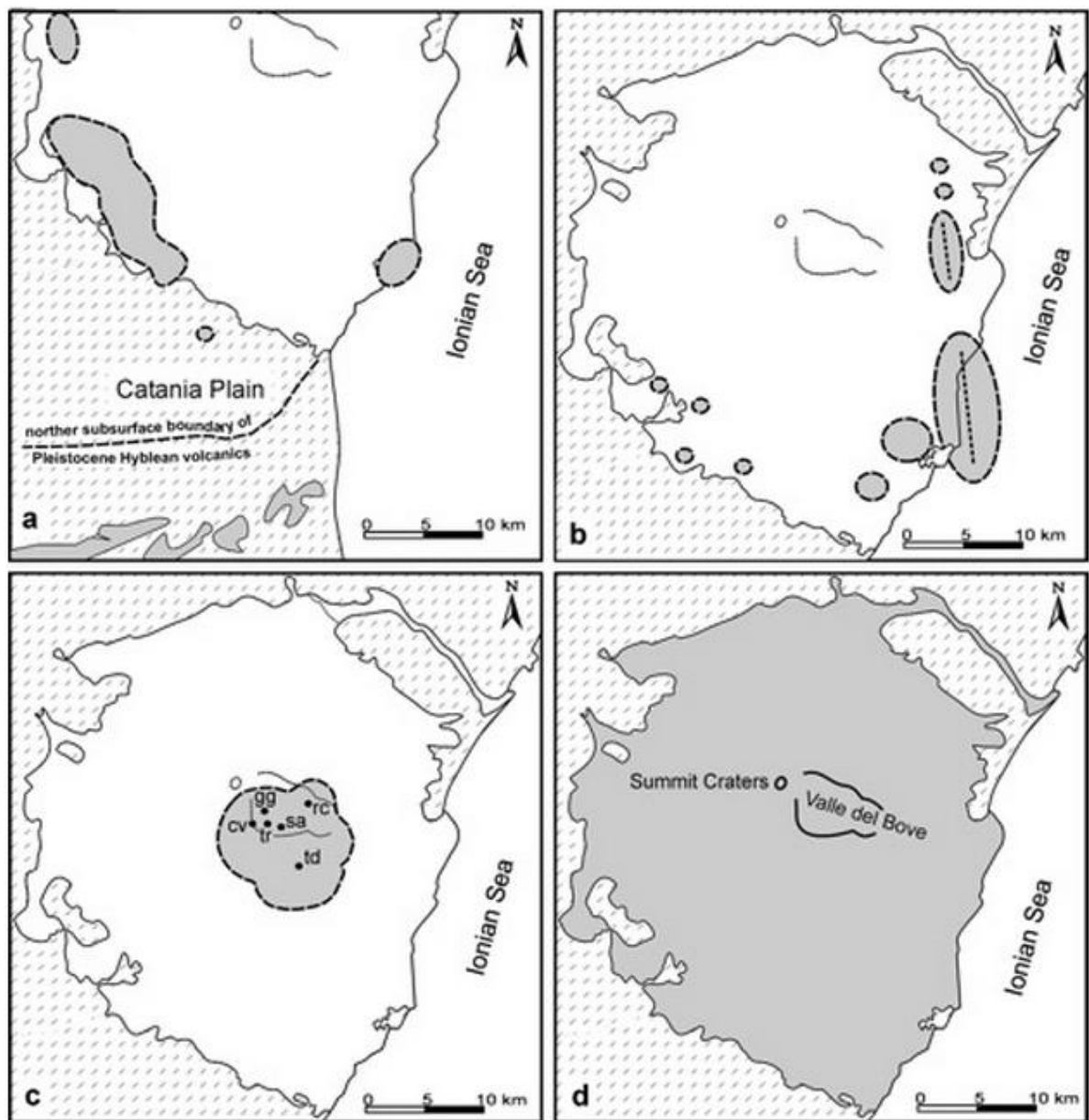
Figure 25 – Eruptive centers and distribution of the product of eruptions for each of the four main phases of volcanism in the Etna area. a) Basal Thoeelite phase; b) Timpe phase; c) Valle del Bove phase; d) Stratovolcano phase. Figure reproduced after Branca et al., (2004).

the Simeto river paleovalley floor accompanied by a general uplift of the area (Di Stefano and Branca, 2002). A long period of erosion (~ 100 ka) interested this newly formed lava plateau and the sedimentary terrains marking the transition from the *Basal Tholeiitic* to the *Timpe* phase (Branca et al., 2011b). Overall, the products of the *Basal Tholeiitic phase* are tholeiitic basalts (Branca et al., 2008) with a composition similar to the magma currently erupted at Kilauea, Hawaii.

The (2) *Timpe phase* occurred between about 220 ka and 129 ka ago (De Beni et al., 2011) and consisted mainly of repetitive effusive eruptions through N-S oriented fissures along the Timpe fault system (Figure 25b) (Branca et al., 2011b). The products of this phase are related to the first primitive composite volcano interpreted as a lava shield elongated 22 km on a NNW-SSE basis in correspondence of the actual Acireale scarps on the east flank of the volcano (Branca et al., 2008, 2011b). During this eruptive period, sporadic eruptive activity interested also the lower southwestern and southeastern sectors of the Etna edifice. The products of this phase are mainly constituted by alkali basaltic lavas (Branca et al., 2008; Corsaro and Pompilio, 2004).

The (3) *Valle del Bove phase* occurred about 110 ka ago and the volcanism shifted from the Ionian coast into the area now occupied by the *Valle del Bove* (Figure 25c). During this period the volcanic activity of Mt. Etna underwent a profound change: from the sporadic fissure eruption of the first two phases it shifted to a central-type polygenetic volcano (De Beni et al., 2011). During a period comprised from 110 ka and 65 ka ago (De Beni et al., 2011) about seven main volcanic centers took place. The principal activity occurred from *Trifoglietto* volcano (~107 – 99 ka ago) on the southern flank of *Valle del Bove.* It was mainly characterized by effusive lava flows and explosive activity during the final phases which ended with a plinian eruption which generated a thick sequence of pumice and flow deposits (Branca et al., 2011a). The *Trifoglietto* edifice reached a maximal elevation of about 2600 m (Branca et al., 2011b). Other minor volcanic centers formed subsequently on the flanks of *Trifoglietto* and their activity continued until ~60 ka ago.

After the construction of volcanoes of the *Valle del Bove* the volcanism shifted NNW giving raise to the last (4) *Stratovolcano phase* (Figure 25d). The composition of the erupted lava changed from alkali-basalt to trachytes (Corsaro and Pompilio, 2004) and

was marked by the construction of *Ellittico volcano*, the main eruptive center recognized in Etna region. *Ellittico volcano* reached a maximal elevation of about 3600 m and was characterized by both explosive and effusive activity, most from the summit vents and subordinated flank fractures (Branca et al., 2011b). *Ellittico volcano* began his growth about 57 ka ago and slowly expanded his flanks until it reached, almost 20 ka ago, its maximal areal expansion having a maximum diameter of about 45 km that corresponds to the actual boarders of Mt. Etna volcano (Figure 26). The final stage of *Ellittico volcano* was characterized by four plinian eruptions, occurring about 15.5 – 15 ka ago, which
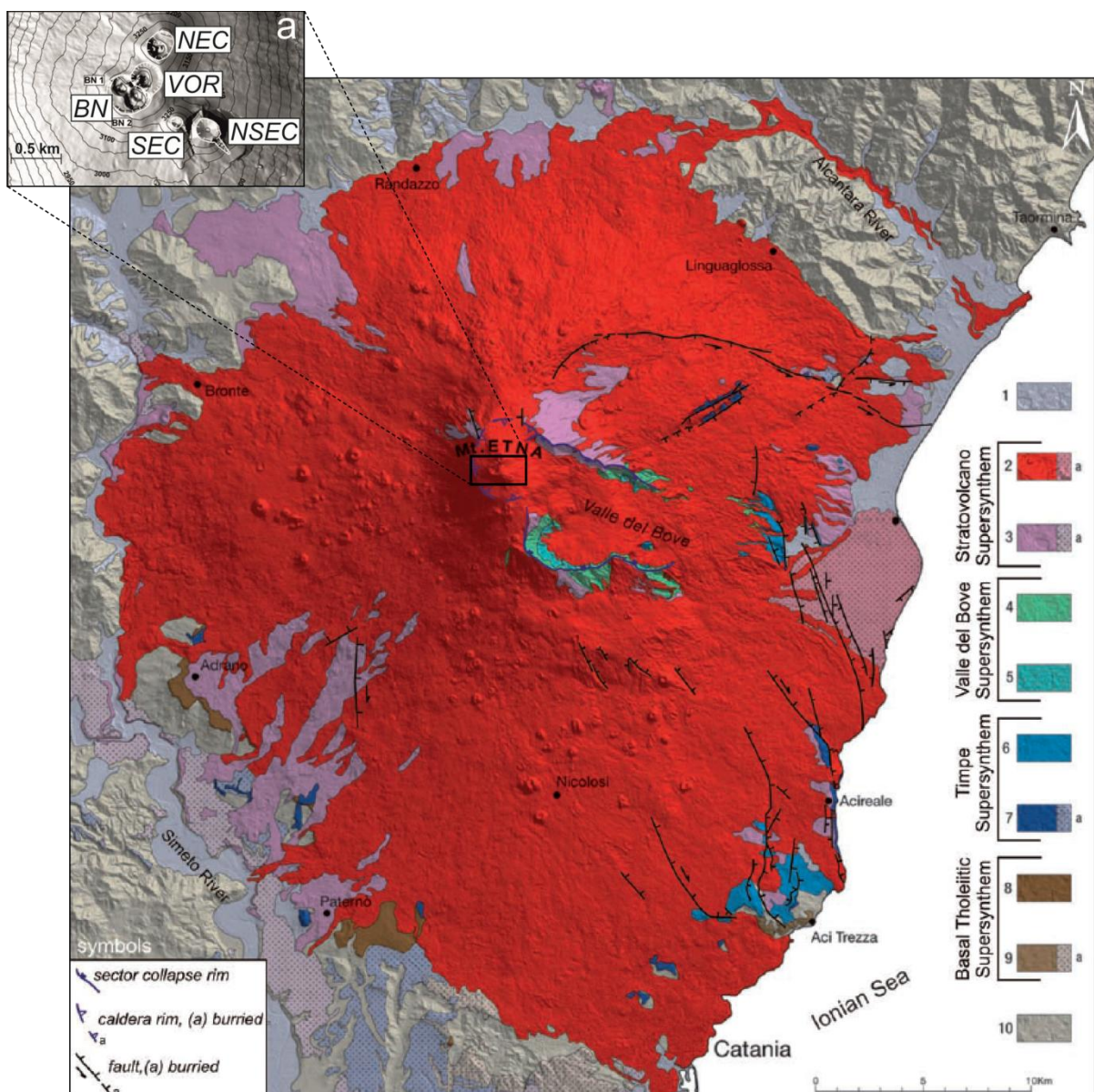
Figure 26 – Scheme of the outcropping deposits of the four phases of volcanism on Etna volcano. Reproduced after Branca, (2011). a) DEM particular of the summit of Mt. Etna with the acronym of the actual active craters, reproduced after Cannata et al., (2015).

ended the *Elittico phase* and produced a collapse of the summit area which formed the *Ellittico* caldera (Branca et al., 2011b). Since 15 ka ago the volcanic activity shifted to the actual active vents at the summit of Mt. Etna, namely the *Mongibello* volcano was born. Effusive summit eruptions gradually filled the *Ellittico* caldera and many flank fissures generated lava flows which reached the Ionian coast.

About 10 ka ago a catastrophic collapse involved the eastern flank of the Etna edifice and formed the huge collapse depression of the *Valle del Bove* (Calvari et al., 1994). In 122 BC the largest explosion of *Mongibello* occurred, this was a plinian eruption (Coltelli et al., 1998) that produced widespread pyroclastic scoria fall deposits and huge damage to the ancient Roman town of Catania (Branca et al., 2011b). In 1669 the largest flank eruption of modern times occurred at low altitude in correspondence of *Monti Rossi* nearby Nicolosi. The lava flow which originated reached and destroyed part of the town of Catania and many villages on the Etna steps. Since the 17th century the eruptive activity is characterized by both periods of explosive activity (strombolian to lava fountains) and the occurrence of sporadic flank activity which appear to have no systematic relationship with the central activity (Branca and Carlo, 2005).

3.1.3 Structural framework

The structural framework of Mt. Etna results from the complex interaction between regional tectonic, flank instability and basement geometry (e.g. Azzaro et al., 2013; Borgia et al., 1992; Bousquet, 2004; Bousquet and Lanzafame, 2013; McGuire and Pullen, 1989; Norini and Acocella, 2011; Rasà et al., 1996; Rust et al., 2005).

The main structural lineaments of the unstable flanks of Mt. Etna are the following fault systems (Figure 27, Azzaro et al., 2013): Pernicana, Ragalna, Tremestieri-Trecastagni, Timpe and Ripe della Naca-Pedimonte-Calatabiano.

The eastern sector of the volcano appears very active from a seismic point of view (Azzaro et al., 2013) which is in agreement with the high deformation rate recorded on the eastern/south-eastern flank of the volcano (e.g. Bonaccorso et al., 2006; Bonforte et al., 2011). The Pernicana fault system (PF) is identified as the northern boundary of this
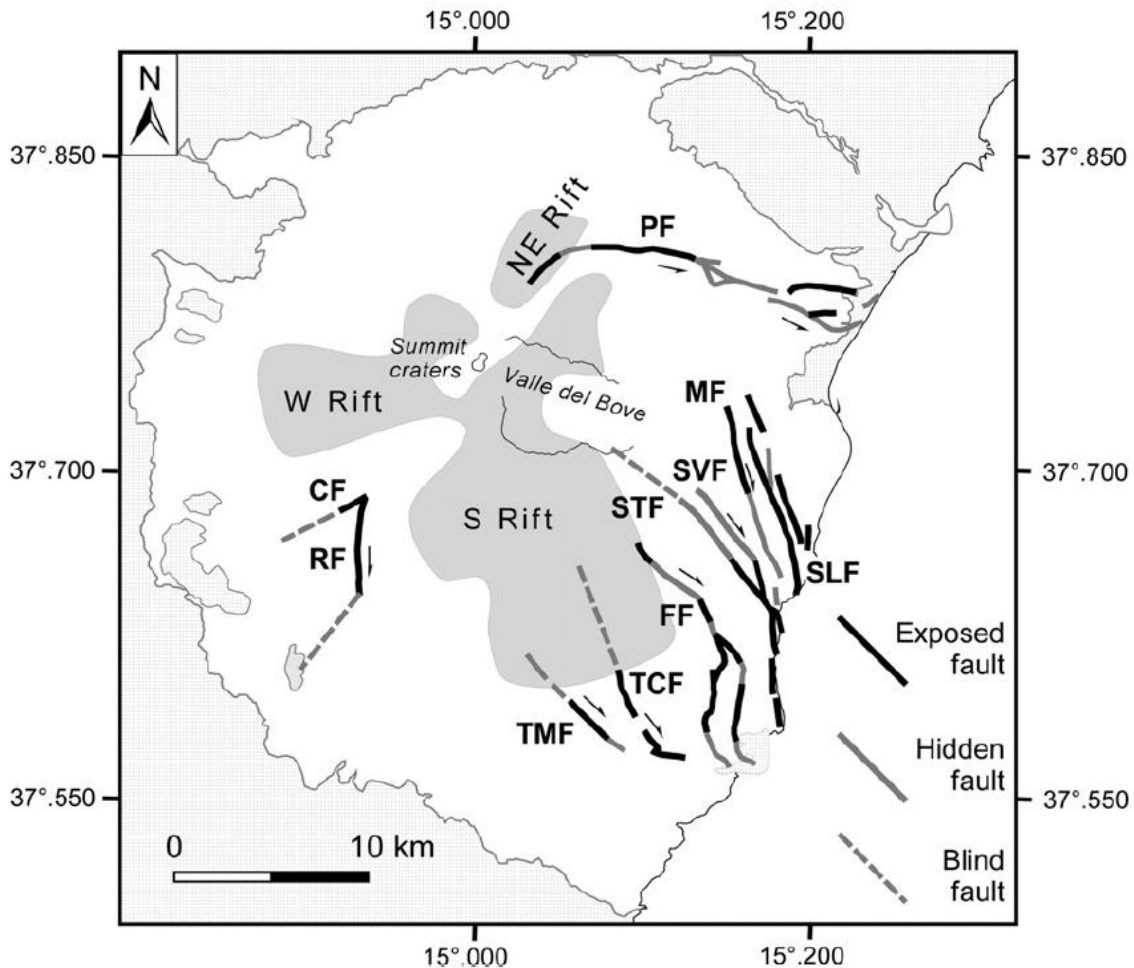
Figure 27 – Tectonic sketch map and active faults on Mt. Etna volcano. Fault abbreviations: PF, Pernicana; RF, Ragalna; CF, Calcerana; TMF, Tremestieri; TCF, Trecastagni; FF, Fiandaca; ARF, Acireale; STF, S; Tecla; MF, Moscarello; SLF, S. Leonardello; RP, Ripe della Naca; PD, Pedimonte; CL, Calatabiano; SVF, S. Venerina. The arrows indicate the strike-slip components; the contour of the rift zones is in grey. Figure reproduced after Azzaro et al., (2013).

unstable sector (Alparone et al., 2013 and references therein) while the southern part is represented by the south-rift (Rasà et al., 1996) and the Tremestieri-Trecastagni faults systems (Figure 27). These structures join with a displacement plane located roughly at a depth of 2-4 km b.s.l. which also corresponds to the maximum depth of the earthquakes recorded along the Pernicana fault (Alparone et al., 2013). The sliding of the eastern flank of the volcano towards the sea is thought to favor the extension and the depressurization of the central part of the volcano thus facilitating magma ascent at shallower levels (Bonaccorso and Patanè, 2001). The relation between the unstable condition of flank sliding and the magmatic system was also confirmed by Privitera et al., (2012) through the computation of Coulomb stress changes retrieved from numerical

simulations of volcanic-tectonic events. However, these dynamics do not allow for strong pressurization of the shallow plumbing system as the deformation induced by magma emplacement is accommodated by the displacement of the eastern flank (Bonaccorso et al., 2011a).

The complex geodynamic of Mt. Etna and its flanks has been proven to play an important role on the actual volcanism. Hence, the analyses of LP events have to be carried out considering the complex structural context in which they occur.

3.1.4 Recent history of summit craters

I give a brief description of the actual morphology of the summit of Mt. Etna volcano. All the acronyms and the locations of the summit craters are sketched in Figure 26a.

The modern central crater (CC) came into existence in the late 17th century following the collapse of the previous summit cone during the 1669 flank eruption (Behncke et al., 2004). The external morphology of the CC was almost unchanged since the mid-19th century (Behncke et al., 2004; Guest, 1973) although its internal morphology has changed frequently in function of intracrater activity. The CC was completely filled after the 1964 eruption (Behncke et al., 2004). The actual craters present at the summit of Mt. Etna are a product of the activity of the last 100 years (Figure 26). In particular, during the eruption of 1911 a new crater formed at the base of the summit cone (Ponte, 1920), later named the Northeast crater (NEC). The NEC was reactivated frequently during the 20th century and the cone reached its maximal elevation of 3350 m.a.s.l. in 1981 (Tanguy and Patané, 1984), tough its later collapse reduced its height to 3329 m (Neri et al., 2008). The Voragine (VOR) formed in 1945 in the northeastern portion of the CC and in 1968 the Bocca Nuova (BN) appeared as a third vent (the second was called the 1964 crater) inside the CC. The Southeasth crater (SEC) formed in May 1971 at the southeast base of the summit cone (Alparone et al., 2003; Behncke et al., 2006, 2008, 2014; Calvari et al., 1994). The youngest cone is the New Southeast crater (NSEC) which appeared in 2009 and grew during a series of lava fountaining episodes in 2011-2012 (Behncke et al., 2014).

3.2 Long Period activity at Mt. Etna

The sustained volcanic activity of Mt. Etna offers many opportunities to scientists to get new information about the dynamics of the volcano during rest and unrest periods. The first study concerning Long Period (LP) events on Mt. Etna was proposed by Falsaperla et al., (2002). They studied the seismic activity recorded during the 1992 eruption. They were able to identify four different families of LP events based on waveforms similarities which were interpreted as result of pressure transients in dike like structures located beneath the Northeast Crater (NEC). They results showed the high number of LP events occurring daily on the volcano and a possible source mechanism related to gas/fluid dynamics relying the shallow feeding system to a deep depressurizing magma body.

Since November 2003 the installation of the first permanent broad-band network allowed for the identification of LP activity as the most common seismic signature at Mt. Etna (Lokmer et al., 2007, 2008; Saccorotti et al., 2007). The LP events on Etna occur in swarms or as independent events (Falsaperla et al., 2002) and they are also recorded during both rest and unrest periods of the volcano (Cannata et al., 2009a; Cauchie et al., 2015; Lokmer et al., 2008). Lokmer et al., (2007, 2008) and Saccorotti et al., (2007) focused their attention on the LP activity recorded during the 2004-2005 eruption. As recognized before by Falsaperla et al., (2002) for the 1992 events, the LP events recorded during the 2004-2005 eruption showed spectra and waveform similarities which were interpreted as a repetitive non-destructive source mechanism (Cannata et al., 2009a; Lokmer et al., 2007, 2008; Saccorotti et al., 2007). Same considerations were made lately in occasion of the June 2008 lava fountain by De Barros et al., (2009) who were able to distinguish two main families of LP events with similar waveforms. First LP analysis on Mt. Etna attributed the source mechanism to a resonant fluid filled crack (Falsaperla et al., 2002; Lokmer et al., 2008; Saccorotti et al., 2007). Saccorotti et al., (2007) analyzed the quality factor Q of LP's coda waves and indicated that the most likely candidate fluid for sustaining the resonance of the filled crack was a bubbly basalt or a water-vapour mixture with very low gas-volume fractions. They also recognized a correlation between LP and VLP signals. They argued that the source trigger of the deeper VLP events was relied to

mass transfer. The subsequent mass injection in overlying cavities could have driven the pressurization of a reservoir filled of hydrothermal fluids, thus triggering the LP resonance. An analog interpretation was given by Cannata et al., (2009a) who found slightly different locations for the shallow LP and the deeper VLP events. They suggested that two different interconnected sources could explain this difference. In their model, slow movements of fluids between connected cracks could have driven pressure transients in a shallower dyke. They supported their hypothesis by the fact that the onset of the LP events preceded slightly the VLP record. Lokmer et al., (2008) performed the first moment tensor (MT) inversion of short duration LP signals on Mt. Etna. They suggested that "gas pulsing" from the magmatic column into an oriented crack could have triggered the short LP resonance. Lately De Barros et al., (2011) identified two families of similar LP events and performed MT inversion identifying two different interconnected source mechanisms. During their experiment an eruptive fissure opened below the source of the LP events on the flank of the volcano. In their model they hypothesized that two orthogonal cracks located below the summit could be excited by the injection of gas coming from the main conduit. They supposed that the summit degassing and the flank lava flow drained the cone, producing a decrease of pressure and a consequent destabilization of those fractures. Cannata et al., (2015) recognized an increase in LP amplitude just the two months preceding the explosion which occurred at *Bocca Nuova* in Spetember 2013. They suggested that this change in amplitude could be connected to gradual pressurization of the shallow Etna plumbing system. They supported their model comparing the LPs and volcanic tremor activity with CO_2 gas measurements. Cauchie et al., (2015) analyzed a set of LP events recorded in 2005 during a rest period of the volcano. They performed an amplitude distribution analysis and compared their results with a dataset of LP events recorded on Stromboli volcano (Italy). They end up proposing a model where an intermittent degassing process occurring at depth could explain the LP activity. In absence of clear surface evidence for the degassing pulses (as it occurs at Stromboli) they also argued that the LP events could be indirectly related to the degassing at depth. They imagined that stress changes associated to the degassing pulses could be likely to explain the recorded amplitude and inter event time distribution of the LP events. These recent interpretations are implicitly consistent with

the recent work of (Bean et al., 2014) who developed an alternative source model based on the deformation of weak, compliant material of the shallow portion of the volcanic edifice (as described in the above section 2.2.7).

Chapter 4

Velocity Structures on Mt. Etna volcano

In this Chapter I investigate, through synthetic tests, the role played by the choice of a particular velocity model on the reliability of the MT inversion solution. An exhaustive summary of the work is proposed in the Abstract. The Chapter has been organized as a peer-reviewed publication as the work has been submitted to the Geophysical Journal International (GJI) journal.

Long Period (LP) Events on Mt. Etna volcano (Italy): the influence of Velocity Structures on Moment Tensor Inversion

Trovato C.[1],[2]*, Lokmer I.*[3] *, De Martin F.*[1]*, Aochi H.*[1]

[1]_ BRGM (Bureau de Recherches Géologiques et Minières), Orléans, France

[2]_ ISTO (Institut des sciences de la Terre d'Orléans), 1A bis, rue de la Férollerie, Orléans, France

[3]_ School of Earth Sciences, University College Dublin (UCD), Dublin, Ireland

Abstract

Since a few decades volcanic Long Period (LP) events have been recorded on many active volcanoes and their study has been recognized as an important tool to characterize volcanic activity. LP event analyses through moment tensor (MT) inversions have led to kinematic descriptions of various source mechanisms. These inversions focusing on the understanding of the physical origin of LP events supposed a relatively simple structure of the medium and few studies focused on the uncertainty derived from the choice of a particular geological model. We carry out several tests of inversions on Mt. Etna volcano (Italy). Four geological models with topography are considered with increasing vertical complexity. First, synthetic scenarios are computed in in the most complex model and then inverted in the other three geological models with/without constraining the mechanism (moment tensor and single forces). Although the solutions among the three velocity models are similar, the model with a surface layer offers the best results in terms of source location and obtained mechanism. The homogeneous model gives the lowest misfit value, but source location and mechanism decomposition are inaccurate. When a complex model different from the original one is used, we get high misfit values and a wrong solution. Subsequently we perform a MT inversion of an LP event recorded on Mt Etna in 2008. Here we obtain very different solutions between the three models in terms of source location and mechanism decomposition. The overall shape of

the retrieved source time functions are similar, but some amplitude differences arise, especially for the homogeneous model. Our work highlights the importance of including the unconsolidated surface materials in the computation of Green's functions. Complex models of the volcano which do not correspond to reality can lead to significant errors and to misinterpretation of the source mechanism.

4.1 Introduction

The understanding of the origin of seismic signals on volcanoes is of fundamental importance to enhance our knowledge of volcanic systems and to monitor their activity. Volcanoes can exhibit a wide variety of seismic signal types (e.g. Chouet, 1996 and references therehein). Here we focus our attention on long period (LP) seismic signals. LP events are characterised by low frequency waveforms (0.2 – 2 Hz) and are thought to have magmatic or hydrothermal origin (Chouet, 2003a). They are often considered to be associated with resonance of fluid filled cavities (Aki et al., 1977; Chouet, 1996, 2003a; Jousset et al., 2004; Nakano et al., 2003; Neuberg et al., 2000) and their understanding is crucial to illustrate the shallow plumbing system of volcanoes. Recently, Bean et al., (2014) developed the work of Harrington and Brodsky, (2007) and proposed a new model for explaining shallow LP seismicity. They analyzed the pulse-like nature of some LP events recorded on volcanoes and stated that their origin is likely a consequence of failure in materials close to the brittle-ductile transition. Their conclusions suggest that careful attention should be paid in using LP events as direct indicators of magmatic/hydortermal fluids.

An important tool to describe LP sources is moment tensor (MT) inversion (Davi et al., 2010; De Barros et al., 2011; Jousset et al., 2004, 2013; Kumagai, 2002b; Kumagai et al., 2005; Lokmer et al., 2007; Nakano, 2005; Nakano et al., 2003). Many MT inversions on LP volcanic signals infer a tensile crack source mechanism (Eyre et al., 2013; Jousset et al., 2013; Kumagai, 2002b; Kumagai et al., 2005; Nakano et al., 2003) . These cracks span from sub-horizontal to sub-vertical mechanism interpretation. A different interpretation was proposed by Davi et al., (2010) on Arenal volcano (Costa Rica) where their analysis of LP signals led to an isotropic source mechanism. Although the inversion process itself is well estabilished many questions on uncertainies arise due to the lack of knowledge of the properties of

materials traversed by seismic waves (Bean et al., 2008; Jousset et al., 2004). The long wavelengths of LP events are mostly insensitive to small variations of the volcanic structure. Thus a homogeneous or two-layers models might be sufficient to recover the LP source process. However recent works show that the assumption for a homogenous model may be incorrect (Bean et al., 2008; Cesca et al., 2008; Kumagai et al., 2005; Neuberg et al., 2000). The strong lithological heterogeneity, such as fracturing of near-surface rocks and vertical variations in lithology (dykes), observable on volcanoes lead to an important impedance contrast which could strongly influence the wave propagation. Although many inversions were conducted in a homogeneous half-space (Kumagai, 2002b; Legrand et al., 2000), the complex stratigraphy of volcanoes has a strong impact on the seismic wavefield (Bean et al., 2008; Neuberg et al., 2000). Topography is taken into account with a homogeneous medium (De Barros et al., 2011; Jousset et al., 2004; Lokmer et al., 2007; Ohminato and Chouet, 1997), two-layers medium (Bean et al., 2008) or a heterogeneous medium (Davi et al., 2010; Eyre et al., 2015; Jousset et al., 2013). Including realistic structures in the calculation model is crucial to correctly obtain the source mechanism, but little is mentioned about the quantification of the introduced error in the case where the model is completely or partially incorrect. At present, detailed velocity structures of volcanoes are still rarely available (Davi et al., 2010). Here we develop the work of Bean et al., (2008) on the influence of the velocity structures on moment tensor inversion. We will analyze the effect of different geological models with increasing complexities regarding their influence on successful source inversions.

We focus our attention on one of the most studied volcanos in the world, Mt. Etna, located in eastern Sicily island (Italy), the largest active volcano in Europe. More than 600.000 people live nearby this active volcano (Chiarabba et al., 2000). It covers an area of about 1,250 km^2 and reaches a maximum elevation of ~3.330 m. It's characterized by almost continuous

eruptive activity from its summit craters and frequent lava flow eruptions from fissures opened on the flanks (Patanè et al., 2011). Due to the high volcanic activity many seismic signals are now recorded continuously (Saccorotti et al., 2007). Since 2003 the permanent network of broadband stations has been installed by the INGV (Istituto Nazionale di Geofisica e di Vulcanologia) and LP events have been addressed in a number of strudies (Cannata et al., 2009a, 2013; De Barros et al., 2009, 2011; Lokmer et al., 2007, 2008; Saccorotti et al., 2007). They appeared in periods of quiescence or during unrest episodes (Lokmer et al., 2007; Saccorotti et al., 2007). They are often difficult to be distinguished from the sustained volcanic tremor accompanying eruptions (Lokmer et al., 2008), but they may not be directly related to the eruption processes (De Barros et al., 2011; Saccorotti et al., 2007). The mechanism of the LP events suggested resonating phenomena at a relative shallow depth (~300-1200 m. below the summit) (De Barros et al., 2011; Lokmer et al., 2008). Recently, Bean et al., (2014) proposed a new model for explaining the shallow LP seismicity recorded in occasion of the 2008-2009 eruption of Mt. Etna (De Barros et al., 2009, 2011). They recognized that, while summit stations recorded pulse-like low-frequency signals, the same records on further stations appeared as classical resonating LP signals. They attributed the apparent resonance of these low-frequency seismic events caused by propagation effects and not being source related. Their model hypothesizes that those LP events are consequence of failure in materials close to the brittle-ductile transition. The brittle-ductile transition in shallow volcanic material is not supposed to be related to high temperature and pressure, but to the low friction angles of the unconsolidated shallow volcanic deposits. Similar conclusions have been drawn by Eyre et al., (2015) for Turrialba volcano, Costa Rica.

In this study we carry out a synthetic inversion verification test. We build four different structure models with increasing geological complexity. We suppose that the fourth most complex model corresponds to reality (state of reality) and that the three other models

correspond to the best knowledge we have of the geological properties of the volcano (state of knowledge). Hence, we compute Green's functions for the first three models and synthetics data in the fourth most complex model for a tensile crack source mechanism. Thus, we will perform moment tensor inversion for the three models with and without constraining the components and varying the number of receivers. For this synthetic scenario, we will discuss how well the inversion procedure can reproduce the original location, mechanism and source time functions using the different structure models and stations configuration. The use of synthetic scenarios allows us to investigate if adding complexities in the model for Green functions computation can improve our ability to retrieve the correct source mechanism. We then extend the work of De Barros et al., (2011) analyzing a real event by mean of the three geological models investigated in this work.

4.2 Models and Method

4.2.1 Velocity Models

Geological mappings of Mt. Etna volcano have been performed since more than a century. Surface units have been mapped since De Beaumont, (1836) and the first geological maps of Etna volcano were published in the 19th century (Waltershausen, 1844, 1880). In the last decades, official geological maps were updated twice (Branca et al., 2011a; Romano et al., 1979) and many geological surveys have been carried out to map deposits along the steeps of Valle del Bove (Calvari et al., 1994; Coltelli, 1994) and integrate in the Italian geological map of the surroundings (Branca et al., 2009, 2011a; Pasquare et al., 1992). On the other hand, many geophysical seismic surveys have been also carried out (Cardaci et al., 1993; Cauchie and Saccorotti, 2013; Chiarabba et al., 2000; Cristiano et al., 2010; Hirn et al., 1991; Laigle et al., 2000; Luca et al., 1997; Patane et al., 2002; Villaseñor et al., 1998) analyzing the velocity

structure properties of the edifice. Following this studies we prepare four different models of the velocity structure by increasing its complexity on the depth variation. All the models constructed with help of a meshing tool (CUBIT-13.2 from *Sandia Laboratories)* include topography from the Digital Elevation Model (DEM) of Mt. Etna with a 50 m spacing. Horizontally we prepare a model extending 19.6 km in the EW and 16 km in the NS direction, with a max height of about 3.300m (Fig. 1), large enough to minimize reflections from the model boundaries.

We use 4 different models shown in Fig. 2. Model (S1) is homogeneous with P-wave velocity of 2000 m/s and Vp/Vs ratio of 1.73 (the value of 2000 m/s is taken from De Barros et al., 2009) The second model (*S2)* takes into account a low-velocity surface layer of 300 m thickness inferred from Bean et al. (2008). The third (*S3*) and the fourth (*S4*) models are more complex. In these two models we adopt the gradient model of Mt. Etna according to the geological map of Branca, (2011). The strong stratigraphic-gradient of the volcano is represented by different piled layers, thus are characterized by topography shape and become flatter with depth (towards a proportional smoothing function) until the sea level. We define the velocities at depth according to Patanè, (2002), Branca, (2009), Chiarabba, (2000) and Cristiano, (2010). Model *S3* has a homogeneous surface layer of 300 m (Fig. 2). Model *S4* (Fig. 2) has a strong gradient structure in the shallow depths down to 360 m as inferred from Cauchie and Saccorotti, (2013). P-wave velocities (Vp) are derived from S-wave velocities (Vs) as, $Vp = \sqrt{3} \, Vs$ assuming a constant Poisson's ratio of 0.25. The material densities are computed following the formula proposed by Potter, (1998) in function of Vp. We use models *S1*, *S2* and *S3* to compute Green's functions for the inversion while model *S4* is used to compute the synthetic data.

In order to investigate if the four velocity models differ enough among each other at typical frequencies for LP events (0.2 − 2 Hz), we compare their elastodynamic response to a plane

wave (SH). We take advantage of a *Thomson-Haskell* (Haskell, 1953; Thomson, 1950) propagator matrix to compute the complete response of a layered structure to an impulsive source. We build four models consisting of the layers with the geological properties and thickness corresponding to the velocity models described above. Fig. 3a shows the filtered (0.2 – 2 Hz) velocity traces at the surface for an impulse source placed at 3 km depth. The shape of the impulsive source is almost unchanged for models *S1* and *S3* while models *S2* and *S4* are more subjected to reflections/transmission effects due to the higher velocity contrast of the shallow layers. Model *S3* shows arrival times comparable to the reference model *S4,* while models *S1* and especially model *S2* arrivals are considerably delayed (~1-1.5 s). The amplitudes are higher for model S4 decreasing towards models S1. The frequency content of the recorded velocity traces (Fig 3b) shows a single peak for model *S4* (f ~1.2 Hz) while the other models show different peaks with the main energy focused at lower frequencies. This simple comparison is obviously not representative of the complex Mt. Etna geological context. Including topography and not equally spaced layers strongly influences the recorded waveforms. For our purposes of the blind test, the *Thomson-Haskell* propagator implies that models *S1, S2* and *S3* may not represent perfectly model *S4.*

4.2.2 Methodology

In an elastic medium, the *n*-th component of the displacement (*u_n*) at a point *x* at a time *t* is given by the convolution between the source-time function of the moment tensor/single force and the medium response, i.e. Green's functions (GFs) (Aki and Richards, 2002):

$$\boldsymbol{u}_n(\boldsymbol{x},t) = M_{pq}(t) * G_{np,q}(\boldsymbol{x},t) + F_p(t) * G_{np}(\boldsymbol{x},t) \qquad n,p = 1,2,3$$

Eq (1)

where M_{pq} is the *pq*-component of the seismic moment, F_p is the single force acting in the *p* direction and G_{np} represents the medium response (Green's function) for the *n*th-component displacement due to a unit single force F_p and $G_{np,q}$ means the spatial derivative with respect to the *q*-component at the source position. The asterisks indicate an operation of convolution and the Einstein summation convention is applied. To calculate GFs in the elastic medium with irregular surface topography, we use a 3D-full wavefield numerical simulation taking advantage of a spectral element code *EFISPEC3D* (De Martin, 2010, 2011). We put potential source positions within a volume of 1.000 x 1.000 x 800 m^3 located below the main crater of Etna volcano between 2.2 km a.s.l. and 3 km a.s.l. (Fig. 1). Among the 28 receivers used in this study, 13 receiver locations correspond to the stations of the permanent network operated by INGV (Istituto Nazionale di Geofisica e Vulcanologia), 12 are from temporary surveys (De Barros et al., 2009; Lokmer et al., 2007; Saccorotti et al., 2004) and 3 receivers are added to guarantee the azimuthal coverage for our synthetic test (Fig. 1). In order to treat a large number of source locations we take advantage of the reciprocity (Aki and Richards, 2002) to calculate GFs.

We carry out the inversion in frequency domain for eq. (1), which is schematically written as a vector equation:

$$\boldsymbol{u} = \boldsymbol{Gm}$$

Eq (2)

where **u** is the data matrix, **G** contains the Green's functions and **m** is the moment tensor and single forces components that we aim to obtain. We perform the inversion for the model parameters **m** without applying any a priori constraints to the solution (hereafter called "unconstrained inversion"). We define the misfit (R) function as:

$$R = \frac{(\boldsymbol{u} - \boldsymbol{Gm})^T (\boldsymbol{u} - \boldsymbol{Gm})}{\boldsymbol{u}^T \boldsymbol{u}}$$

Eq (3)

where superscript T denotes a transposed matrix. The least-squares solution of eq. (2) is given by (e.g., Menke, 1989):

$$\boldsymbol{m}^{est} = (\boldsymbol{G}^T \boldsymbol{G})^{-1} \boldsymbol{G}^T \boldsymbol{u}$$

Eq (4)

This inverse problem (eq. 2) can be solved either for six independent moment tensor components (MT) (assuming no single forces), or six moment tensor plus three single forces (MT+F). The inversion is carried out for each position of the source (14196 positions at 40 m spacing). Comparing the value of the misfit R from each inversion we can estimate the best fitting source position. For analyzing the estimated solution in terms of their mechanism, we use the principal component analysis (PCA) through a singular value decomposition (SVD) (Vasco, 1989). This technique assumes the existence of a unique source time function (STF) for all the six components of the moment tensor (see Vasco, 1989 for further details). We then decompose the moment tensor solution into isotropic (M_{ISO}) and deviatoric ($M_{CLVD} + M_{DC}$) parts after Vavrycuk, (2001).

Additionally, we also perform a constrained inversion following the approach by Lokmer et al., (2007), assuming either a tensile crack or isotropic source mechanism. Eq. (2) is rewritten as

$$\boldsymbol{u} = \boldsymbol{G}\, M_0\, \boldsymbol{f}(\phi, \theta)$$

Eq. (5)

where $\boldsymbol{f}$ is a function of strike ϕ and dip θ, independent of frequency. Our inversion reduces to finding a single parameter $M_0(\omega)$. We perform the grid search spanning from 0° to 360° for strike (ϕ) and from 0° to 90° for dip (θ), every 10° for the tensile crack mechanism. For an isotropic source one inversion is enough as the function $\boldsymbol{f}$ has a unique expression.

4.2.3 Synthetics data

Previous inversions of LP signals on Etna volcano (De Barros et al., 2011; Lokmer et al., 2007) suggest quasi-vertical crack orientations. Hence we simulate, as the synthetic source mechanism, a point source of a vertical tensile crack ($\phi=45°$, $\theta=90°$) at two different depths located below the summit craters: at 2.880 m.a.s.l. (shallow source, ~400 m depth) and at 2.240 m.a.s.l (deep source, ~1.2 km depth). We use a Ricker wavelet as source time function with the main energy in the frequency range 0.2 – 1.2 Hz (typical for LP events, (Chouet, 2003a) and an amplitude of 4 x 10^{10} Nm. As already mentioned, Model S4 was used to calculate the data. Time step was $\Delta t = 1$ x 10^{-4} s, for a duration $t_{tot} = 20$ s. A single simulation of 2.3 x10^{6} hexahedron elements takes about 18 hours on 192 cores on our local server (AMD Abu Dhabi at 1.6 GHz).

4.3 Results

We first carry out the unconstrained inversion in order to investigate the reliability of the solution and the uncertainty between the different velocity models.

In the following, we will discuss the source location, the source mechanism and the source time function obtained from MT/MT+F inversions with models *S1, S2* and *S3*. The 12 stations located nearby the summit, offering a proper azimuthal coverage, are used (Fig. 4 and Fig. 5). We choose to include only 12 stations located in the near-intermediate field as synthetic results (not showed here) including further stations show comparable solutions.

4.3.1 Source location

First, for the two given source depths (~400 m and ~1.2 km depth), we explore how well the inversion procedure can retrieve the original position in different structure models. We evaluate the misfit from the moment tensor plus single force (MT+F) inversions. The comparisons of the waveforms for the shallow and deep source, respectively, are shown in Fig. 4 and Fig. 5 for the best hypocenter position in each model. The overall shape of the original signals is well reproduced by all three models and we do not recognize any significant difference between the solutions. The stations nearby the source location reproduce the original source time function (STF) shape better as the amplitude and phase are less subjected to attenuation, scattering and reflection phenomena. This is the case for stations *et08*, *et06* and *et09*, while differences on the waveforms are stronger for farther stations (e.g. *cl01* and *et99*). We find that model *S3* tends to introduce additional phases in the coda (e.g. stations *cl02* and *et99* for the shallow source and stations *cl01* and *cl02* for the deep source).

Figure 6 shows the misfit *R* for the MT inversion at all possible source locations for each velocity model and the misfits are summarized in Tables 1 and 2. For shallow source, the minimal misfit found in model *S2* coincides with the original source position. For models *S1* and *S3* the obtained source locations are shallower than the original one, at the upper limit of our parameter search. For the deep source we get good (~200 m distance from the original

position) horizontal and vertical resolution for both *S1* and *S2* models. For model *S2* the location is slightly better constrained, the lowest misfit value sharply converges to a single position. For model *S1* we can observe a large spreading of the lowest values, even if the lowest misfit still points to the right source position. Model *S3* points to a quite distant (~400 m from the original position) source location and the value of misfit (Table 1) is considerably higher than the two other models.

4.3.2 Source mechanism

For the best source position obtained above, the estimated source orientations and isotropic/deviatoric decomposition for each model are listed in Table 1(shallow source) and Table 2 (deep source).

4.3.2.1 Shallow source

The crack strike (ϕ) is well retrieved for both inversions (MT+F and MT only) while the crack dip (θ) is close to a solution of a horizontal crack rather than a vertical one for the solution including single forces. The minimum misfit R is found for model *S1*. In terms of isotropic/deviatoric decomposition, the MT+F inversion points to the right ratio, letting the predominant component in C_{ISO}, C_{DC} tend to zero and C_{CLVD} show values close to the given one for all three models. The MT inversion without single forces points to a very low C_{CLVD} value and a high C_{DC}. In this case the mechanism would be interpreted differently with a strong double-couple component and a mixed ISO/DC solution.

4.3.2.2 Deep source

Table 2 shows the results for the deep vertical crack. Again the lowest misfit values are found for the *S1* model (both MT+F and MT solutions). Model *S3* shows a very high misfit value. The crack strike (ϕ) and dip (θ) angles are very similar to those expected for all three models, best solutions are obtained for model *S1* (MT+F) and *S2* (MT+F) leading to the expected values for both strike (ϕ) and dip (θ). In terms of mechanism, the decomposition for models *S1* and *S2* give a low C_{DC} component and the crack solution is well retrieved, while model *S3* tends to overestimate the C_{DC} component (16% for the MT+F solution).   The same observations are brought for the MT inversion except that we find higher misfit values and higher C_{DC} component contributions.

In summary, we find that model *S1* gives the lowest misfit value for both MT+F and MT inversions at both depths. The crack orientation is better retrieved by model *S2* such as the isotropic/deviatoric decomposition. The MT+F inversion gives always the best result.

4.3.3 Source time function

Figs. 7 and 8 show the comparison between the original source time function and the retrieved one for MT+F and MT inversions respectively.

4.3.3.1 MT+F

In the MT+F inversion the force terms show high amplitudes especially for model *S1* (Fig. 7). This is consistent with De Barros et al., (2013) who showed that spurious single forces were generated to accommodate converted waves at layered interfaces. A force with an amplitude of 10^8 N s is comparable to a seismic moment of 10^{11} Nm (Aki and Richards, 2002; De Barros et al., 2013), i.e. leading to waves of the same order of amplitude. For the shallow source inversions, the misfit values between the original and the retrieved source time functions

(considering only the MT terms) are very high for the three models. Model *S1* shows the highest value (misfit = 28.972). Model *S2* shows the best match with the original solution. The original STF is generally well reproduced (especially models *S2* and *S3*), but the M_{zz} component suffers of high amplitude overestimation thus leading to the high computed misfit values. For the deep source, amplitudes of the seismic moment are always underestimated. The misfit values are considerably lower than for the shallow source with model *S1* showing better correspondence with the original source time function. Anyway, the overall shape of the retrieved STF is similar and well reproduced for all different models.

4.3.3.2 MT only

The MT inversion (Fig. 8) shows similar results, but the misfit values are considerably lower than the solution including forces. Again, the M_{zz} component of the shallow source does not match the original solution especially for the simplest model *S1*. This is probably due to the *quasi*-horizontal layering in which the wave conversions occur and that is barely taken in account by the homogeneous model *S1*. Models *S2* and *S3* show comparable misfit values (~0.85) and the amplitudes of the moment tensor components are comparable to the original STF even if M_{xx} is underestimated. For the deep source the misfit values are lower, as seen for the MT+F solution. Best matching between the original and the retrieved solution is obtained by model *S1* (misfit = 0.545). The overall amplitude of the STF is in general underestimated; this is particularly evident for the radial component M_{xx} that, as for the shallow source solution, shows the larger underestimation.

4.3.4 Constrained Inversion

Finally we perform the constrained inversions. The results under the different mechanisms of hypothesis (tensile crack or isotropic source) led to the lowest misfit value for a crack solution (Table 3). Misfit results for the crack mechanism are shown in Figs. 9 and 10. All models show a good solution with the lowest misfit indicating the correct angles (strike (ϕ) and dip (θ)) for both the shallow and the deep source in the given parameter ranges. Figs. 11 and 13 show the comparison between the original and the retrieved STF for all three models and depths from the inversions with and without single forces, respectively. The retrieved amplitude in models *S1* is overestimated in all the inversions. The amplitude is twice than expected for the shallow source. STF shape is well retrieved in both models *S2* and *S3* for the solutions with and without singles forces. For the deep source a phase shift between the original and retrieved STF occurs due to the different velocity model. Generally both models *S2* and *S3* offer a good solution in both angle pairs and STF, while model *S1* tends to overestimate the STF amplitude.

In summary, the synthetic test shows that the deep source mechanism is correctly retrieved by both the MT+F and MT only solutions. The shallow source, on the opposite, suffers from high errors in the retrieved STF which strongly influence the mechanism decomposition. The MT+F solutions and the MT only solution for model *S1* would be interpreted as a shallowly deeping tensile crack. The MT only solution for models *S2* and *S3* point to a quasi-vertical crack as expected, but the appearance of the non-existing double-couple components complicates the mechanism interpretation. We now extend the synthetic test by applying the same MT inversion configuration to a real event.

4.4 Real Case: an LP event in 2008

Despite our synthetic test has been designed to reproduce reality, in the real world MT inversion is subject to uncertainties which strongly influence our ability in retrieving the correct solution. Here we want to show the influence of the choice of a particular velocity model on the inversion process, thus we end up performing an inversion of an LP event recorded on Etna in 2008 during a high resolution seismic survey (De Barros et al., 2009, 2011). The considered event was recorded on June 19, 2008 and belongs to the second family of events identified in De Barros et al. (2009). The source mechanism was analyzed (De Barros et al., 2009, 2011): a) by locating the event with a time delay technique based on cross correlation and b) by identifying the source mechanism performing a MT inversion using a homogeneous model (same velocities as our model *S1)*. The mechanism was retrieved as a sub-vertical crack oriented ϕ=N340° E and inclined θ=50° (see De Barros et al., (2011) for further details). While De Barros et al., (2011) used 16 stations in their inversion, we choose 12 stations with a good azimuthal distribution around the source (Fig. 13) in order to reproduce a context similar to the one chosen for our synthetic test. Fig. 13 shows the comparison between the original filtered data and our synthetics resulting from the MT inversion for the three models separately. Stations *etsm* and *et08* show the highest amplitude signal and thus contribute more to the final solution. The waveforms comparison for these two stations shows a good correspondence between the observed and the retrieved signals for all three models. Farther stations do not reproduce the increased complexity in the original signal, for example at stations *emfs* and *emcn.* For the MT+F inversion, the location solution (Fig. 14) for model *S2* shows the lowest misfit value and is also closest to the location determined by De Barros et al. (2011); our location is shifted horizontally by about 450 m and vertically by 200 m. Models *S1* and *S3* suggest deeper locations with higher horizontal differences ($\approx$ 650 m). We then apply PCA on the obtained solutions in each inversion. Similar to De Barros et al., (2011), we obtain a high M_{ISO} component in both MT+F and MT

inversions (Table 4). Model *S2* for the MT+F solution shows the lowest M_{ISO} value (79 %) and a relatively high M_{DEV} (21%) component. Like De Barros et al., (2011), we perform a Vasco, (1989) decomposition on the M_{DEV} part of our MT inversion solution. For model *S2* the results show a strike of $\phi=90°$ and a dip of $\theta=21°$, i.e. a sub-horizontal crack instead of the sub-vertical one obtained by De Barros et al., (2011). The solution from models *S1* and *S3* also varies, in particular in terms of strike. The dip of $\theta=67°$ from model *S3* is comparable to the one found by De Barros et al., (2011). Fig. 15 shows the retrieved STF for the three models after the MT inversion. Here model *S1* shows higher amplitude than the two other models. As MT and MT+F solutions are often used to estimate the volume of fluids or gas mobilized at the source (Davi et al., 2010; Hidayat et al., 2002; Jousset et al., 2013; Ohminato et al., 1998), the significant difference among velocity models causes high uncertainties. This amplitude difference is still present when we consider the existence of single forces but it is less remarkable. The overall shapes of the retrieved STFs for the three models are quite similar and model *S2* shows the simplest solution. For all the three models, the diagonal of the moment tensor is largely dominant while non-diagonal elements show clear lower amplitude. Non-diagonal elements in the solution without single forces tend to be overestimated compared to the solution including forces. The high C_{ISO} component suggests a possible isotropic source mechanism and so does the constrained inversion which shows slightly lower misfit values for the explosion solution (Table 5). In terms of the orientation of the crack solution, the parameter search does not indicate a clear orientation (Fig. 16). The solution including forces shows a narrow range of misfit values spanning from 0.44 to 0.5 for models *S1* and *S2,* and from 0.5 to 0.6 for model *S3*. The minimum misfit solution found for model *S2* shows a strike orientation similar to the one found by De Barros et al., (2011), but the inclination of the fault once again results in a sub-horizontal instead of a sub-vertical crack. The solution without single forces results more stable, and all three models point to the same

solution ($\phi = \approx 300°$ and $\theta = \approx 50°$), but the misfit values are very high (≈ 0.8). As the misfit values for the constrained inversion fall in a very narrow range, the solution is subject to difficult interpretations, i.e. the isotropic source solution could be preferable.

4.5 Discussion

We performed a synthetic test to investigate the sensitivity of inversion results to the choice of the structural model. Defining a single model which works the best is difficult. Model *S1* is simple and shows low misfit values, but the retrieved STFs strongly deviate from the original ones especially for the shallow source. On the opposite hand, the complex model (*S3*), which should better represent the complexity of model *S4*, does not give the better expected results. This could be because: 1) an intrinsic approximation is done in the velocity model implementation (i.e. velocities are not the same) or 2) the low velocity surface-layer of model *S3* does not take in account for a strong velocity contrast for the unconsolidated surface materials. Despite the small differences in the solutions, model *S2* seems to offer the best result in our synthetic test. It is worth nothing that the lowest misfit values obtained for the shallow source with model *S1* do correspond to the highest misfit values computed between the observed and retrieved STF. Finally we analyzed a real event recorded on Mt Etna during a high resolution seismic campaign in 2008. Our results show that, in this particular case, the model with the lowest misfit value is the surface layer model *S2*. The solution obtained with model *S2* is also the one which approaches more closely to the solution found by De Barros et al., (2011). Even at the considered long wavelengths, it seems that a major role is played by the low-consolidated materials present near the surface. The real LP event analysis highlights the influence of the choice for a particular velocity model on the retrieved solution. In the synthetic test the results are similar and an approximately good solution can always be

retrieved for each considered velocity model. On the opposite hand, the inversion performed for the real LP event is clearly influenced by the choice of the geological model, i.e. the interpretation of the source mechanism varies for each considered velocity setting. It's worth nothing that our results are delimited in a narrow frequency band ($0.2 - 1.2$ Hz) and for these frequencies the velocity model definition appears to play a major role in our source mechanism understanding. As stated by Thun, (2015) once we filter the analyzed signal we loose informations about the complete history of the source motion. Thus, further analysis including different and wider frequency ranges should be performed, i.e. find a lower limit frequency (if it exists) for wich the inversion process is not influenced by the velocity model. After our synthetic tests we can state that:

1. recognized the presence of unconsolidated surface materials, a low velocity surface-layer should be included when performing MT inversion for LP signals; on the other hand, careful attention should be paid in including deeper geological features which may not be realistic or just representative of a small volume of the volcanic edifice;

2. The solutions for the shallow source are strongly influenced by the lateral heterogeneities of model *S4* and the mechanism interpretation is misleading. Model *S4* is supposed to represent the strong velocity contrast occurring in the shallow unconsolidated materials typically observed on volcanoes, thus, even with good stations covering, shallow sources should be carefully interpreted.

3. Lowest misfit values are not synonym of best solution. The lowest residual obtained for the shallow source towards MT+F for model *S1* gives the highest misfit between original and retrieved STF i.e. the real STF amplitudes are strongly overestimated.

4. Moderately high, inexistent double-couple components arise in all models interpretations and are particularly important in the MT only solutions. This must be considered when trying to interpret real events showing non-negligible shear components.

4.6 Conclusion

We investigated the influence of the choice of a particular velocity model on the moment tensor (MT) inversion. Four models, including topography of Mt. Etna volcano and increased geological complexity, have been used in our synthetic test. The low velocity surface-layer model (*S2*) delivered better results in terms of location and mechanism understanding. Source locations towards MT inversion led to roughly precise positions suggesting that, when possible, other location methods (such as amplitude decay, cross-correlation coefficient and semblance e.g. Cannata et al., (2013) and references therein) should be used in locating real LP events. Once the event located and the unconstrained MT inversion performed we suggest performing a constrained MT inversion in order to find out the most plausible source mechanism and angles orientation. Solutions obtained for a homogenous model (*S1*) tend to overestimate the real amplitude of the source time function, hence estimations of gas/fluids volumes involved in the LP generation should be carefully interpreted. The retrieved solution is unique for the considered velocity model, but it's worth nothing that careful attention should be paid in considering the geological context where the process occurs and, if necessary, a deep analysis of many similar events and a better understanding of the contemporary state of activity of the volcano could help in constraining further the solution. Synthetic tests with different velocity configuration are strongly recommended before starting

a moment tensor inversion. The test presented in this paper can help constraining the solution and interpreting the results.

We performed a synthetic test on Mt. Etna volcano, thus our results are specifically referred to a particular volcanic context and the conclusions presented in this work should carefully tested on other volcanoes. We demonstrated that adding unrealistic geological complexities in the velocity model can lead to misinterpretation of the source process, but our test highlights also the importance of including realistic geological features in moment tensor inversion. Further works on the understanding of the material properties of volcanoes and their response to waves with wider frequency content would strongly improve our understanding of the physical mechanism beyond LP events generation.

Figures

1) Map of Mount Etna and receivers locations used in this study, the straight hash line indicates the source area for which the Green functions are calculated.

2) *Vs* velocity profiles of the four considered models. *S1, S2* and *S3* are the models used for the inversion while *S4* is the model used to prepare the synthetics.

3) Average *Vs* velocities for the four considered models for different depths. Most complex model *S4* shows the highest average velocity variation along the profile. Average velocities are computed below summit of Etna volcano vertically from 0 to 1400 m depth.

4) Waveform comparison between the synthetic (velocity model *S4*) and retrieved signals after the inversion using velocity models *S1, S2,* and *S3* for the shallow source. Three components of displacement for each station (x, y, z) are represented. The central map represents the stations used in the inversion. Numbers nearby each stations name are related to the corresponding box where waveforms are compared. The true and the retrieved hypocenter positions are plotted in the center panel.

5) Waveforms comparison between the synthetic (velocity model *S4*) and retrieved signals after the inversion using Green's functions from velocity models *S1, S2,* and *S3* for the deep source. See also the caption of Fig. 5.

6) Source location for shallow (left) and deep (right) source obtained in the inversion of minimum R using different structure models. Axes represent the relative source location with a 40 m spacing. The real source position is represented by (0,0,0). From top to bottom velocity models *S1, S2,* and *S3* used for the inversion. Lowest misfit value is represented by the synthetic slices intersection for each velocity model.

7) Comparison between original (blue) and retrieved (red) source time functions for the MT+F (including forces) inversion for three velocity models and for both source depths. Six moment tensor components and three single forces are represented.

8) Comparison between original (blue) and retrieved (red) source time functions for the MT inversion for three velocity models and for both source depths. Six moment tensor components are represented for each model

9) Misfit in parameter search (strike ɸ, dip θ) under MT+F inversion supposing a tensile crack. The minimum retrieved misfit is represented by a [*x*] and the given value by [+].

10) Misfit in parameter search (strike ɸ, dip θ) under MT inversion supposing a tensile crack. The minimum retrieved misfit is represented by a [*x*] and the given value by [+].

11) Comparison between original and best retrieved source time function in the constrained MT+F inversion for a tensile crack. (a) Shallow source, (b) Deep source. Three structure models are used.

12) Comparison between original and best retrieved source time function in the constrained MT inversion for a tensile crack. (a) Shallow source, (b) Deep source. Three structure models are used.

13) Waveforms comparison between the filtered (0.1 – 1.2 Hz) observed signals and the synthetics filtered. The used receiver position and the obtained hypocenter location from each inversion for the LP event recorded on Mt. Etna (2008) are shown. A star represents the solution obtained by De Barros et al. (2009).

14) Misfit with respect to the source position for the LP event. The location through MT inversion is conducted in three different velocity models (*S1, S2* and *S3* respectively). The axes in meters represent the relative distance to the original source location determined by De Barros et al. (2011). Original solution (x, longitude, 49950 Km, y, latitude, 4178450 Km, z, height, 3 Km)

15) Comparison of source time functions for each MT and MT+F inversion in each of the three velocity models.

16) Misfit plot of the crack orientation (strike ϕ and dip θ) supposing a tensile crack in constrained MT+F and MT inversion for each structure model.

Table 1 Summary of the results in MT+F and MT inversions for the shallow vertical crack, using different structure models (S1, S2 and S3), respectively. For the best misfit in each inversion, the fault mechanism (strike, dip) are calculated and the decompositions are performed.

Inversion	Structural model	Misfit	ϕ	θ	ISO (%)	CLVD (%)	DC(%)
MT+F	S1	0.123	53.5	17.4	54	40	6
	S2	0.155	47.1	17.4	52	35	12
	S3	0.219	48.5	19.1	55	39	6
MT	S1	0.174	44.9	27.7	55	2	43
	S2	0.240	41.3	65.4	45	15	40
	S3	0.291	42.0	60.7	45	6	48
Given Parameters	**S4**	**-**	**45**	**90**	**55**	**45**	**0**

Table 2 Summary of the results in MT+F and MT inversions for the deep vertical crack. See also the caption of Table 1.

Inversion	Structural model	Misfit	ϕ	θ	ISO (%)	CLVD (%)	DC(%)
MT+F	S1	0.250	45.4	91.7	47	48	6
	S2	0.269	46.4	90.9	48	46	6
	S3	0.412	51.8	79.0	53	31	16
MT	S1	0.341	43.3	88.0	57	26	17
	S2	0.344	45.1	87.9	58	26	16
	S3	0.490	50.3	83.2	55	34	11
Given Parameters	**S4**	**-**	**45**	**90**	**55**	**45**	**0**

Table 3 Obtained minimum misfit values in constrained inversion (crack and explosion) and crack orientation (φ,ϑ). Note that the given crack mechanism is a tensile with φ=45° and ϑ=90°. Parameter searches are performed every 10°.

Oriented Crack

	MT+F			MT		
			Shallow			
Structural model	*Misfit*	ϕ	θ	*Misfit*	ϕ	θ
S1	0.324	40	90	0.303	40	90
S2	0.327	40	90	0.385	40	80
S3	0.384	40	90	0.443	40	80
			Depth			
S1	0.358	50	90	0.470	50	90
S2	0.404	50	90	0.485	50	90
S3	0.550	50	90	0.608	50	90

Explosion

	MT+F			MT		
			Shallow			
S1	0.3852	-	-	0.5655	-	-
S2	0.4275	-	-	0.6297	-	-
S3	0.5162	-	-	0.6692	-	-
			Depth			
S1	0.8395	-	-	0.9422	-	-
S2	0.8388	-	-	0.9333	-	-
S3	0.8654	-	-	0.9517	-	-

Table 4 Inversion results for a LP event recorded on Etna in different inversion settings. For comparison, the result of De Barros et al. (2011) is also shown at the bottom.

Inversion	*Structural model*	*Misfit*	*ϕ*	*θ*	*ISO (%)*	*CLVD (%)*	*DC(%)*
MT+F	*S1*	0.386	85.8	82.4	92	2	6
	S2	0.349	90.0	21.4	79	14	7
	S3	0.453	48.1	67.2	90	3	7
MT	*S1*	0.637	78.9	12.7	82	1	17
	S2	0.703	-	-	-	-	-
	S3	0.684	27.0	71.5	78	12	10
De Barros (2011)		-	340	50	80	-	-

Table 5 Constrained inversion results (misfit and mechanism) for a tensile crack and an explosion for the 2008 LP event occurred on Etna.

Crack

Structural model	MT+F			MT		
	Misfit	ϕ	θ	*Misfit*	ϕ	θ
S1	0.454	70	70	0.806	310	50
S2	0.446	290	20	0.833	300	40
S3	0.544	30	40	0.817	310	60

Explosion

Structural model	MT+F			MT		
S1	0.443	-	-	0.953	-	-
S2	0.425	-	-	0.629	-	-
S3	0.545	-	-	0.975	-	-

Figures

1)

2)

3)

a)

b)
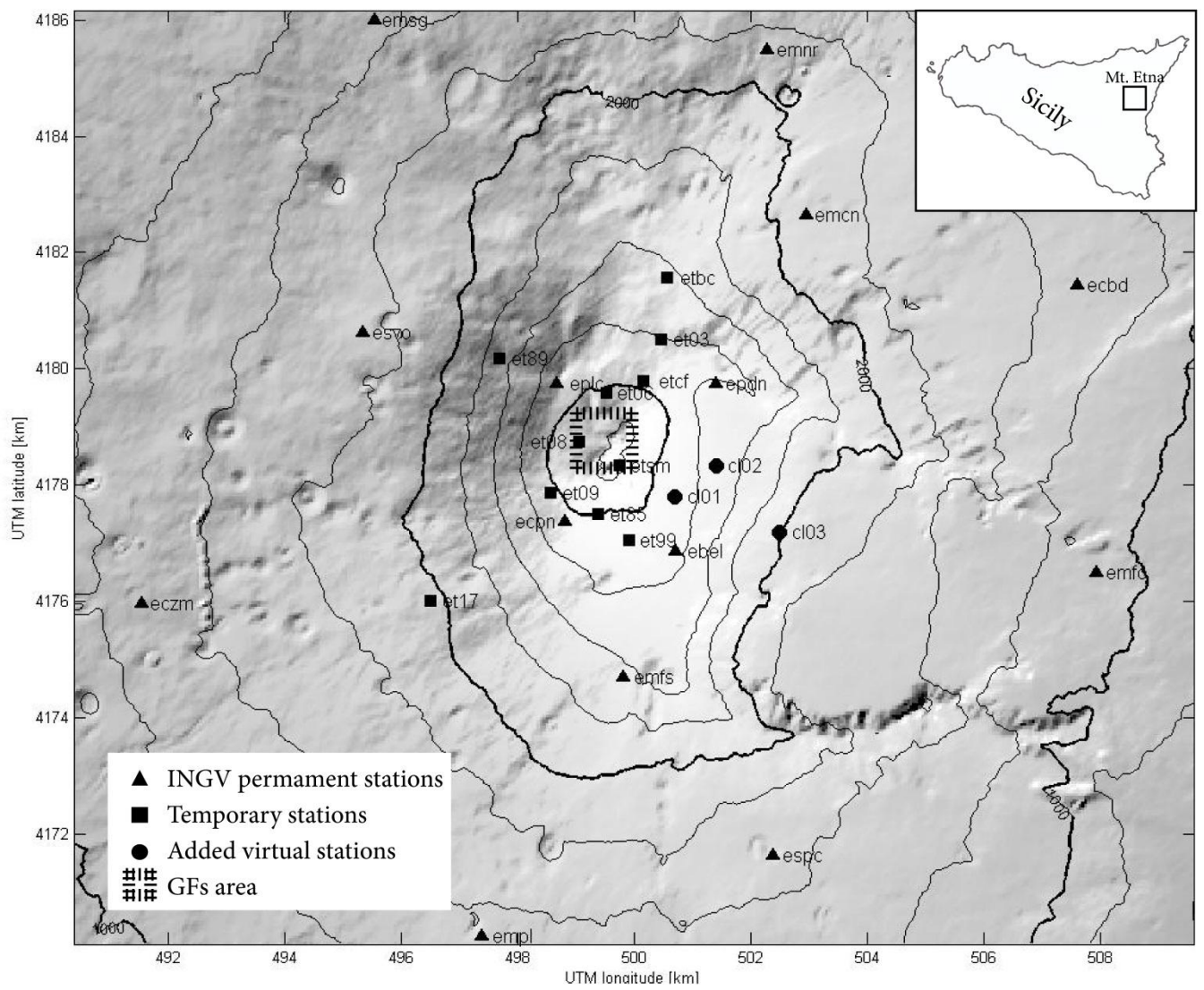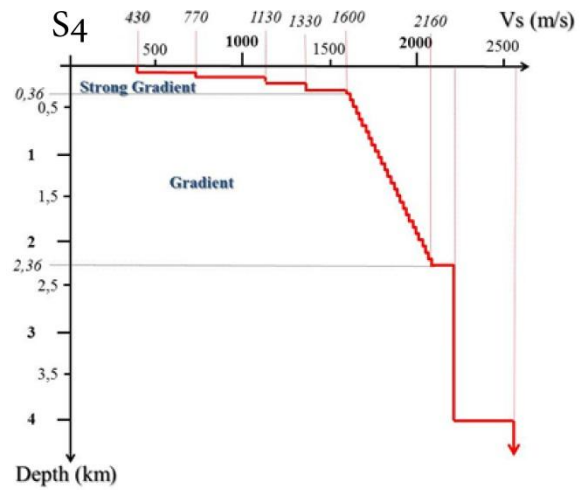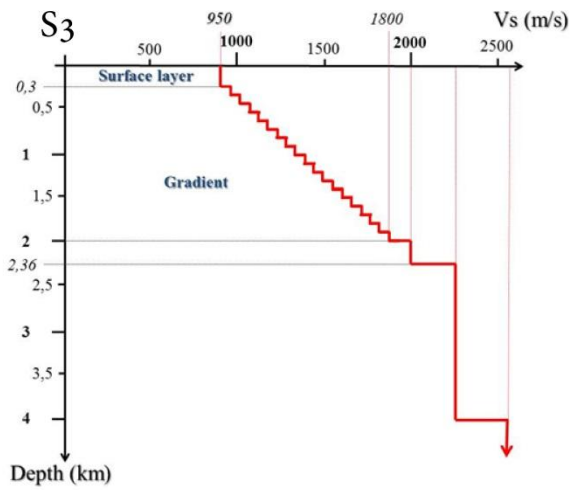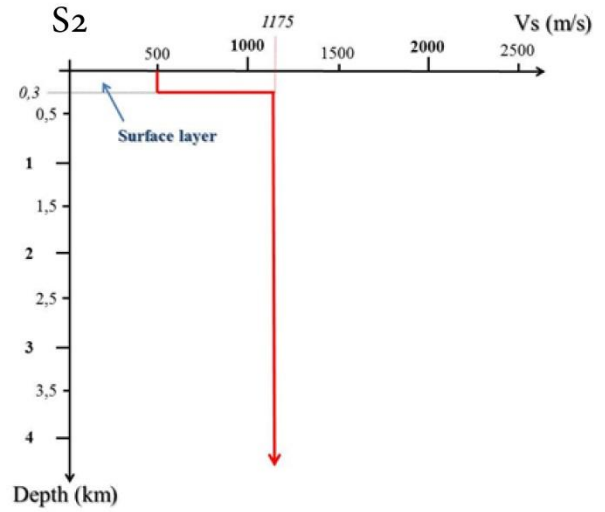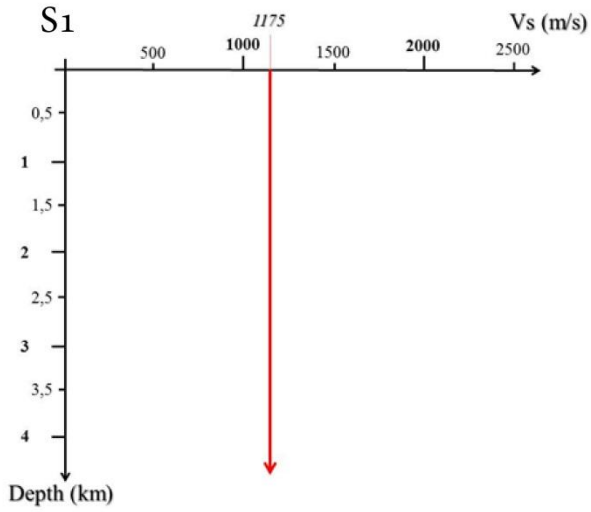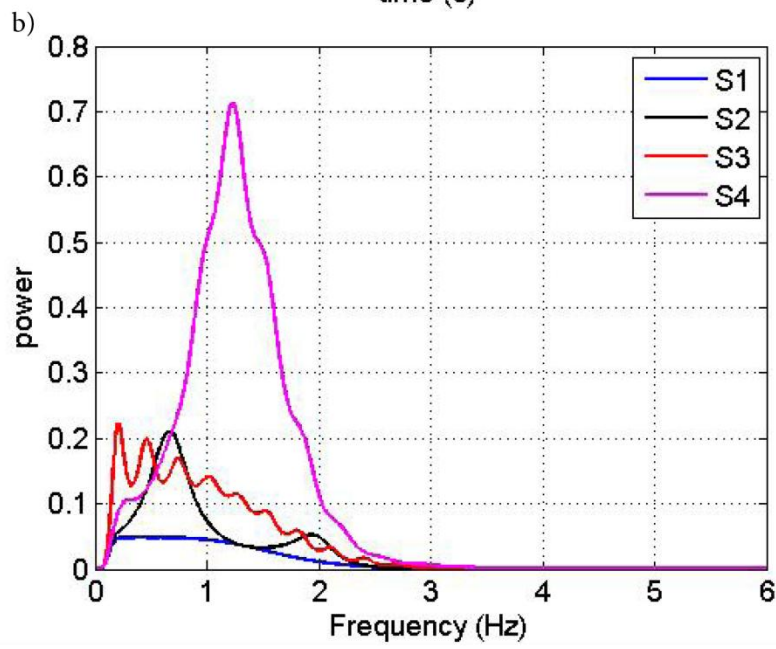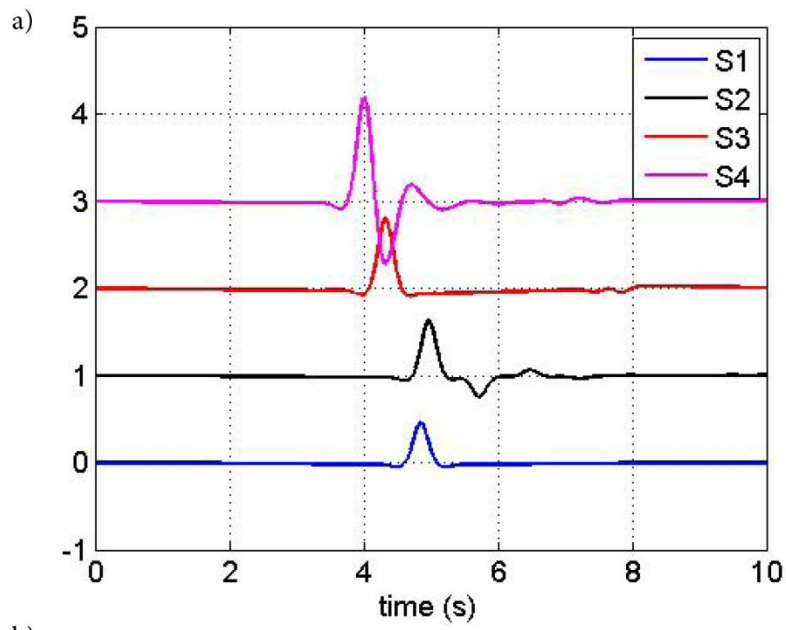
4)
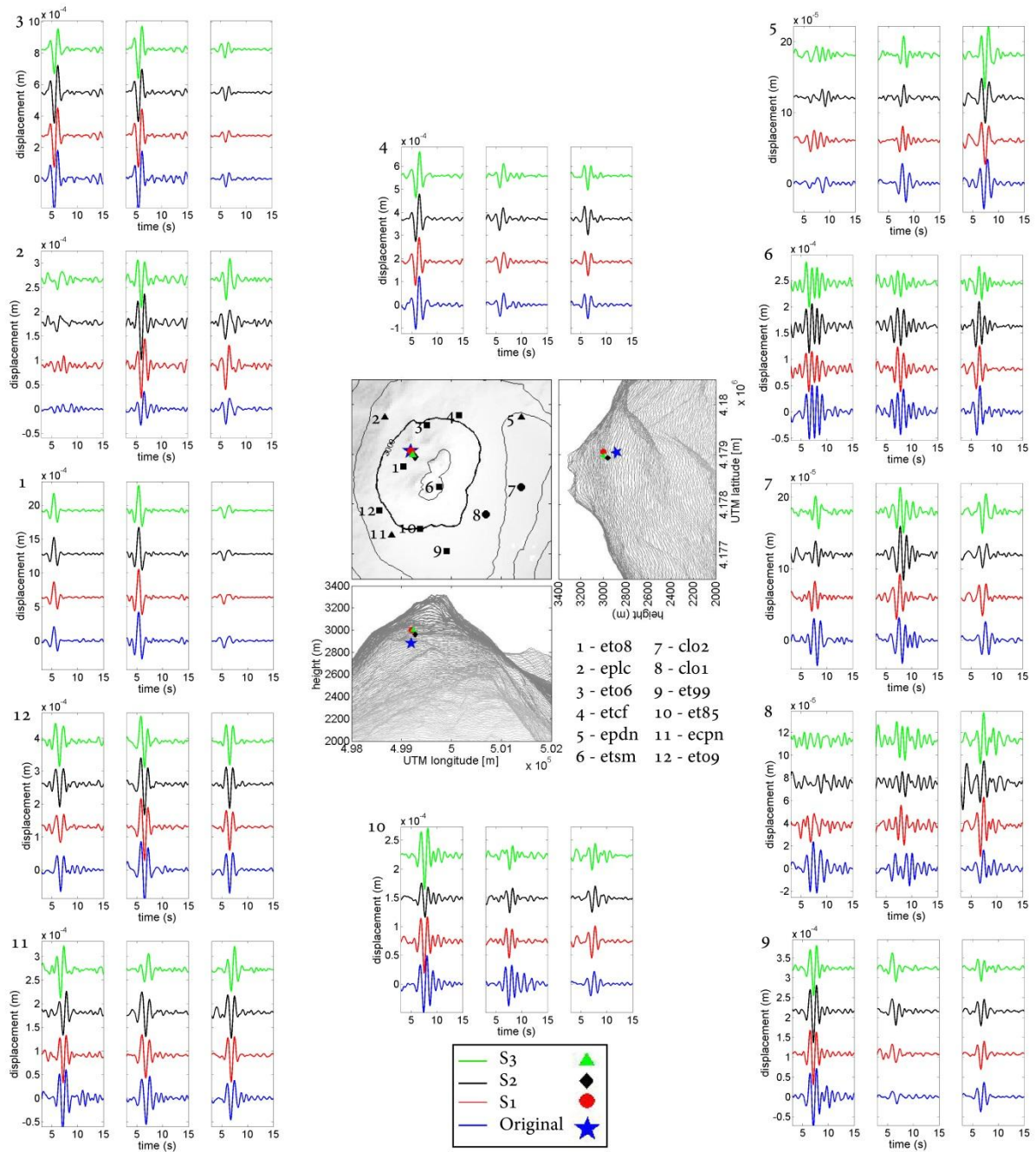
5)
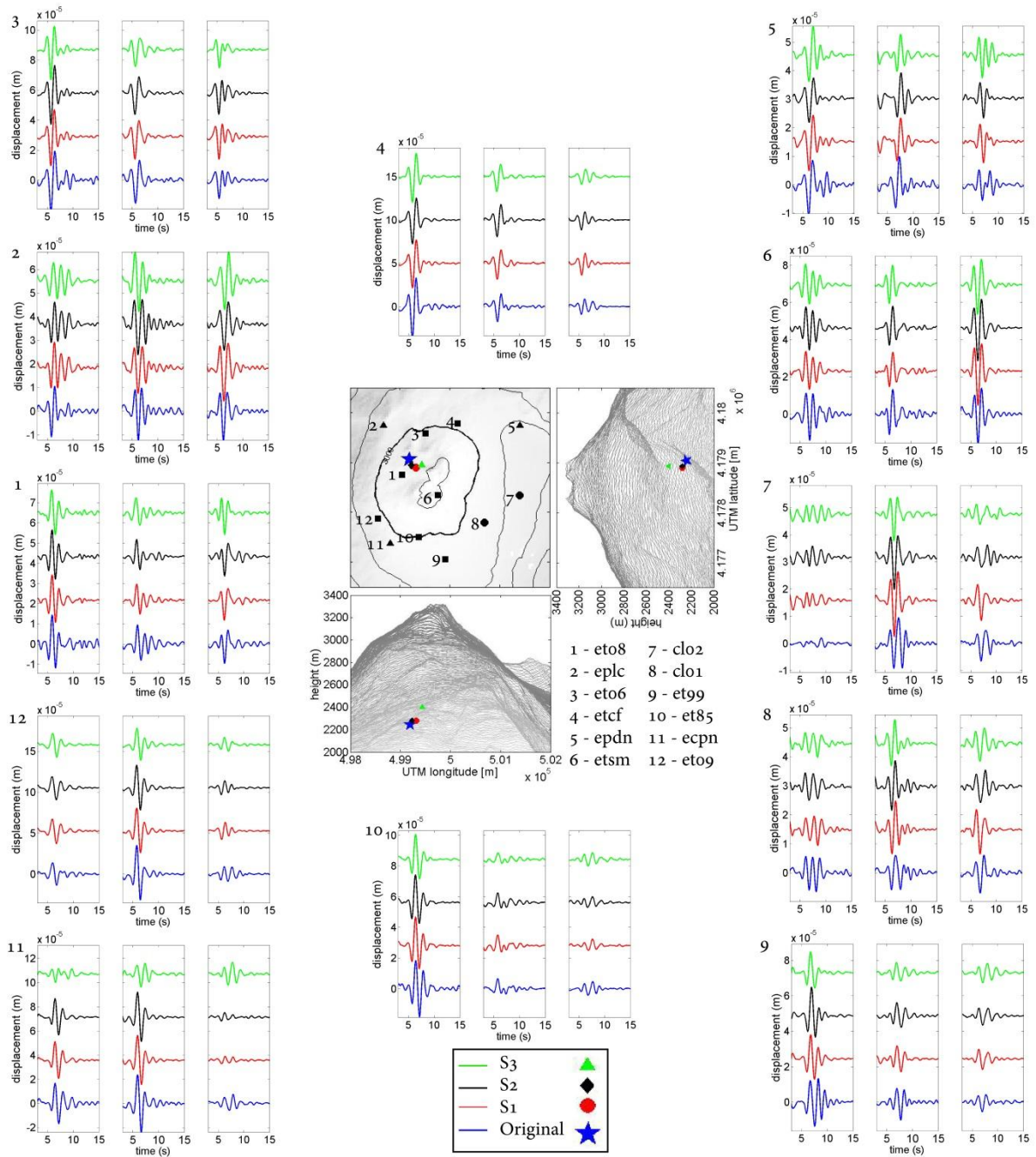
6)
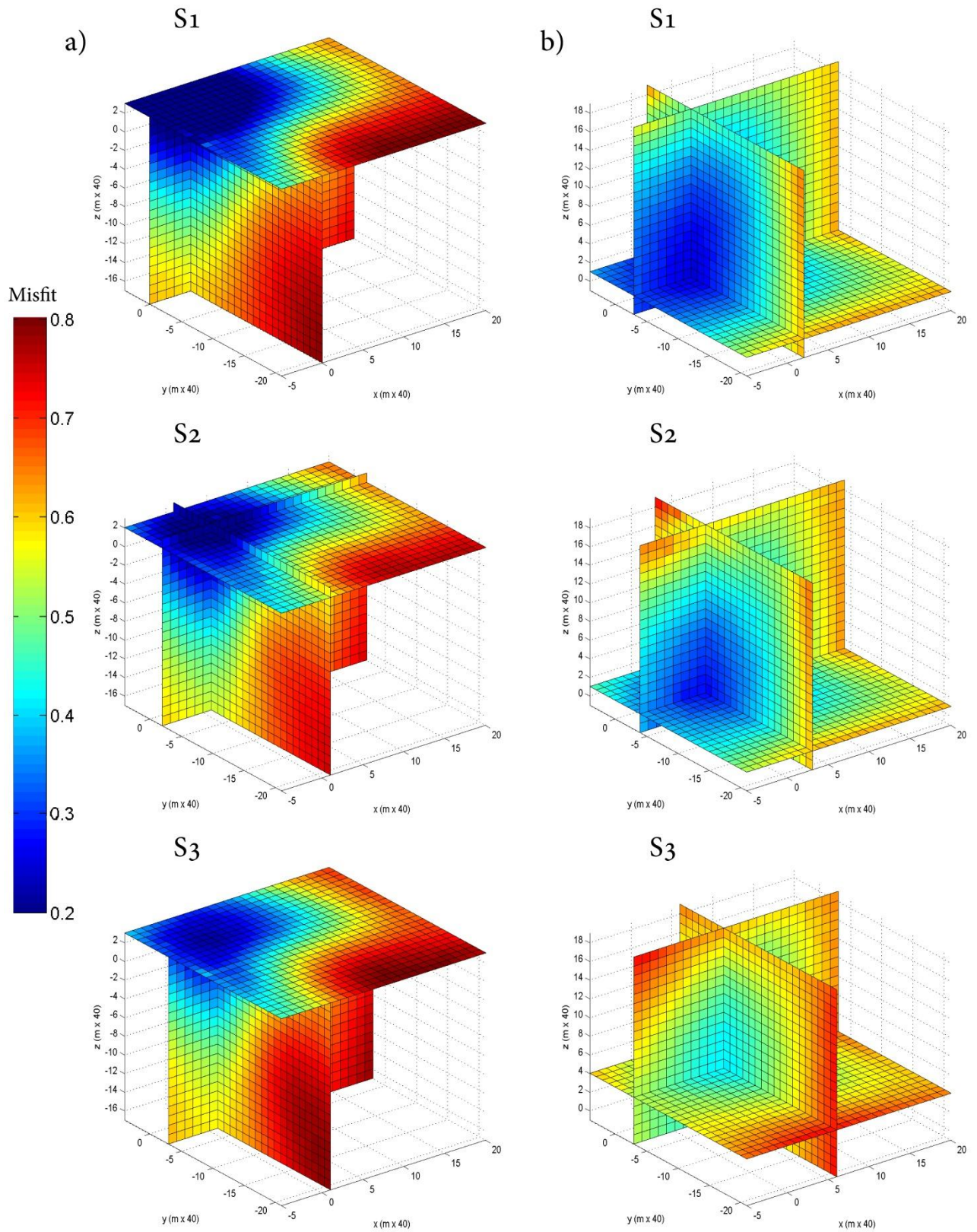
7)
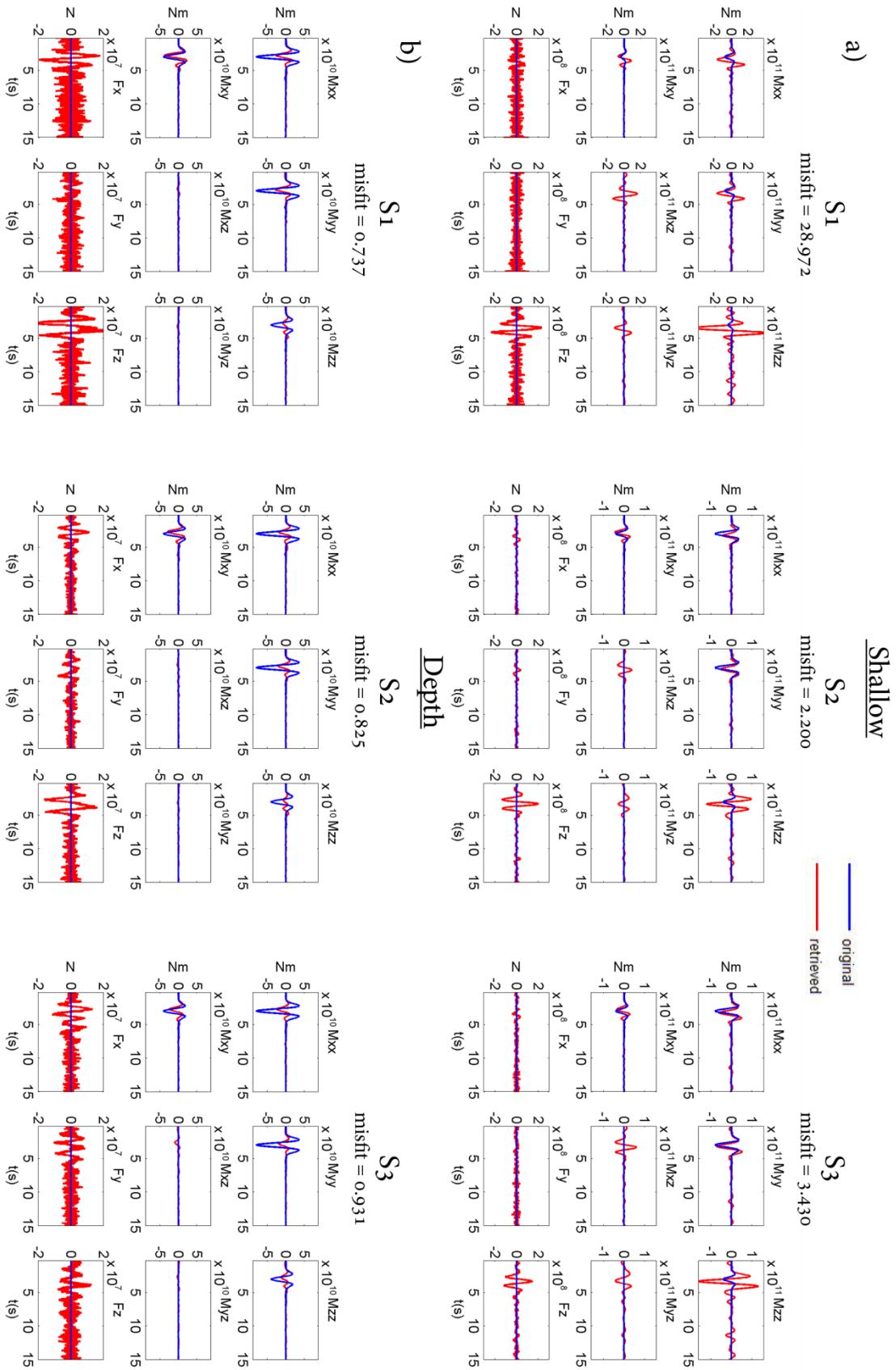
8)
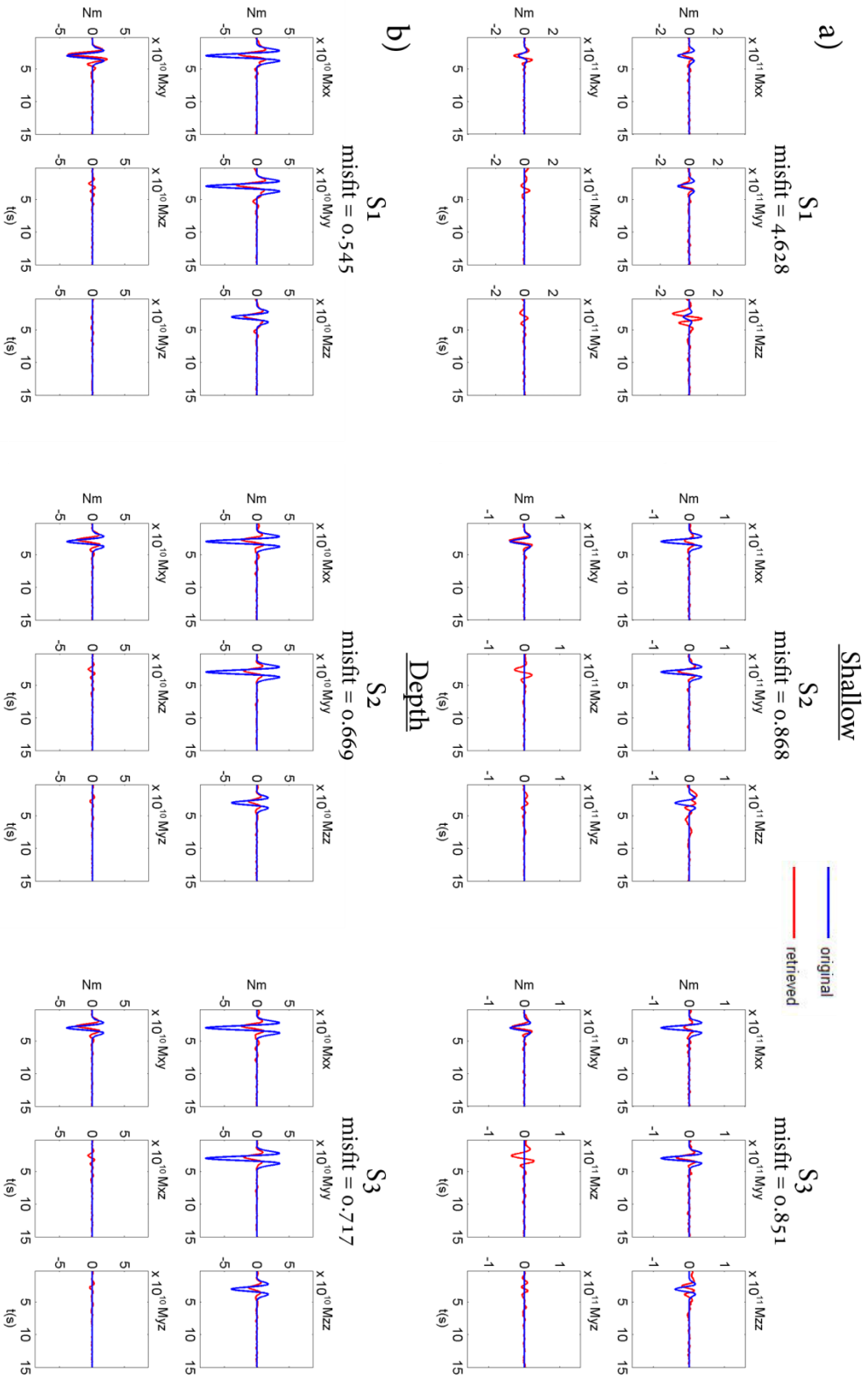
9)
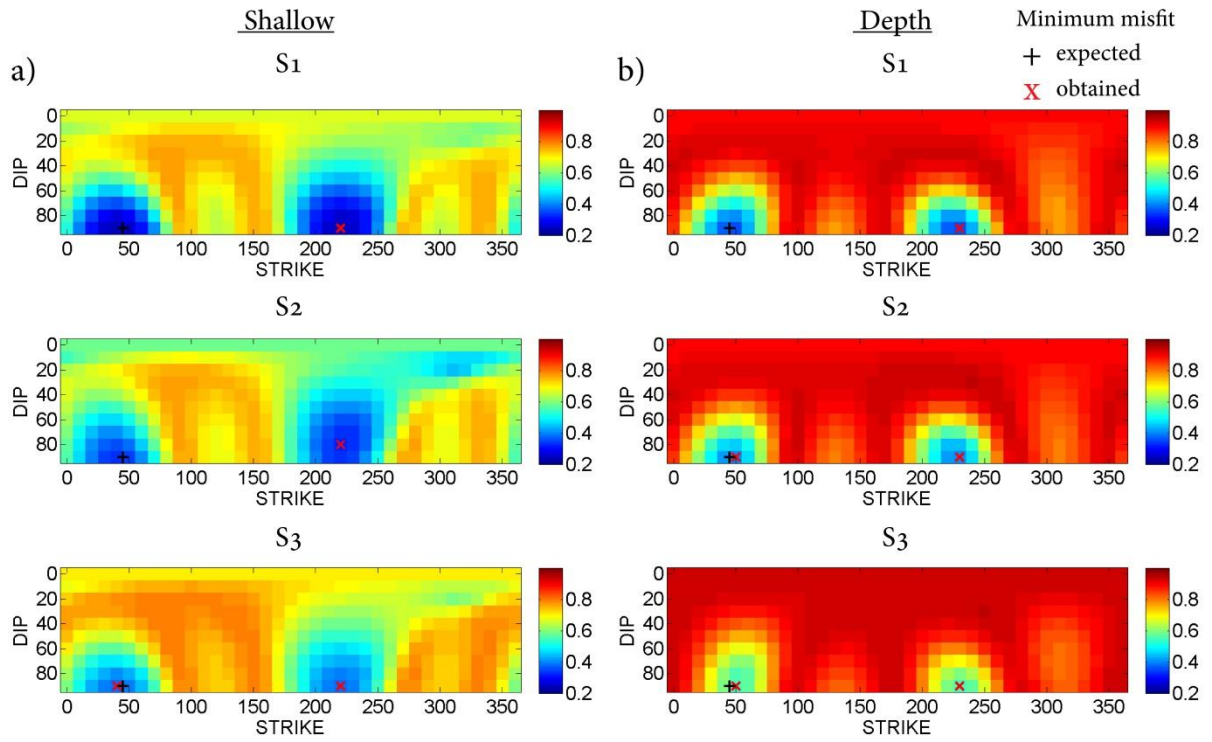
10)
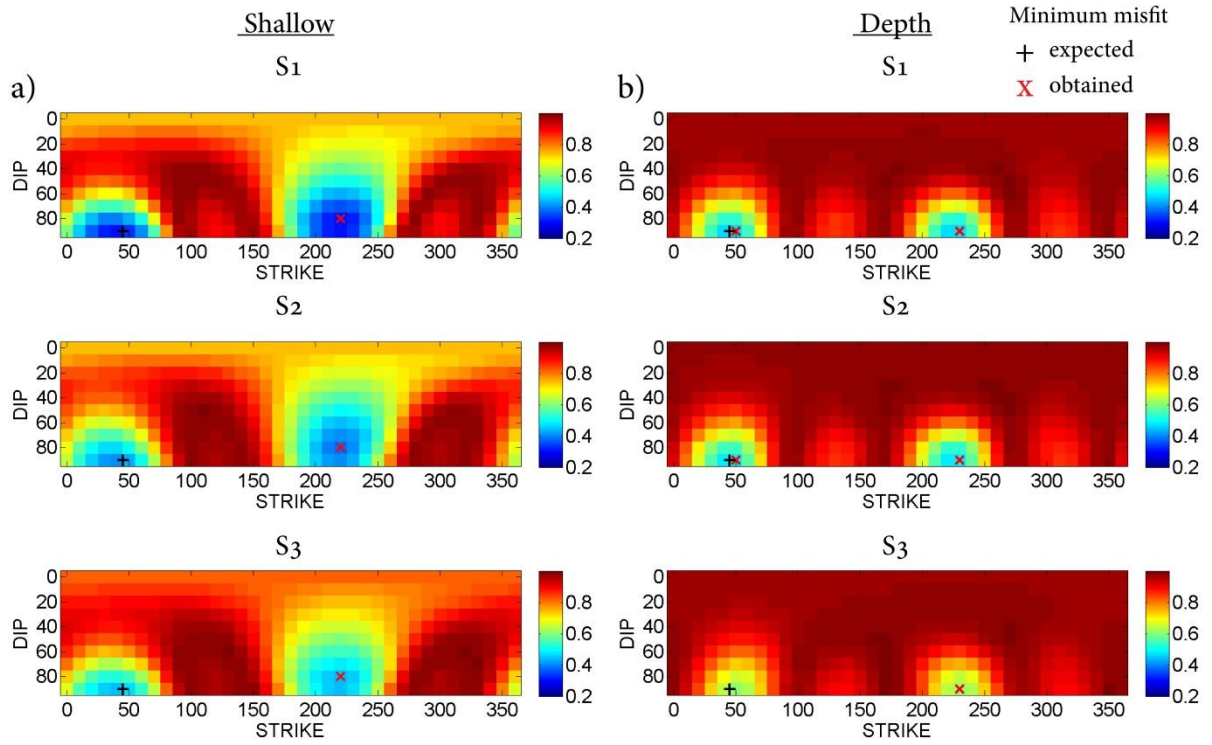
11)
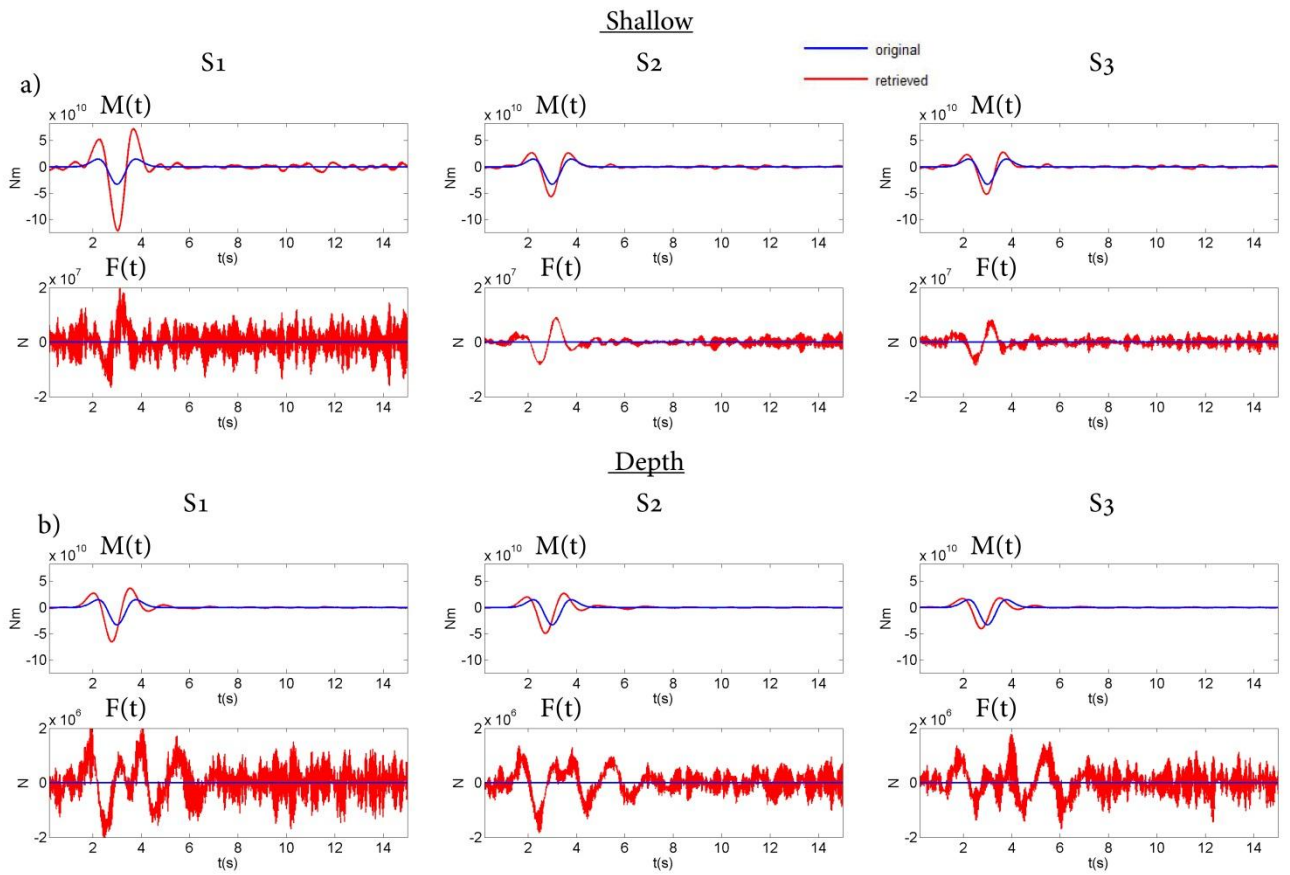
12)
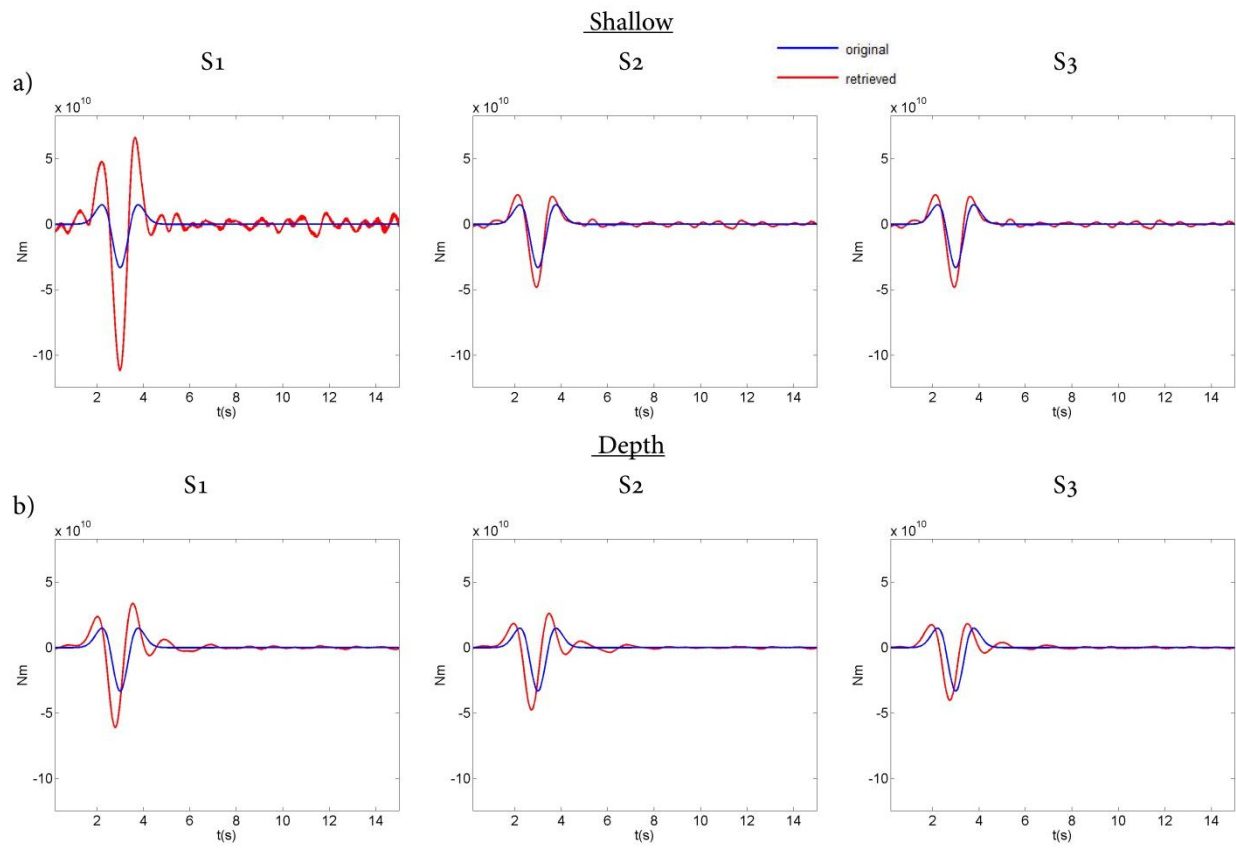
13)
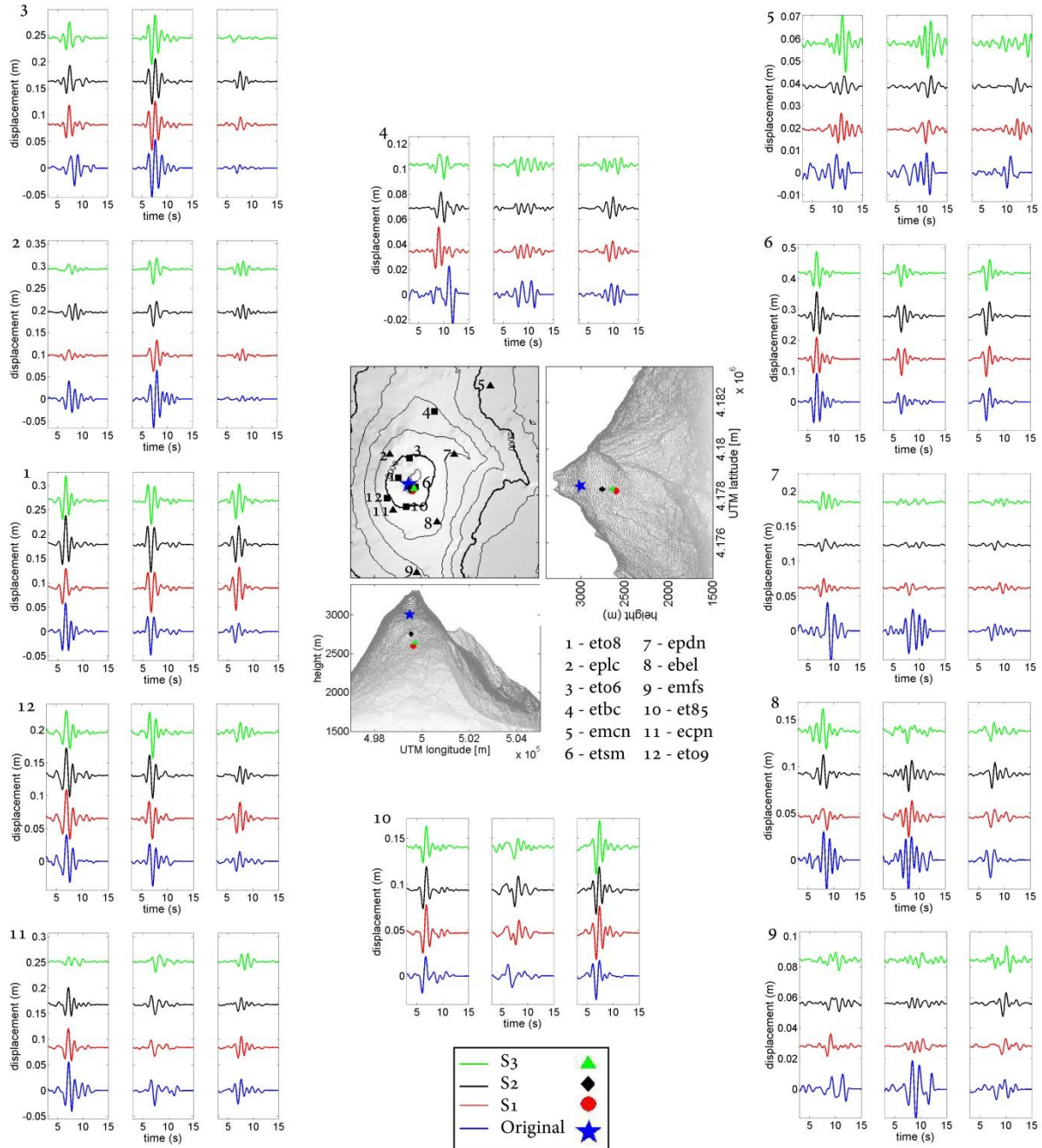
14)
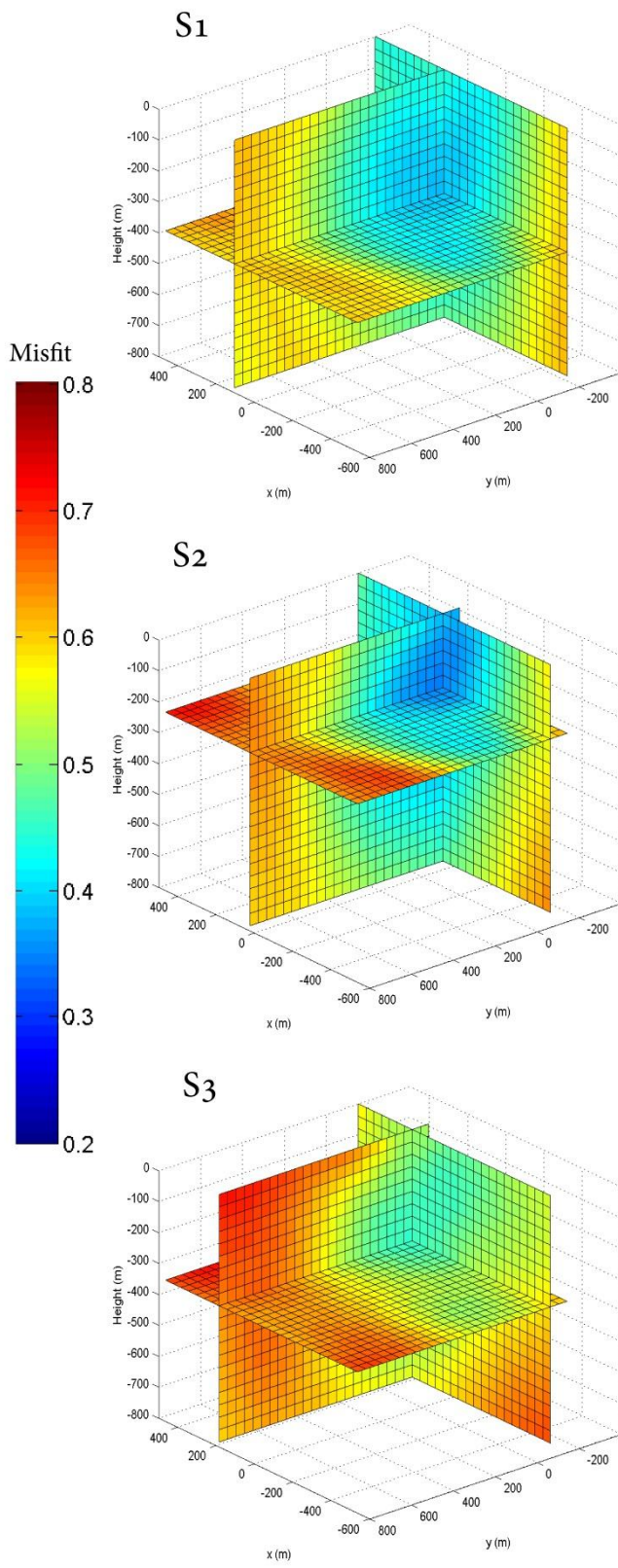
15)
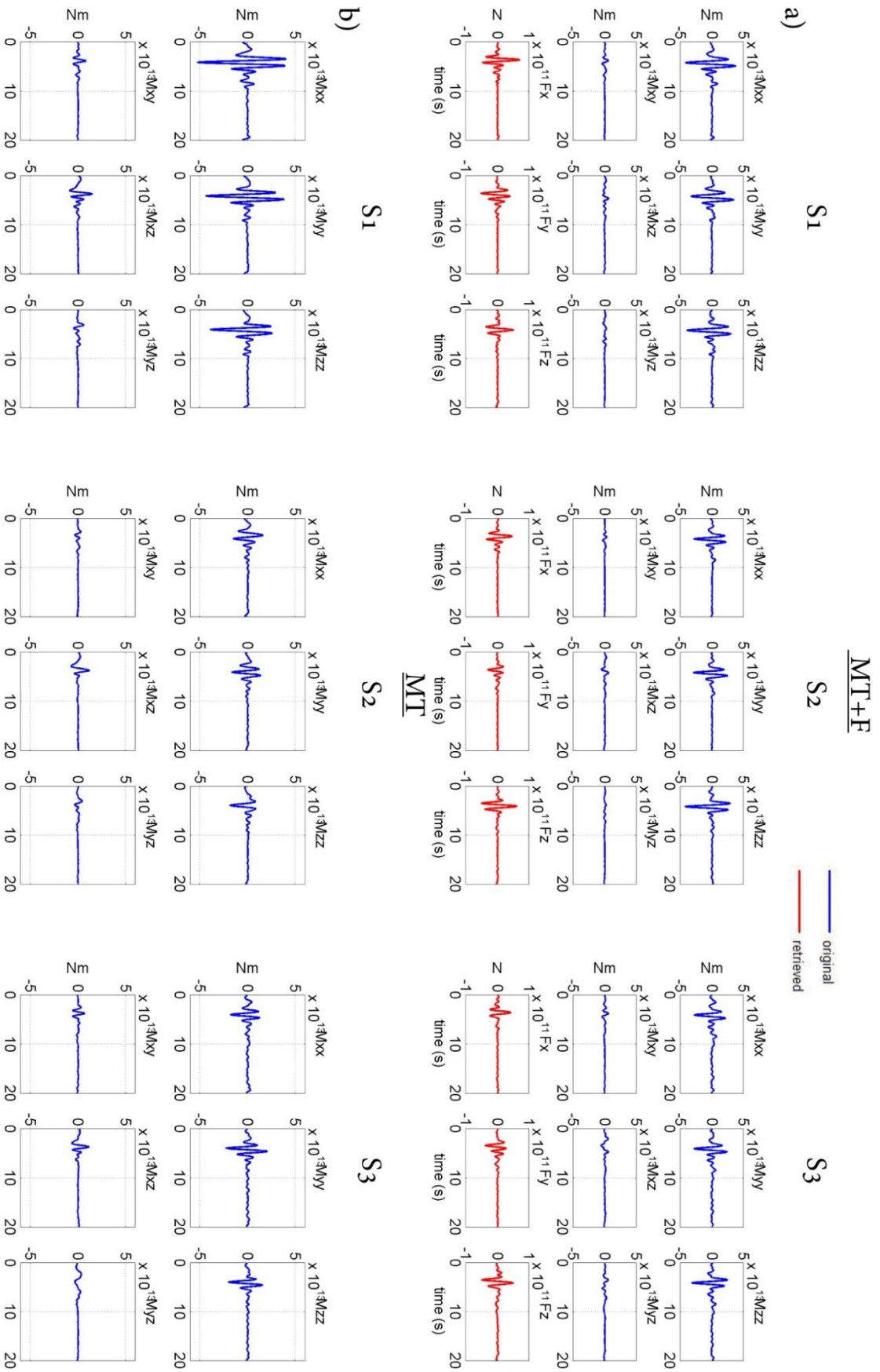
16)
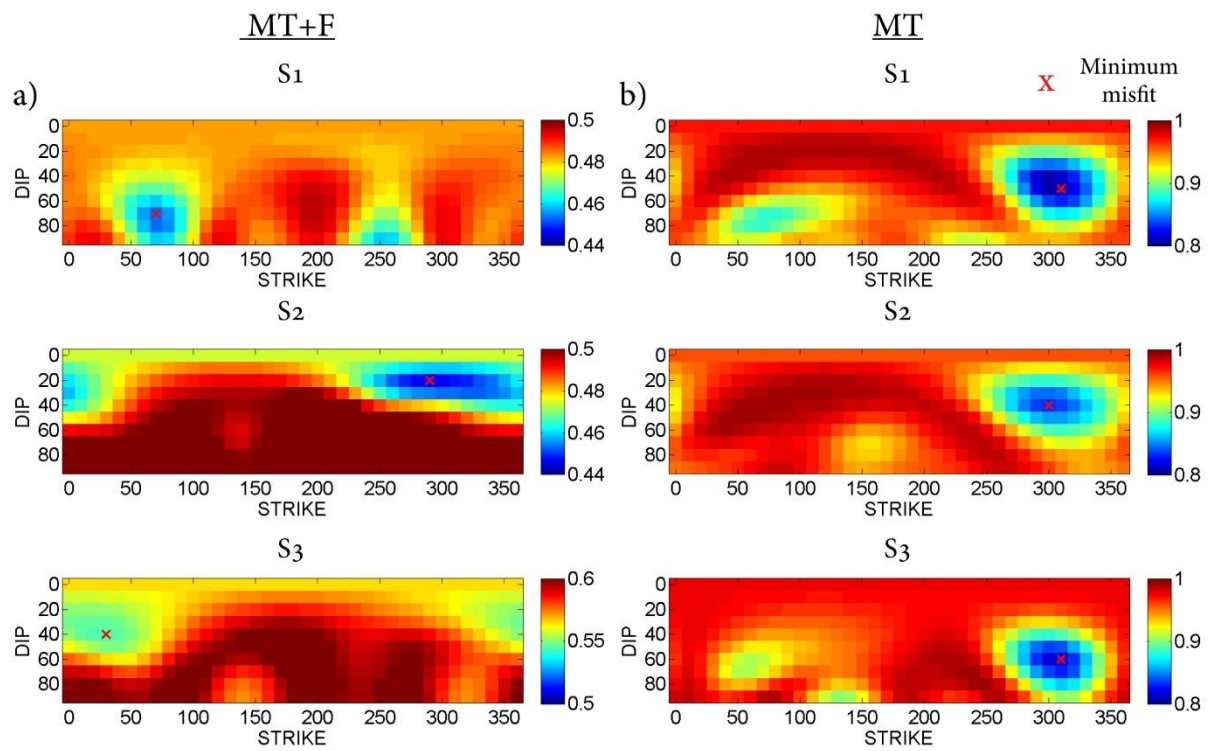
References

Aki, S., K., Fehler, M., and Das, I. (1977). Source mechanism of volcanic tremor: fluid-driven crack models and their application to Kilauea eruption. 2.

Aki and Richards (2002). Quantitative Seismology, Second Edition. (University Science Books.).

Bean, C., Lokmer, I., and O'Brien, G. (2008). Influence of near-surface volcanic structure on long-period seismic signals and on moment tensor inversions: Simulated examples from Mount Etna. J. Geophys. Res. 113.

Bean, C.J., De Barros, L., Lokmer, I., Metaxian, J.-P., O/' Brien, G., and Murphy, S. (2014). Long-period seismicity in the shallow volcanic edifice formed from slow-rupture earthquakes. Nat. Geosci 7, 71–75.

Branca, F., S., Coltelli, M., Groppelli, G., and Pasquarè, G. (2009). Note illustrative alla carta geologica d'Italia alla scala 1:50.000. Foglio 625 Acireale.

Branca, F., S., Coltelli, M., Groppelli, G., and Lentini, F. (2011). Geological map of Etna volcano, 1:50,000 scale. 130.

Calvari, S., Groppelli, G., and Pasquarè, G. (1994). Preliminary geological data on the south-western wall of the Valle del Bove, Mt Etna, Sicily. Acta Volcanol. 5, 15–30.

Cannata, A., Hellweg, M., Grazia, G.D., Ford, S., Alparone, S., Gresta, S., Montalto, P., and Patanè, D. (2009). Long period and very long period events at Mt. Etna volcano: Characteristics, variability and causality, and implications for their sources. J. Volcanol. Geotherm. Res. 187, 227–249.

Cannata, A., Di Grazia, G., Aliotta, M., Cassisi, C., Montalto, P., and Patanè, D. (2013). Monitoring Seismo-volcanic and Infrasonic Signals at Volcanoes: Mt. Etna Case Study. Pure Appl. Geophys. 170, 1751–1771.

Cardaci, C., Coviello, M., Lombardo, G., Patanè, G., and Scarpa, R. (1993). Seismic tomography of Etna volcano. 56.

Cauchie, L., and Saccorotti, G. (2013). Probabilistic inversion of Rayleigh-wave dispersion data: an application to Mt. Etna, Italy. J. Seismol. 17, 335–346.

Cesca, S., Battaglia, J., Dahm, T., Tessmer, E., Heimann, S., and Okubo, P. (2008). Effects of topography and crustal heterogeneity on the source estimation of LP events at Kilauea volcano. Geophys J Int 172, 1219–1236.

Chiarabba, C., Amato, A., Boschi, E., and Barberi, F. (2000). Recent seismicity and tomographic modeling of the Mount Etna plumbing system. J. Geophys. Res. Solid Earth 105, 10923–10938.

Chouet, B. (1996). New methods and future trends in seismological volcano monitoring (Monitoring and mitigation of volcanic hazards Scarpa/Tilling (eds). Springer-Verlag Berlin Hieldelberg).

Chouet, B. (2003). Volcano seismology. Pure Appl. Geophys. 160, 739–788.

Coltelli, M. M.andGarduno, V.H.andNeri, M.andPasquaré, G.andPompillo (1994). Geology of the northern wall of Valle del Bove, Mt Etna (Sicily). 5.

Cristiano, L., Petrosino, S., Saccorotti, G., Ohrnberger, M., and Scarpa, R. (2010). Shear-wave velocity structure at Mt. Etna from inversion of Rayleigh-wave dispersion patterns (2 s < T < 20 s). Ann. Geophys. 53.

Davi, R., O'Brien, G.S., Lokmer, I., Bean, C.J., Lesage, P., and Mora, M.M. (2010). Moment tensor inversion of explosive long period events recorded on Arenal volcano, Costa Rica, constrained by synthetic tests. J. Volcanol. Geotherm. Res. 194, 189–200.

De Barros, L., Bean, C.J., Lokmer, I., Saccorotti, G., Zuccarello, L., O'Brien, G.S., Métaxian, J.-P., and Patanè, D. (2009). Source geometry from exceptionally high resolution long period event observations at Mt Etna during the 2008 eruption. Geophys. Res. Lett. 36.

De Barros, L., Lokmer, I., Bean, C.J., O'Brien, G.S., Saccorotti, G., Métaxian, J.-P., Zuccarello, L., and Patanè, D. (2011). Source mechanism of long-period events recorded by a high-density seismic network during the 2008 eruption on Mount Etna. J. Geophys. Res. 116.

De Barros, L., Lokmer, I., and Bean, C.J. (2013). Origin of spurious single forces in the source mechanism of volcanic seismicity. J. Volcanol. Geotherm. Res. 262, 1–6.

De Beaumont, E. (1836). Recherche sur la structure et l'origine du Mount Etna. ser. 3, 9.

De Martin, F. (2010). Influence of the nonlinear behavior of soft soils on strong ground motions. Ecole Centrale Paris.

De Martin, F. (2011). Verification of a Spectral-Element Method Code for the Southern California Earthquake Center LOH.3 Viscoelastic Case. Bull. Seismol. Soc. Am. 101, 2855–2865.

Eyre, T.S., Bean, C.J., De Barros, L., O'Brien, G.S., Martini, F., Lokmer, I., Mora, M.M., Pacheco, J.F., and Soto, G.J. (2013). Moment tensor inversion for the source location and mechanism of long period (LP) seismic events from 2009 at Turrialba volcano, Costa Rica. J. Volcanol. Geotherm. Res. 258, 215–223.

Eyre, T.S., Bean, C.J., De Barros, L., Martini, F., Lokmer, I., Mora, M.M., Pacheco, J.F., and Soto, G.J. (2015). A brittle failure model for long-period seismic events recorded at Turrialba Volcano, Costa Rica. J. Geophys. Res. Solid Earth 120, 1452–1472.

Harrington, R.M., and Brodsky, E.E. (2007). Volcanic hybrid earthquakes that are brittle-failure events. Geophys. Res. Lett. 34, n/a – n/a.

Haskell, N.A. (1953). The dispersion of surface waves on multilayered media. Bull. Seismol. Soc. Am. 43, 17–34.

Hidayat, D., Chouet, B., Voight, B., Dawson, P., and Ratdomopurbo, A. (2002). Source mechanism of very-long-period signals accompanying dome growth activity at Merapi volcano, Indonesia. Geophys. Res. Lett. 29, 33–1 – 33–34.

Hirn, A., Nercessian, A., Sapin, M., Ferrucci, F., and Wittlinger, G. (1991). Seismic heterogeneity of Mt Etna: structure and activity. Geophys. J. Int. 105, 139–153.

Jousset, P., Neuberg, J., and Jolly, A. (2004). Modelling low-frequency volcanic earthquakes in a viscoelastic medium with topography. Geophys. J. Int. 159, 776–802.

Jousset, P., Budi-Santoso, A., Jolly, A.D., Boichu, M., Surono, Dwiyono, S., Sumarti, S., Hidayati, S., and Thierry, P. (2013). Signs of magma ascent in {LP} and {VLP} seismic events and link to degassing: An example from the 2010 explosive eruption at Merapi volcano, Indonesia. J. Volcanol. Geotherm. Res. 261, 171–192.

Kumagai, H. (2002). Waveform inversion of oscillatory signatures in long-period events beneath volcanoes. J. Geophys. Res. 107.

Kumagai, H., Chouet, B.A., and Dawson, P.B. (2005). Source process of a long-period event at Kilauea volcano, Hawaii. Geophys. J. Int. 161, 243–254.

Laigle, M., Hirn, A., Sapin, M., Lépine, J.-C., Diaz, J., Gallart, J., and Nicolich, R. (2000). Mount Etna dense array local earthquake P and S tomography and implications for volcanic plumbing. J. Geophys. Res. Solid Earth 105, 21633–21646.

Legrand, D., Kaneshima, S., and Kawakatsu, H. (2000). Moment tensor analysis of near-field broadband waveforms observed at Aso Volcano, Japan. J. Volcanol. Geotherm. Res. 101, 155–169.

Lokmer, I., Bean, C.J., Saccorotti, G., and Patanè, D. (2007). Moment-tensor inversion of LP events recorded on Etna in 2004 using constraints obtained from wave simulation tests. Geophys. Res. Lett. 34.

Lokmer, I., Saccorotti, G., Di Lieto, B., and Bean, C.J. (2008). Temporal evolution of long-period seismicity at Etna Volcano, Italy, and its relationships with the 2004–2005 eruption. Earth Planet. Sci. Lett. 266, 205–220.

Luca, G.D., Filippi, L., Patanè, G., Scarpa, R., and Vinciguerra, S. (1997). Three-dimensional velocity structure and seismicity of Mt. Etna Volcano, Italy. J. Volcanol. Geotherm. Res. 79, 123–138.

Menke, 1989 (1989). Geophysical data analysis: discrete inverse theory, revised edition.

Nakano, M. (2005). Waveform inversion of volcano-seismic signals assuming possible source geometries. Geophys. Res. Lett. 32.

Nakano, M., Kumagai, H., and Chouet, B.A. (2003). Source mechanism of long-period events at Kusatsu–Shirane Volcano, Japan, inferred from waveform inversion of the effective excitation functions. J. Volcanol. Geotherm. Res. 122, 149–164.

Neuberg, J., Luckett, R., Baptie, B., and Olsen, K. (2000). Models of tremor and low-frequency earthquake swarms on Montserrat. J. Volcanol. Geotherm. Res. 101, 83–104.

Ohminato, T., and Chouet, B.A. (1997). A free-surface boundary condition for including 3D topography in the finite-difference method. Bull. Seismol. Soc. Am. 87, 494–515.

Ohminato, T., Chouet, B.A., Dawson, P., and Kedar, S. (1998). Waveform inversion of very long period impulsive signals associated with magmatic injection beneath Kilauea volcano, Hawaii. J. Geophys. Res. Solid Earth 103, 23839–23862.

Pasquare, G., Servizio geologico., Italy., Consiglio Nazionale delle Ricerche., and Commissione per la Cartopgrafia Geologica e Geomorfologica. (1992). Carta geologica d'Italia, 1: 50.000 : guida al rilevamento (Rome: Servizio Geologico Nazionale).

Patane, D., Chiarabba, C., Cocina, O., De Gori, P., Moretti, M., and Boschi, E. (2002). Tomographic images and 3D earthquake locations of the seismic swarm preceding the 2001 Mt. Etna eruption: Evidence for a dyke intrusion. Geophys. Res. Lett. 29, 135–1 – 135–4.

Patanè, D., Aliotta, M., Cannata, A., Cassisi, C., Coltelli, M., and Di Grazia, G. (2011). Interplay between Tectonics and Mount Etna's Volcanism: Insights into the Geometry of the Plumbing System. New Front. Tecton. Res. - Midst Plate Converg. Dr Uri Schattner Ed.

Potter, R.R. C.C.andStewart (1998). Density predictions using Vp and Vs sonic logs. 10.

Romano, R., Lentini, F., and Sturiale, C. (1979). Carta geologica del Monte Etna, scala 1:50.000 (Mem. Soc. Geo. Italiana).

Saccorotti, G., Zuccarello, L., Del Pezzo, E., Ibanez, J., and Gresta, S. (2004). Quantitative analysis of the tremor wavefield at Etna Volcano, Italy. J. Volcanol. Geotherm. Res. 136, 223–245.

Saccorotti, G., Lokmer, I., Bean, C.J., Di Grazia, G., and Patanè, D. (2007). Analysis of sustained long-period activity at Etna Volcano, Italy. J. Volcanol. Geotherm. Res. 160, 340–354.

Thomson, W.T. (1950). Transmission of Elastic Waves through a Stratified Solid Medium. J. Appl. Phys. 21, 89–93.

Thun, J., Lokmer, I., and Bean, C.J. (2015). New observations of displacement steps associated with volcano seismic long-period events, constrained by step table experiments. Geophys. Res. Lett. 42, 3855–3862.

Vasco, D.W. (1989). Deriving source-time functions using principal component analysis. Bull. Seismol. Soc. Am. 79, 711–730.

Vavryčuk, V. (2001). Inversion for parameters of tensile earthquakes. 106.

Villaseñor, A., Benz, H.M., Filippi, L., De Luca, G., Scarpa, R., Patanè, G., and Vinciguerra, S. (1998). Three-dimensional P-wave velocity structure of Mt. Etna, Italy. Geophys. Res. Lett. 25, 1975–1978.

Waltershausen, W.S. (1844). Atlas des Aetna (Berlin: Gottingen, Weimar).

Waltershausen, W.S. (1880). Der Aetna (Engelman, Leipzig).

Chapter 5

MT inversion of LP signals on Mt. Etna volcano

In this Chapter I take advantage of the lessons learned through the synthetic tests of Chapter 4 and I analyze three sets of LP events recorded on Mt. Etna during different states of volcanic activity. First, I perform some synthetic tests in order to check the uncertainties in the MT solution due to the station network and the velocity model. I then perform full MT inversion for each set of events separately. At the end of each section I propose a source model able to explain the recorded LP events in each characteristic volcanic activity context.

5.1 INGV seismic network

The recent history of Mt. Etna has been characterized by frequent unrest episodes (Allard et al., 2006; Behncke et al., 2014; Bonaccorso et al., 2011b; Cannata et al., 2015; Patanè et al., 2011) accompanied by diffuse degassing activity during rest periods (Patanè et al., 2011). I focus my attention on three periods of observations which are characteristics of different states of activity of the volcano. The data sets of seismic traces analyzed in this study have been recorded by the permanent network of seismic stations deployed by INGV (Instituto Nazionale di Vulcanologia, section of Catania). The network consists of 19 stations closest to the summit area. These stations are equipped with broadband (40s cutoff period), three component Trillium seismometer
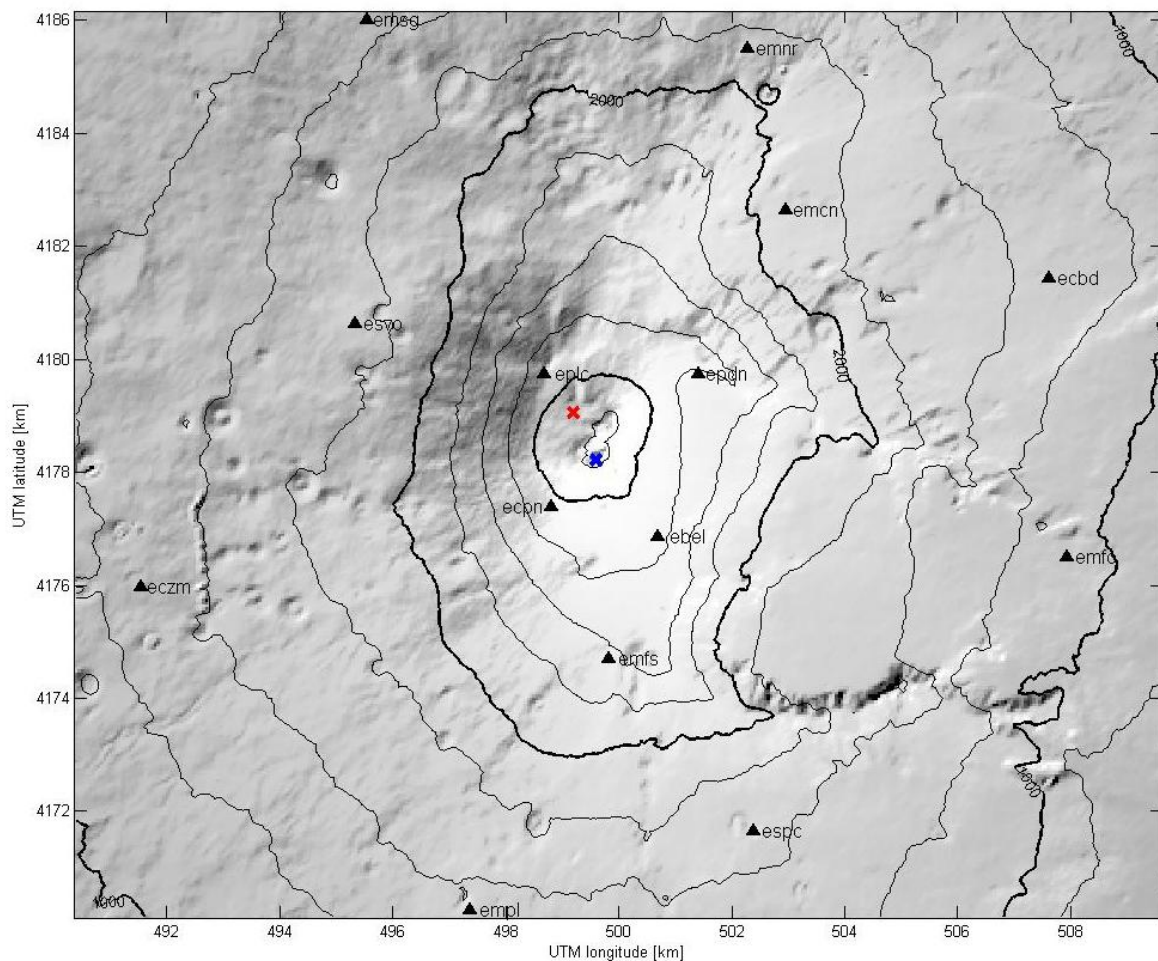
Figure 28 – Mt. Etna digital elevation model and seismic stations of the permanent network of the INGV used in this study. Colored crosses correspond to the horizontal source locations for the synthetic tests: red) synthetic data and Green's functions computed in the same velocity model; blue) synthetic data and Green's functions computed in two different velocity models; blue cross corresponds to the Bocca Nuova (BN) crater location.

(Nanometrics[TM]) acquiring in real time and at a sampling rate of 100 Hz (Cannata et al., 2015). The calculation of the GFs computed in the previous section included 14 of the 19 stations of the permanent INGV network. All the summit stations and those deployed on the flank of the volcano are used (Figure 28). The network, as designed, should guarantee enough azimuthal coverage around the summit and on the flanks of the volcano as suggested by De Barros et al., (2011) and Bean et al., (2008) to make the MT inversion stable and accurate. The only portion of the volcano without stations is the *Valle del Bove* that, due to the inaccessibility of its flank and the frequent lava flows, is uncovered. It is worth nothing that station *ebel* was destroyed during the paroxysmal episode of 28 February 2013, thus its recording is unavailable for the third set of analyzed events.

5.2 Synthetic test of full MT inversion

5.2.1 Green's functions and synthetics data computed in the same velocity model

Before analyzing the data through full moment tensor inversion, the method itself has to be tested to ensure that it is implemented correctly. Further, I need to check the ability of the network of stations in successfully constraining the source parameters. Hence, I perform moment tensor inversion for different possible source types and orientations computed synthetically. I choose to perform the tests for an explosion and two differently oriented cracks (one horizontal and one vertical) as these are the most plausible sources for LPs on Etna (Cannata et al., 2009a, 2015; De Barros et al., 2011; Lokmer et al., 2007). The simulations are performed for sources at two targeted depths: at the top of the GF volume (499.198 km east 4179.060 km north and 2880 m.a.s.l., UTM coordinates, Figure 28) and at the bottom (499.198 km east 4179.060 km north and 2240 m.a.s.l., UTM coordinates). The source time function used for simulations is a Ricker wavelet with a central frequency of 0.8 Hz (Figure 29), as this is similar to the most energetic part of LPs recorded on Etna. The simulations are computed in the same velocity model as the one used to calculate Green's functions. The chosen velocity model is the surface layer model (S2) described in the previous chapter and the choice for this model is abundantly discussed in chapter 4. As the same velocity model is used for

synthetic and GFs, the source waveform and mechanism should be perfectly reconstructed by the MT inversion.

It is worth nothing that at the time of computing the GFs the code EFISPEC3D (De Martin, 2011) had a slightly different implementation for the computation of the source and receiver positions. Thus some small differences of the order of ~10 m could arise between the receivers positions computed for GFs and forward simulations.
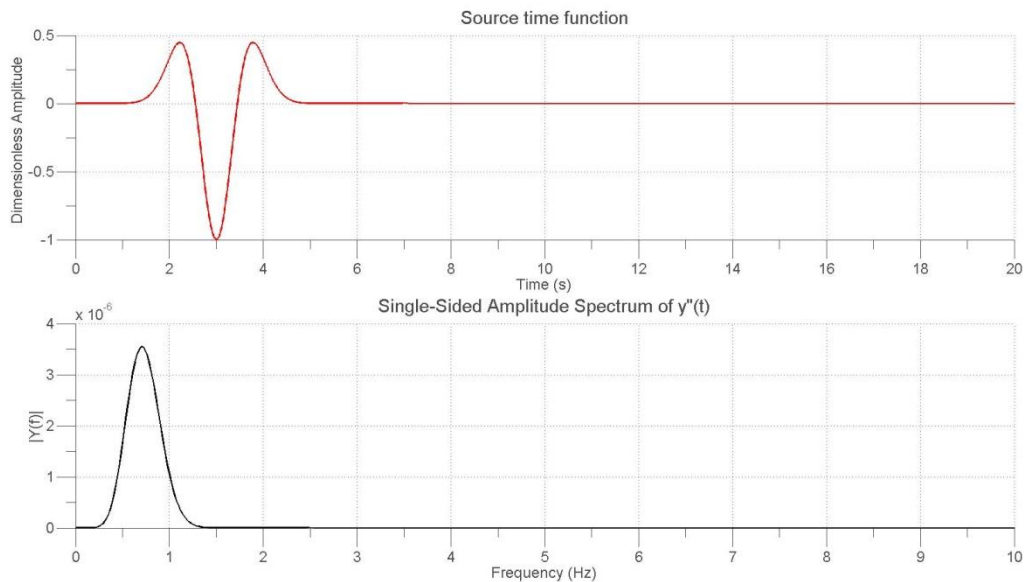
Figure 29 – top) Ricker source time function used for the computation of the observed data for the MT inversion synthetic test on Mt. Etna volcano; bottom) power spectral density showing the low frequency content of the source time function.

5.2.1.1 Explosion source

I begin by testing the explosion which is simulated as an isotropic source using $M_{xx} = M_{yy} = M_{zz} = 1$ and $M_{xy} = M_{xz} = M_{yz} = 0$. Results of the inversion are plotted in Figure 30. The Ricker wavelets are well reconstructed and the $1:1:1:0:0:0$ ratio is correct for both moment + Single forces (M+F) and moments only (MT-only) inversions (λ_n values in Table 5). Figure 31 shows the fit between the synthetic data and the obtained moment tensor convolved with the Green's function, i.e. the reconstructed data. The fit appears almost perfect except for some slightly differences in the coda of some farther stations (e.g. *eczm* and *empl*). Finally, I apply the Vasco, (1989) and the (Vavryčuk, 2001, 2015) decompositions as described in section 2.3. The eigenvalues ratio (λ_n values in Table 5) of $1:1:1$ well represents the original isotropic source with the orientation angles φ and θ
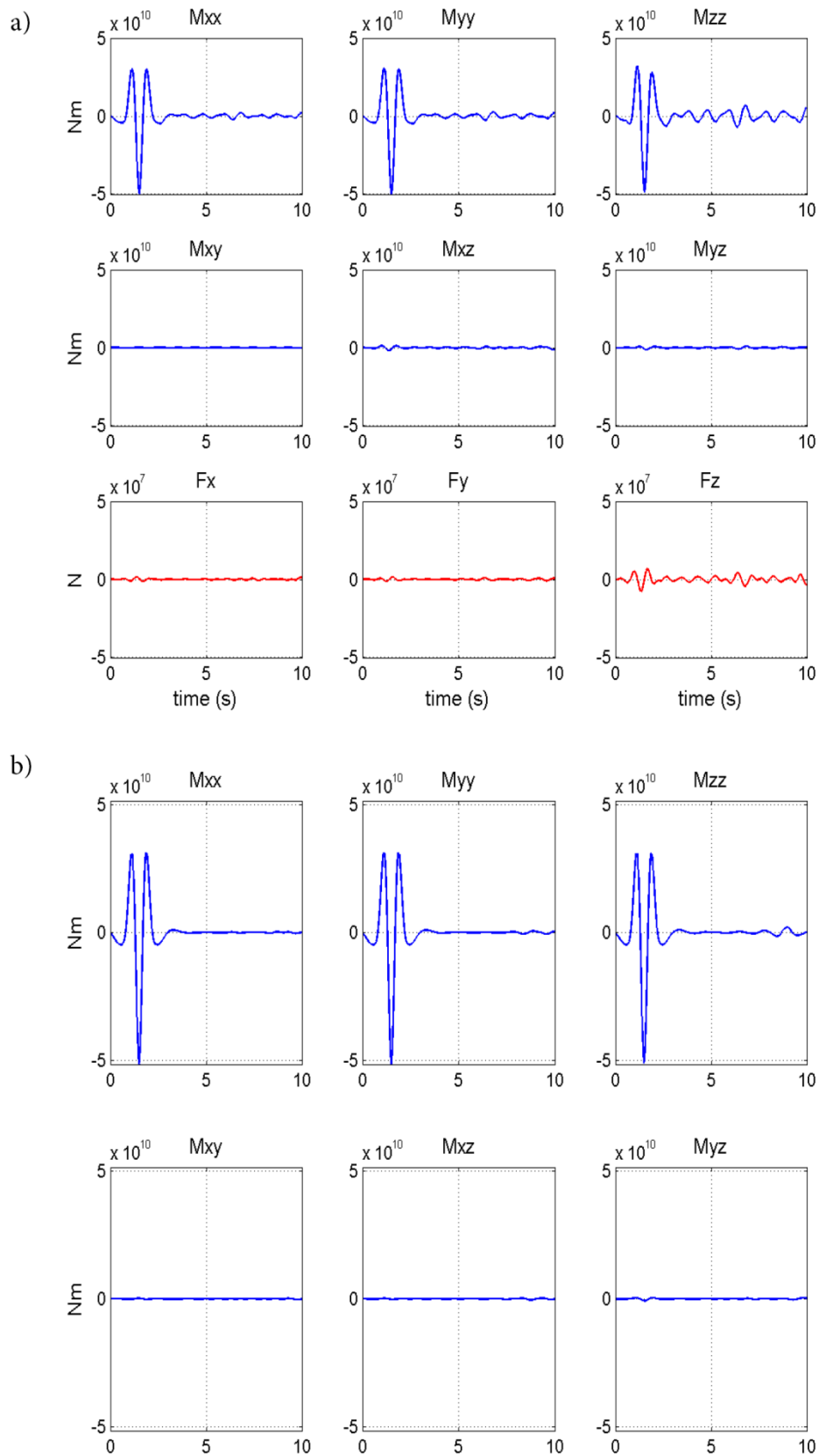
Figure 30 – a) MT inversion solution including forces for a shallow isotropic source and 14 stations of the INGV permanent network. b) MT inversion solution excluding forces for the same synthetic case as (a).
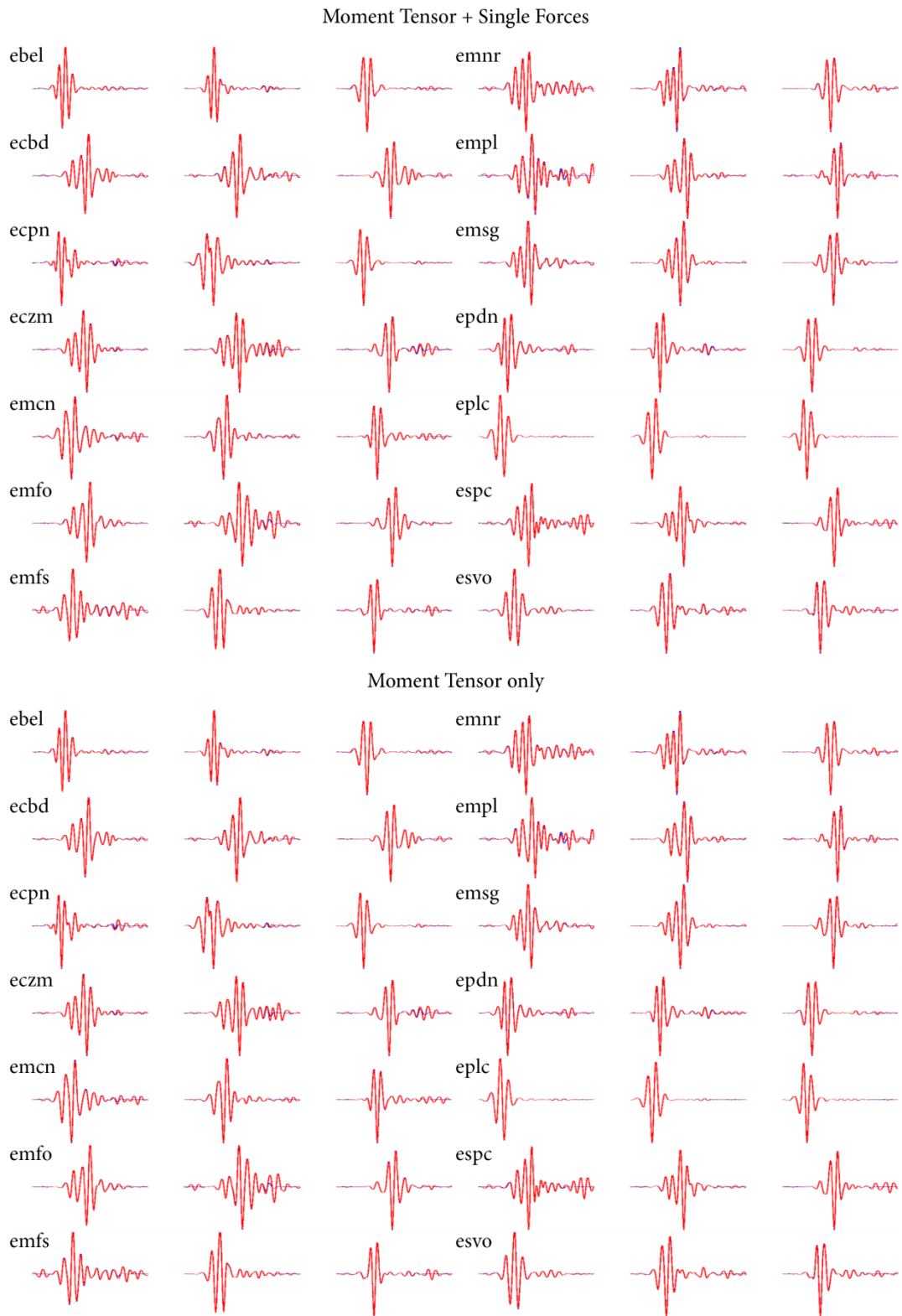
Figure 31 – Comparison between the synthetic observed data and the retrieved solution for an explosive source embedded at a shallow depth. Blue lines correspond to the observed data and red lines to the retrieved solution.
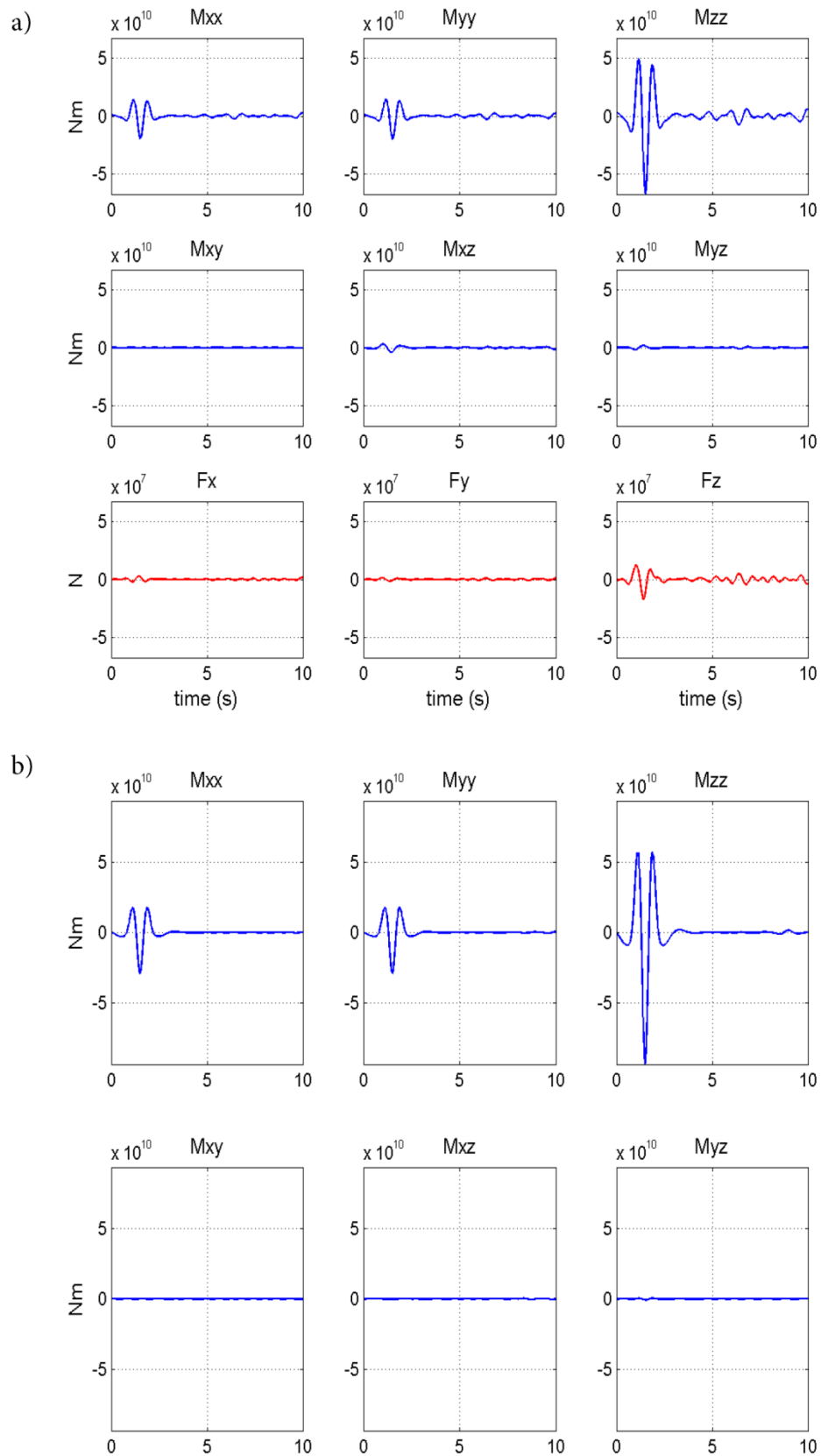
Figure 32 – a) MT inversion solution including forces for a shallow horizontal crack and 14 stations of the INGV permanent network. b) MT inversion solution excluding forces for the same synthetic case as (a).

Moment Tensor + Single Forces

Moment Tensor only
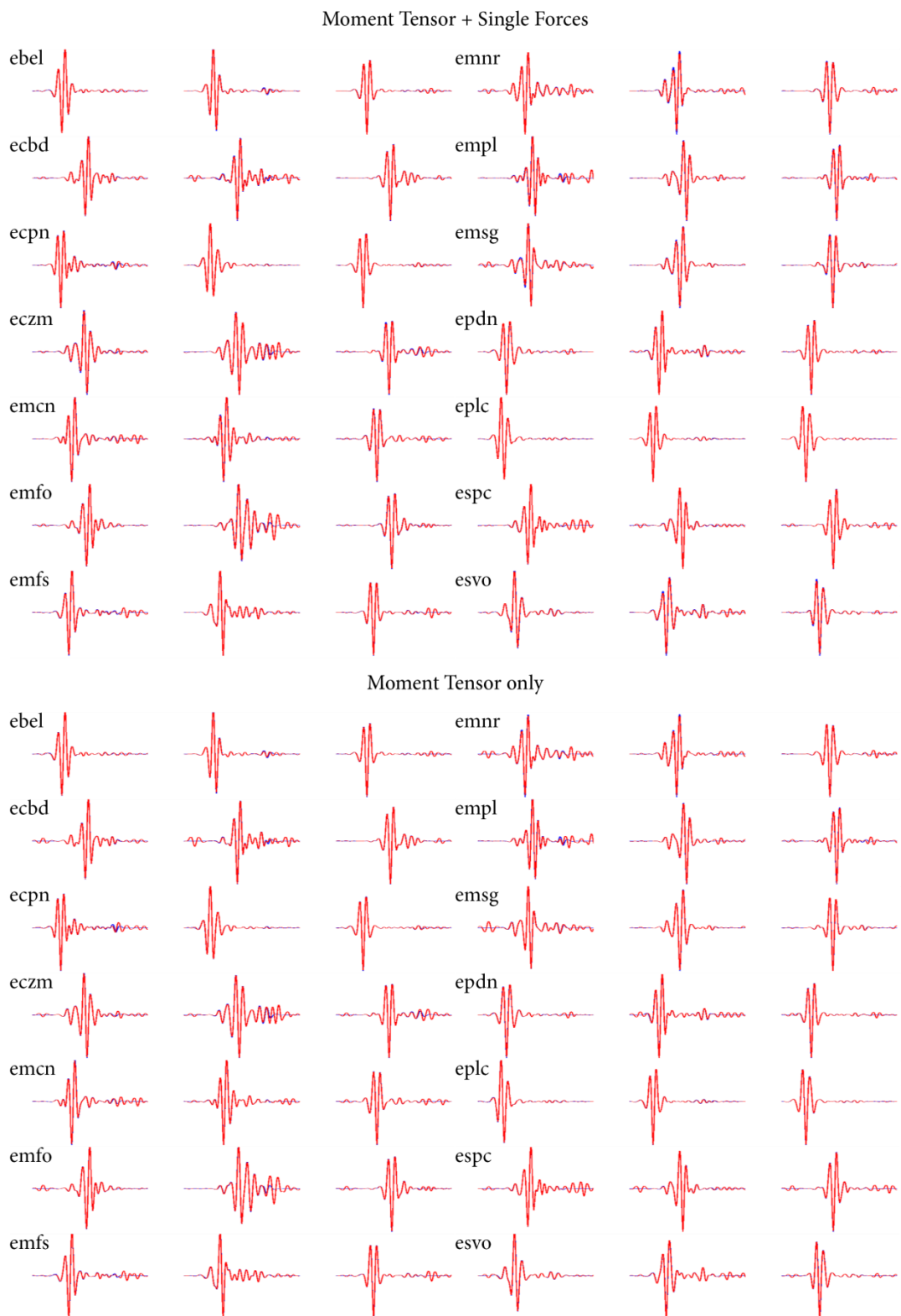
Figure 33 – Comparison between the synthetic observed data and the retrieved solution for a shallow horizontal crack. Blue lines correspond to the observed data and red lines to the retrieved solution.
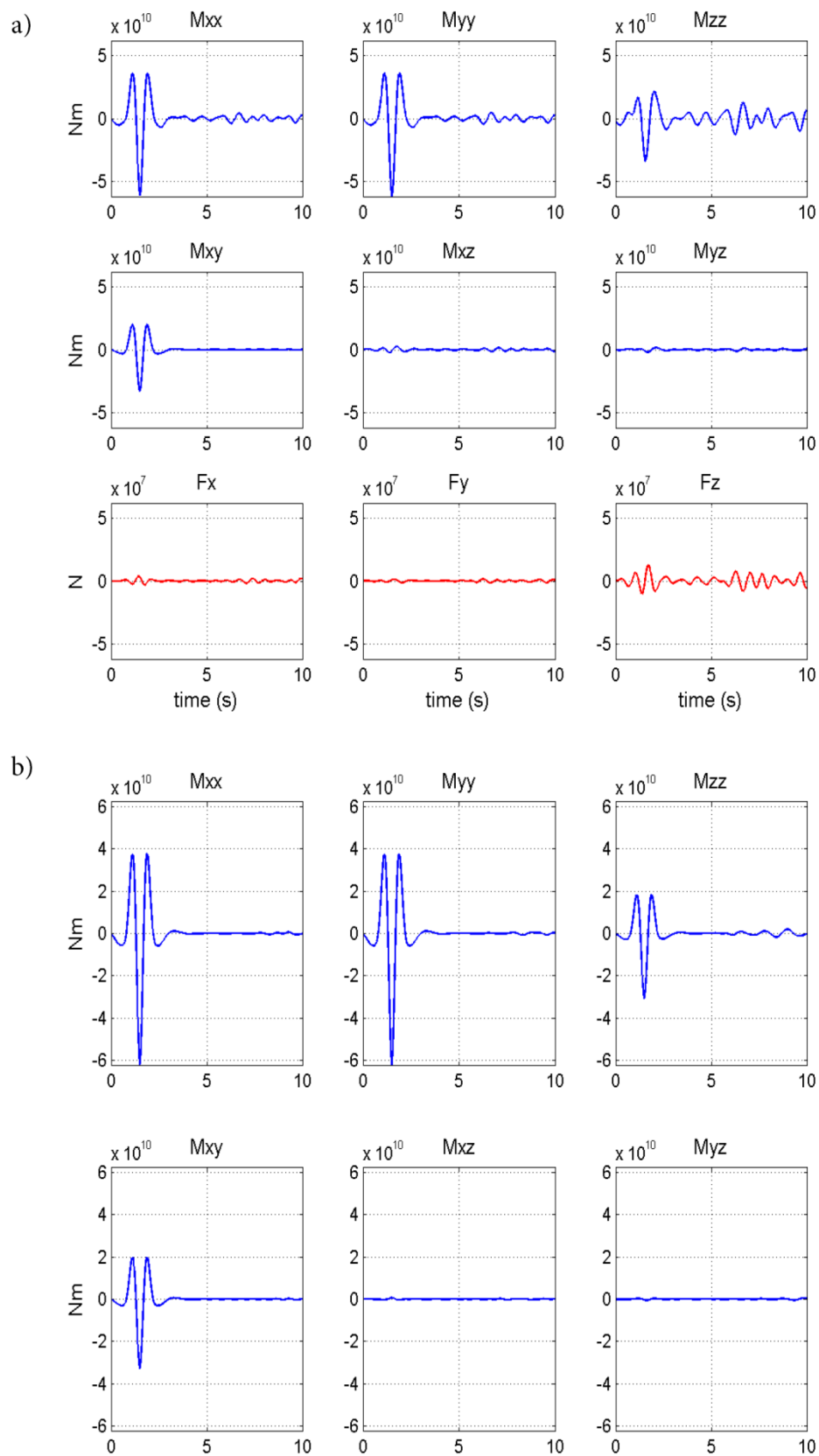
Figure 34 – a) MT inversion solution including forces for a shallow vertical crack and 14 stations of the INGV permanent network. b) MT inversion solution excluding forces for the same synthetic case as (a).

Moment Tensor + Single Forces

Moment Tensor only
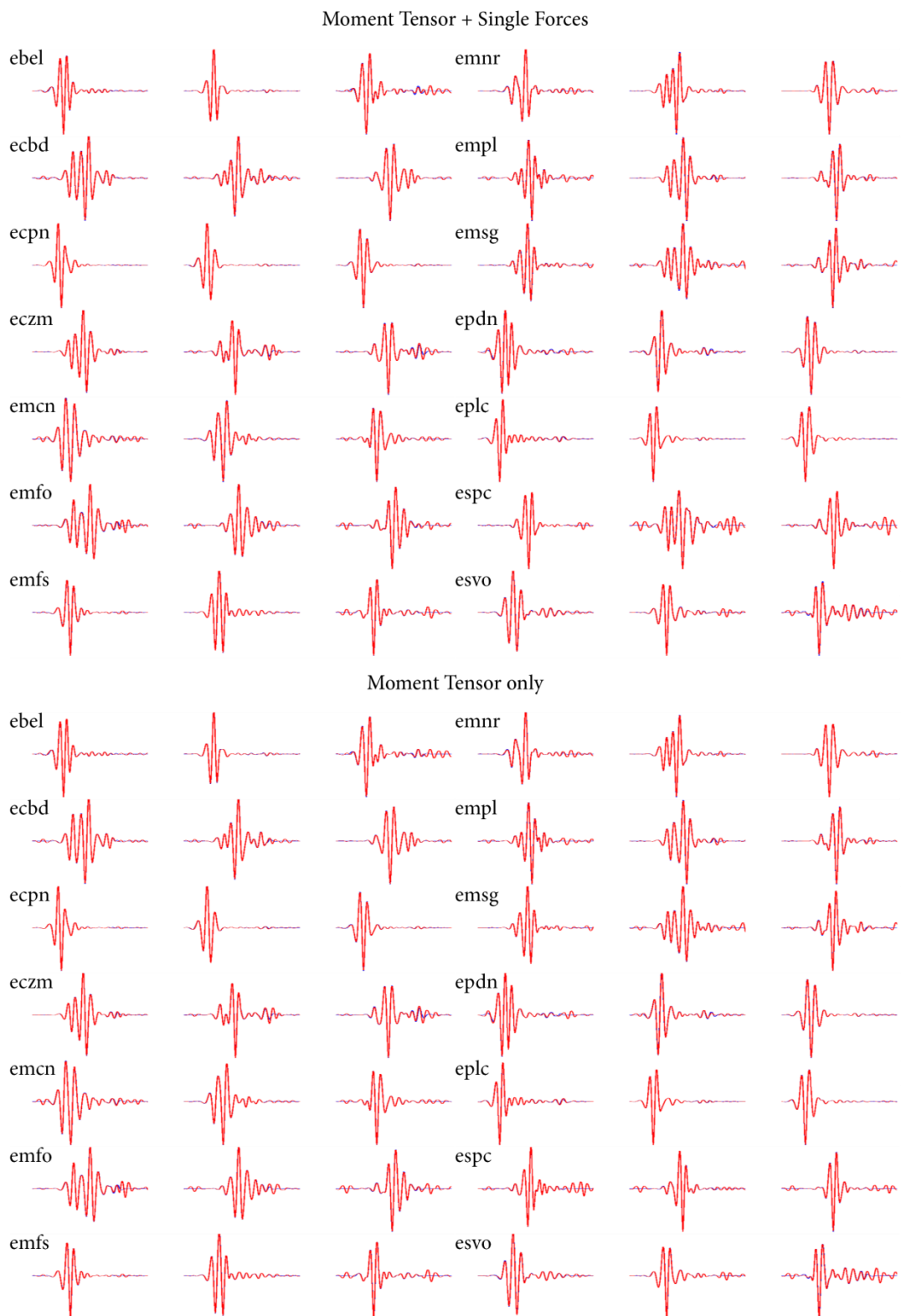
Figure 35 – Comparison between the synthetic observed data and the retrieved solution for a shallow vertical crack. Blue lines correspond to the observed data and red lines to the retrieved solution.
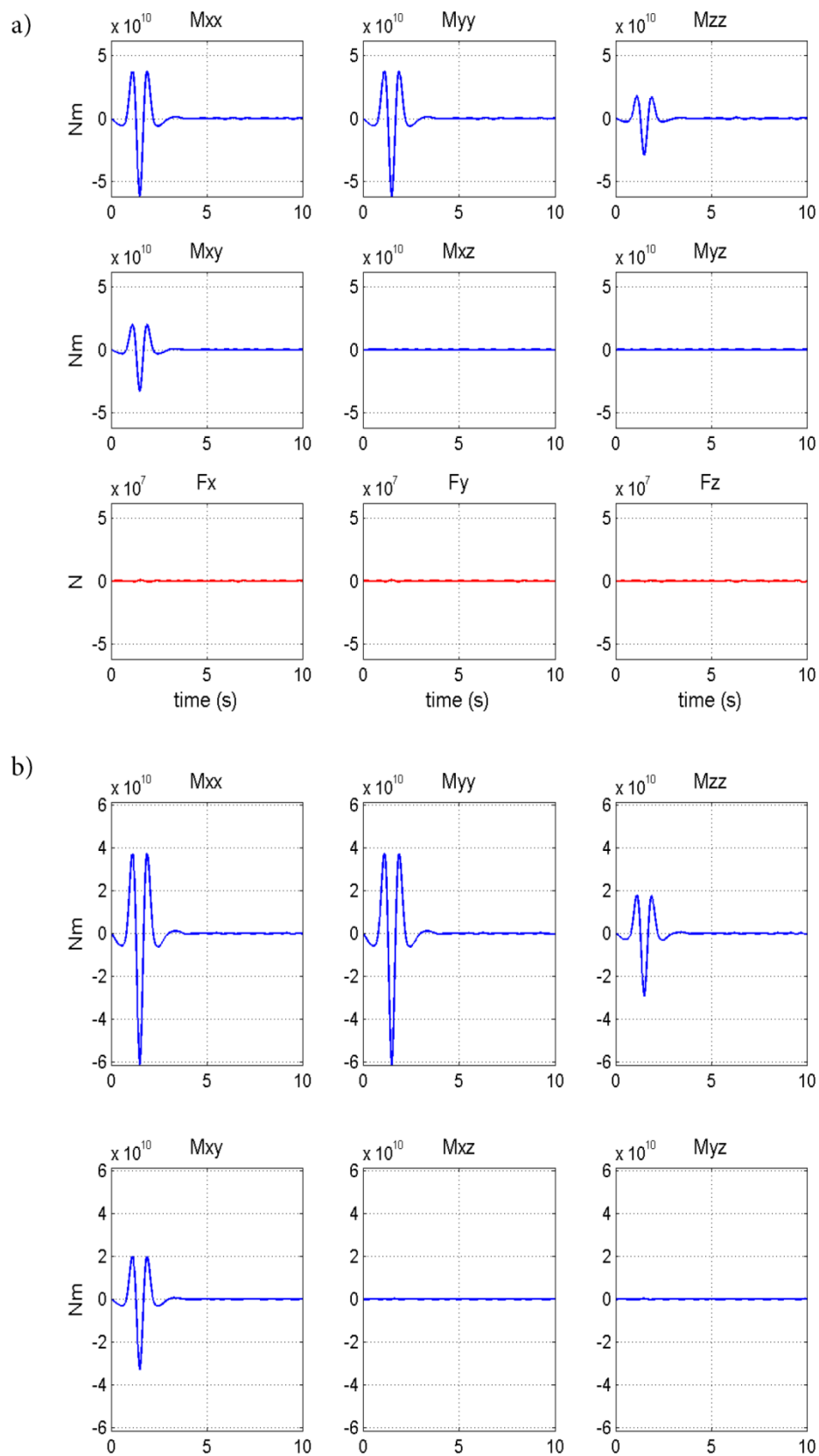
Figure 36 – a) MT inversion solution including forces for a deep vertical crack and 14 stations of the INGV permanent network. b) MT inversion solution excluding forces for the same synthetic case as (a).

Moment Tensor + Single Forces

Moment Tensor only
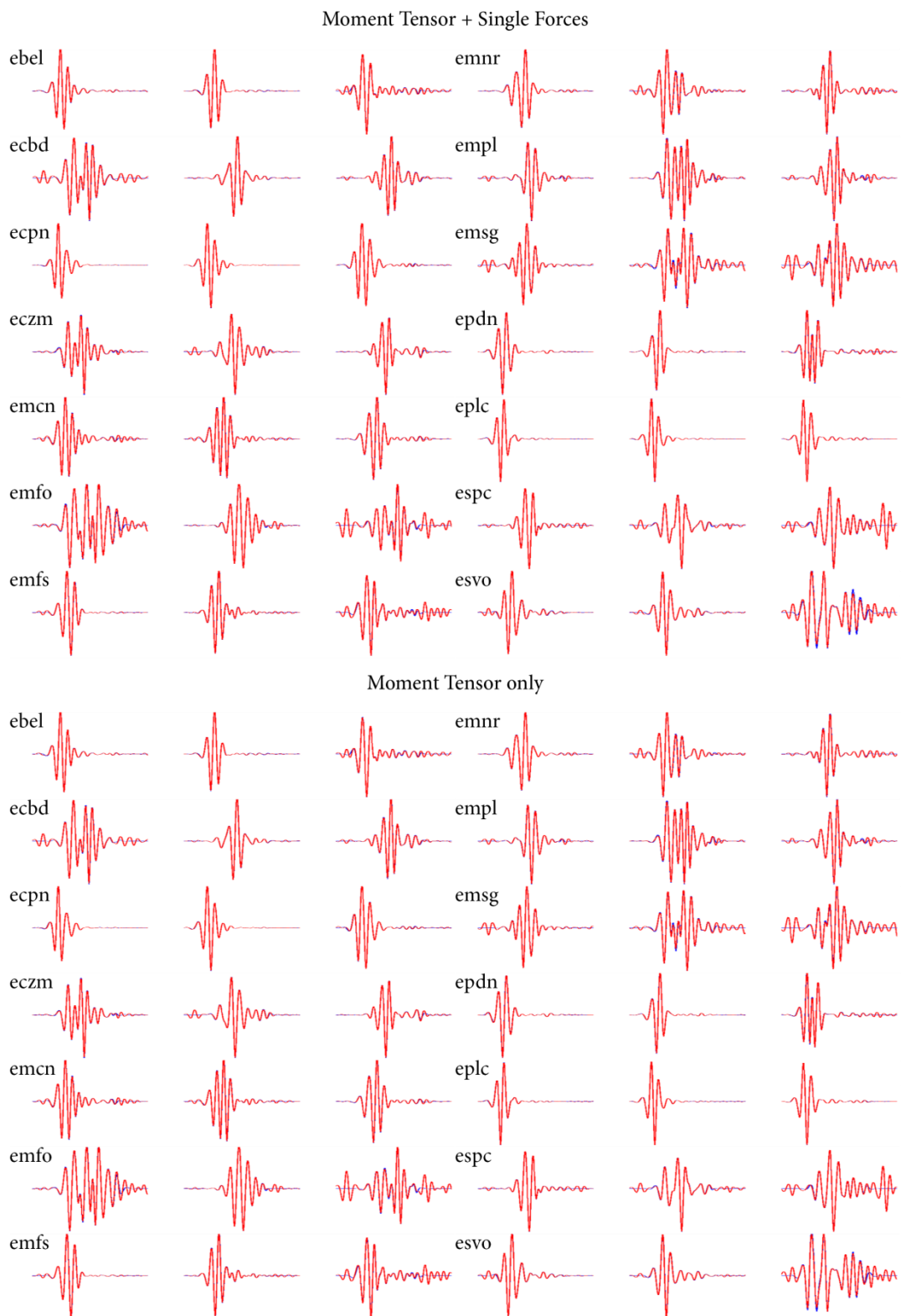
Figure 37 – Comparison between the synthetic observed data and the retrieved solution for a deep vertical crack. Blue lines correspond to the observed data and red lines to the retrieved solution.

Table 5 – Results of the synthetic inversions for shallow sources. Misfit values are computed between observed and retrieved data. Mechanism decomposition and principal component analysis have been performed following the in indications of Vasco, (1989) and (Vavryčuk, 2001, 2015), see section 2.3 for details.

M+F	misfit	λ_1	λ_2	λ_3	φ (°)	θ (°)	C_{ISO}	C_{CLVD}	C_{DC}
Explosion	0.005	1.0	1.03	1.05	/	/	0.98	0.01	0.01
Crack Horizontal	0.008	1.0	1.03	3.47	285	4	0.53	0.46	0.01
Crack Vertical	0.004	1.0	1.12	3.22	45	89	0.55	0.41	0.04

Only M	misfit	λ_1	λ_2	λ_3	φ (°)	θ (°)	C_{ISO}	C_{CLVD}	C_{DC}
Explosion	0.006	1.0	1.02	1.03	/	/	0.98	0.01	0.01
Crack Horizontal	0.009	1.0	1.01	3.23	4	1	0.54	0.46	0
Crack Vertical	0.004	1.0	1.07	3.22	45	90	0.55	0.43	0.02

Table 6 – Results of the synthetic inversions for depth sources. See caption Table 5

M+F	misfit	λ_1	λ_2	λ_3	φ (°)	θ (°)	C_{ISO}	C_{CLVD}	C_{DC}
Explosion	0.003	1.0	1.0	1.0	/	/	1.0	0.0	0.0
Crack Horizontal	0.008	1.0	1.02	3.35	15	0	0.53	0.46	0.01
Crack Vertical	0.003	1.0	1.01	3.28	45	90	0.54	0.46	0.0

Only M	misfit	λ_1	λ_2	λ_3	φ (°)	θ (°)	C_{ISO}	C_{CLVD}	C_{DC}
Explosion	0.003	1.0	1.0	1.0	/	/	1.0	0.0	0.0
Crack Horizontal	0.009	1.0	1.01	3.26	356	1	0.54	0.46	0
Crack Vertical	0.004	1.0	1.02	3.28	45	90	0.54	0.45	0.01

insignificant in describing an explosive source. The principal component analysis for describing the percentage of isotropic/deviatoric contributions still points to the right solution with a 98% isotropic and only 2% deviatoric part (Table 5). The moment tensor inversion works correctly as the original solution is well reconstructed in both the source time function and the fit between the observed and retrieved data. It is worth nothing

that the moment tensor solution including forces shows some noise on the coda of the retrieved STFs especially for the vertical component (M_{zz}, Figure 30).

Further, the F_z component, despite it is not realistic, show a small, but still important, amplitude which would not be expected for such a synthetic test. The small differences in the synthetics signals and in the mechanism decomposition could be generated by this spurious force. I continue testing the other synthetic source mechanisms to highlight the importance of this unwanted force.

5.2.1.2 Horizontal tensile crack source

The second test is performed for a horizontal tensile crack. A tensile crack produces a $\lambda : \lambda : (\lambda + 2\mu)$ ratio of moment tensor eigenvalues (Aki and Richards, 2002) which is 1 : 1 : 3.23 for a Poisson's ratio of 0.236 as in my synthetic case for sources deeper than ~300 m from the free surface. This crack source is oriented horizontally and is therefore simulated using $M_{xx} = M_{yy} = 1$, $M_{zz} = 3.23$ and $M_{xy} = M_{xz} = M_{yz} = 0$. The moment tensor solution is shown in Figure 32. As for the explosion source case the Ricker wavelet STF is well reproduced by both M+F and only M moment tensor inversions. Again, some noise appears especially on the M_{zz} component of the solution including forces. The misfit between observed and retrieved solution is very low (Table 5) and the waveforms of the observed data are almost perfectly reconstructed (Figure 33) in both MT+F and MT-only solutions. Decompositions of the moment tensors give the expected results (1 : 1 : 3.23) for the M only solution, while the result is slightly overestimated in the third component for the M+F solution (1 : 1 : 3.47). I'm only interested in the inclination of the crack normal which should correspond to $\theta = 0°$ for a horizontal crack. The eigenvectors orientation point to a very close value ($\theta = 1°$) for the M only solution, while the inclination is slightly higher ($\theta = 4°$) for the solution including forces. Using the principal components analysis (Vavryčuk, 2001) the source is described as 54% isotropic and 46% CLVD in both cases. Again, the mechanism is almost perfectly reconstructed in both M+F and MT-only solutions. The small differences arising from the spurious single force are still present. Hence, I end up analyzing a vertical crack and I will then discuss the origin of the unwanted force.

5.2.1.2 Vertical tensile crack source

The last case I consider is a vertical oriented (φ=45° and θ=90°) tensile crack. Using equation (31) the oriented crack is simulated as $M_{xx} = M_{yy} = 1.9$, $M_{zz} = 0.9$, $M_{xy} = 1$ and $M_{xz} = M_{yz} = 0$ for Lame's parameters computed using velocities and density of the second layer of model *S2*. Recall that the source is situated at the interface between the surface low velocity layer and the half space at the bottom hence Lame's parameters are computed for the second layer. As stated before a tensile crack is described by an eigenvalues ratio of $1:1:3.23$ for a Poisson's ratio of 0.236 (Aki and Richards, 2002). Thus this ratio can be computed after diagonalization of the moment tensor. The moment tensor solution for this case is shown in Figure 34. The given STF is well reconstructed with correct eigenvalue ratio, but again the vertical component is noisy with the presence of a weak, but unwanted force (F_z). Synthetic comparison (Figure 35) shows good matching (misfit 0.004 for both simulations) and the orientation of the eigenvectors point to the right source mechanism for both solutions (Table 5). After principal component analysis the isotropic/CLVD/DC ratios are well reconstructed. In order to investigate the origin of this unwanted single forces component I perform the same inversion for a deeper source. For comparison, the results for the same vertical crack embedded at a higher depth are shown in Figure 36. In this case the moment tensor solution with and without single forces is more stable without unwanted features. Synthetic comparison and moment tensor decomposition show analog results to the shallower crack solution (Figure 37).

Analyzing the results all together the vertical single force appears in all shallow sources simulations and induces some unwanted oscillations in the vertical component (M_{zz}) of the moment tensor. Small oscillations can be seen also for the deep source, but the influence of single forces is less important. An explication can be found in the spatial position of the far receivers. Stations *empl, eczm, emfo, ecbd, emnr* and *emsg* are all at the border of the numerical domain. Thus, even if the absorbing boundaries work efficiently, some unexpected reflections propagate from the boarder of the model. As the Green's functions have been computed taking advantage of the reciprocity theorem, these reflections occur earlier than in the forward simulations. Hence, a small difference

arises between the Green's functions and the model used for computing the synthetic forward simulations. This can clearly be seen as a Ricker wavelet appearing at the beginning of the reconstructed signals in all the test cases especially for *emsg* and *emfo* stations which are closest to the boarders.

Consequently, the degree of freedom is higher in inversion including single forces, the forces tend to accommodate the error (De Barros et al., 2013) originating from this difference producing the unwanted oscillations. The oscillation is more evident for the shallow sources because the unwanted wave is principally a surface wave which induces higher differences in phase arrivals for the forward and reciprocity simulations.

Anyway, the synthetic test shows that I'm able to catch the most important information from the signals and that the inversion method is reliable. I have to keep in mind that for shallow sources single forces will tend to compensate errors due to the Green's functions (wrong velocity model compared to the reality) and for this unwanted reflection from the boundaries. Thus, careful attention should be paid in the interpretation of the real data.

5.2.1 Green's functions and synthetic data computed in different velocity models

In order to test further the network capability in reproducing the source process, I perform here a synthetic test following the methodology applied in Chapter 4. In this test the synthetic data have been computed for the complex velocity model *S4* (see Chapter 4) while the Green's functions used for the MT inversion have been computed in the low-velocity surface layer model (*S2* in Chapter 4). I perform moment tensor inversion for three source types: two tensile cracks (one horizontal and one vertical) and a double-couple source which fault plane is horizontal. The choice for a double-couple source comes from the fact that Bean et al., (2013) recently proposed a source model for the LP events which implies slow rupture brittle-failure of unconsolidated shallow materials (see section 2.2.7).

The simulations and the MT inversions are performed for the three source mechanisms located at 499.598 km east, 4178.22 km north and 2520 m.a.s.l. in UTM coordinates (Figure 28). The target location is roughly below the BN (Bocca Nuova) crater

where many LP events on Mt. Etna have been located (e.g. Cannata et al., 2009a, 2015). The Ricker source time function used for the synthetic signals computation is identical to the one described in the previous section. I report the original values and all the results for the MT inversion and the MT decomposition in Table 7.

Table 7 – Results of the synthetic inversions for the three targeted sources. For each solution I report the original values of each source model. The Misfit values are computed between observed and retrieved data. Mechanism decomposition and principal component analysis have been performed following the in indications of Vasco, (1989) and (Vavryčuk, 2001, 2015), see section 2.3 for details.

Crack Hor	Misfit DATA	Misfit STF	λ_1	λ_2	λ_3	φ (∘)	θ (∘)	C_{ISO}	C_{CLVD}	C_{DC}
Original	/	/	1.0	1.0	3.0	/	0	0.56	0.44	0.0
M+F	0.444	1.375	1.0	1.17	1.79	4	5	0.74	0.16	0.1
M only	0.629	1.172	1.0	2.0	2.26	70	102	0.77	0.15	0.08

Crack Ver	Misfit DATA	Misfit STF	λ_1	λ_2	λ_3	φ (∘)	θ (∘)	C_{ISO}	C_{CLVD}	C_{DC}
Original	/	/	1.0	1.0	3.0	0	90	0.56	0.44	0.0
M+F	0.276	0.846	1.0	1.47	2.58	14	4	0.65	0.17	0.18
M only	0.361	0.773	1.0	1.23	2.21	2	85	0.67	0.22	0.11

DC	Misfit DATA	Misfit STF	λ_1	λ_2	λ_3	φ (∘)	θ (∘)	C_{ISO}	C_{CLVD}	C_{DC}
Original	/	/	/	/	/	/	90	0	0	1.0
M+F	0.351	1.387	1.0	3.25	4.63	-45	98	0.17	0.08	0.75
M only	0.365	0.889	1.0	53.8	56.0	43	90	0.02	0.0	0.98

As highlighted in the previous chapter, for the three source mechanisms the best fit between the original and the retrieved data is obtained for the solutions including single forces. On the opposite, the best fit between the original and the retrieved source time functions (STF) is obtained for the MT-only solutions (Figure 38 and Table 7). The results of MT inversions can be so summarized:

a) *Horizontal crack:* The original source mechanism is well reproduced. The misfit values between the observed and the retrieved data are considerably lower for the solution including single forces which is also the solution which points to the right orientation angles after MT decomposition. The eigenvalue ratio is better resolved for the solution including forces. The percentages of isotropic/deviatoric components point to a tensile crack source as expected. Despite the solution including forces introduces a strong spurious vertical force, the original STF is well reproduced (Figure 38a). On the opposite, the STF waveforms of the MT-only solution are not able to reproduce the original STF (Figure 38a).

b) *Vertical crack:* misfit values are considerably lower than the horizontal crack solution for both the data and the STF fits. The best misfit between the original and the retrieved data is obtained again for the solution including single forces, but the MT decomposition points to an erroneous crack orientation (horizontal instead of vertical). The eigenvalues ratio points to a crack mechanism, but the second eigenvalue is slightly higher (1.47) than expected. The PCA shows a high spurious double-couple component which complicates the interpretation of the source mechanism. The original shape of the STF is well reproduced, but *Myy* component is highly underestimated, leading to the wrong MT decomposition (Figure 38b). The strong vertical single force appearing in the solution accentuates this underestimation. The solution for MT-only, on the opposite, points to the right orientation angles. The double-couple component is still present, but less remarkable. The original STF shape is well reproduced. *Myy* component is again underestimated (Figure 38b), but not enough to affect the MT decomposition and the retrieved source orientation;

c) Double-couple: the DC solution is well retrieved for both MT inversions including and without single forces. The MT decomposition for the moment

only solution perfectly reproduces the original source mechanism (C_{DC} = 98%) and orientation angles (θ = 90°). The STF shows the appearance of some unwanted waveforms in the diagonal of the MT, but the *Mxy* component is predominant as expected. The amplitude of the non-diagonal component is slightly underestimated in respect to the original STF (Figure 38c). The solution including forces points to roughly the right orientation angle (θ = 98°) but the PCA introduces some unwanted isotropic and C_{CLVD} components. The C_{DC} is anyway predominant (C_{DC} = 75%) so that a DC source mechanism is assessed. The analysis of the retrieved STF shows slightly higher amplitudes of the diagonal components if compared to the solutions for MT-only (Figure 38c).

In conclusion, the horizontal crack and the double-couple source mechanisms are well reproduced and the MT inversions are interpreted correctly. The vertical crack suffers from the low summit coverage and the solution including forces is misinterpreted as a horizontal crack. On the opposite, the MT-only solution points to the right source mechanism. In this case the lowest misfit value does not correspond to the right source mechanism. The analysis of the real LP events on Mt. Etna will be conducted carefully taking advantage of the lessons learned from the synthetic tests, in particular noticing the limitations due to the sparse network of stations.
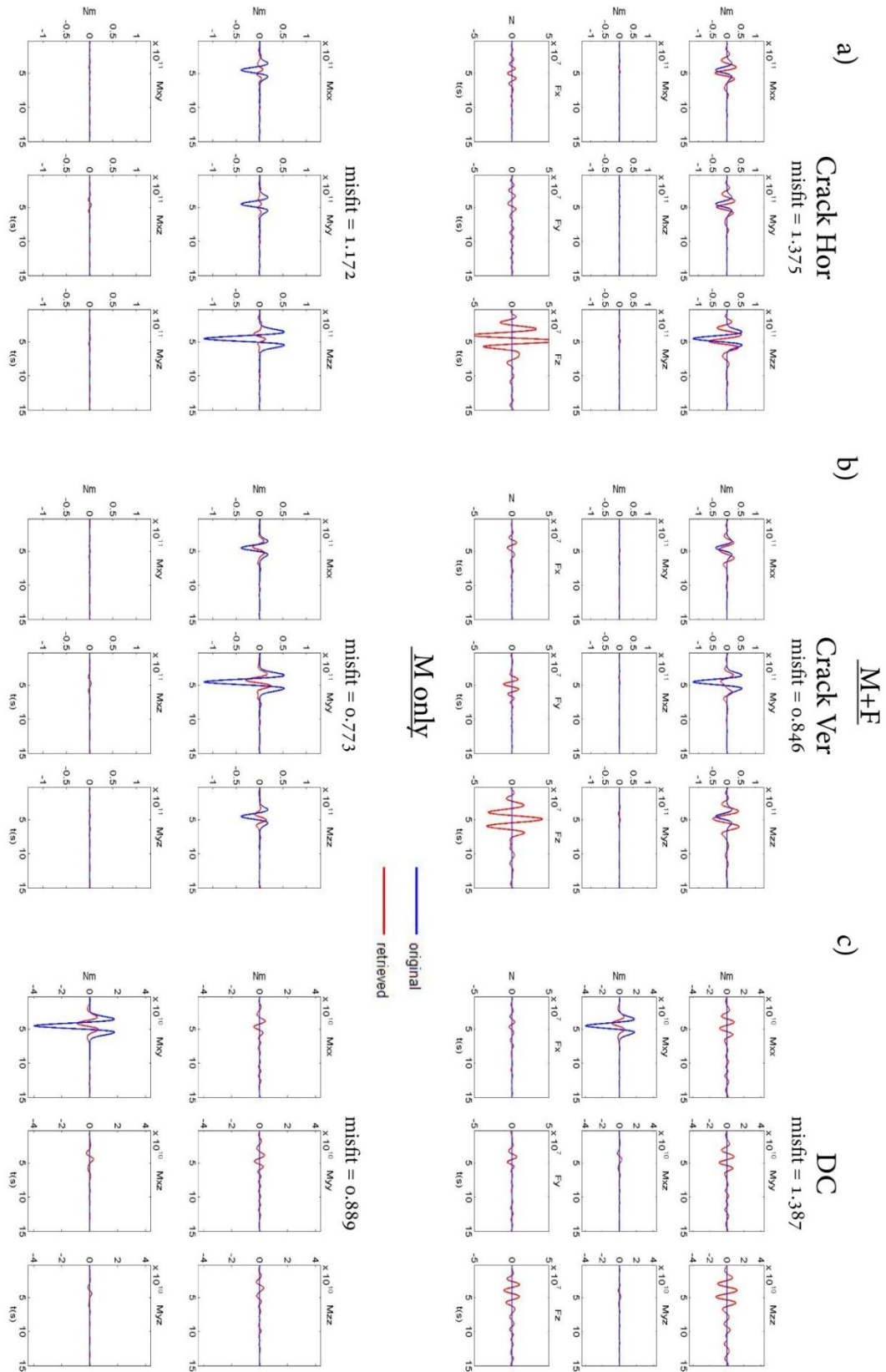
Figure 38 - Comparison between original (blue) and retrieved (red) source time functions for the MT inversions including (M+F) and without (M only) single forces. Six moment tensor components (both solutions) and three single forces (only the M+F solution) are represented. MT solutions for: a) horizontal tensile crack source; b) vertical tensile crack source; c) double couple source. For each solution I report the misfit between original and retrieved STF.

5.3 Monochromatic LPs (June 2009)

The first set of data considered occurred during the 2008-2009 flank eruption. After the 2006 flank eruption, Mt. Etna was mainly in a recharging phase (Bonaccorso et al., 2011b). During this recharging period the eruptive activity of Etna was characterized by several short duration lava fountains and explosive activity occurred at a pit crater
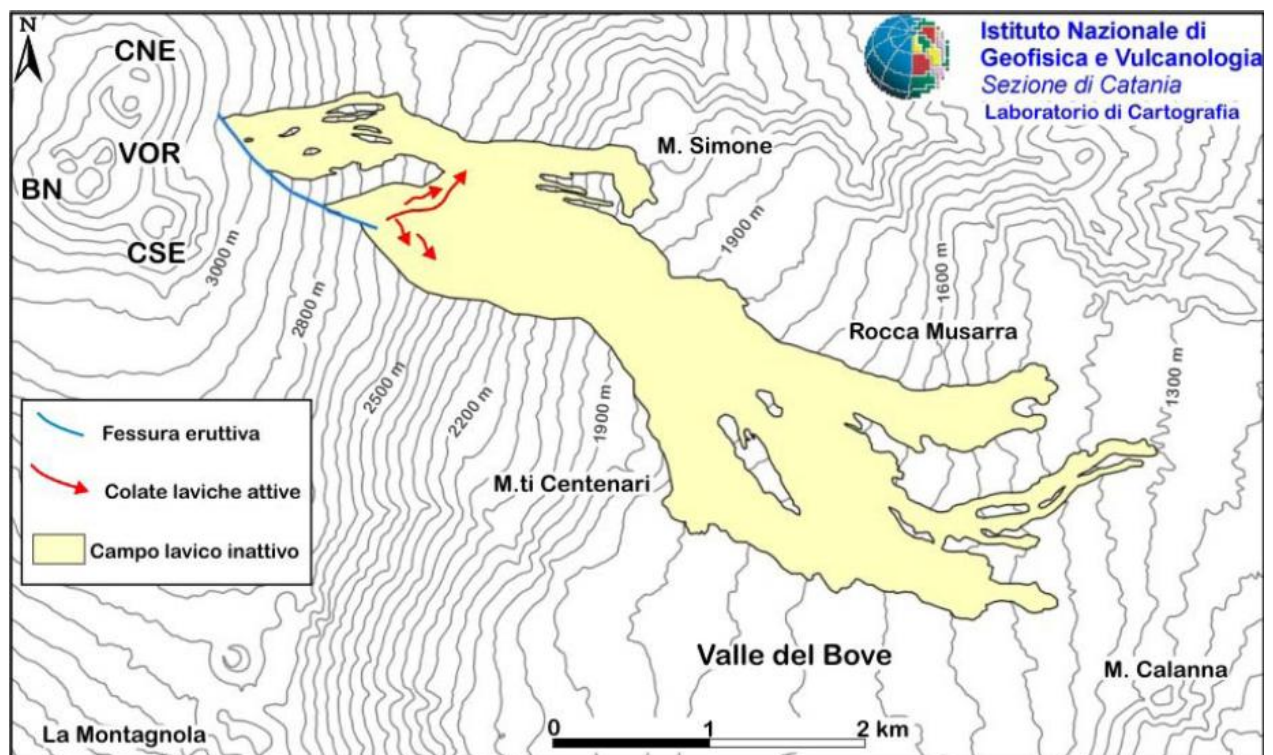
Figure 39 – Schematic map of the lava field uploaded at 22th May 2009. Blue line represents the eruptive fissure, the red lines are the active lava flows and the yellow surface represents the extension of the lava field since the beginning of the eruption in May 2008 (INGV internal reports)

formed on the eastern flank of South East Crater (SEC, Aiuppa et al., 2010; Andronico et al., 2008; Cannata et al., 2011; INGV internal reports; Neri et al., 2008). On the 13th May 2008, the episodic activity of SEC culminated in a proper effusive eruption preceded by seismic swarms (Cannata et al., 2009b) and pronounced ground deformation (Bonaccorso et al., 2011b). The eruption of the 13th of May marked the beginning of this new eruptive phase. Episodes of increasing and decreasing of the eruptive activity were recorded until July 2009 when this eruptive phase ended. The first period of the eruption was characterized by strombolian activity at the upper vents, while the effusive episodes

were mainly located on the lower flank of the SEC (Cannata et al., 2011). Overtime, the lava output produced a lava flow field which spread into the *valle del Bove* (Figure 39). The events analyzed in this work have been recorded in the last period of activity during the 5th and 6th of June 2009. During the month preceding the recordings the volcano showed intense degassing from the North East Crater (NEC), Bocca Nuova (BN) and the South East Crater (SEC). The degassing activity was mainly concentrated at the summit craters, but the fissure which opened on the 13th of May 2008 was still active. At this stage the fissure was active between 3000 and 2600 m.a.s.l. on the higher portion of the eastern flank of the volcano. At higher altitude (~2800/2900 m.a.s.l.) the fissure was mainly degassing, while at lower altitude (~2600 m) the effusive activity was still in place (Figure 39). Two small vents produced two distinct lava flows with some degassing structures located in between. The SO_2 degassing measured during the two targeted days showed a maximum of ~3800 t/d during the 5th June and a minimum the day after (INGV internal reports).
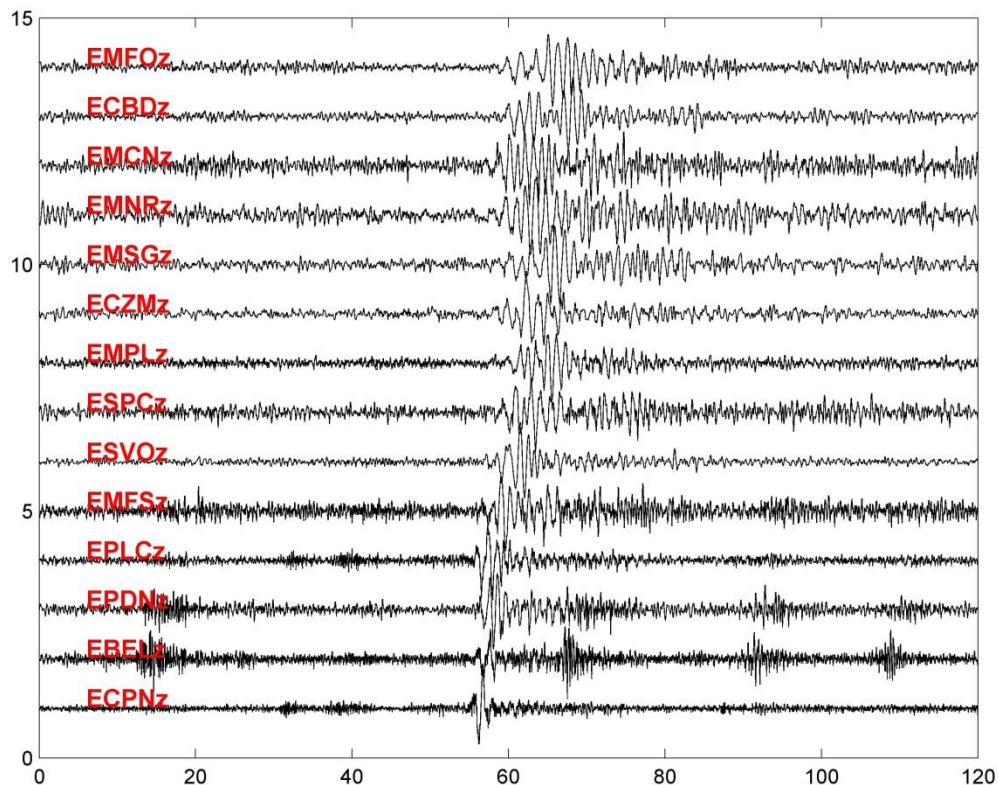
Figure 40 – Stack of vertical velocity traces recorded at all stations for the monochormatic set of events, source INGV.

.
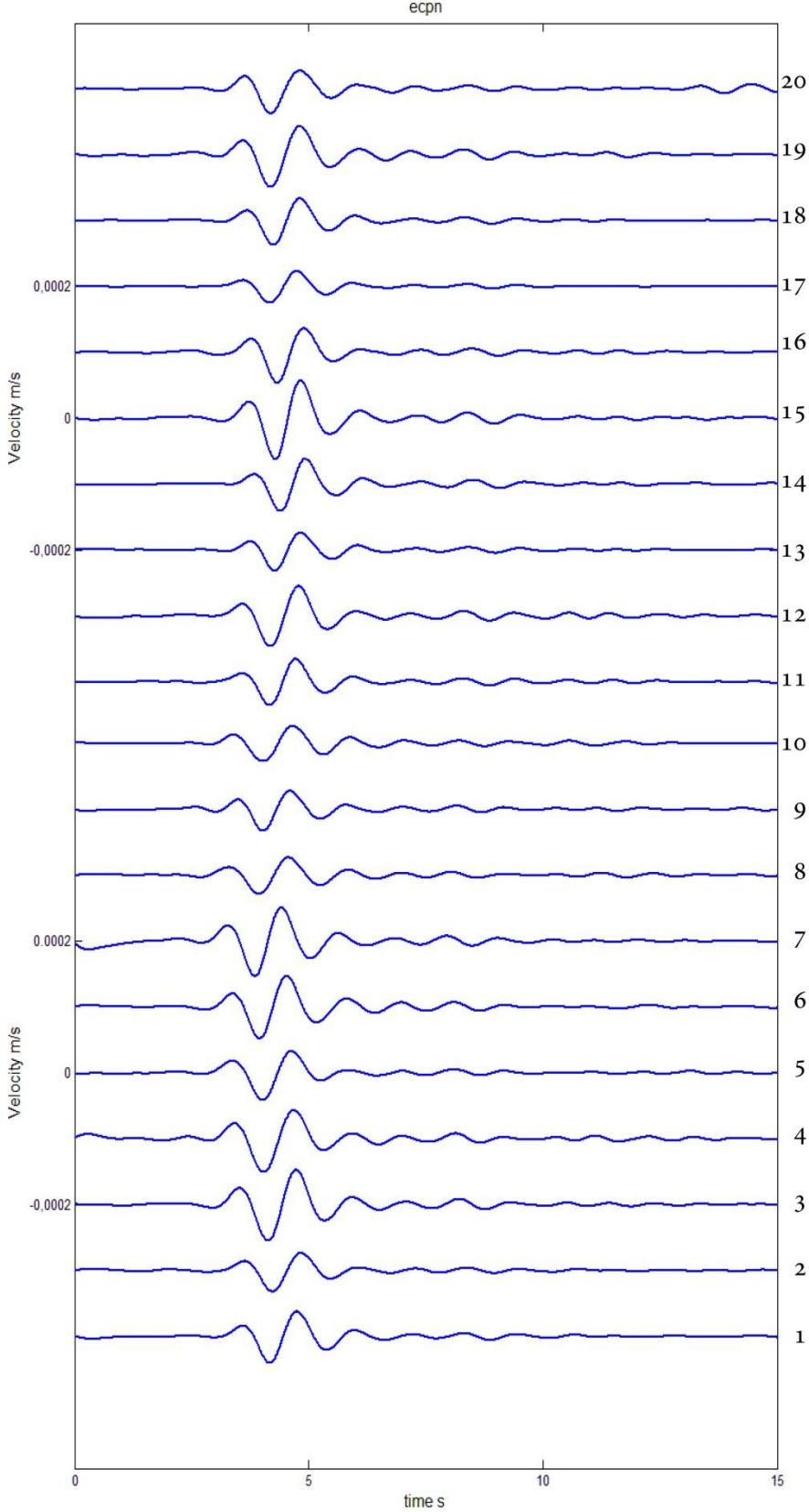
Figure 41 – Stack of velocity filtered (betwenn 0.2 and 1.3 Hz) seismograms for ecpn station vertical component. The high degree of similarity between the recorded waveforms is evident. Event numbers are reported on the right.

a)

b)

c)
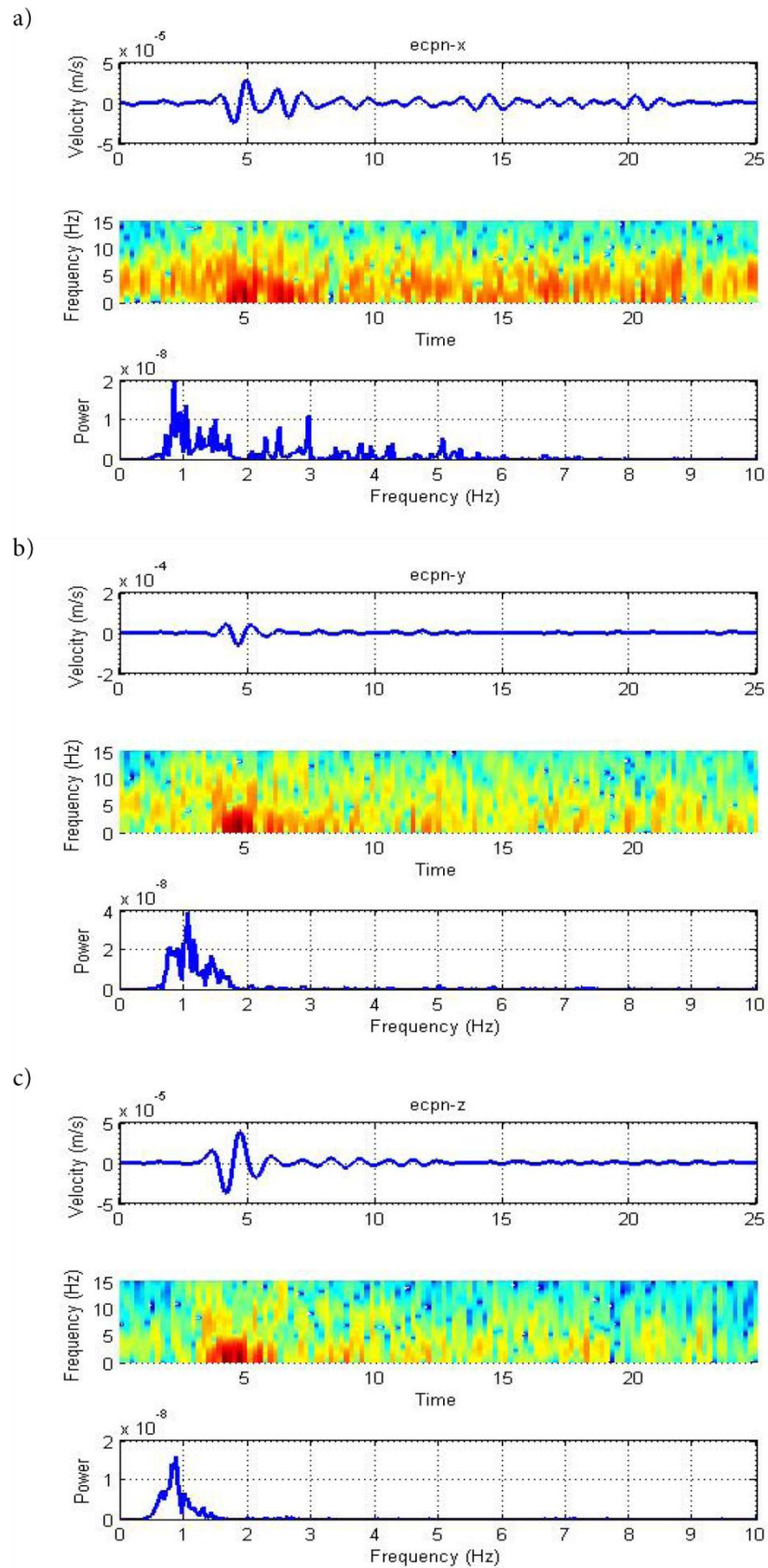
Figure 42 - a) top: x-component of velocity recorded at station ecpn for event 1. The seismic trace is filtered between 0.2 and 1.3 Hz; middle: short time Fourier transform plot of the unfiltered velocity trace, red correspond to high power towards blue lower; bottom: power spectral density of the unfiltered velocity trace. b) and c) same as a), for –y and –z components respectively.
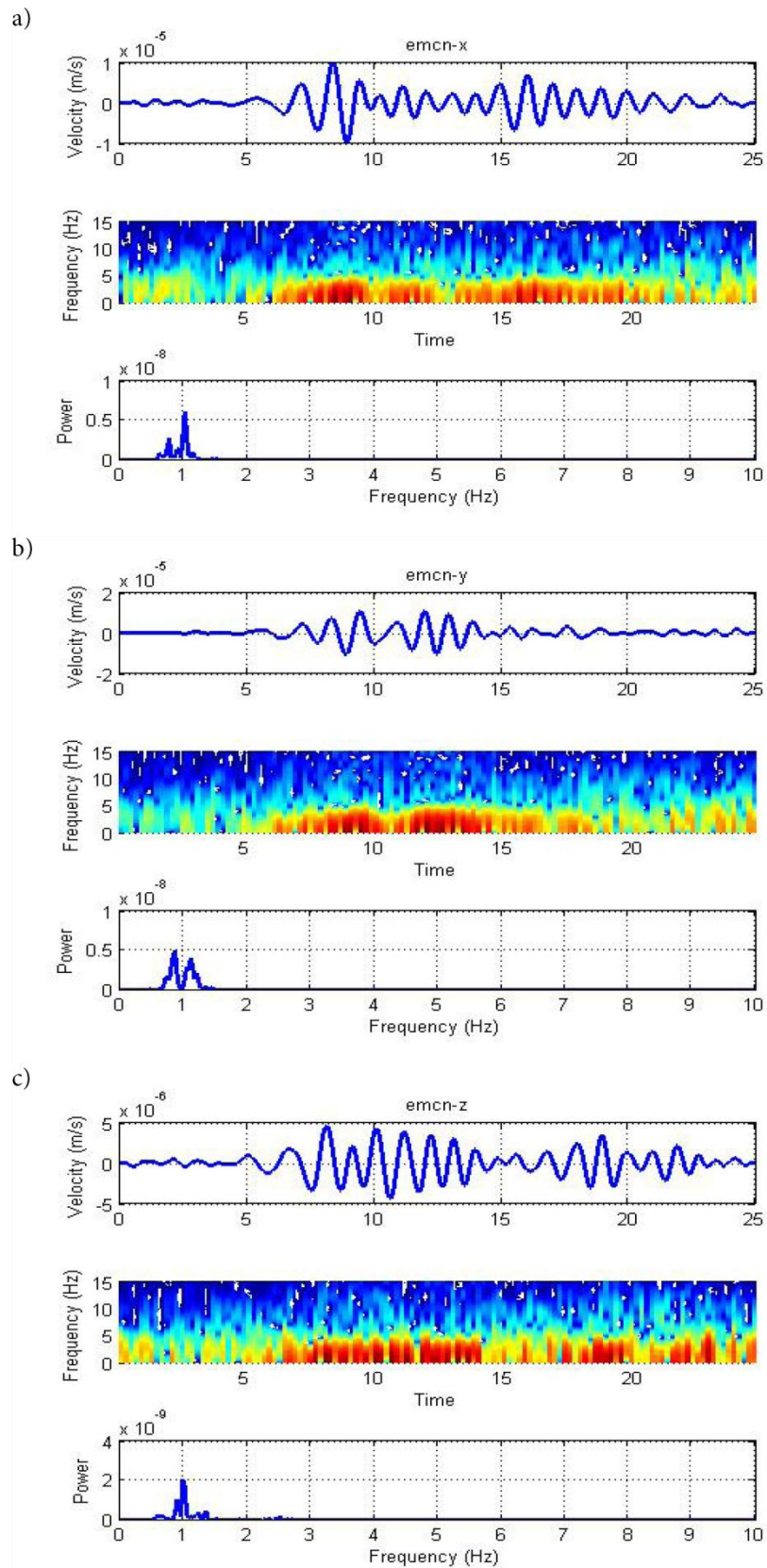
Figure 43 - a) top: x-component of velocity recorded at station emcn for event 1. The seismic trace is filtered between 0.2 and 1.3 Hz; middle: short time Fourier transform plot of the unfiltered velocity trace, red correspond to high power towards blue lower; bottom: power spectral density of the unfiltered velocity trace. b) and c) same as a), for –y and –z components respectively.

5.3.1 Data

The set of data spans 36 hours on the 5th and 6th of June 2009. During this time 20 LP events with significant energy were recorded by the permanent INGV network. An example of the first event recorded on 14 stations is shown in Figure 40.The events are characterized by emergent onset, weak amplitude (10^{-5} m/s) and fast decaying coda as usual for LPs recorded on Mt. Etna (Cannata et al., 2009a). For each recorded event, I plot (Figure 41) the vertical component of *ecpn* station which shows the simplest recorded waveforms as it is located close to the summit craters nearby the usual location for LP events (Cannata et al., 2009a; Saccorotti et al., 2007). The events filtered with a Butterworth band-pass filter between 0.2 and 1.3 Hz and aligned following their onset show a high degree of waveform similarity. Figure 42 and Figure 43 show an example for *event 1* recorded at station *ecpn* and at the farther station *emcn* respectively. The influence of the complex geology of the volcano on the recorded waveforms appears clearly for station *emcn* which shows longer decaying coda and the appearance of a reflected wave (or another event) at the end of the recording (particularly evident in the vertical component at 17 s, Figure 43 c). A peculiar characteristic of these events is that they are highly monochromatic. In fact their frequency content is restricted in a narrow band between 0.5 and 1.3 Hz (Figure 42 and Figure 43).

5.3.2 Location results

I begin by locating the 20 events towards moment tensor inversion (the method is discussed in detail in Chapter 2). The velocity traces are first band-pass filtered between 0.2 and 1.3 Hz, then integrated to displacement and detrended to ensure stability in the inversion and avoid contributions from very low frequencies. The optimum position for each event is obtained towards a grid search among 14196 sources spaced 40 m in a volume (1 x 1 x 0.8 km) located below the summit craters and by taking the lowest value of misfit between observed and retrieved data. According to this method the events are located for both inversions with and without single forces. The results for all 20 LP

Table 8 -– MT inversion location results for the monochromatic set of 20 events. Residuals data between observed and synthetics are reported with the respective source coordinates. M+F corresponds to the results including forces. M only corresponds to the solutions without forces. At the bottom the average location for the whole set of events found by INGV.

	M+F				M only			
	misfit	x (km)	y (km)	z (m)	misfit	x (km)	y (km)	z (m)
event_01	0.589	499.478	4179.220	2600	0.697	499.518	4179.220	2360
event_02	0.592	499.518	4179.220	2640	0.694	499438	4179.220	2360
event_03	0.579	499.518	4179.220	2640	0.690	499.438	4179.220	2360
event_04	0.589	499.518	4179.220	2640	0.706	499.558	4179.220	2440
event_05	0.596	499.478	4179.220	2600	0.720	499.558	4179.220	2320
event_06	0.584	499.518	4179.220	2640	0.701	499.478	4179.220	2360
event_07	0.546	499.598	4179.220	2720	0.651	499.518	4179.220	2320
event_08	0.557	499.598	4179.220	2720	0.671	499.518	4179.220	2320
event_09	0.595	499.518	4179.220	2600	0.702	499.438	4179.220	2360
event_10	0.606	499.518	4179.220	2640	0.705	499.518	4179.220	2280
event_11	0.580	499.518	4179.220	2640	0.683	499.438	4179.220	2360
event_12	0.610	499.438	4179.220	2400	0.717	499.398	4179.220	2360
event_13	0.603	499.518	4179.220	2600	0.708	499.438	4179.220	2360
event_14	0.607	499.598	4179.220	2720	0.707	499.518	4179.220	2320
event_15	0.616	499.598	4179.220	2720	0.716	499.518	4179.220	2320
event_16	0.600	499.558	4179.220	2720	0.712	499.518	4179.180	2320
event_17	0.580	499.518	4179.220	2640	0.691	499.438	4179.220	2360
event_18	0.597	499.518	4179.220	2600	0.699	499.438	4179.220	2400
event_19	0.601	499.518	4179.220	2640	0.706	499.438	4179.220	2360
event_20	0.567	499.598	4179.220	2720	0.681	499.598	4179.220	2400

INGV Location	x (km)	y (km)	z (m)
	499.060	4178.010	2080
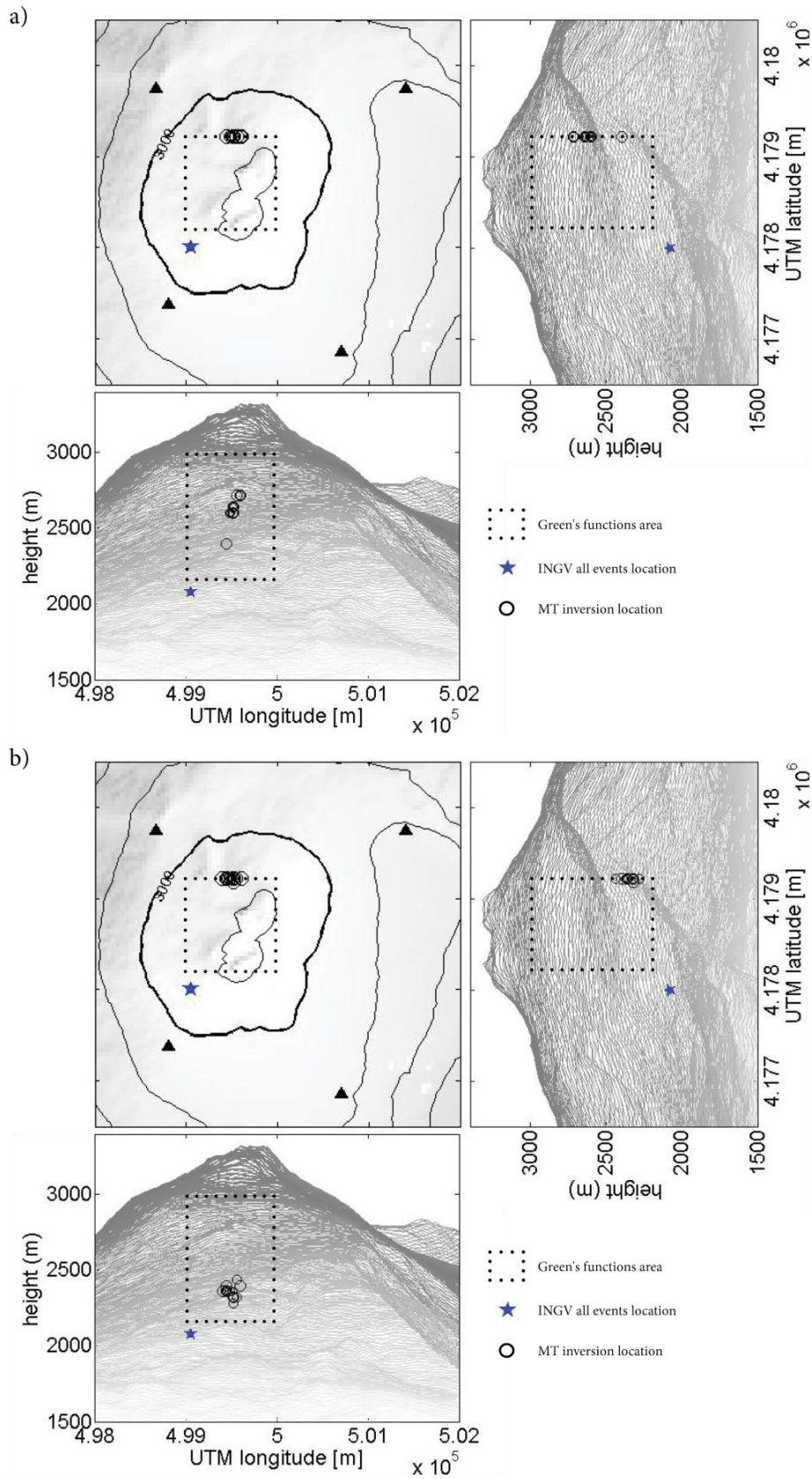
Figure 44 – Graphical representation of the location results for the first analyzed set of events reported in Table 8. a) MT inversion with single forces location results. The summit area of Mt. Etna with respective cuts east-west and north-south in UTM coordinates are represented. The dot line square corresponds to the Green's functions area, circles are the event locations and blue star is the average whole family INGV location.

events are listed in Table 8 and shown in Figure 44. The results are similar for both cases demonstrating the robustness of the solutions. The solutions including single forces point to a structure oriented east-west and located to the top north side of the Green's functions volume just below the North East Crater (NEC). The minimum residual is obtained for *event* 7 (0.546) located in UTM coordinates 499.598 km east, 4179.22 km north and 2720 m.a.s.l. The horizontal solution is very stable while vertically the locations span ~300 m from 2400 to 2720 m.a.s.l. Anyway, all the solutions are localized around ~2650 m.a.s.l., while the only event located at 2400 m.a.s.l. is *event 12* which shows a slightly higher misfit value (0.61) if compared to the other events (~0.58, Table 8). It is impossible to further constrain the solutions due to the lack of an accurate velocity model. The solutions without forces point to the same horizontal sector, while the events result in deeper locations (~2350 m.a.s.l.). For comparison, I also report the average location found by INGV (INGV internal reports) towards semblance + R^2 method (see Cannata et al., 2013, 2015 for more details) of the whole set of events. The location found by INGV shows (Figure 44) a *quasi*-identical longitude location compared to my solutions, while latitude points to the opposite side of the Green's functions volume towards south instead of north in a position roughly below BN (Bocca Nuova, Figure 26 for craters locations). The vertical location found by INGV is deeper than the MT solution (~2080 m.a.s.l.) more similar to the solution without single forces. It is worth nothing that the INGV solution is located outside the Green's functions volume (~150 m far from the south-west corner). In Figure 45 I explore how converged the inversion results are. For three selected events I plot the slice contour of the obtained residuals for the whole set of grid points Green's functions used to estimate the best source location. The shallowest event (*event* 7 and lowest misfit value), the deepest vertical location (*event 12* and highest misfit value) and an intermediate one (*event 1*) are plotted for comparison. The solutions without including forces appear to be less constrained, i.e. the solutions appear to be dispersed in the whole Green's functions domain both horizontally and vertically. This could be due to the erroneous velocity model not representative of the complexity of the geology of Mt. Etna. The errors generated by mismodelling of the velocity structure would affect the location solutions and the single forces help "absorbing" these errors (De Barros et al., 2011, 2013). Hence, the solution including single forces is thought to be
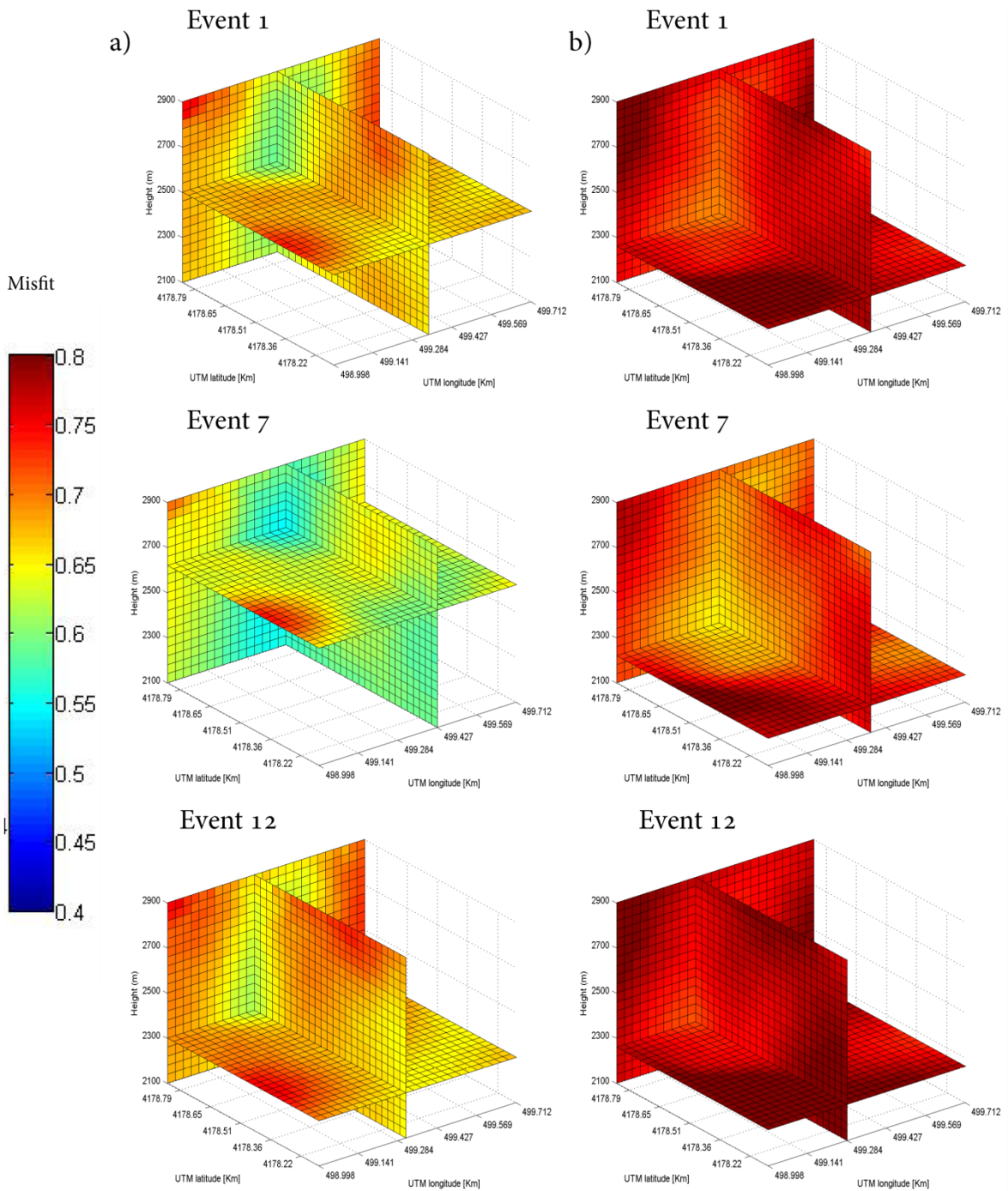
Figure 45 – Slice plot of the residuals for the whole Green's functions volume a) solution of MT including single forces; b) solution for MT only. The events are chosen on the basis of their location depth and residual value. Event 1 (top) intermediate location, event 7 (middle) shallowest location (and lowest absolute misfit), event 12 deepest location (and highest misfit).

more accurate. For the solution including forces the horizontal locations point to a well-defined cluster for all the three selected events. The vertical locations appear to be more dispersed. This could be due to the poor stations coverage around the source which does not help in constraining the solution vertically, but also to the computation of Green's function and the appearance of the reflected wave from the boarders of the domain as investigated in the synthetic test (see section 5.2) particularly affecting farther stations. The dispersion along the vertical and the INGV solution could suggest a deeper location for the set of events. This eventuality will be explored in the next section.

5.3.3 Source mechanism

Moment tensor inversion is performed for all the 20 analyzed events for the respective lowest residual locations (Table 8). The results for the solutions including forces and for MT-only are reported in Table 9 and Table 10 respectively. First, I give a general overview of the solutions retrieved for both cases and I will then analyze deeply a couple of selected events.

The retrieved solutions including forces (Table 9) are very similar between all events in terms of residuals and eigenvalues decomposition (λ_n). The isotropic component is high with a minimum value of 61% for event 15 and a maximum of 81% for event 12 (average = 69%). The CLVD percentage varies a lot (between ~10 and 30%, STD = 0.078) while the DC component is rather constant (~10-15%, STD =0.039). Thus, it seems that the lower values of the isotropic component computed for some events are best accommodated by the CLVD more than the DC component. In first approximation, the orientation angles computed towards moment tensor decomposition (φ = strike, θ = dip, Figure 2 for the coordinate system) point to a quasi-horizontal tensile crack mechanism for all the studied events. The solutions for MT-only (Table 10) show slightly higher misfit values and comparable eigenvalue ratios to the solution including forces. On the opposite hand, the orientation angles computed towards moment tensor decomposition (φ = strike, θ = dip) point to a vertical instead of a horizontal crack (average θ = 91°). In order to better investigate this strong difference I have to deeply analyze the solutions.

Table 9 – Results of MT inversion including single forces for the monochromatic set of events for the lowest residual source location. Misfit values are computed between observed and retrieved data. Mechanism decomposition and principal component analysis have been performed following the in indications of Vasco, (1989) and (Vavryčuk, 2001, 2015), see section 2.3 for details.

M+F	misfit	λ_1	λ_2	λ_3	φ (°)	θ (°)	C_{ISO}	C_{CLVD}	C_{DC}
event_01	0.589	1.0	1.37	2.03	-6	21	0.72	0.09	0.18
event_02	0.592	1.0	1.3	2.14	-5	20	0.69	0.17	0.14
event_03	0.579	1.0	1.35	2.08	-8	21	0.71	0.12	0.17
event_04	0.589	1.0	1.34	2.08	-5	21	0.71	0.13	0.16
event_05	0.596	1.0	1.39	2.02	-6	23	0.73	0.08	0.19
event_06	0.584	1.0	1.31	1.97	5	17	0.72	0.12	0.16
event_07	0.546	1.0	1.22	2.5	-1	15	0.63	0.28	0.09
event_08	0.557	1.0	1.2	2.5	4	16	0.63	0.29	0.08
event_09	0.595	1.0	1.29	2.24	1	18	0.67	0.2	0.13
event_10	0.606	1.0	1.28	2.09	-1	15	0.7	0.17	0.13
event_11	0.580	1.0	1.31	2.04	-7	20	0.71	0.14	0.15
event_12	0.610	1.0	1.6	1.81	16	44	0.81	0.1	0.09
event_13	0.603	1.0	1.3	2.23	1	18	0.68	0.19	0.13
event_14	0.607	1.0	1.16	2.54	3	15	0.62	0.32	0.06
event_15	0.616	1.0	1.18	2.59	2	14	0.61	0.32	0.07
event_16	0.600	1.0	1.24	2.37	-2	17	0.65	0.25	0.1
event_17	0.580	1.0	1.34	2.08	-4	22	0.71	0.13	0.16
event_18	0.597	1.0	1.3	2.15	-1	20	0.69	0.17	0.14
event_19	0.601	1.0	1.32	2.14	-6	20	0.69	0.16	0.15
event_20	0.567	1.0	1.2	2.5	1	16	0.63	0.29	0.08
Average	0.590	1.0	1.3	2.2	-1.0	19.6	0.69	0.18	0.13
STD	0.018	0.0	0.1	0.2	5.6	6.3	0.05	0.09	0.04

Table 10 – Results of MT inversion including single forces for the monochromatic set of events for the lowest residuals source location. Misfit values are computed between observed and retrieved data. Mechanism decomposition and principal component analysis have been performed following the in indications of Vasco, (1989) and (Vavryčuk, 2001, 2015), see section 2.3 for details.

M only	misfit	λ_1	λ_2	λ_3	φ (°)	θ (°)	C_{ISO}	C_{CLVD}	C_{DC}
event_01	0.697	1.0	1.55	1.84	57	94	0.8	0.08	0.13
event_02	0.694	1.0	1.7	2.2	55	89	0.74	0.05	0.2
event_03	0.690	1.0	1.41	1.88	53	87	0.76	0.02	0.22
event_04	0.706	1.0	1.68	2.31	63	88	0.72	0.01	0.27
event_05	0.720	1.0	1.57	2.01	67	90	0.76	0.04	0.2
event_06	0.701	1.0	1.47	2.11	49	89	0.72	0.06	0.22
event_07	0.651	1.0	1.41	1.69	42	100	0.81	0.04	0.15
event_08	0.671	1.0	1.93	2.44	50	98	0.73	0.09	0.17
event_09	0.702	1.0	1.62	2.01	54	90	0.77	0.07	0.17
event_10	0.705	1.0	1.44	1.91	50	89	0.76	0.01	0.23
event_11	0.683	1.0	1.58	2.09	56	86	0.74	0.02	0.24
event_12	0.717	1.0	1.72	2.17	52	89	0.75	0.07	0.17
event_13	0.708	1.0	1.58	2.01	53	88	0.76	0.05	0.19
event_14	0.707	1.0	1.78	2.01	57	94	0.79	0.13	0.08
event_15	0.716	1.0	1.67	1.91	55	95	0.8	0.11	0.09
event_16	0.712	1.0	1.62	1.92	73	85	0.79	0.09	0.13
event_17	0.691	1.0	1.61	2.15	54	88	0.74	0.02	0.24
event_18	0.699	1.0	1.76	2.39	53	90	0.72	0.04	0.24
event_19	0.706	1.0	1.64	2.18	53	89	0.74	0.03	0.24
event_20	0.681	1.0	1.19	1.36	-17	121	0.87	0.01	0.12
Average	0.698	1.0	1.6	2.0	51.4	91.9	0.76	0.05	0.19
STD	0.017	0.0	0.2	0.2	17.4	7.8	0.04	0.03	0.05

I decide to show the results for two selected events which better represent in average the whole set of results. I focus my attention on *event 7* which shows the lowest misfit value and high CLVD component and on *event 5* which shows a slightly higher residual and the highest DC component. The moment tensor results from the full moment tensor inversion for LP *event 7* inverted for the lowest residual source location are shown in Figure 46. Waveforms fits between the real data and data reconstructed from the moment tensor solution convolved with the green's functions can also be seen in Figure 47. The fits are generally good for stations closest to the summit of the volcano (e.g. *eplc*, *ecpn* and *ebel*), but poor for the stations farther from the summit. Such characteristic is expected due to the stronger path effect contribution to distant stations. However, due to the low amplitudes recorded at farther stations, they contribute less to the final retrieved solution.

Same procedure has been applied to *event 5.* The moment tensor solution is showed in Figure 48 and the waveforms comparison in Figure 49. Same considerations done for the waveform fits between observed and retrieved data for *event 7* apply to *event 5.* It is worth noting that for *event 7* the record for station *emcn* is missing. As station *emcn* is not one of the summit stations, its absence could explain the slightly lower misfit value obtained for this event. The maximum amplitude for the M_{zz} moment tensor component is obtained for *event 5* ($\sim 1\ 10^{12}$ Nm) for the solution including forces. For both events the forces have comparable amplitude to the moments with $F_{z\ =}\sim 1\ 10^{9}$ for *event 5* (De Barros et al., 2013), but as they tend to accommodate errors their presence cannot be taken as evidence of their existence. The solutions for both inversions with and without single forces show a slowly decaying coda (~10 s) source time functions (Figure 46b and Figure 48a/b). This characteristic is particularly evident for *event 5* and in particular for the solution without forces. In case of *event 7,* solution with forces, the decaying coda appears to be more a repetition of a first pulse like waveform (Figure 46b). However, the retrieved oscillating features cannot be directly interpreted. The apparent oscillations could be due either by an oscillating tensile source mechanism (Chouet, 2003a and reference therein) or by complex path effects due to the contribution of farther stations (Bean et al., 2014).

In order to better understand the solution the moment tensors have been

decomposed into their principal components using SVD (singular value decomposition) and PCA (principal component analysis) (Chouet, 2003a; Vasco, 1989; Vavryčuk, 2001, 2015). The results are listed in Table 9 and Table 10. For all the solutions the decomposition produces two shorter axis eigenvectors and a longer eigenvector. As discussed in the synthetic test (section 5.2) a tensile crack source mechanism produces an eigenvalues ratio $(\lambda : \lambda : (\lambda + 2\mu))$ of $1 : 1 : 3$ (Aki and Richards, 2002) for a Poisson's ratio of 0.25 and $1 : 1 : 2$ for a Poisson's ration of 0.35. My results for both solutions including and without single forces fall in this range thus, the source mechanism can be interpreted as a tensile crack mechanism.

The orientations of the longest axis are consistent between events, but if for the solutions including forces, as hinted before, the average dip angle points to a quasi-horizontal crack, the solutions without forces point to a vertical mechanism. This opposite orientation between the two solutions is of difficult understanding. Looking at the source time functions (STF) of event 7 (Figure 46) and event 5 (Figure 48), for the solution without forces (b) the three diagonals of the STF (M_{xx}, M_{yy} and M_{zz}) show comparable amplitudes and the appearance of non-negligible off-diagonal (M_{xy}, M_{xz} and M_{yz}) components (~1/3 of diagonal components). In the solution including forces the off diagonal components show negligible amplitude if compared to the main diagonal components. The synthetic test of section 5.2.2 highlighted that, with the available network of station, vertical cracks could be misinterpreted as horizontal cracks when considering the MT inversion solution including forces. The PCA for the MT-only solution shows a strong isotropic mechanism with a high double couple component and a low C_{CLVD} which suggests a source mechanism of difficult interpretation. It is difficult to imagine a full isotropic source with so high shear component. As I do not have any other element to discriminate between the solutions, I tend to the solution including single forces because: 1) the retrieved STF have shorter waveforms compatible with the pulse-like nature of the summit stations records; 2) the MT decomposition and PCA seem to point to a more stable solution, i.e. the high C_{DC} component of the MT-only solution is hard to couple with the strong isotropic source mechanism; 3) the single forces should help in accommodating errors due to mismodelling of the velocity structure (De Barros et al., 2011, 2013).

In order to check the stability of my solutions, I perform full moment tensor inversion for the whole set of events, but for a mislocated source location. As the events were located far away from the average location found by INGV I perform the inversion for this source location. As the Green's functions have not been computed for the INGV retrieved location I take the nearest source point (UTM longitude 499.078 km east, latitude 4178.220 km north and 2200 m.a.s.l.) inside the Green's functions volume ~100 m far from the original INGV location. It is worth nothing that this new location is ~ 1 km far away from the average source location found towards moment tensor inversion (hereafter called solution *A* for comparison). Results for all the events for the solution including single forces are reported in Table 11.

The misfit values are slightly higher compared to solution *A* (Table 9) with an average residual of ~0.69. After SVD (Vasco, 1989) the average eigenvalues ratio is 1 : 1.3 : 1.6 which could be interpreted as a combination between a tensile crack mechanism (ratio 1 : 1 : 2 for a Poisson's ratio of 0.35) and an explosion (eigenvalues ratio of 1 : 1 : 1). An isotropic solution is also suggested by the high C_{ISO} ratio (81 % of isotropic component in average for whole set of events), but the high C_{DC} component (15% in average), if realistic, complicates the interpretation.

I focus again my attention on *event 5* for comparison, but inverted for the INGV location. The results for the moment tensor and residuals between observed and retrieved data are plotted in Figure 50 and Figure 51 respectively. If I focus my attention on the solution including forces, the amplitude of the main diagonal moment STF is slightly lower than the amplitude found for solution *A*. The three main diagonal components show comparable amplitude values, which was not the case for solution *A* where the M_{zz} component was almost double of M_{yy}. Generally, the STF waveforms are more pulse-like and the oscillating feature observed in the coda of solution *A* is less remarkable. Moreover, the forces (especially F_y) seem to contribute more to the final solution. The comparison between synthetics and observed data (Figure 51) does not add any particular detail to the mechanism understanding. The full moment tensor inversion for the mislocated source suggests that an isotropic source mechanism cannot be

Table 11 – Results of MT inversion including single forces for the monochromatic set of events for the INGV source location. Misfit values are computed between observed and retrieved data. Mechanism decomposition and principal component analysis have been performed following the in indications of Vasco, (1989) and (Vavryčuk, 2001, 2015), see section 2.3 for details.

M+F	misfit	λ_1	λ_2	λ_3	φ (°)	θ (°)	C_{ISO}	C_{CLVD}	C_{DC}
event_01	0,698	1,0	1,23	1,51	59	7	0,83	0,02	0,15
event_02	0,684	1,0	1,22	1,65	83	15	0,78	0,09	0,13
event_03	0,705	1,0	1,36	1,59	33	11	0,83	0,05	0,12
event_04	0,704	1,0	1,17	1,44	-65	6	0,84	0,05	0,12
event_05	0,707	1,0	1,15	1,43	75	7	0,84	0,06	0,1
event_06	0,702	1,0	1,28	1,56	67	13	0,82	0	0,18
event_07	0,653	1,0	1,58	1,77	36	6	0,82	0,11	0,07
event_08	0,677	1,0	1,23	1,69	85	19	0,77	0,09	0,14
event_09	0,686	1,0	1,27	1,58	-16	4	0,81	0,02	0,17
event_10	0,685	1,0	1,15	1,23	74	61	0,92	0,03	0,05
event_11	0,689	1,0	1,33	1,63	-36	11	0,81	0,01	0,18
event_12	0,688	1,0	1,4	1,82	-74	11	0,77	0,01	0,22
event_13	0,704	1,0	1,25	1,77	87	10	0,76	0,1	0,14
event_14	0,673	1,0	1,38	1,82	-73	14	0,77	0,02	0,21
event_15	0,692	1,0	1,28	1,67	-62	9	0,79	0,04	0,17
event_16	0,712	1,0	1,2	1,39	65	16	0,86	0,01	0,13
event_17	0,705	1,0	1,32	1,61	73	14	0,82	0,02	0,17
event_18	0,681	1,0	1,33	1,79	84	11	0,77	0,05	0,18
event_19	0,707	1,0	1,29	1,6	-81	10	0,81	0	0,18
event_20	0,671	1,0	1,35	1,65	74	11	0,81	0,02	0,18
Average	0.691	1.0	1.3	1.6	24.4	13.3	0.81	0.04	0.15
STD	0.015	0.0	0.1	0.1	65.0	11.8	0.04	0.03	0.04
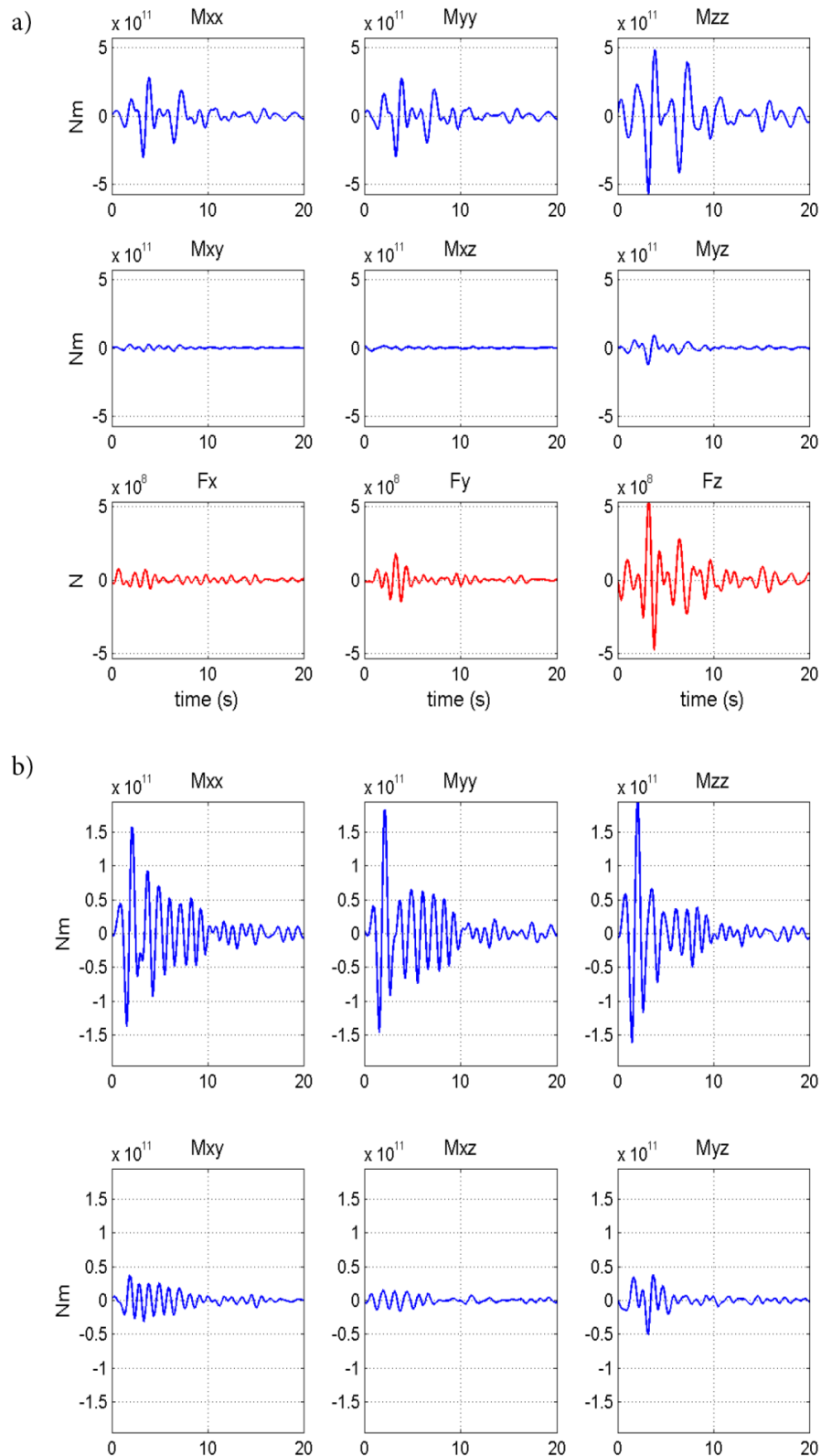
Figure 46 – a) MT inversion solution including forces for event 7 of the monochromatic set of events for the lowest residual source location and 14 stations of the INGV permanent network. b) MT inversion solution excluding forces for the same event.
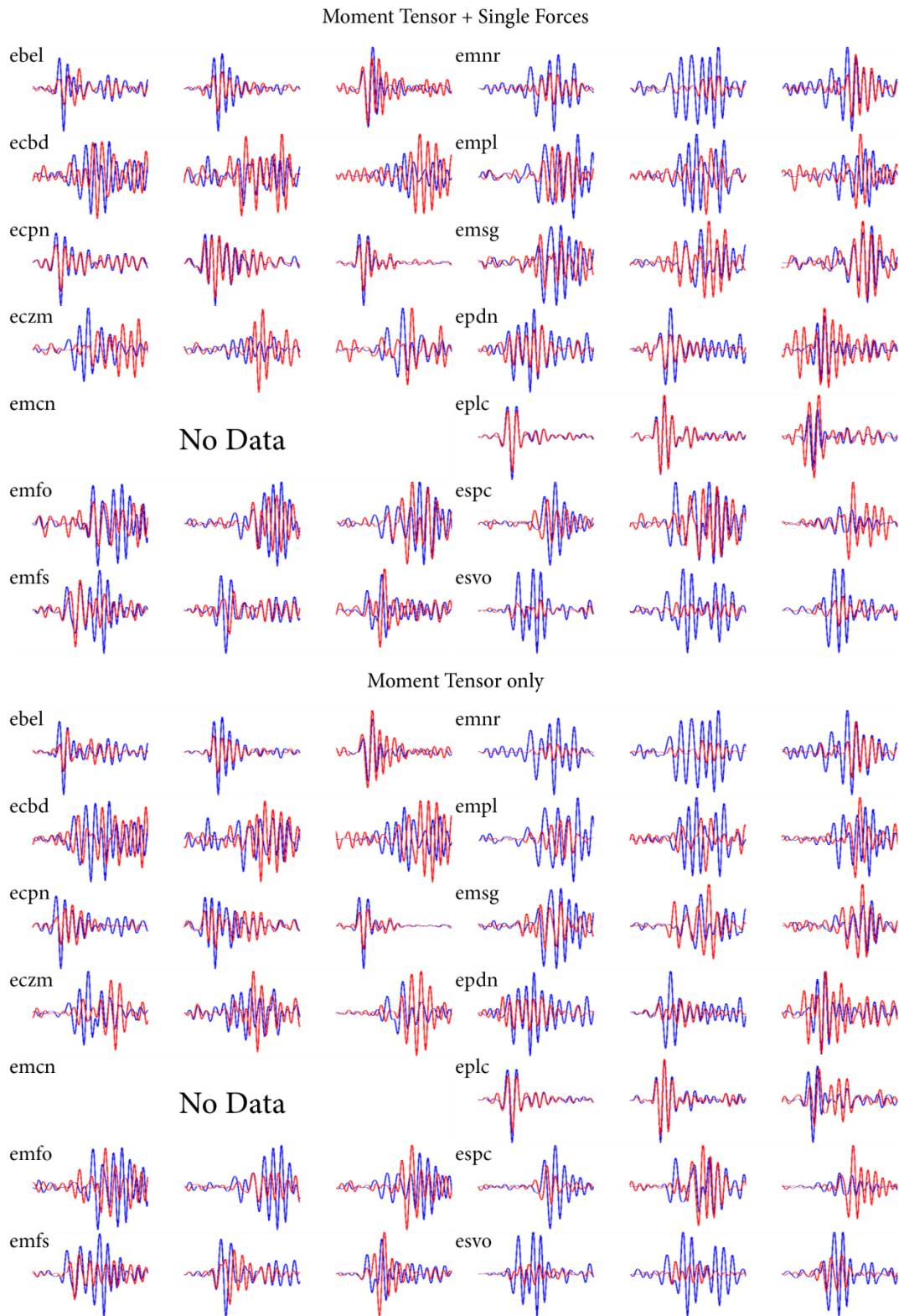
Figure 47 – Comparison between the observed data and the MT solution convolved with the Green's functions for event 7 of the monochromatic set of events. Blue lines correspond to the observed data and red lines to the retrieved solution. Data records for event 7 at emcn station are missing.
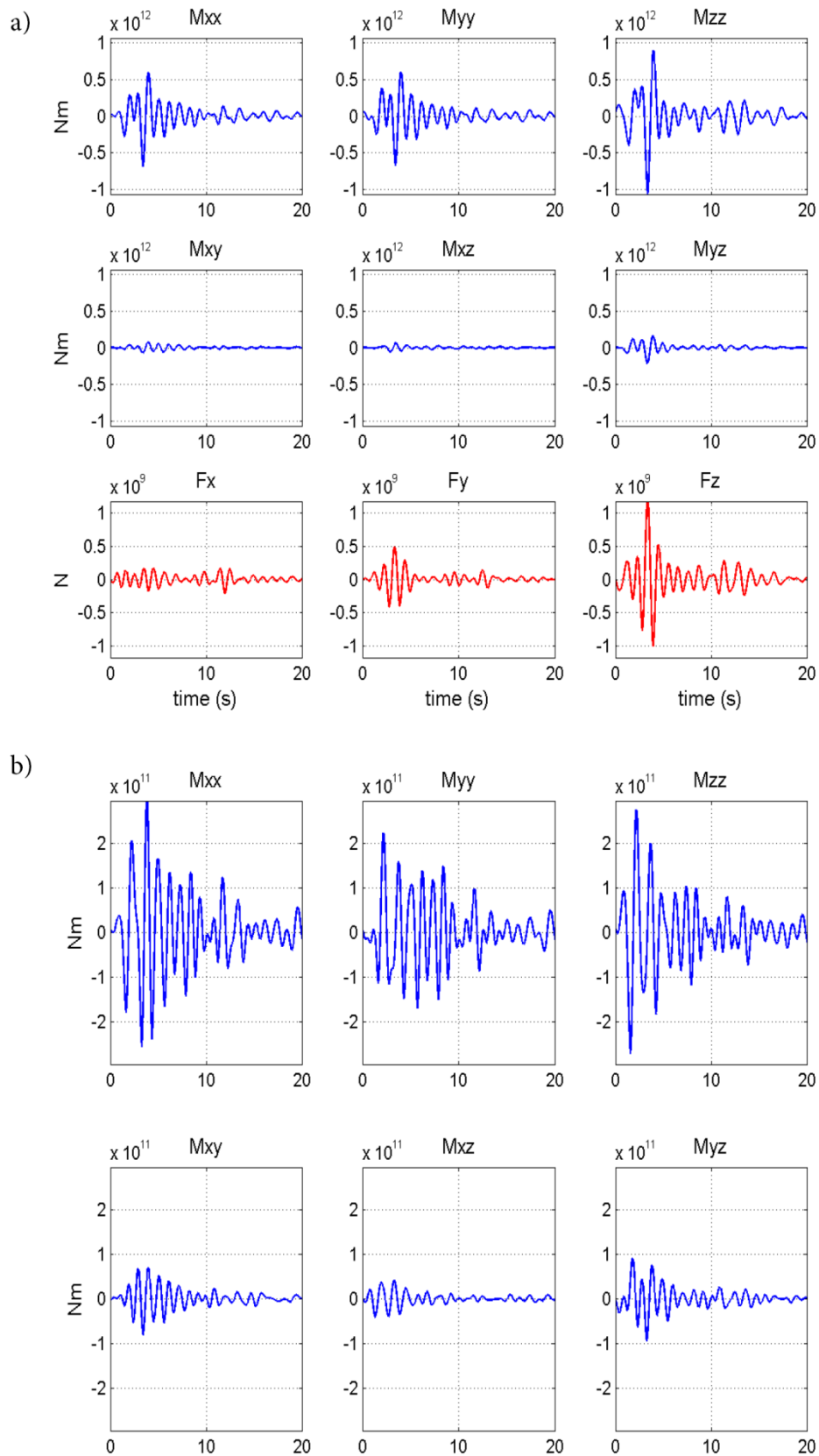
Figure 48 – a) MT inversion solution including forces for event 5 of the monochromatic set of events for the lowest residual source location and 14 stations of the INGV permanent network. b) MT inversion solution excluding forces for the same event.
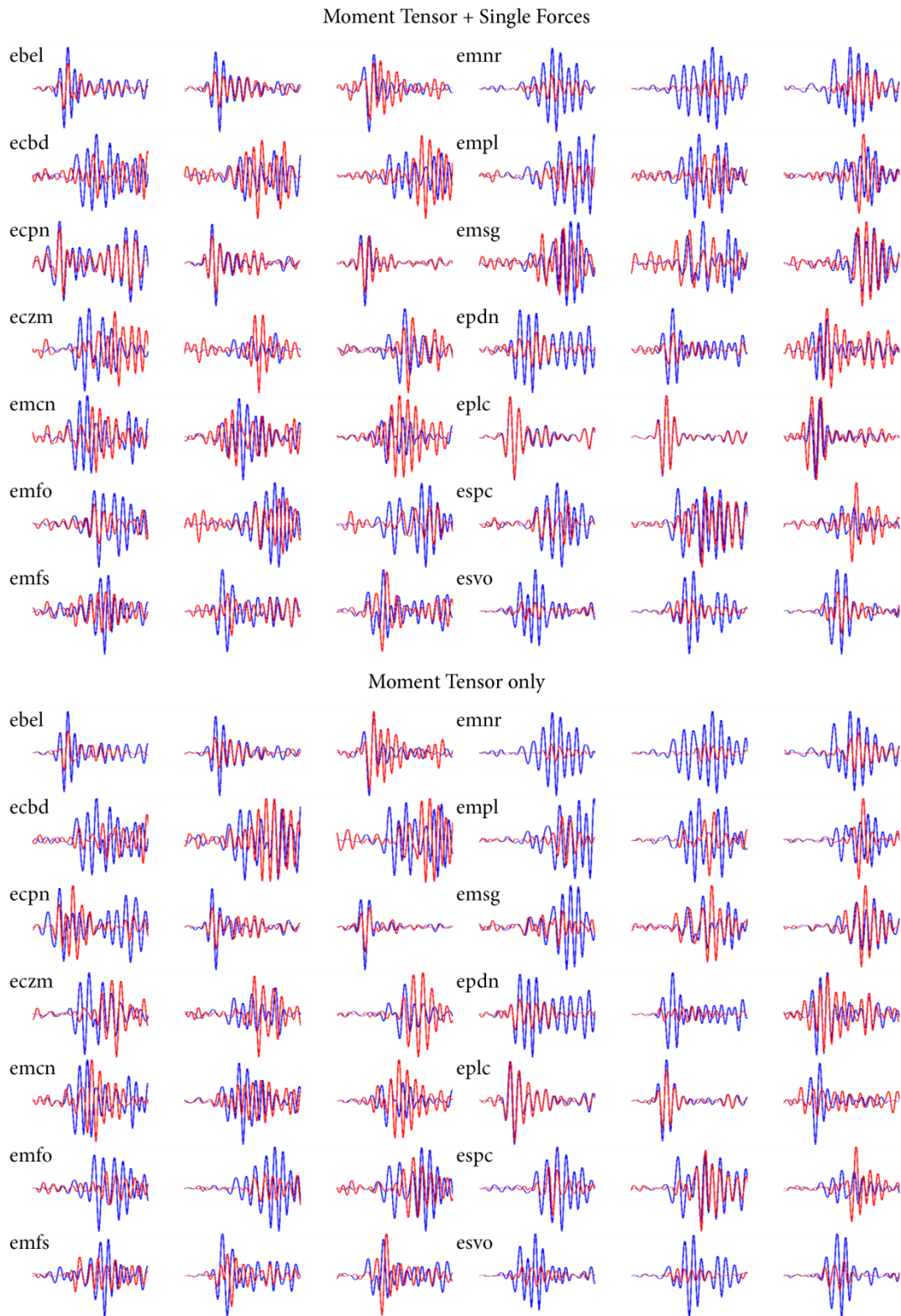
Figure 49 – Comparison between the observed data and the MT solution convolved with the Green's functions for event 5 of the monochromatic set of events. Blue lines correspond to the observed data and red lines to the retrieved solution.
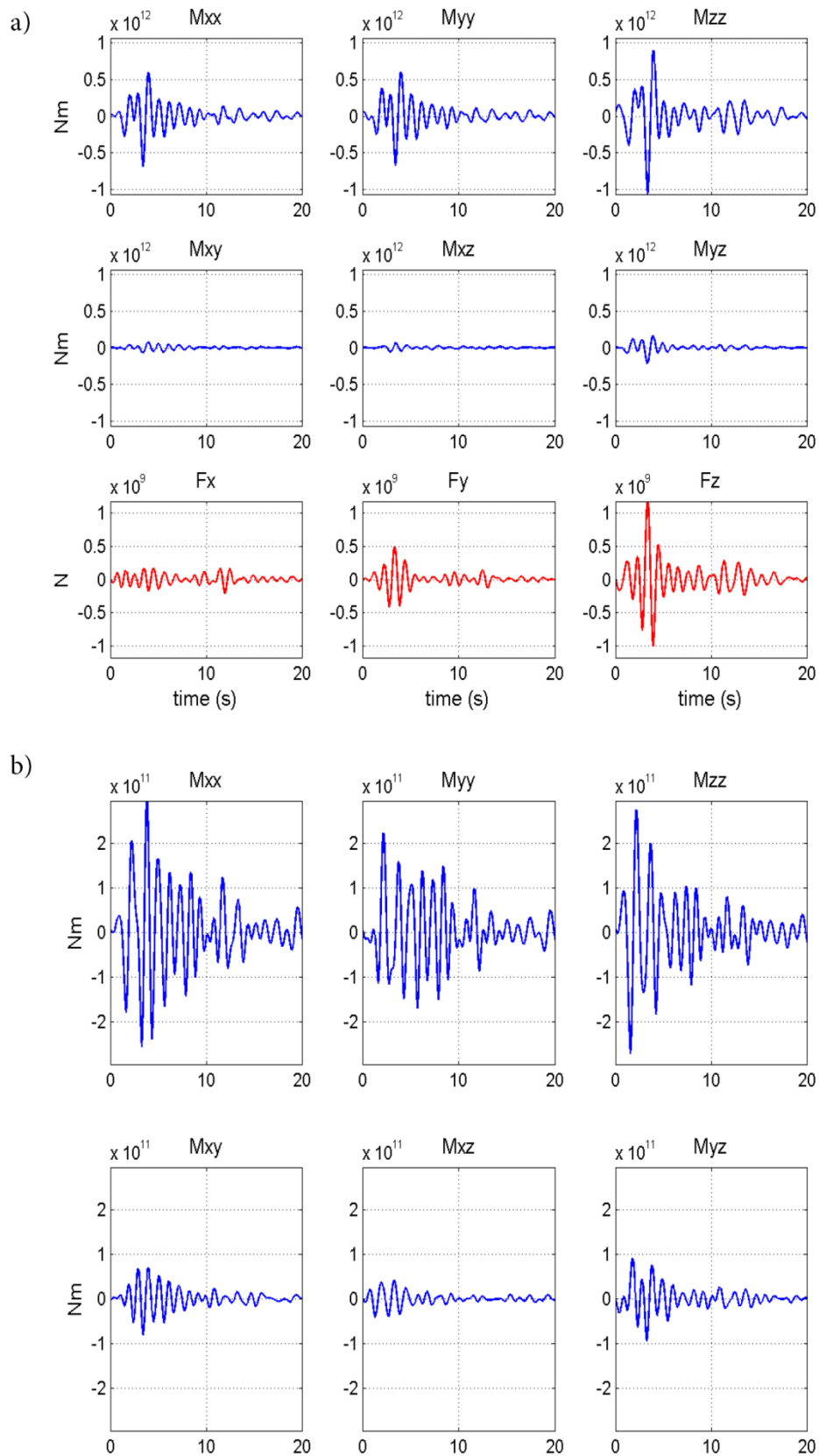
Figure 50 – a) MT inversion solution including forces for event 5 of the monochromatic set of events for the INGV source location and 14 stations of the INGV permanent network. b) MT inversion solution excluding forces for the same event.

Moment Tensor + Single Forces

Moment Tensor only
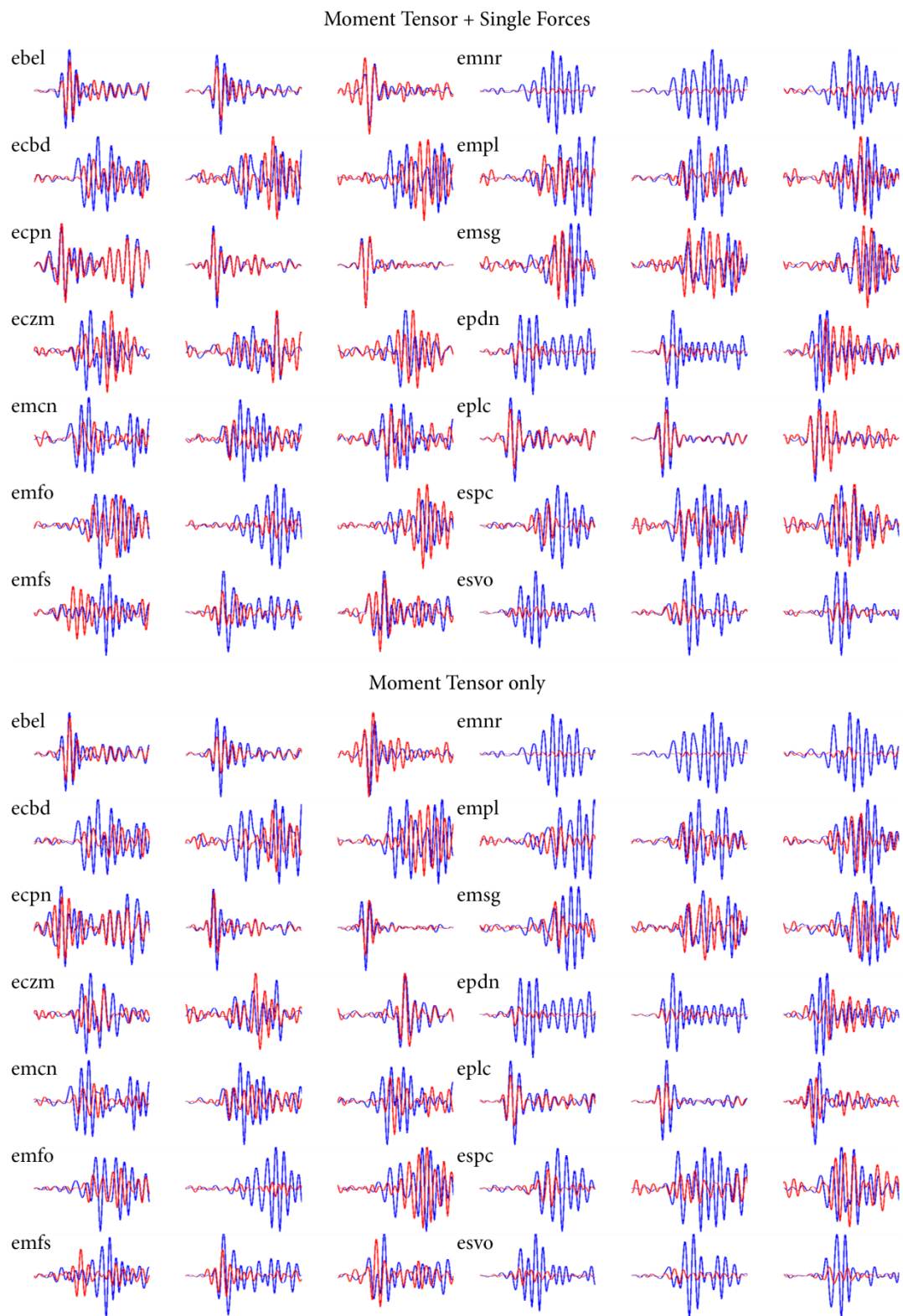
Figure 51 – Comparison between the observed data and the MT solution convolved with the Green's functions for event 5 of the monochromatic set of events and source location found by INGV. Blue lines correspond to the observed data and red lines to the retrieved solution.

Table 12 – Results for the constrained MT inversion for the solution including and without single forces for the monochromatic set of events and lowest residual location. Lowest residual obtained for an isotropic mechanism (Misfit exp) and for a tensile crack mechanism (Misfit crack). I also report the couple of orientation angles for the lowest crack residual.

	M+F				M only			
	Misfit exp	**Misfit crack**	**φ ($\circ$)**	**θ ($\circ$)**	**Misfit exp**	**Misfit crack**	**φ ($\circ$)**	**θ ($\circ$)**
event_01	0.792	0.765	10	40	0.927	0.885	270	80
event_02	0.794	0.768	360	30	0.927	0.887	270	90
event_03	0.811	0.778	180	40	0.935	0.880	270	80
event_04	0.798	0.770	260	80	0.939	0.881	270	80
event_05	0.799	0.775	0	40	0.940	0.885	270	80
event_06	0.798	0.777	0	30	0.936	0.889	270	80
event_07	0.776	0.739	190	40	0.924	0.875	180	30
event_08	0.787	0.755	190	40	0.928	0.887	180	30
event_09	0.800	0.772	0	30	0.924	0.891	270	80
event_10	0.804	0.777	280	70	0.946	0.886	290	80
event_11	0.797	0.769	180	40	0.931	0.880	270	80
event_12	0.807	0.778	0	40	0.916	0.893	300	60
event_13	0.805	0.775	0	30	0.935	0.891	270	80
event_14	0.807	0.783	190	40	0.936	0.906	180	30
event_15	0.809	0.777	270	80	0.941	0.900	180	30
event_16	0.831	0.786	190	40	0.959	0.892	90	90
event_17	0.793	0.768	260	80	0.929	0.880	90	90
event_18	0.802	0.767	0	30	0.930	0.891	270	80
event_19	0.803	0.790	270	80	0.931	0.895	270	80
event_20	0.794	0.754	190	40	0.931	0.889	180	30
Average	0.800	0.771	151	47	0.933	0.888	232	68
STD	0.011	0.012	121	19	0.009	0.007	64	23
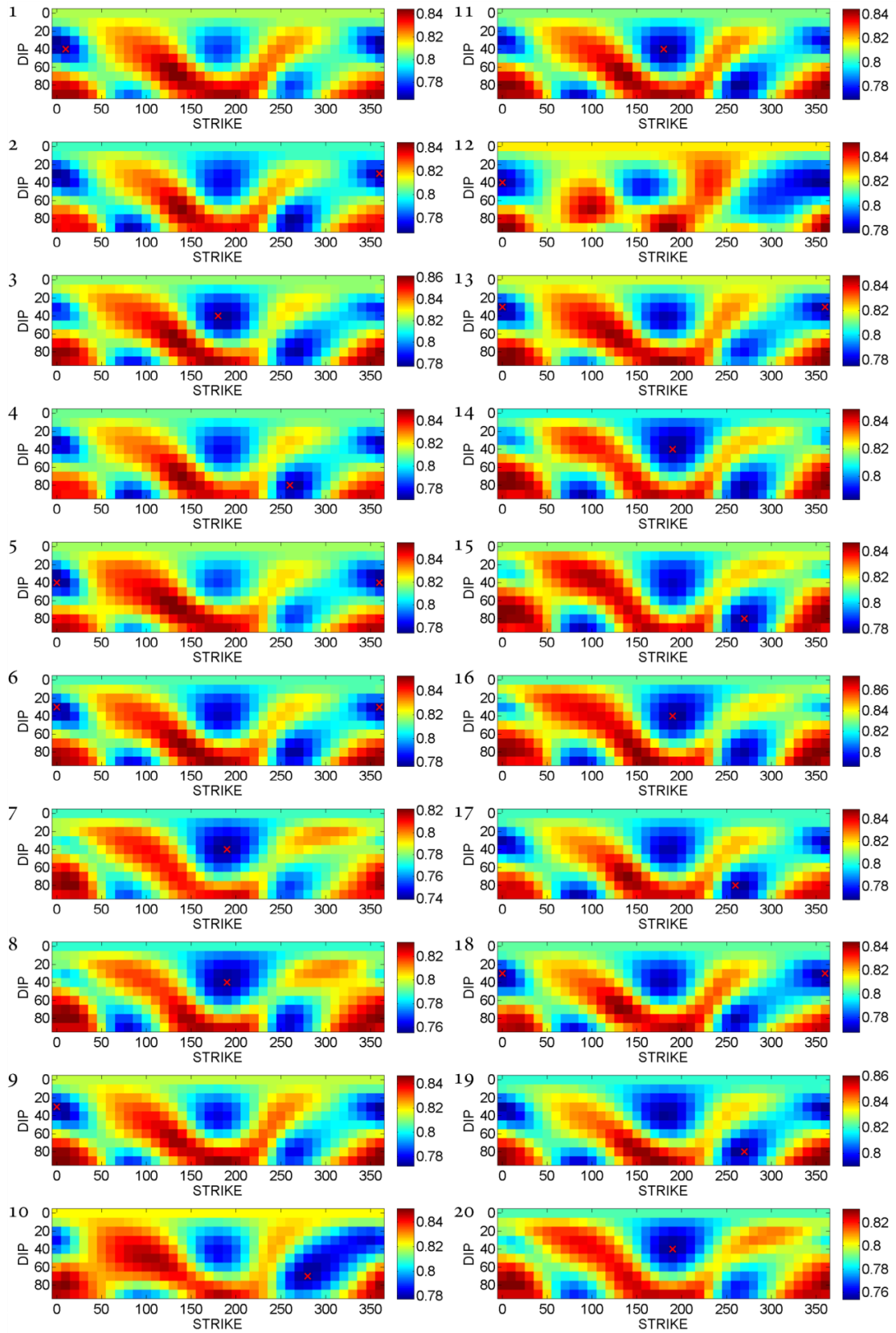
Figure 52 – Constrained inversion residuals plot for the tensile crack solution for the solution including single forces for the monochromatic set of events. Event number is reported on the top left of each contour plot, misfit range legend on the right side. Red cross indicates the lowest retrieved minima misfit.
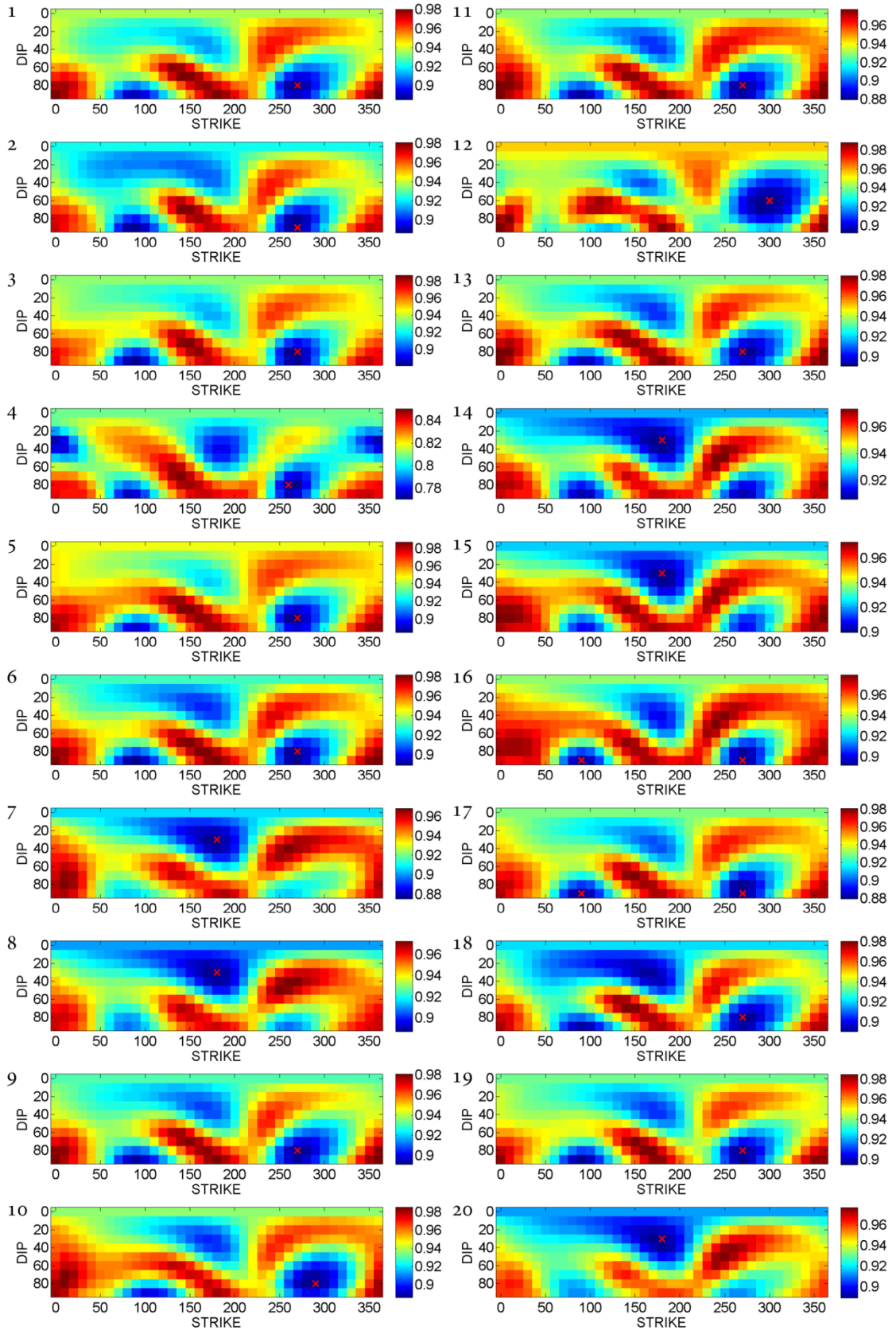
Figure 53 – Constrained inversion residuals plot for the tensile crack solution for the solution without single forces for the monochromatic set of events. Event number is reported on the top left of each contour plot, misfit range legend on the right side. Red cross indicates the lowest retrieved minima misfit.

discharged as a possible solution.

Hence, I perform a constrained inversion for all the set of events for the original lowest residual locations (solution *A*). The procedure is described in detail in chapter 2, section 2.3. During the inversion the mechanism is constrained to (1) an isotropic source and (2) a tensile crack with a grid search for the best possible set of angles orientations (azimuth and dip). Results for both solutions with and without single forces are reported in Table 12. Results for best tensile crack orientation angles for the solution including and without forces are reported in Figure 52 and Figure 53 respectively.

The misfit values for the explosion mechanism are slightly higher (average M+F residual = 0.8) than those found for the crack solution (average M+F residual 0.77) for both the inversions including and without single forces (Table 12). If I focus on the orientation angles for the crack solution the results are way more dispersed than the solution obtained after eigenvalues decomposition (Table 9 and Table 10) with values spanning the whole space of possible solutions for azimuth orientation (φ = 0-360°) and giving sub-horizontal to sub-vertical crack dips. This seems strange, but when the solutions are analyzed more thoroughly the reason becomes clear. The plots with the misfit values for all the crack angle sets considered (Figure 52 and Figure 53) show at least two main minima residual possible solutions. For both the solutions with and without single forces at least two main minima residuals can be found for a sub-horizontal crack and a sub-vertical one oriented ~80°/260° azimuthally. Thus the lowest misfits fall in either the sub-horizontal or the sub-vertical crack for each considered event. The results for the constrained inversion are coherent with the eigenvalues decomposition and explain the opposite mechanisms found for the solutions with and without forces. The high C_{ISO} component found for both the solutions (M+F and MT-only) and the mislocated source highlight the possibility that the source mechanism could be considered as an explosion, this is also confirmed by the small difference between the residuals for the constrained crack/explosion. Anyway, as stated before, the C_{DC} components are high and comparable to the CLVD components, thus a double couple component in the source mechanism cannot be discharged. In order to study deeply this aspect I develop the PCA (principal component analysis, Vavryčuk, 2001, 2015) and I try to find out the real contribution from the shear source. As I tend to the solution including forces the following analyses are

developed on this solution (Table 9).

Here I want to check the possibility that the observed events can be thought as tensile earthquakes (an earthquake with tensile faulting or combining shear faulting and tensile faulting, e.g. Eyre et al., 2015). A tensile earthquake can be described using a slip vector (labeled $[\vec{u}]$) that is not restricted to orient within the fault plane (Σ) thus causing its opening or closing. The angle α (Equation (64)) represents the depart of the slip vector from the fault surface (Figure 18), β (Equation (65)) represents the angle between the normal to the fault and the tension ($\vec{T}$) axis and δ (Equation (66)) represents the orientation of the fault plane from the vertical. From the C_{ISO}/C_{CLVD} ratio I can compute parameter κ (Equation (67)) which represents the λ/μ ratio of the medium surrounding the source region. In order to compute a unique value of κ I use the average values obtained from the PCA. The average values (Table 9) for the whole set of events are: C_{ISO} = 69%, C_{CLVD} = 18% and C_{DC} = 13% giving a κ of 4.25. The standard deviation for the isotropic, CLVD and DC components are low (5%, 8% and 4% respectively), thus validating the choice for the computation of κ on the average value. Following Vavryčuk, (2001), for a given κ the proportion of isotropic, CLVD and double couple versus the angle α can be plotted as shown in Figure 54. The lower the value of α, the higher is the shear faulting contribution to the solution as the slip vector is almost parallel to the fault plane. The average values for the mixed ISO/DC mechanism are: α = 54°, β = 72° and δ = -52°. The retrieved value of α is quite surprising as it suggests a real mixed isotropic/double-couple mechanism in contrast with the low computed values of C_{DC}. It is worth nothing that some events (*events 7, 8, 14, 15 and 16*) show a value of α ~90°, i.e. a pure tensile mechanism. If these events are not taken in account in the computation of the average value of α, it becomes α ~40°. However, as the principal models of LP source mechanisms attribute them to fuids/gas oscillation processes, the double-couple components are often interpreted as insignificant or explained as errors resulting from the calculation of the Green's functions (Eyre et al., 2015). In such case it would be possible to interpret the source mechanism of the analyzed events as a tensile crack, but it would be difficult to justify the CLVD component while ignoring the double-couple. Moreover, the pulse-like nature of the waveforms recorded at the summit stations (Figure 41) is difficult to reconcile with the classical models for LP generation.
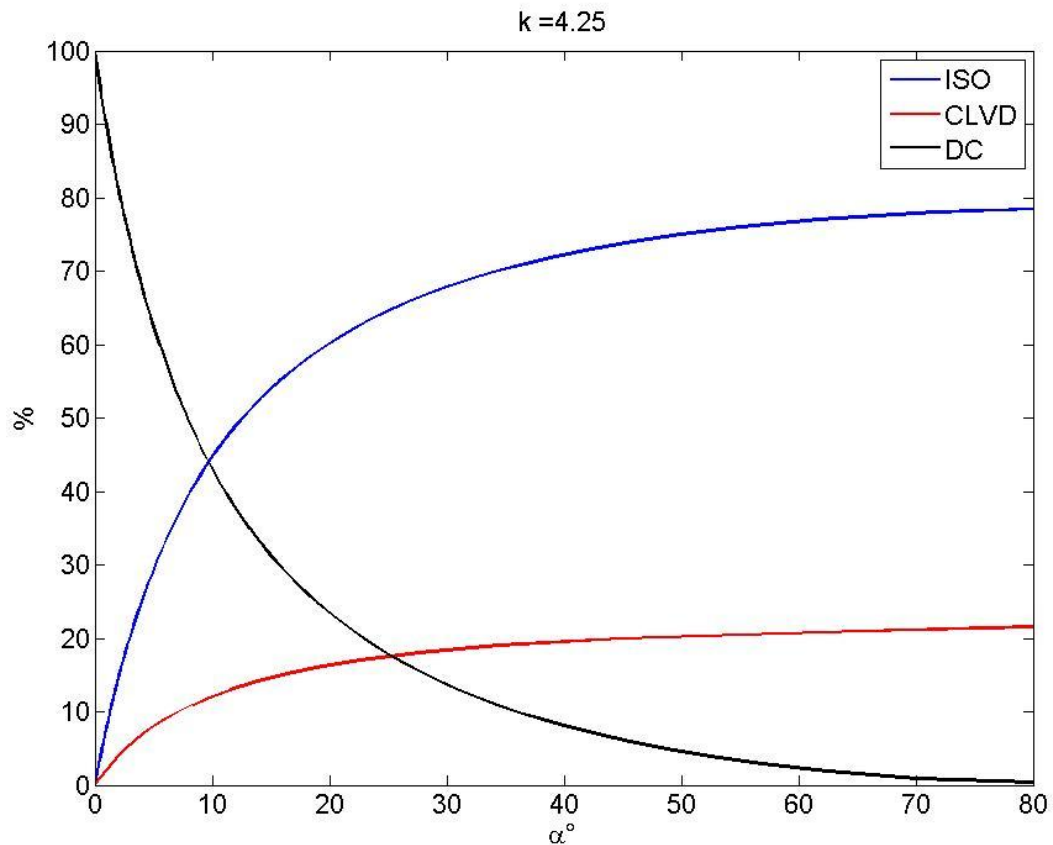
Figure 54 – Relationship between α and the double-couple (DC), isotropic (ISO) and CLVD components for the source mechanism of events with k=4.25 using the relationship of Vavryčuk, (2001).

5.3.4 Interpretation of the source mechanism

The best-fit mechanism for the LP events is obtained towards the MT inversion including forces for the lowest residual location. The solutions point to a crack mechanism shallowly dipping towards north at approximately 20°. A crack mechanism has been inferred at many volcanoes as the possible source process for the generation of LP signals (e.g. De Barros et al., 2011; Chouet, 1996; Eyre et al., 2013; Kumagai et al., 2005; Lokmer et al., 2007). The most widely source model used to interpret such signals attributes them to the resonance of a fluid filled cavity (Chouet, 1988). For the analyzed events the oscillations of the source are not clearly observable. The solution including forces shows rather a pulse like source mechanism than oscillations at the source (Figure

178

48). The short duration of the LP perturbation in the source time functions (~5 s) is coherent with the analysis performed by Lokmer et al., (2007) who identified gas "pulsing" as a possible trigger mechanism for the LP events recorded on Mt. Etna during 2004. Shallowly dipping cracks were identified as the cause of LP events at Kilauea, Hawaii (Kumagai et al., 2005) and Kusatsu-Shirane volcano, Japan (Kumagai, 2002a). Both authors hypothesized that the LP events source mechanism was mainly related to hydrothermal fluids rather than of magmatic origin, but their model implied the resonance of the crack structure triggered by rapid release of pressurized fluids. A compatible model with the pulse like nature of the analyzed LP events has been proposed by Eyre et al., (2013) on Turrialba volcano, Costa Rica. They identified in hydrofracturing the possible origin of the pulse like source mechanism. In their model uprising gas would infiltrate in *quasi*-horizontal fractures located around the main conduit. Due to the weakness of the staked up materials the fractures would propagate with shallow dip angles. LPs observed during hydrofracturing of shale gas reservoirs show similar features and are believed to be caused by slow slip induced by the high pore fluid pressure (Das and Zoback, 2011). Moreover, Benson et al., (2008), through laboratory experiments on Etna basalts, found that LP events can be generated by a combined result of fluid interactions within both the damage zone and the conduit, thus highlighting that a weak component of shear faulting would be in agreement with the source model for LPs.

The hydrofracturing model (Figure 55) would be coherent with the important double-couple component found for the analyzed events. The similarity obtained between all events suggests that a non-destructive source is repeatedly excited. The slightly variability in the source position could be referred to fractures developed around the main conduit, but close to each other. For supporting such a model a source of heating and an important gas uprising is required to explain the LP events generation. In the days preceding and during the recorded events a lava flow was draining the east flank of the volcano at a depth comparable to the locations of the LP events (~2500 m.a.s.l.). On the opposite, the horizontal location of the events is not coherent with the lava flow and is located ~2 km far from the eruptive fissure below the summit craters. The location found by INGV points to a position located slightly south, but at comparable distance from the

active eruptive fissure. Hence, the LP signals should not be directly related to the magmatic activity. At the same time important degassing was recorded at the summit craters suggesting that the magmatic body was drained by the lateral fissure while gas was mainly present in the central conduits uprising towards the surface. The period preceding the opening of the lava flow fissure (until June 2008) could be associated to high fluid pressures destabilizing the edifice. This recharging period could have entrained the reactivation of fractures in the upper part of the volcano. Once the lava flow took place the cone could have been drained producing a decrease of pressure (De Barros et al., 2011) which could have led to instabilities of those fractures and triggered the LP events by uprising gas. This hypothesis is coherent with the state of the activity of the volcano which was in the ultimate phase of the eruption which began in summer 2008 and ended just one month later the recorded events (July 2009).

I compute the volume of fluid/gas involved in the source process by means of both Equations (70) and (71) as discussed in section (2.4). Thus the M_0 value considered for the computation corresponds to the maximal peak to through amplitude of the retrieved source time functions for the lowest residual constrained crack solution. I take the peak to through maximum amplitude as I expect that the total displaced fluid/gas volume corresponds to the whole deflation/inflation process occurring at the source. The Lame's parameters are computed for the *Vp, Vs* and density of the velocity model *S4* (chapter 4) for the location depth of the targeted event retrieved towards MT inversion. Although the rigidity of the medium can differ considerably from the velocity of the source region (Lokmer et al., 2007), I use the values from model *S4* as it is the best approximation of the geological properties of the volcano at depth in my possession. Averaging the resulting volume variations for the whole set of events I obtain a $\Delta V = 386 - 695$ m^3 for the solution including forces. These values are higher than those found by Lokmer et al., (2007), $\Delta V = 50$ m^3 and De Barros et al., (2011), $\Delta V = 15$ m^3 for Mt. Etna volcano, but comparable to the results obtained by Jousset et al., (2013), $\Delta V = 220 - 2250$ m^3 for some VLP events recorded during the 2013 eruption of Merapi volcano, Indonesia and $\Delta V = 3000$ m^3 for VLP events recorded at Kilauea, Hawaai (Ohminato et al., 1998). The VLP events were thought to be connected to magmatic injection (Jousset et al., 2013; Ohminato et al., 1998), but
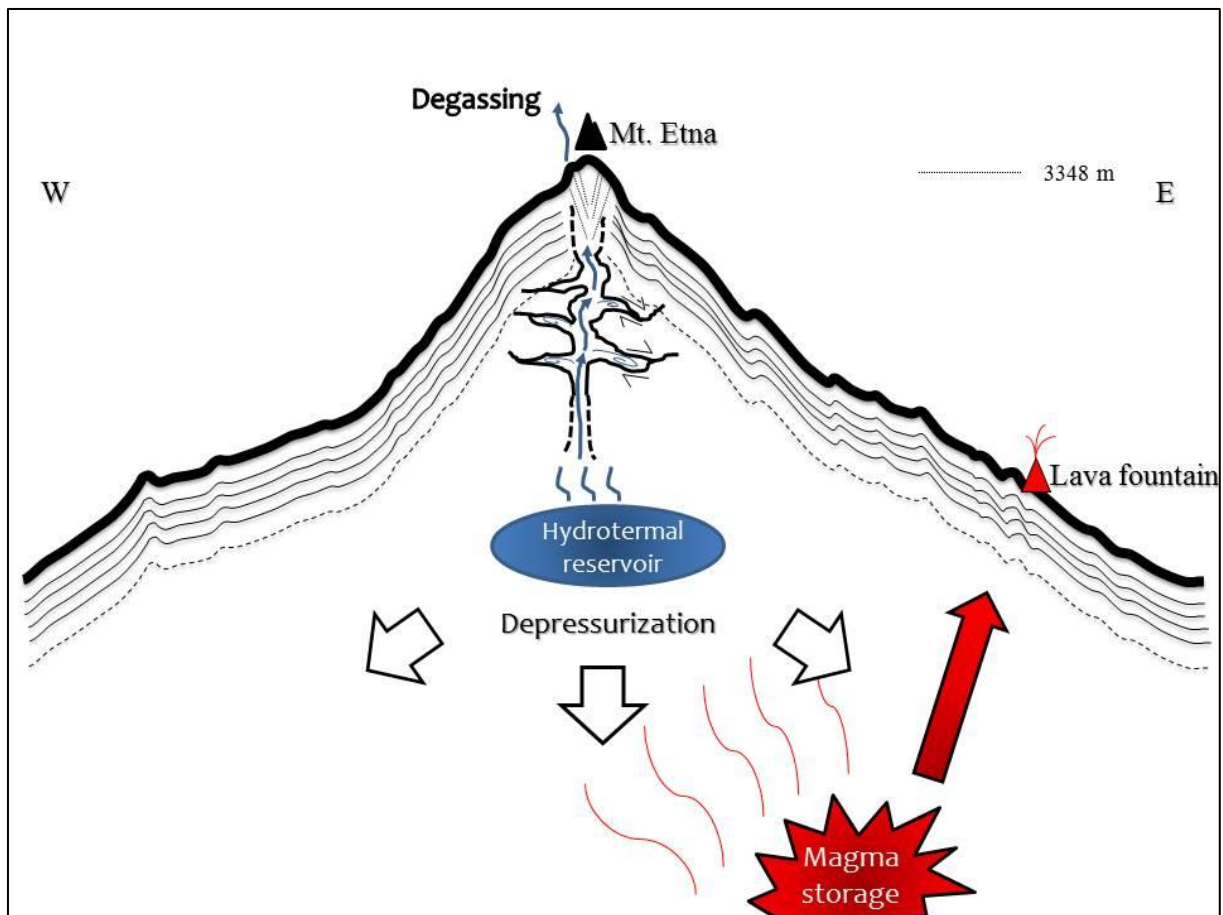
Figure 55 – Sketch of the possible source model for the monochromatic set of events at Mt. Etna volcano. Hot, high pressure hydrothermal fluids within the hydrothermal system cause hydrofracture generating LP events. Hydrofracture can generate both tensile and shear mechanism and could take place in the unconsolidated shallow materials. Note that the sketch is very speculative as the structures of the hydrothermal system and the magma storage are unknown. The figure is not drawn to scale.

for the particular context in which the LPs were recorded on Mt. Etna, gas is the most probable involved phase. The retrieved volume variations correspond to a normal displacement of 4 – 7 cm for a 100 m sided square crack which seems to be a quite large value for supporting the hydrofracturing model. As stated in the previous chapter, the volume variation could be overestimated due to errors in the velocity model used for the MT inversion. In order to further investigate the reliability of such volume variations I should compare the results with the recorded gas emissions at the surface. Such computation would be feasible, but it lacks precise values of gas emissions/composition, temperature and a reliable model for lithostatic pressure. Hence, further considerations on the relationship between the volume variation of the LP events and the volcanic activity remain difficult.

The pulse-like nature of the recorded LP events and the important volume variation computed at the source are difficult to interpret with the resonant crack model (Chouet, 1986). On the other hand, the high double-couple component of the analyzed events would be more coherent with the recent model of Bean et al., (2014) involving a mechanical failure mechanism of the shallow volcanic edifice. Small-scale deformations of the upper part of the volcanic edifice due to the drainage of the eruptive fissure would be coherent with the hydrofracturing model and a mixed shear-tensile source mechanism could better explain the computed volume and the crack dimensions. Cauchie et al., (2015) suggested the brittle failure model as a possible explication for some LP events recorded on Mt. Etna in 2005. Moreover, Eyre et al., (2015) studied the relationship between magnitude and corner frequency of LP events recorded at Turrialba, Costarica and found that pulse-like LP events behaved as conventional earthquakes. Further work is necessary to explore the brittle failure nature of LP event generation.

5.4 Polychromatic LPs (October 2010)

The second set of signals analyzed in this work occurred at the beginning of October 2010. From the end of the 2008-2009 flank eruption until the first months of 2010 Mt. Etna was relatively quiescent (Cannata et al., 2015). The volcanic activity resumed in March with high-temperature degassing at the SEC (Andronico et al., 2013). Several short-lasting episodes of ash emissions followed at the summit craters (mainly BN and secondarily SEC) during the rest of 2010. The volcanic tremor recorded continuously on the volcano showed an increase in the root mean square (RMS) amplitude at the end of August. The tremor location during this period of activity was mainly restrained to a small volume of 1km^3 centered around 1500 m.a.s.l. below the east rim of the NEC (Andronico et al., 2013; INGV internal reports). An increasing in intensity and frequency of the explosive activity and a shallower tremor location were observed since November 2010. This explosive activity phase terminated on the 12th of January 2011 with the onset of a new lava fountain from the SEC (Patanè et al., 2013). Around 35 explosive events of moderate intensity were recorded at the summit craters during the whole year. Only three events showed significantly higher intensity. Despite the normal activity of Mt. Etna, this period showed a high frequency occurrence of explosive events. The set of data analyzed was recorded at the beginning of October, before the increase in the explosive activity observed in November. The week preceding the recorded events (1th and 2nd October 2010), the degassing was moderate at the summit craters (NEC and BN) without any particular intense explosive evidence. On 2nd of October the degassing showed an increasing in intensity, but still without any evidence of explosive activity (INGV internal reports).

5.4.1 Data

The set of data analyzed in this study spans 20 hours on the 1th and 2nd of October 2010. During this period 20 mixed events (events showing wide frequency content) were recorded by the permanent network of stations of the INGV. These events are characterized by a more impulsive onset, higher amplitude (10^{-4} m/s) and longer coda than the set of events analyzed in the previous section. The events are band pass filtered

between 0.2 and 4 Hz and stacked following their onset. The results are plotted in Figure 56. The events show a quite high complexity and it is difficult to state if a certain degree of similarity between the waveforms and the length of the signals exists. The high frequency content prevents from making further considerations, hence I plot the same signals, but band pass filtered in a narrow frequency band (0.3 – 1.3 Hz, Figure 57). Apart for some events with low amplitude a certain similarity between the waveforms can now be recognized. The events look similar especially in length with the coda showing roughly the same amplitude as the first part of the signal. It seems that a repetition of the same source mechanism occurs twice inside the same record. I analyze in detail the shape and the frequency content for *event 12* recorded at station *ecpn* (Figure 58*)* and farther station *emcn* (Figure 59*)*. *Ecpn* station shows a high polychromatic frequency content. Several peaks in the power spectrum can be recognized with high energy content until ~5 Hz and a very long (more than 10 s) slowly decaying coda. The same event plotted for *emcn* station shows different features. The frequency content is lower than for station *ecpn* and only one major peak in the power spectrum can be recognized around 1 Hz. The length of the signal is considerably longer, as expected. In order to check the different frequency content between the two stations, I compare the same plots, but for *event 9*. The results are shown in Figure 60 and Figure 61 for stations *ecpn* and *emcn* respectively. The comparison shows results coherent with the previous event. Hence, it appears that the high frequency component strongly attenuates far from the source. In order to investigate signals with such wide frequency content, I would need a better network resolution and Green's function definition because high frequency signals are more sensitive to structure inhomogeneity. As high frequencies strongly attenuate far from the summit craters I suppose that I can focus my attention on the low frequency part of the signals (0.3 – 1.3 Hz) following the fact that the waveforms show good similarity and comparable lengths at all stations in this frequency range.
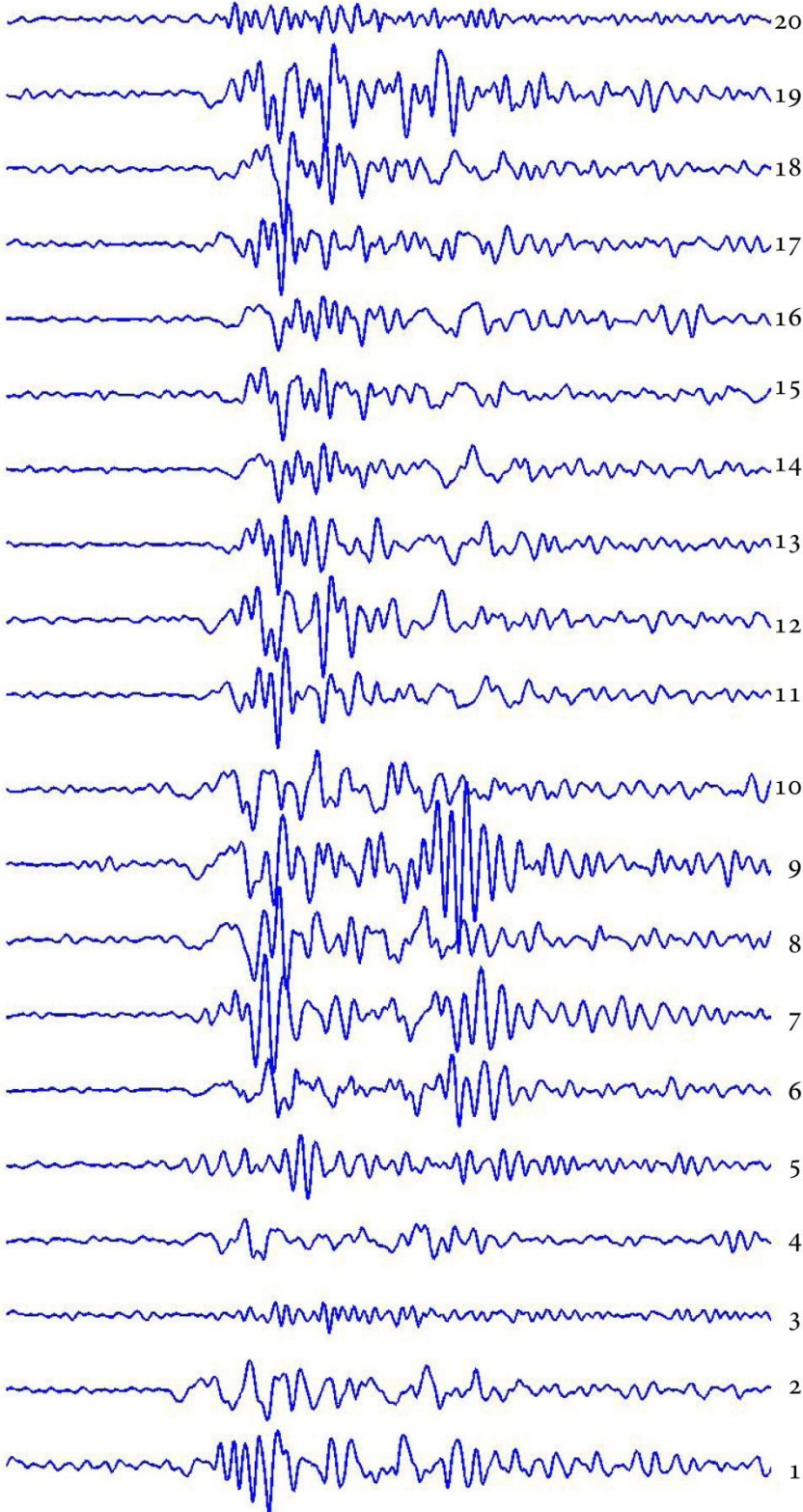
Figure 56 – Stack of velocity filtered (betwenn 0.2 and 4 Hz) seismograms for ecpn station vertical component. The high frequencies make difficult to identify very similar events even if a certain degree of similarity between certain events is still recognizable. The event number is reported on the right.
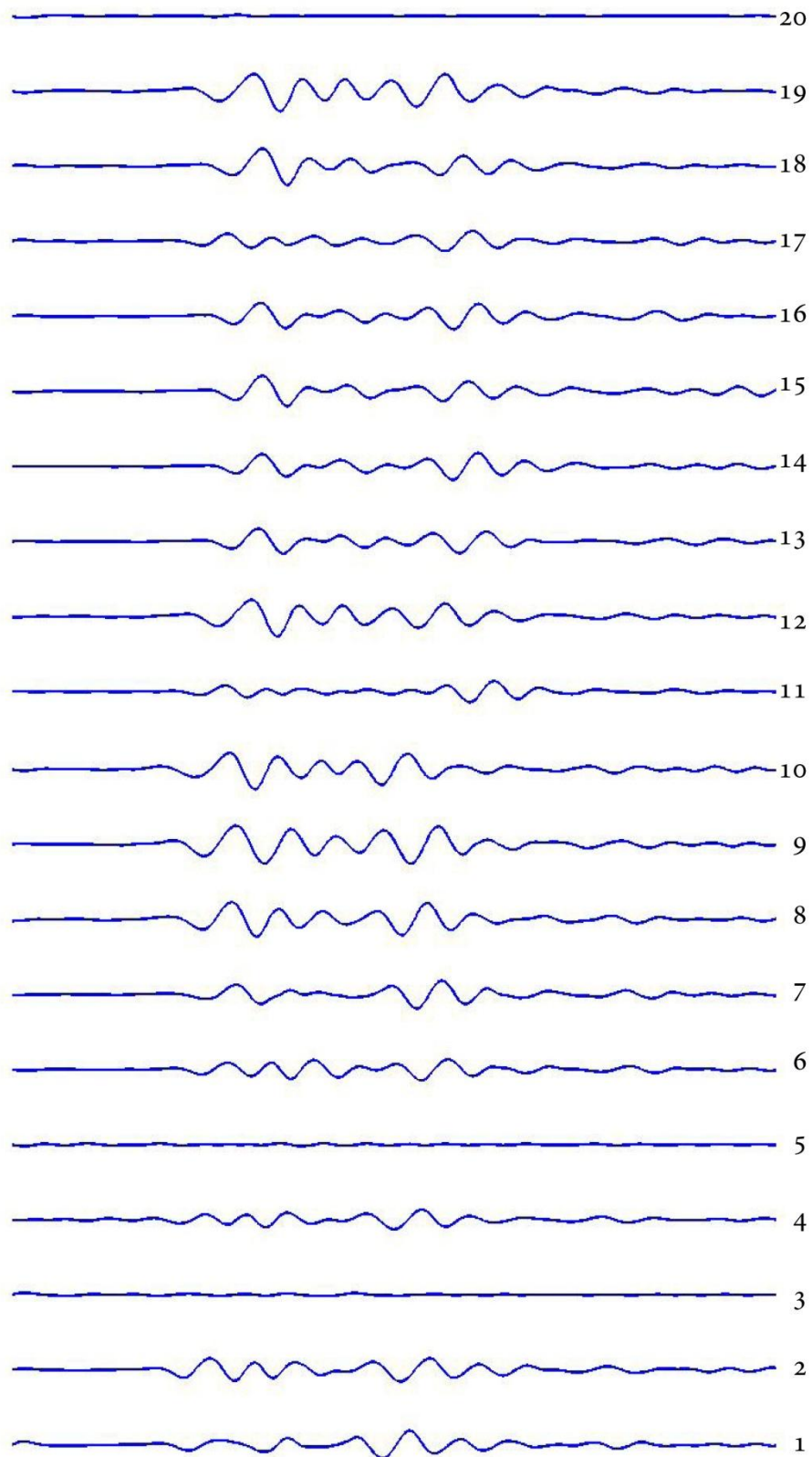
Figure 57 – Stack of velocity filtered (betwenn 0.3 and 1.3 Hz) seismograms for ecpn station vertical component. A certain degree of similarity between the recorded waveforms is recognizable. The signals are longer than the previous set of events analyzed. Some events show low amplitude and a low signal to noise ratio. The event number is reported on the right.
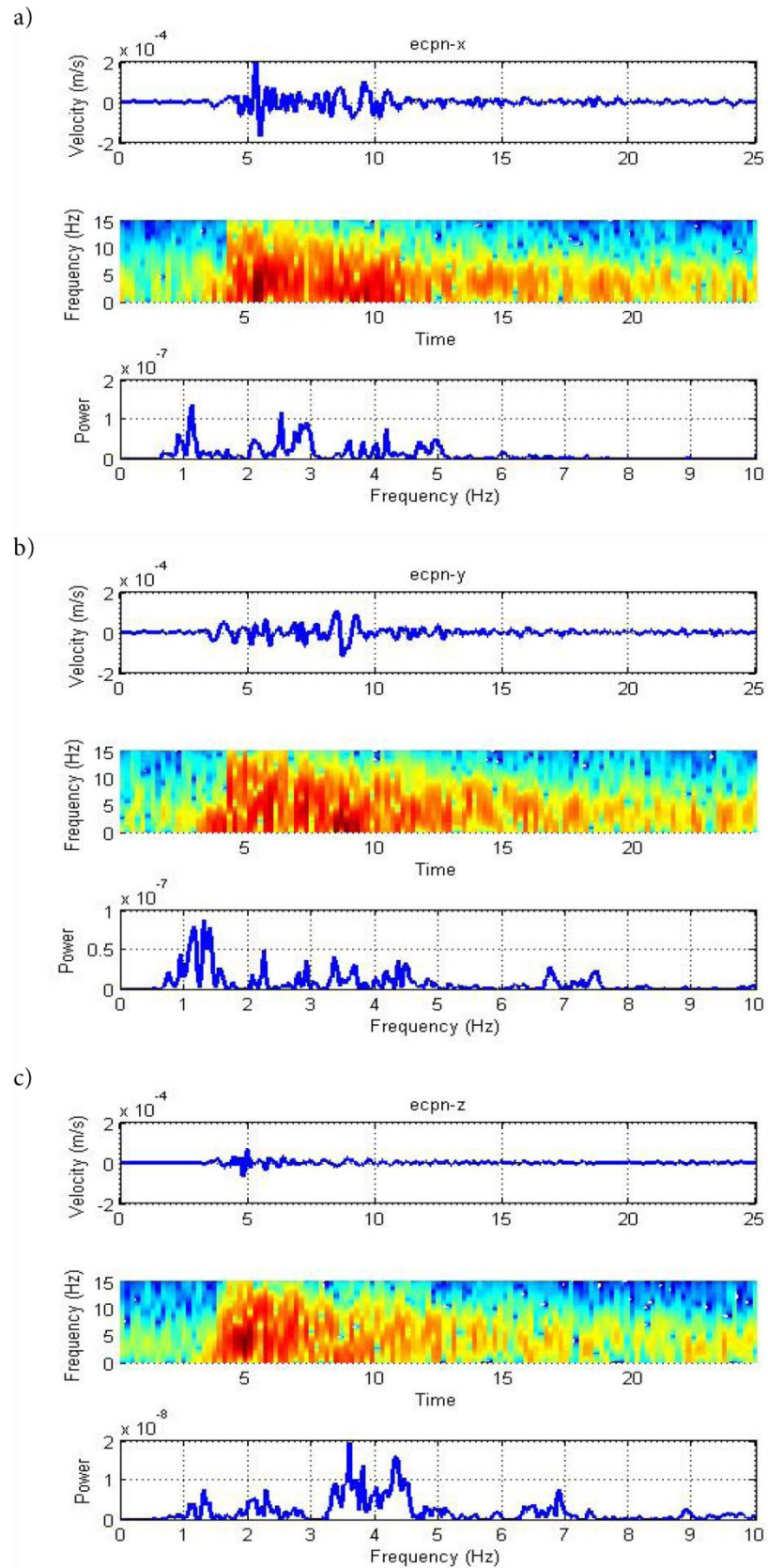
Figure 58 - a) top: x-component of velocity recorded at station ecpn for event 12. The seismic trace is filtered between 0.2 and 4 Hz; middle: short time Fourier transform plot of the unfiltered velocity trace, red correspond to high power towards blue lower; bottom: power spectral density of the unfiltered velocity trace. b) and c) same as a), for –y and –z components respectively.
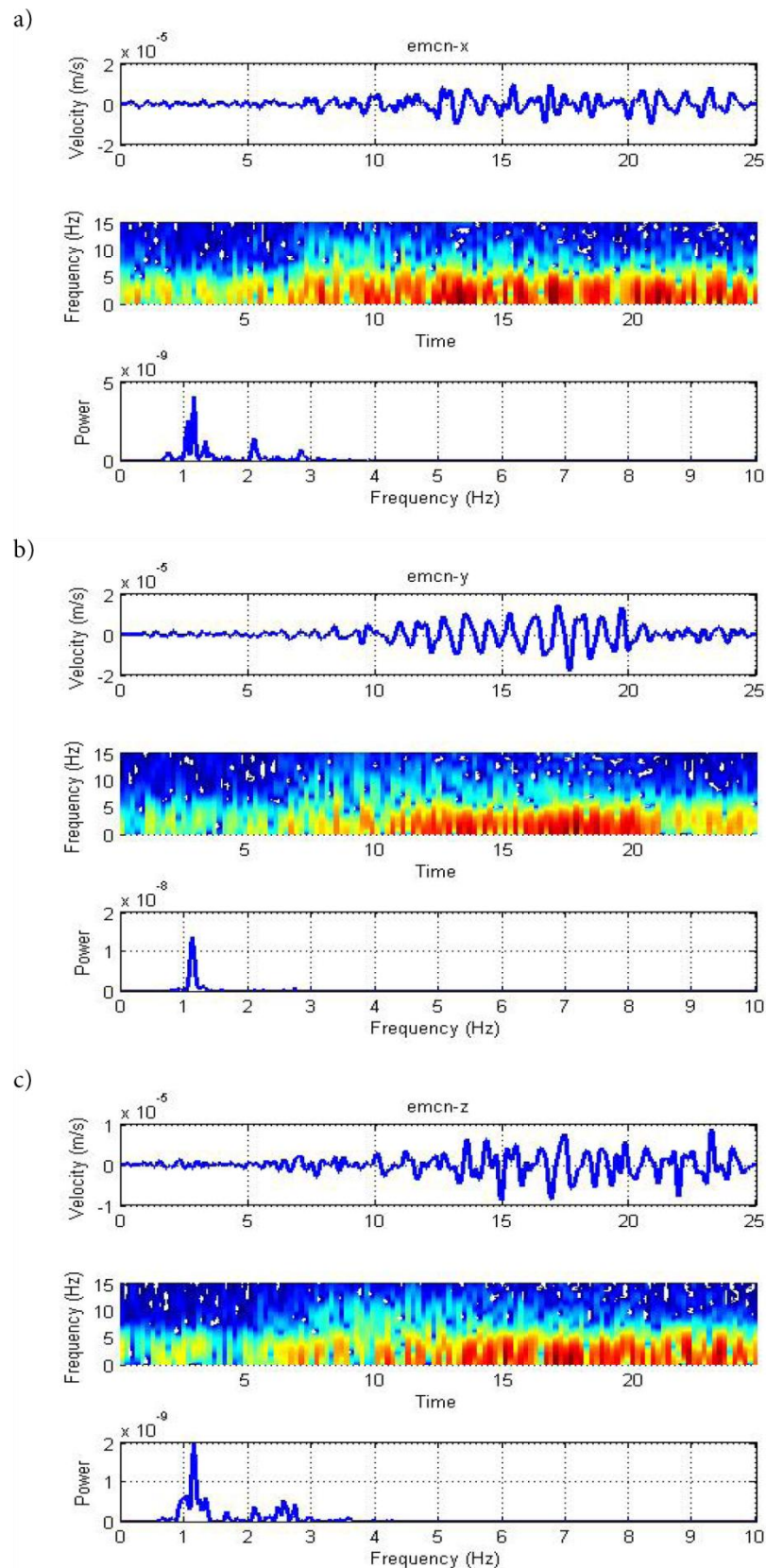
Figure 59 - a) top: x-component of velocity recorded at station emcn for event 12. The seismic trace is filtered between 0.2 and 4 Hz; middle: short time Fourier transform plot of the unfiltered velocity trace, red correspond to high power towards blue lower; bottom: power spectral density of the unfiltered velocity trace. b) and c) same as a), for –y and –z components respectively.

a)

b)

c)
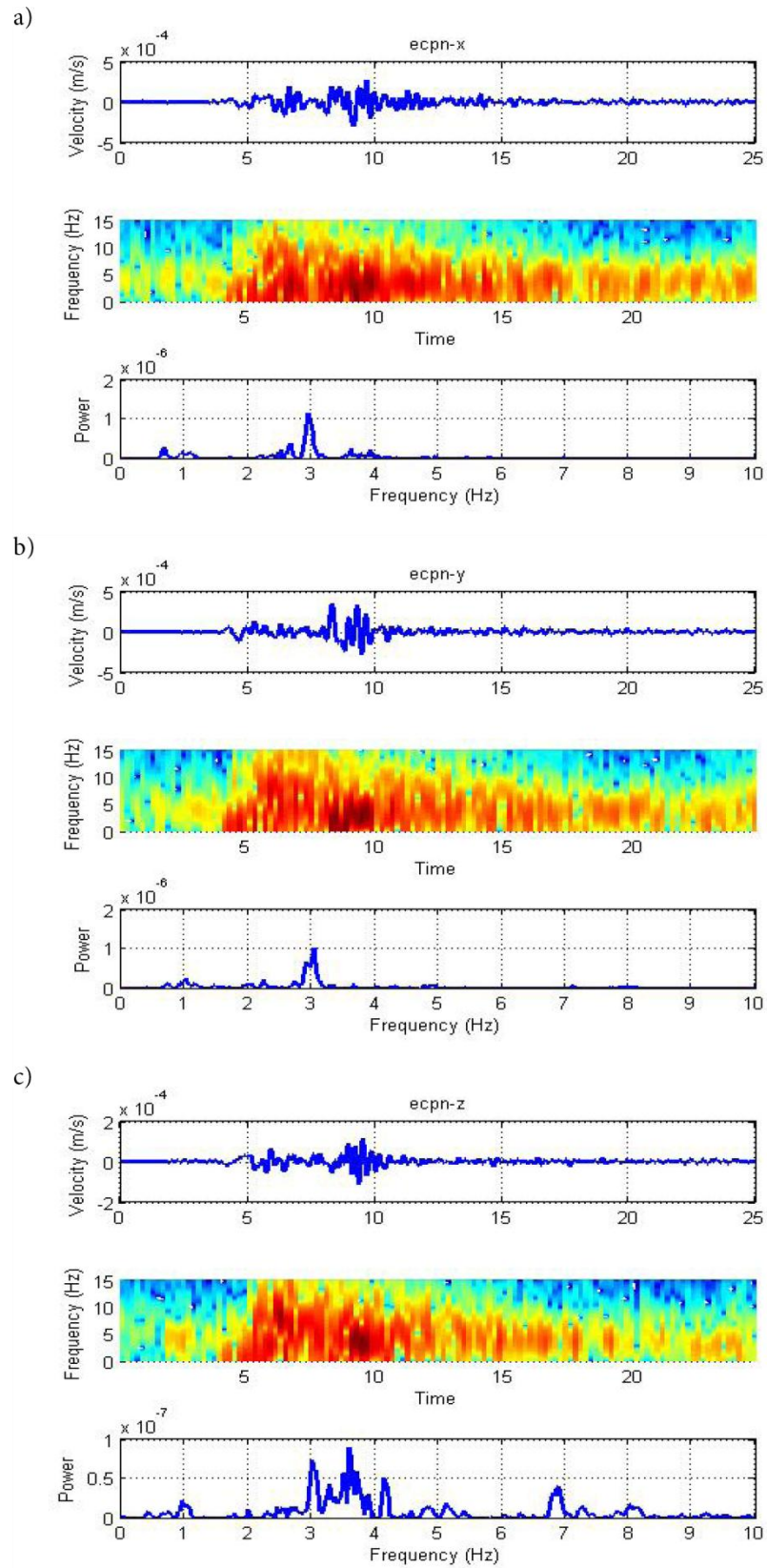
Figure 60 - a) top: x-component of velocity recorded at station ecpn for event 9. The seismic trace is filtered between 0.2 and 4 Hz; middle: short time Fourier transform plot of the unfiltered velocity trace, red correspond to high power towards blue lower; bottom: power spectral density of the unfiltered velocity trace. b) and c) same as a), for –y and –z components respectively.
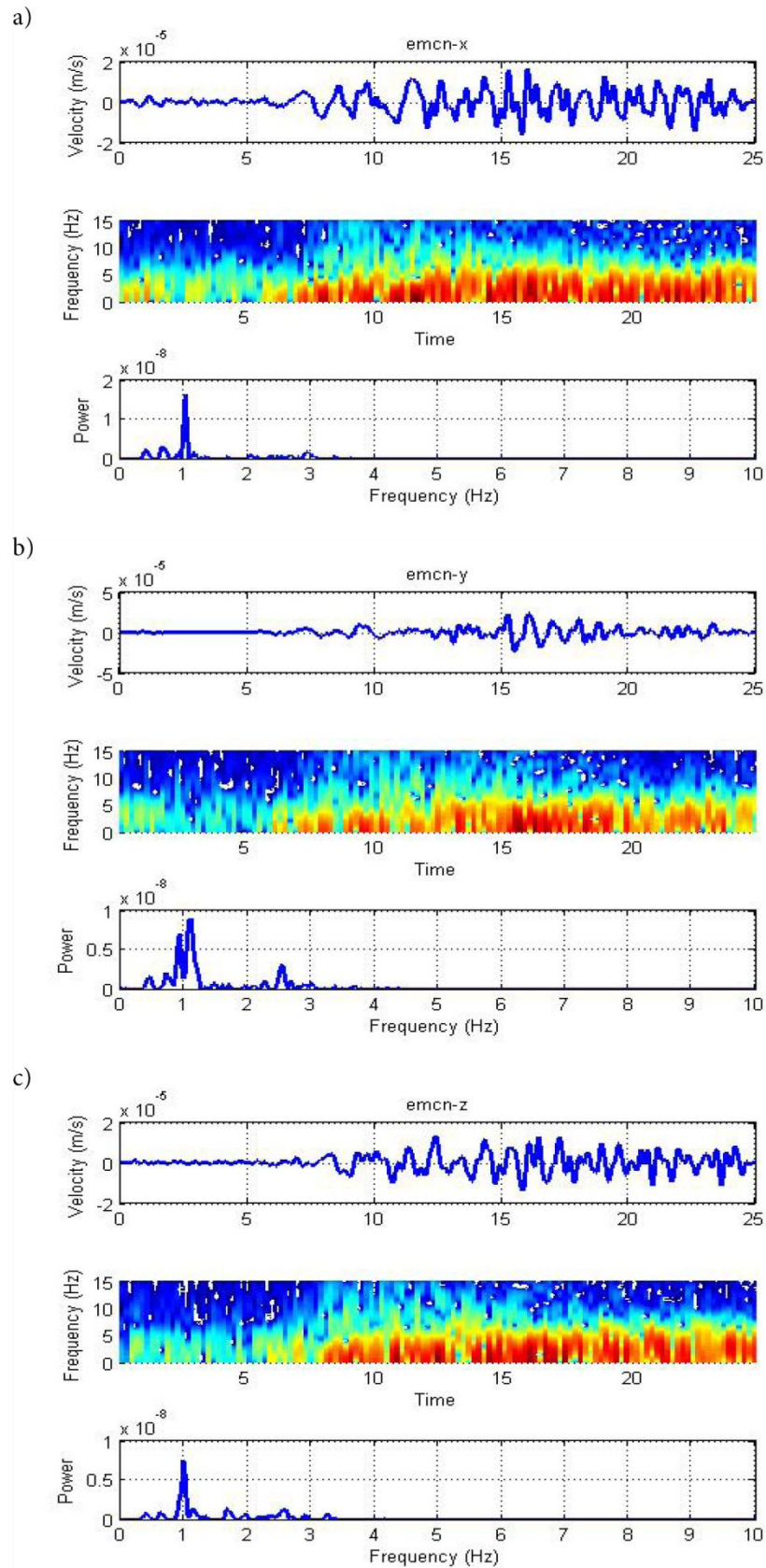
Figure 61 - a) top: x-component of velocity recorded at station emcn for event 9. The seismic trace is filtered between 0.2 and 4 Hz; middle: short time Fourier transform plot of the unfiltered velocity trace, red correspond to high power towards blue lower; bottom: power spectral density of the unfiltered velocity trace. b) and c) same as a), for –y and –z components respectively.

5.4.2 Location results

As for the monochromatic LP events I begin by locating the set of data towards moment tensor inversion (the method is discussed in detail in Chapter 2). The velocity traces are first band pass filtered between 0.3 and 1.3 Hz, then integrated to displacement and detrended to ensure stability in the inversion and avoid contributions from very low frequencies. The optimum position for each event is obtained from a grid search among 14196 sources spaced 40m in a volume (1 x 1 x 0.8 km) located below the summit craters and by taking the lowest value of misfit between observed and retrieved data.

Table 13 and Figure 62 show the results for all the analyzed 20 events with and without including single forces. The results are quite similar for both solutions including and without single forces with higher residuals for the MT-only solutions as expected. The residuals are slightly lower than those found for the previous set of analyzed events (monochromatic events, section 5.3). Almost all the events located including single forces are situated in a structure oriented east-west at the southern border of the Green's functions domain below the BN crater. The events show a shallow location (~2900 m.a.s.l.) apart from *events 3 and 13* located deeper (2240 and 2560 m.a.s.l. respectively). The lowest residual is obtained for *event 14* (0.489) located in UTM coordinates 499.598 km east, 4178.22 km north and 2920 m.a.s.l.

The locations are in general very similar and confirm the possibility of a common source mechanism. The solutions without single forces point to the same sector horizontally, but they are slightly more dispersed vertically with 4 events located ~2500 m.a.s.l. or below (*events 3, 11, 15* and *16*). The similar results for the solutions including and without single forces prove the robustness of the MT inversion. For comparison, I also report the average location found by INGV (INGV internal reports) towards a semblance + R2 method (see Cannata et al., 2013, 2015 for more details) of the whole set of events. The INGV location point to a source slightly shifted towards west from the BN crater at a depth of 2790 m.a.s.l. The MT inversion location including forces shows many points located nearby the INGV solution (~150m far). The MT inversion with forces points to a slightly shallow source, but in general the locations are comparable with the INGV

Table 13 - MT inversion location results for the polychromatic set of 20 events. Residuals data between observed and synthetics are reported with the respective source coordinates. M+F corresponds to the results including forces. At the bottom is reported the average location for the whole set of events found by INGV.

	M+F				**M only**			
	misfit	x (km)	y (km)	z (m)	misfit	x (km)	y (km)	z (m)
event_01	0.499	499.558	4178.220	2960	0.589	499.638	4178.220	3000
event_02	0.497	499.598	4178.220	2920	0.615	499.678	4178.220	3000
event_03	0.578	499.518	4178.220	2240	0.680	499.518	4178.220	2560
event_04	0.496	499.598	4178.220	2920	0.608	499.678	4178.220	3000
event_05	0.590	499.878	4179.220	2960	0.707	499.998	4178.780	2880
event_06	0.499	499.598	4178.220	2920	0.614	499.678	4178.220	3000
event_07	0.511	499.678	4178.220	2920	0.619	499.678	4178.220	3000
event_08	0.521	499.558	4178.220	2960	0.620	499.638	4178.220	3000
event_09	0.524	499.758	4178.220	2880	0.639	499.638	4178.220	3000
event_10	0.511	499.558	4178.220	2960	0.610	499.638	4178.220	3000
event_11	0.623	499.758	4178.340	2840	0.718	499.678	4178.220	2400
event_12	0.511	499.638	4178.220	2960	0.619	499.758	4178.820	2960
event_13	0.522	499.318	4178.220	2560	0.624	499.638	4178.220	3000
event_14	0.489	499.598	4178.220	2920	0.600	499.718	4178.780	2960
event_15	0.524	499.598	4178.220	2920	0.630	499.358	4178.220	2200
event_16	0.526	499.598	4178.220	2920	0.632	499.358	4178.220	2200
event_17	0.500	499.598	4178.220	2920	0.615	499.718	4178.820	2960
event_18	0.496	499.598	4178.220	2920	0.598	499.678	4178.220	3000
event_19	0.522	499.598	4178.220	2920	0.627	499.638	4178.220	3000
event_20	0.511	499.638	4178.220	2920	0.612	499.638	4178.220	3000

INGV Location	x (km)	y (km)	z (m)
	499.290	4178.220	2790
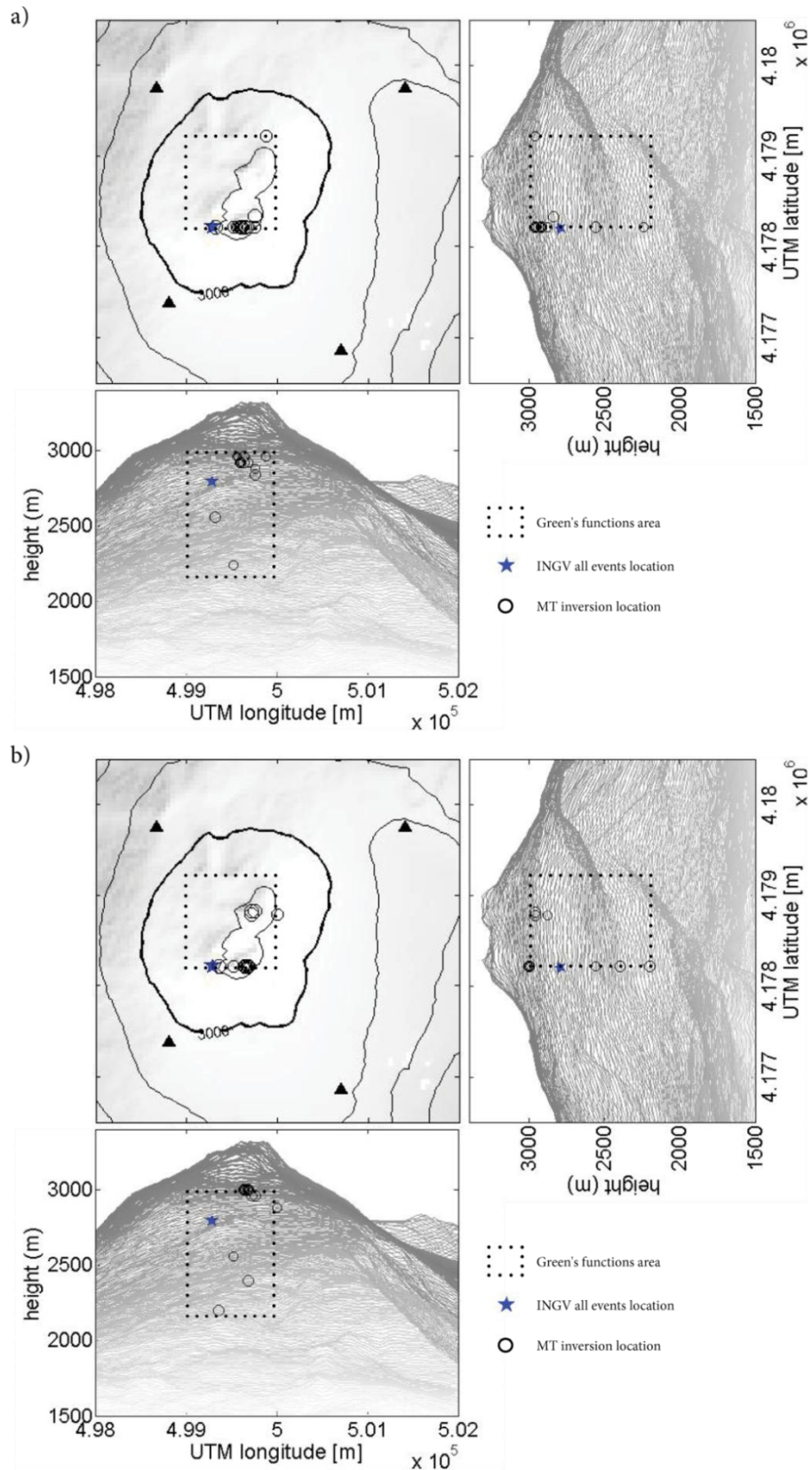
Figure 62 - Graphical representation of the location results for the second analyzed set of events reported in Table 13- a) MT inversion with single forces location results. The summit area of Mt. Etna with respective cuts east-west and north-south in UTM coordinates are represented. The dot line square corresponds to the Green's functions area, circles are the event locations and blue star is the average whole family INGV location.
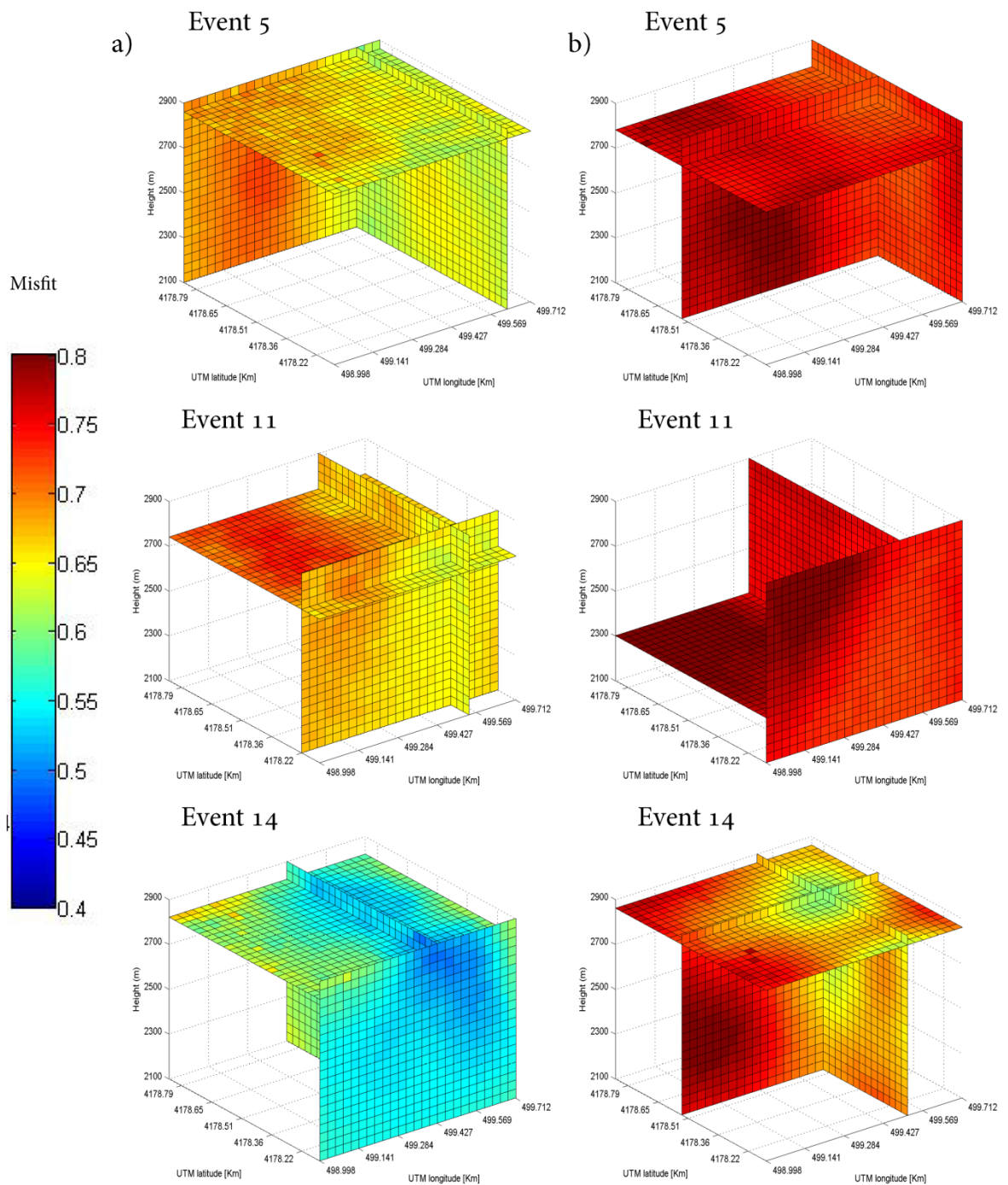
Figure 63 - Slice plot of the residuals for the whole Green's functions volume a) solution of MT including single forces; b) solution for MT only. The events are chosen on the basis of their location and residual value. Event 5 (top) dislocated in respect to the other events (northern boarder of the Green's functions domain), event 11 (middle) highest absolute misfit value, event 14 lowest misfit.

solution. The locations without forces, even if are more scattered inside the Green's functions volume, still show comparable results.

Again, as for the monochromatic events analyzed in the previous section, the solution including forces seems to be more stable. The locations are more coherent among the whole set of analyzed events and eventual errors in the velocity model should be accommodated by single forces components (De Barros et al., 2011, 2013). For comparison, the whole set of residuals retrieved for the entire Green's functions volume is reported in Figure 63 for three selected events (*5, 11* and *14*). *Event 5* is chosen because its location is not coherent with the other location solutions. The event is located far towards the northern border of the Green's functions domain. The misfit values for the MT- only solution are high and quite dispersed even if the eastern portion of the Green's functions domain appear to be the most probable source location (Figure 63). The solution including forces shows a high dispersion of the residuals and a clear location cannot be defined. It is worth nothing that *event 5* shows a very low amplitude and signal to noise ratio (Figure 57) thus, retrieving a stable solution toward MT inversion can be difficult. *Event 11* and *event 14* represent the events with the highest and the minimum absolute misfit values respectively. The solution without single forces points to a well-defined location only for *event 14*. The solutions including forces are comparable. For *event 11* the solution seems to be well constrained horizontally while vertically all the locations could be possible active source points. For *event 14* the solution seems well constrained both vertically and horizontally.

5.4.3 Source mechanism

Moment tensor inversion is performed for all the 20 analyzed events for the respective lowest residual locations (Table 13). The results for both the inversions with and without singles forces are reported in Table 14 and Table 15, respectively. First, I analyze briefly the results for the whole set of events and I will then study further (moment tensor decomposition and mechanism orientation) a couple of selected events. The solutions including forces (Table 14) show misfit values slightly lower than those found for the monochromatic set of events (in average misfit = 0.522). The eigenvalues

Table 14 – Results of MT inversion including single forces for the polychromatic set of events for the lowest residuals source location. Misfit values are computed between observed and retrieved data. Mechanism decomposition and principal component analysis have been performed following the in indications of Vasco, (1989) and (Vavryčuk, 2001, 2015), see section 2.3 for details.

M+F	misfit	λ_1	λ_2	λ_3	φ (°)	θ (°)	C_{ISO}	C_{CLVD}	C_{DC}
event_01	0.499	1.0	1.06	2.27	8	9	0.64	0.34	0.03
event_02	0.497	1.0	1.06	2.25	-6	10	0.64	0.34	0.03
event_03	0.578	1.0	1.27	1.53	-60	17	0.83	0	0.17
event_04	0.496	1.0	1.06	2.25	3	8	0.64	0.33	0.03
event_05	0.590	1.0	1.15	3.1	24	17	0.56	0.39	0.05
event_06	0.499	1.0	1.06	2.27	-9	9	0.64	0.34	0.03
event_07	0.511	1.0	1.06	2.28	-20	10	0.63	0.34	0.03
event_08	0.521	1.0	1.05	2.3	-1	8	0.63	0.35	0.02
event_09	0.524	1.0	1.09	2.36	-43	11	0.63	0.33	0.04
event_10	0.511	1.0	1.06	2.29	3	8	0.63	0.34	0.02
event_11	0.623	1.0	1.11	2.33	-35	7	0.63	0.32	0.05
event_12	0.511	1.0	1.05	2.28	-12	13	0.63	0.34	0.02
event_13	0.522	1.0	1.1	1.82	77	11	0.72	0.22	0.06
event_14	0.489	1.0	1.05	2.28	-6	11	0.63	0.34	0.02
event_15	0.524	1.0	1.05	2.23	-3	11	0.64	0.34	0.02
event_16	0.526	1.0	1.05	2.24	-2	10	0.64	0.34	0.02
event_17	0.500	1.0	1.05	2.25	-6	11	0.64	0.34	0.02
event_18	0.496	1.0	1.06	2.27	-7	11	0.64	0.34	0.03
event_19	0.522	1.0	1.06	2.22	-4	9	0.64	0.33	0.03
event_20	0.511	1.0	1.06	2.24	-7	7	0.64	0.33	0.03
Average	0.522	1.0	1.1	2.3	-5.3	10.4	0.65	0.32	0.03
STD	0.035	0.0	0.1	0.3	26.7	2.7	0.05	0.08	0.03

Table 15 – Results of MT inversion without single forces for the polychromatic set of events for the lowest residuals source location. Misfit values are computed between observed and retrieved data. Mechanism decomposition and principal component analysis have been performed following the in indications of Vasco, (1989) and (Vavryčuk, 2001, 2015), see section 2.3 for details.

M only	misfit	λ_1	λ_2	λ_3	φ (°)	θ (°)	C_{ISO}	C_{CLVD}	C_{DC}
event_01	0.589	1.0	1.4	5.45	-8	12	0.48	0.45	0.07
event_02	0.615	1.0	1.7	6.36	-13	13	0.47	0.42	0.11
event_03	0.680	NaN	NaN	NaN	NaN	0	NaN	NaN	NaN
event_04	0.608	1.0	1.94	6.3	-22	16	0.49	0.36	0.15
event_05	0.707	1.0	3.15	16.64	-53	11	0.42	0.45	0.13
event_06	0.614	1.0	1.63	5.87	-17	15	0.48	0.41	0.11
event_07	0.619	1.0	1.74	5.69	-15	13	0.49	0.38	0.13
event_08	0.620	1.0	1.75	6.26	-9	14	0.48	0.4	0.12
event_09	0.639	1.0	1.57	5.43	-13	14	0.49	0.41	0.1
event_10	0.610	1.0	1.65	6.4	-6	12	0.47	0.43	0.1
event_11	0.718	1.0	1.34	1.86	-55	76	0.75	0.06	0.18
event_12	0.619	1.0	2.37	7.5	-22	6	0.48	0.33	0.18
event_13	0.624	1.0	1.62	5.84	-7	13	0.48	0.41	0.11
event_14	0.600	NaN	NaN	NaN	NaN	0	NaN	NaN	NaN
event_15	0.630	1.0	1.09	1.47	-16	92	0.81	0.13	0.06
event_16	0.632	1.0	1.22	1.56	-11	91	0.81	0.05	0.14
event_17	0.615	NaN	NaN	NaN	NaN	0	NaN	NaN	NaN
event_18	0.598	1.0	1.53	5.2	-15	12	0.5	0.4	0.1
event_19	0.627	1.0	1.55	5.81	-5	12	0.48	0.43	0.09
event_20	0.612	1.0	1.56	5.87	-5	13	0.48	0.43	0.1
Average	0.629	1.0	1.7	5.9	-17.2	21.8	0.53	0.35	0.12
STD	0.034	0.4	0.8	3.7	15.0	28.4	0.12	0.13	0.03

decomposition (λ_n) shows similar values between the whole set of events, thus an average ratio of 1 : 1.1 : 2.25 and a standard deviation STD = 0.3 for the major axis seem to suggest a common tensile crack source mechanism. The orientation angles (φ = strike, θ = dip, Figure 2 for the reference system) are very similar for all the events with average φ = 5° and θ = 10° thus indicating a possible sub-horizontal crack source mechanism. The PCA (principal component analysis, Vavryčuk, 2001, 2015) shows a predominant C_{ISO} component (average C_{ISO} = 65%), an important C_{CLVD} (average C_{CLVD} = 32%) and a very low double-couple contribution (average C_{DC} = 3%). Only *event 03* shows a high C_{DC} value (17%), but it is also the event with the highest residual (misfit=0.578) and the lowest absolute amplitude (Figure 56 and Figure 57). The inversion for MT-only (Table 15) shows slightly higher misfit than the solution including forces. The eigenvalues decomposition points to unrealistic values for the eigenvalues ratio with an average for the principal axis of ~5.9 and a standard deviation of ~3.7. Orientation angles for the main eigenvector show again a sub-horizontal source mechanism, but slightly more sloping (average = 21.8°) with a high standard deviation (STD = 28.4°). The results after PCA (principal component analysis, (Vavryčuk, 2001, 2015) show an average C_{CLVD} value equivalent to the solution including forces, a slightly lower C_{ISO} and a higher C_{DC} (average C_{DC} = 12%). The solution for MT-only is more dispersed than the solution including forces. The high eigenvalues ratio and standard deviation of the MT-only solution suggest that the MT inversion including forces is more stable. As the decomposition results are very similar especially for the solution including forces and that the events seem to show a high degree of similarity a common source is supposed to exist. Thus, I focus my attention on two selected events: *event 14* which shows the lowest misfit value and *event 13* which shows the lowest eigenvalues ratio (1 : 1.1 : 1.82) and the highest C_{ISO} component (Table 14).

The moment tensor results for *event 14* and *event 13* are showed in Figure 64 and Figure 66 respectively. Waveforms fits between observed data and the moment tensor solution convolved with the Green's functions are also reported in Figure 65 and Figure 67. The moment tensor solutions between the two events (Figure 64 and Figure 66) are similar, but the solution for *event 13* looks less complex, i.e. the oscillations are shorter. The source mechanism for both solutions including and excluding forces shows a complex time history and it is difficult to make further considerations on the source

mechanism from simple observation of the waveforms. The retrieved amplitudes are coherent between the two events, the M_{zz} component shows the highest amplitude value in both the solutions including ($\sim 10^{12}$ Nm) and without ($\sim 10^{11}$ Nm) single forces for both events. In the solution for MT-only the non-diagonal components of the moment tensor contribute more to the final solution with comparable amplitudes to the main diagonal components (excluding M_{zz} which amplitude is around double of the second most energetic STF). In the solution including forces the non-diagonal components of the moment tensor are negligible and do not contribute significantly to the solution. Synthetic and observed waveforms comparison shows good matching for stations located nearby the summit of Mt. Etna (*ebel, ecpn, eplc*), while further stations show a degraded solution. Noisy oscillations in the synthetic data arise especially for stations located at the boarder of the numerical domain (e.g. *emsg, espc*). However, nearest stations show higher recorded amplitudes, thus they contribute more to the final solution.

After SVD and PCA both events show an eigenvalues ratio of 1 : 1 : ~2 for the solution including forces (Table 14) which, for a Poisson's ratio of 0.35, should correspond to a tensile crack mechanism. Dip orientation angles are the same for both events ($\theta = 11°$) pointing to a quasi-horizontal crack. As highlighted before *event 13* shows a lower C_{CLVD} value ($C_{CLVD} = 22\%$ for *event 13* and $C_{CLVD} = 34\%$ for *event 14*) and slightly higher C_{ISO} and C_{DC} components. Even if the comparison between the MT-only solutions (Figure 64 and Figure 66) highlights the possibility of a different source mechanism, the PCA shows that the mechanism decomposition points to roughly similar results. The low double-couple components computed for both events coupled with the high C_{CLVD} components suggest a possible tensile crack source mechanism. The solutions for MT-only (Table 15) are more dispersed. For *event 14* the SVD condition that the first singular value must be at least double of the second (see section 2.3.5) is not satisfied. As highlighted in the description of the STF (source time function), the single forces tend to make the solution more stable suppressing the non-diagonal components. Hence, as errors due to mismodelling of the velocity structure should be accommodated by the single forces components (De Barros et al., 2011, 2013) and that the MT-only decomposition seems less stable, the results obtained for the solution including forces should be more reliable.

In order to check the stability of the solution, I perform full moment tensor inversion, but for a mislocated source. I take as reference the location found by INGV (Table 13). The results of the inversion including forces for all the 20 events for the common INGV location are reported in Table 16. The misfit values are considerably higher than the previous inversion (0.691 in average for the mislocated source against 0.522 for the locations found towards MT inversion). Apart from the higher residuals, the solutions after SVD and PCA are similar. The eigenvalues decomposition shows in average a more limited ratio with the second and the third eigenvalues roughly similar. The source mechanism, as seen previously with the monochromatic set of events, could be seen as something in between an explosion (eigenvalues ratio of 1 : 1 : 1) and a tensile crack (eigenvalues ratio of 1 : 1 : 2). Anyway, despite the higher standard deviation values, the orientation angles are coherent with the solution for the MT inversion locations showing a *quasi*-horizontal (θ = 13.3) tensile crack mechanism. The values of isotropic, CLVD and double-couple are, on the opposite, quite different. The solution points in average to a strong isotropic component (C_{ISO} = 81%) a very low CLVD (C_{CLVD} = 4%) and a quite high double-couple component (C_{DC} = 15%).

For comparison, I show the moment tensor solution (Figure 68) and the waveform fitting between observed and retrieved data (Figure 69) for *event 14* and the INGV source location. The moment tensor solution for the mislocated source shows waveforms shape similar to the non-dislocated source. The amplitude ratio, on the opposite, shows a slightly predominant M_{zz} component, but in average the amplitude of the main diagonal components is roughly equivalent. The waveforms fit between synthetics and observed data is generally poorer, stations located nearby the summit of the volcano does not show a good fit especially for vertical component (e.g. stations *ebel* and *ecpn*) which were instead well reproduced for the lowest residual MT locations. In general, the solution for the mislocated source, as it happened for the monochromatic set of events (section 5.2.3), tends to a more isotropic mechanism with stronger double-couple components. Hence, the different source location complicates the solution and opens to a mixed tensile/shear source mechanism.

Table 16 – Results of MT inversion including single forces for the polychromatic set of events for the INGV source location. Misfit values are computed between observed and retrieved data. Mechanism decomposition and principal component analysis have been performed following the in indications of Vasco, (1989) and (Vavryčuk, 2001, 2015), see section 2.3 for details.

M+F	misfit	λ_1	λ_2	λ_3	φ (∘)	θ (∘)	C_{ISO}	C_{CLVD}	C_{DC}
event_01	0.698	1.0	1.23	1.51	59	7	0.83	0.02	0.15
event_02	0.684	1.0	1.22	1.65	83	15	0.78	0.09	0.13
event_03	0.705	1.0	1.36	1.59	33	11	0.83	0.05	0.12
event_04	0.704	1.0	1.17	1.44	-65	6	0.84	0.05	0.12
event_05	0.707	1.0	1.15	1.43	75	7	0.84	0.06	0.1
event_06	0.702	1.0	1.28	1.56	67	13	0.82	0	0.18
event_07	0.653	1.0	1.58	1.77	36	6	0.82	0.11	0.07
event_08	0.677	1.0	1.23	1.69	85	19	0.77	0.09	0.14
event_09	0.686	1.0	1.27	1.58	-16	4	0.81	0.02	0.17
event_10	0.685	1.0	1.15	1.23	74	61	0.92	0.03	0.05
event_11	0.689	1.0	1.33	1.63	-36	11	0.81	0.01	0.18
event_12	0.688	1.0	1.4	1.82	-74	11	0.77	0.01	0.22
event_13	0.704	1.0	1.25	1.77	87	10	0.76	0.1	0.14
event_14	0.673	1.0	1.38	1.82	-73	14	0.77	0.02	0.21
event_15	0.692	1.0	1.28	1.67	-62	9	0.79	0.04	0.17
event_16	0.712	1.0	1.2	1.39	65	16	0.86	0.01	0.13
event_17	0.705	1.0	1.32	1.61	73	14	0.82	0.02	0.17
event_18	0.681	1.0	1.33	1.79	84	11	0.77	0.05	0.18
event_19	0.707	1.0	1.29	1.6	-81	10	0.81	0	0.18
event_20	0.671	1.0	1.35	1.65	74	11	0.81	0.02	0.18
Average	0.691	1.0	1.3	1.6	24.4	13.3	0.81	0.04	0.15
STD	0.015	0.0	0.1	0.2	65.0	11.8	0.04	0.03	0.04
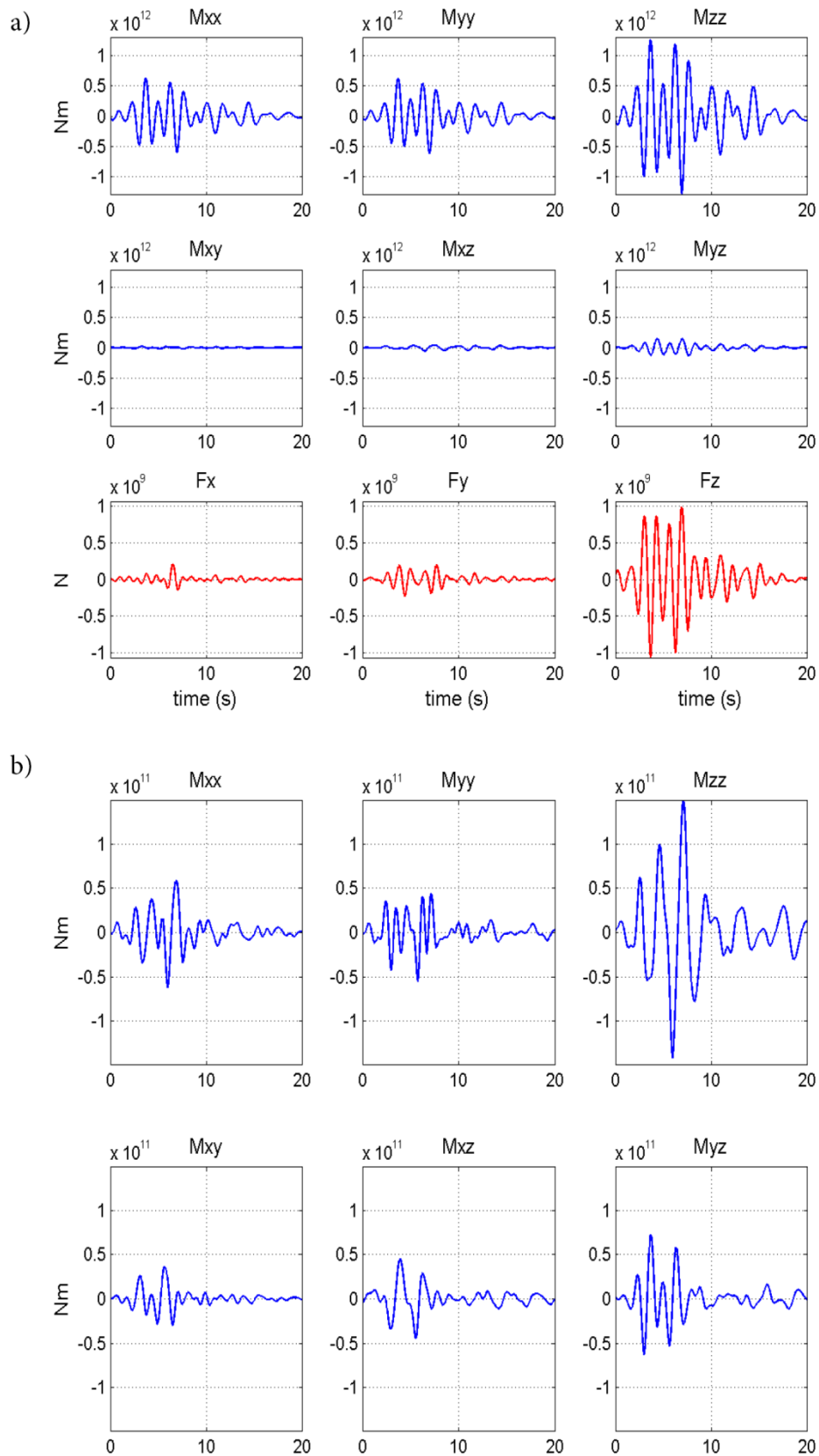
Figure 64 – a) MT inversion solution including forces for event 14 of the polychromatic set of events for the lowest residual source location and 14 stations of the INGV permanent network. b) MT inversion solution excluding forces for the same event.

Moment Tensor + Single Forces

Moment Tensor only
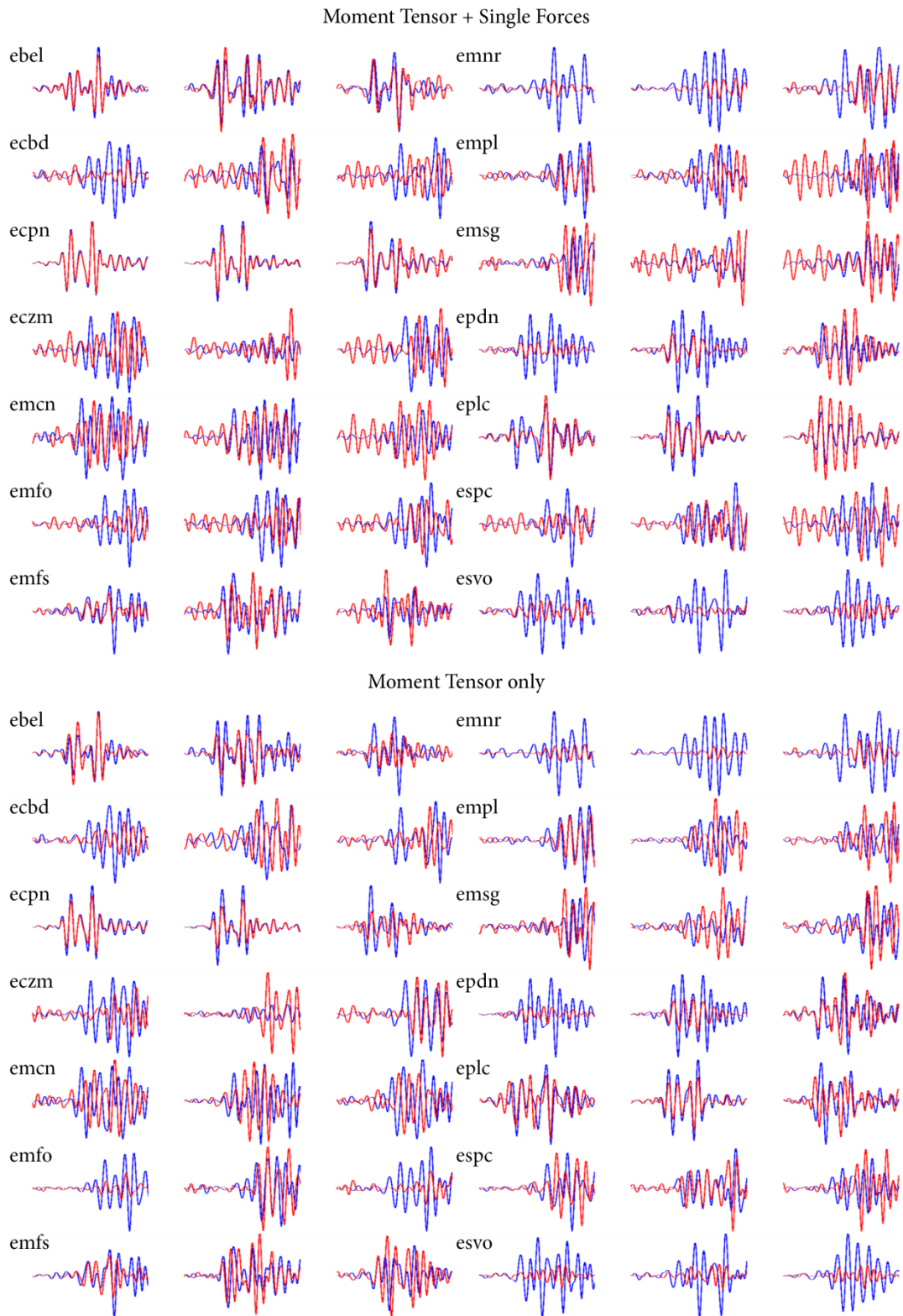
Figure 65 – Comparison between the observed data and the MT solution convolved with the Green's functions for event 14 of the polychromatic set of events. Blue lines correspond to the observed data and red lines to the retrieved solution.
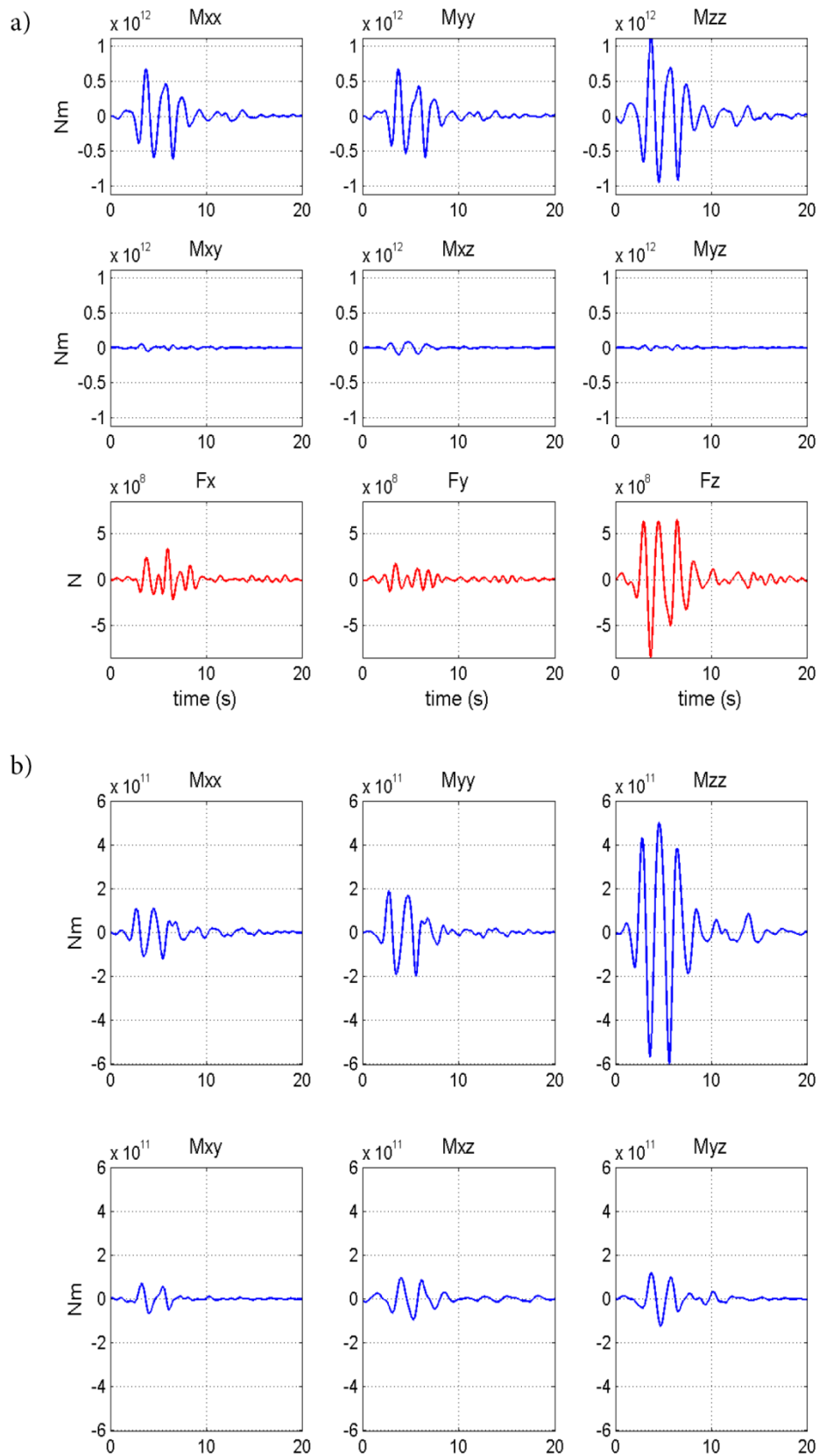
Figure 66 – a) MT inversion solution including forces for event 13 of the polychromatic set of events for the lowest residual source location and 14 stations of the INGV permanent network. b) MT inversion solution excluding forces for the same event.
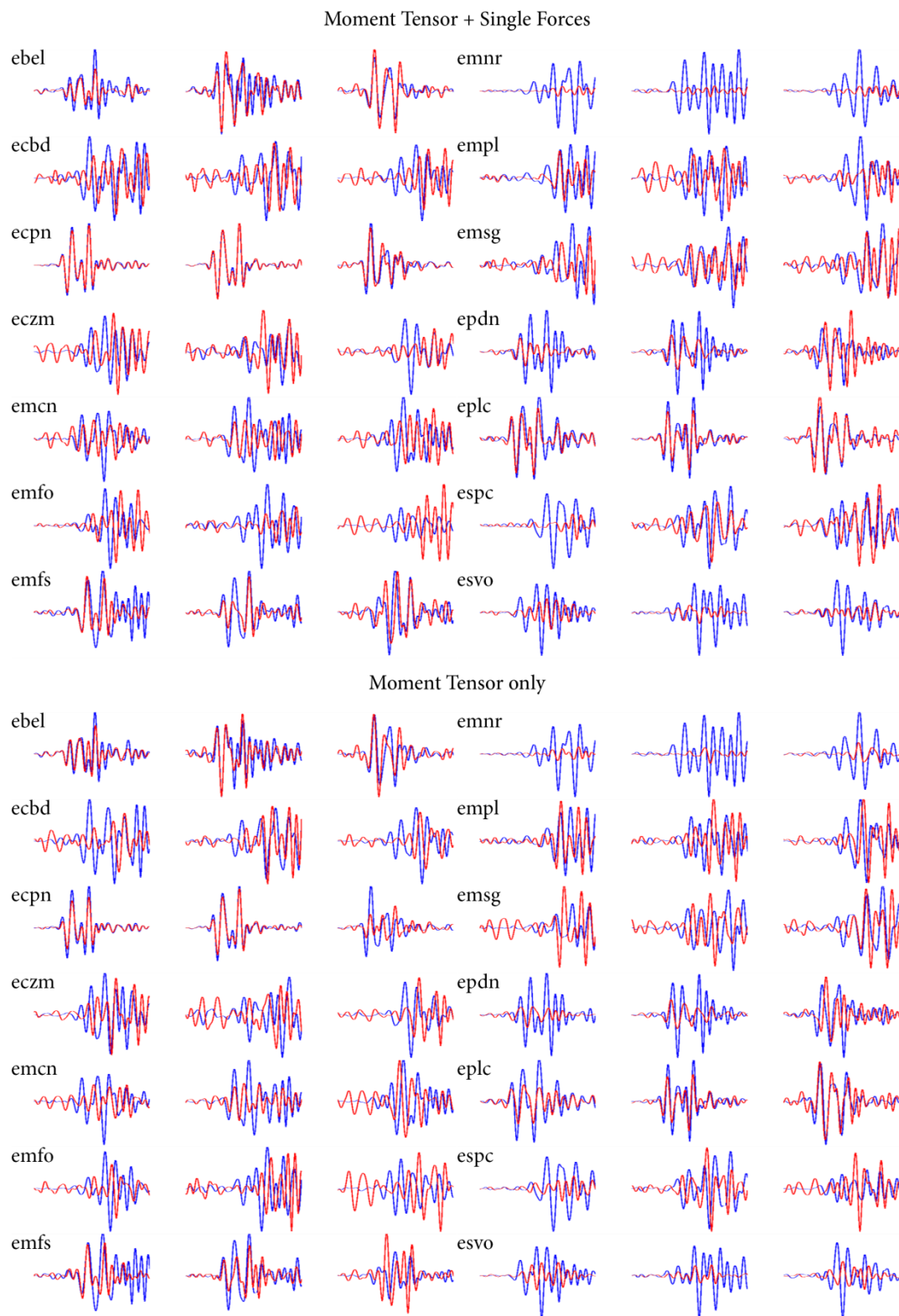
Figure 67 – Comparison between the observed data and the MT solution convolved with the Green's functions for event 13 of the polychromatic set of events. Blue lines correspond to the observed data and red lines to the retrieved solution.
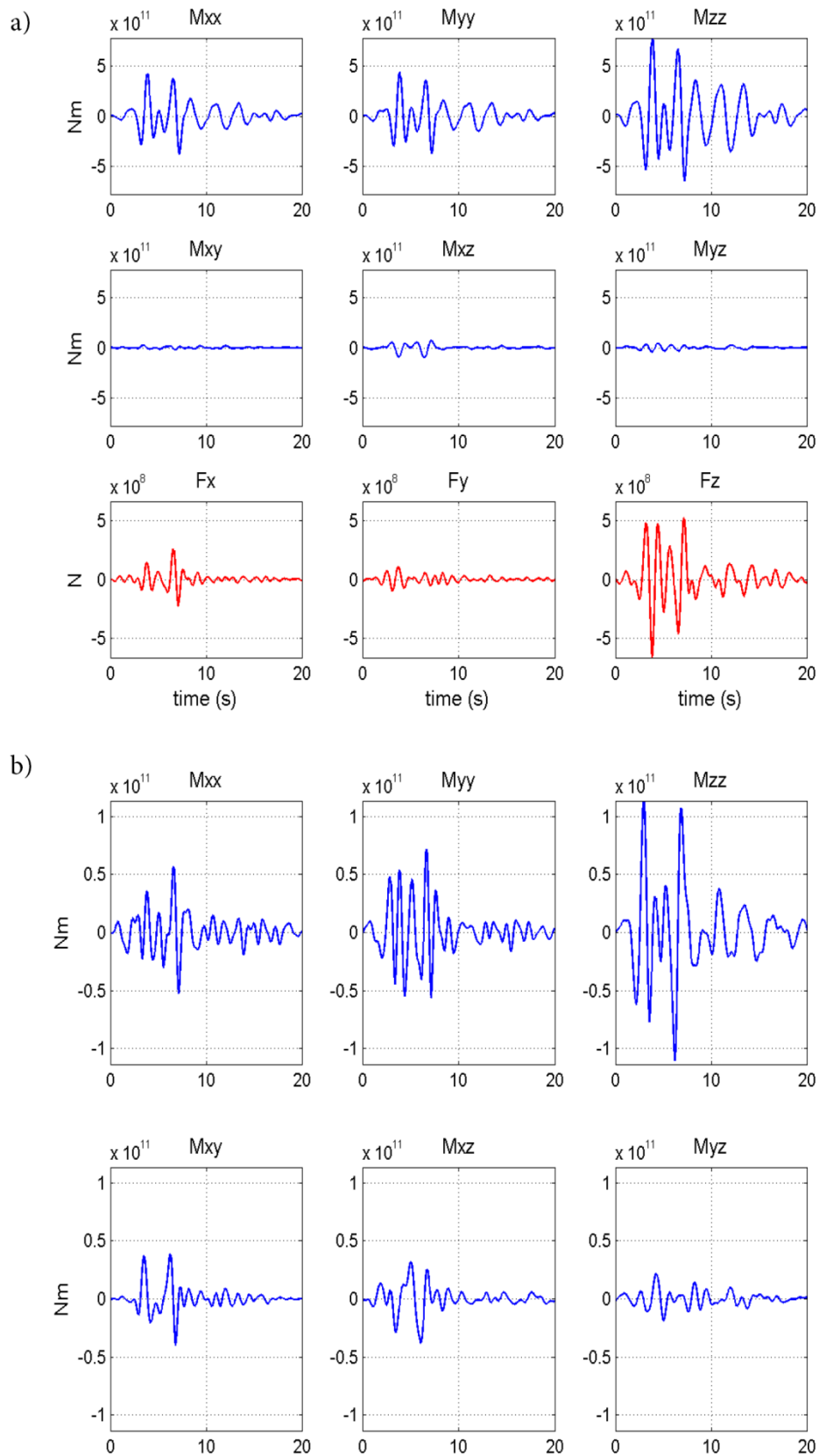
Figure 68 – a) MT inversion solution including forces for event 14 of the polychromatic set of events for the INGV source location and 14 stations of the INGV permanent network. b) MT inversion solution excluding forces for the same event.

Moment Tensor + Single Forces

Moment Tensor only
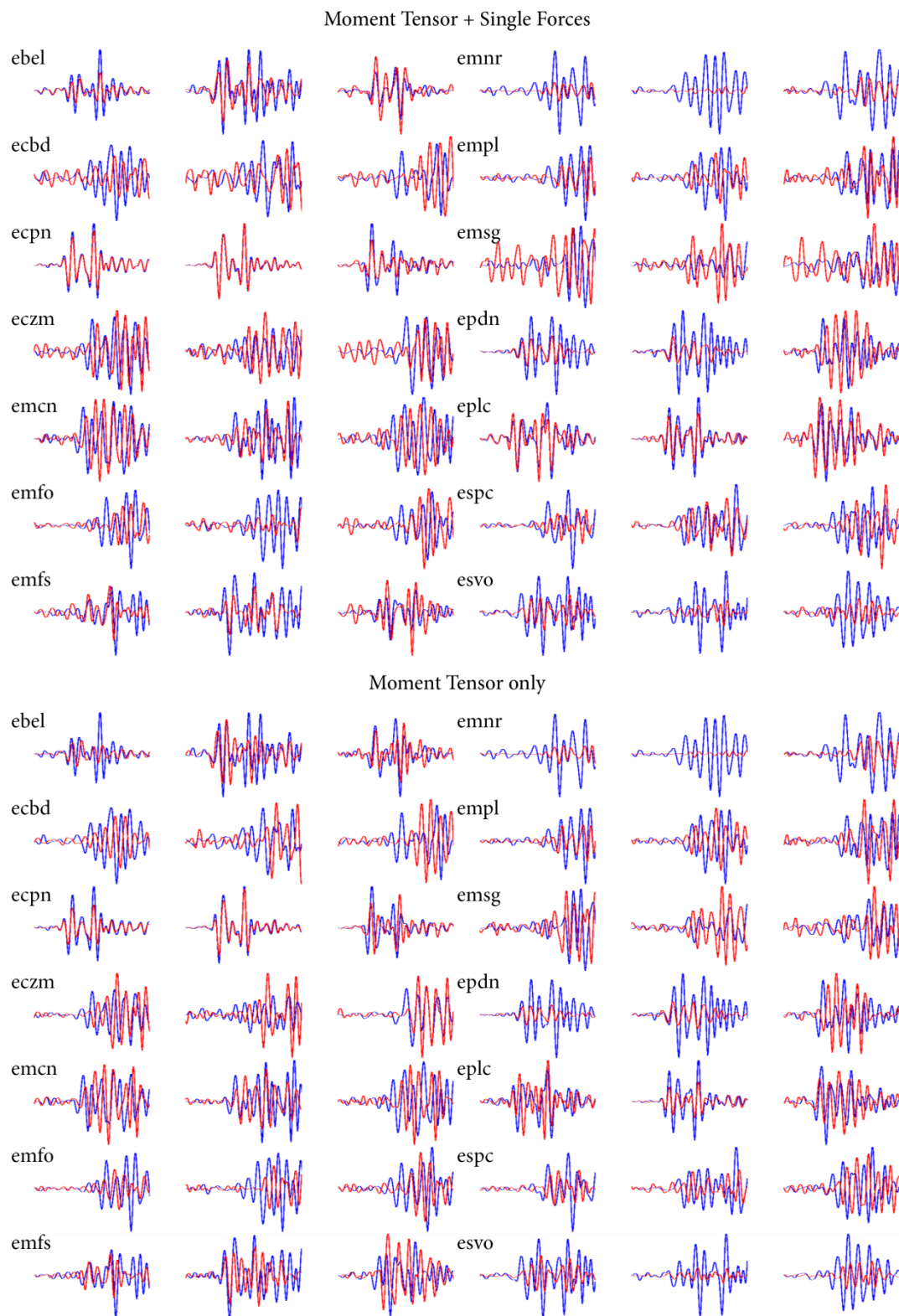
Figure 69 – Comparison between the observed data and the MT solution convolved with the Green's functions for event 14 of the polychromatic set of events for the source location found by INGV. Blue lines correspond to the observed data and red lines to the retrieved solution.

Table 17 – Results for the constrained MT inversion for the solution including and without single forces for the polychromatic set of events and lowest residual location. Lowest residual obtained for an isotropic mechanism (Misfit exp) and for a tensile crack mechanism (Misfit crack). I also report the couple of orientation angles for the lowest crack residual.

	M+F				M only			
	Misfit exp	Misfit crack	φ (°)	θ (°)	Misfit exp	Misfit crack	φ (°)	θ (°)
event_01	0.617	0.623	150	90	0.903	0.820	350	10
event_02	0.652	0.638	160	90	0.923	0.842	0	10
event_03	0.734	0.752	290	50	0.886	0.863	170	80
event_04	0.648	0.628	340	80	0.922	0.850	350	30
event_05	0.805	0.776	0	30	0.968	0.931	100	50
event_06	0.650	0.638	340	80	0.928	0.859	350	20
event_07	0.670	0.638	340	80	0.917	0.828	350	30
event_08	0.675	0.668	240	40	0.924	0.865	350	10
event_09	0.699	0.684	80	80	0.928	0.863	0	0
event_10	0.655	0.648	250	50	0.925	0.846	0	0
event_11	0.827	0.790	120	40	0.951	0.891	120	50
event_12	0.658	0.624	160	90	0.887	0.807	350	30
event_13	0.666	0.690	90	20	0.916	0.851	230	80
event_14	0.640	0.626	340	80	0.909	0.817	350	20
event_15	0.677	0.658	160	90	0.912	0.824	360	10
event_16	0.681	0.659	160	90	0.922	0.838	0	10
event_17	0.660	0.642	340	90	0.922	0.828	350	20
event_18	0.630	0.607	340	80	0.902	0.826	350	20
event_19	0.675	0.670	240	60	0.919	0.843	0	10
event_20	0.665	0.656	340	80	0.906	0.838	350	10
Average	0.679	0.666	224	70	0.919	0.847	224	25
STD	0.053	0.051	108	23	0.019	0.028	155	23
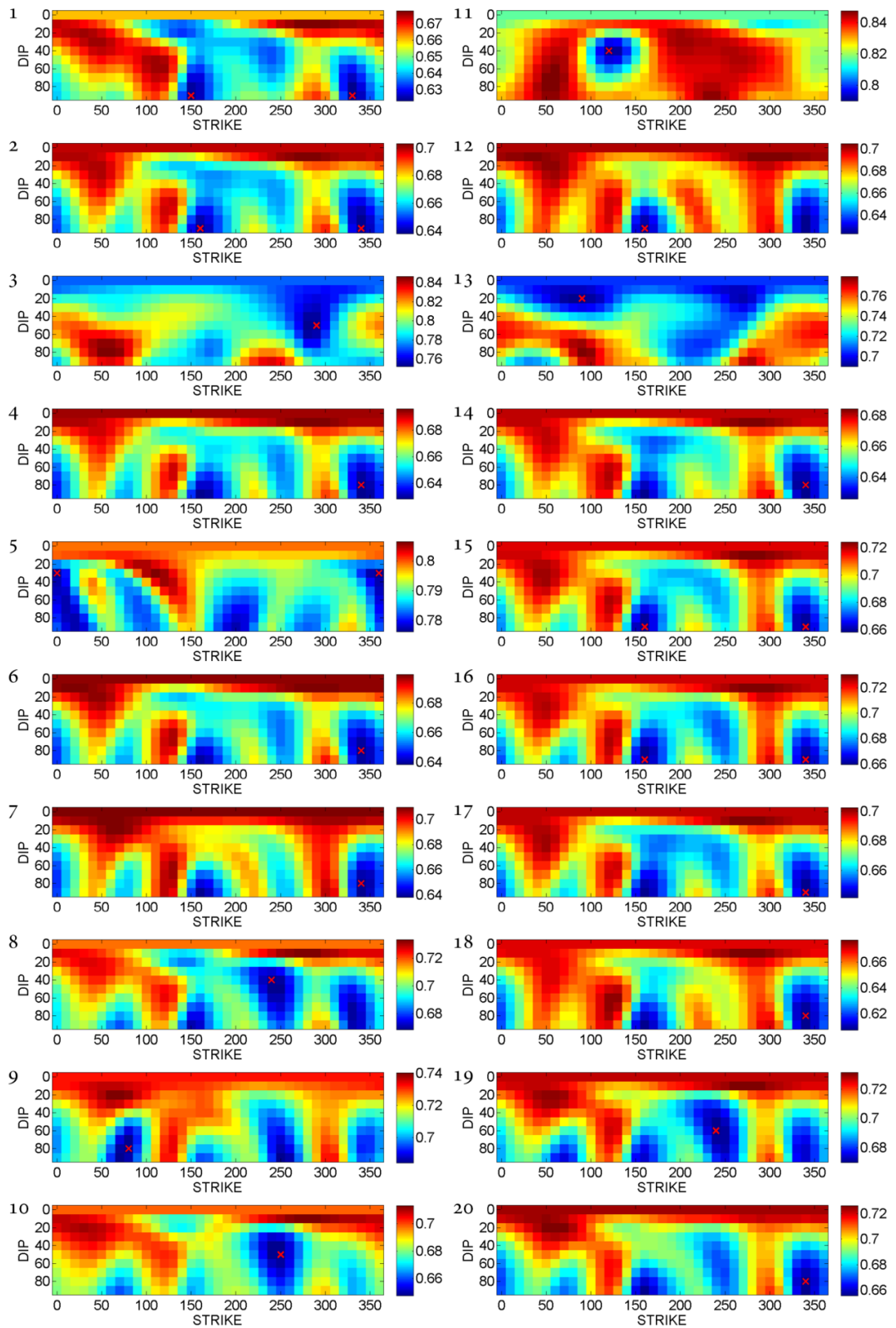
Figure 70 – Constrained inversion residuals plot for the tensile crack solution for the solution including single forces for the polychromatic set of events. Event number is reported on the top left of each contour plot, misfit range legend on the right side. Red cross indicates the lowest retrieved minima misfit.
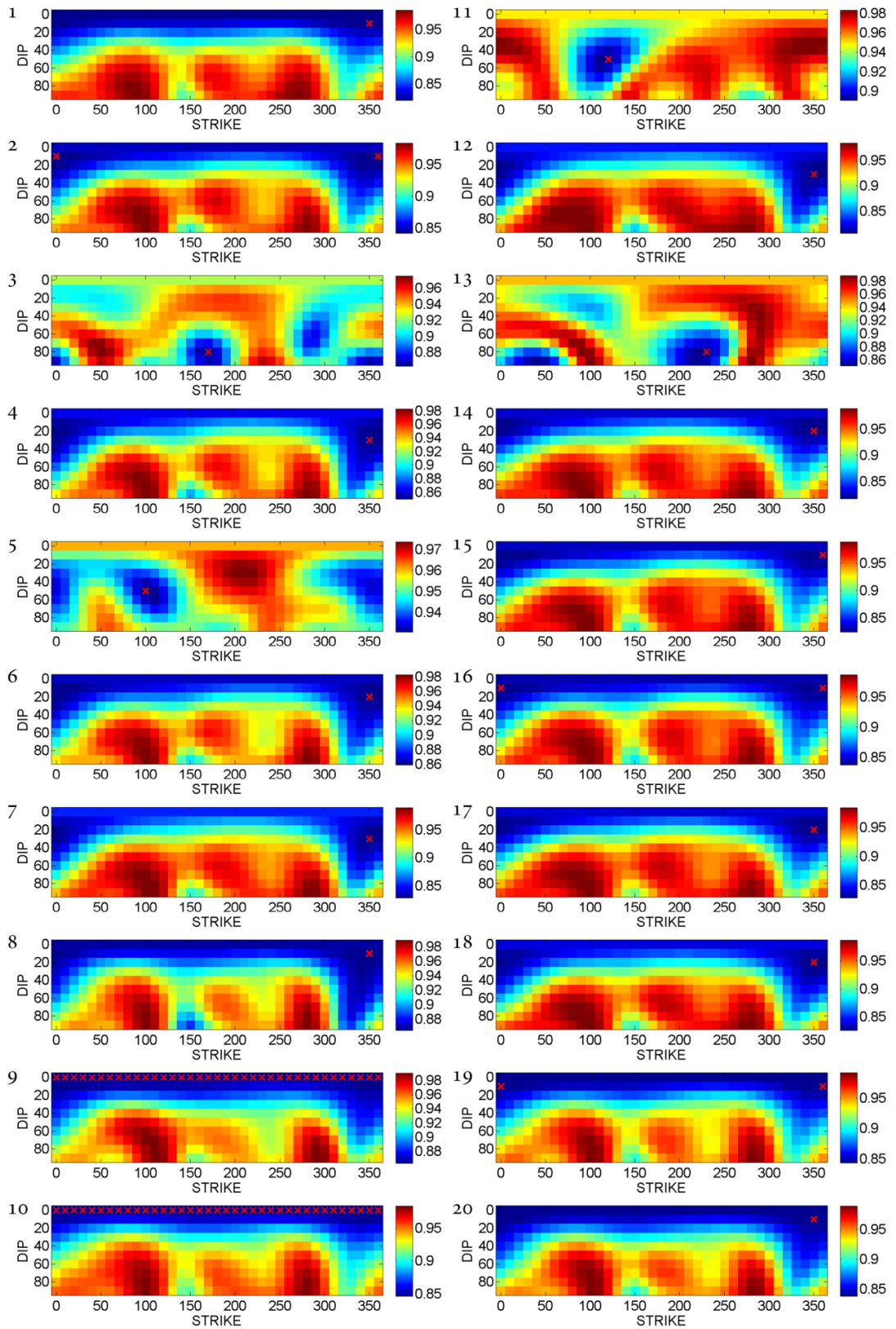
Figure 71 – Constrained inversion residuals plot for the tensile crack solution for the solution without single forces for the polychromatic set of events. Event number is reported on the top left of each contour plot, misfit range legend on the right side. Red cross indicates the lowest retrieved minima misfit.

As the residuals are considerably higher, the solutions for the moment tensor inversion locations seem more reliable. In order to check if an isotropic source is a more suitable interpretation for the source mechanism, I perform a constrained inversion for all the set of events for the original MT inversion lowest residual locations. The procedure is described in detail in chapter 2, section 2.3. During the inversion the mechanism is constrained to (1) an isotropic source and (2) a tensile crack with a grid search for the best possible couple of angles orientations (azimuth and dip). Results for both solutions with and without single forces are reported in (Table 17). Results for best tensile crack orientation angles for the solution including and without forces are reported in Figure 70 and in Figure 71 respectively.

The residuals for the solutions including forces are almost identical (~0.66) for both an isotropic and a tensile crack source. The best orientation angles for the crack solution show a high standard deviation and point to a *sub*-vertical crack oriented SW-NE. The solution without forces shows very high misfit values (~0.9) for both an isotropic and a tensile crack source. The orientation angles, on the opposite, point to a *quasi*-horizontal crack slightly oriented SW-NE. Looking at the plots of the residuals for each couple of angles orientation (Figure 70 and Figure 71) it appears that the solution including forces is highly dispersed, i.e. many different orientation angles orientations show low residuals and the solutions are not consistent between different events. On the opposite, the residuals for the solutions without forces are more coherent between events and almost all solutions point to a *quasi*-horizontal crack. The similar average residuals obtained for the isotropic and the crack source mechanism in the solution including forces do not let discriminate which solution is most suitable. Thus, it seems that single forces in the solution help to fit the data no matter what orientation mechanism is and strongly influence the results of the constrained inversion. Despite the high misfit values obtained in the inversion without forces, the MT-only solutions seem more stable and coherent both between events and with the moment tensor decomposition described previously. Hence, a *quasi*-horizontal tensile crack seems the most plausible source mechanism.

As for the previous set of monochromatic events I develop the principal component analysis in order to find out the possible contribution from a mixed tensile/shear mechanism, the procedure is explained in the previous section (section 5.2.3). As the

results between events for the solutions including forces are very coherent (Table 14) I take the average contribution of C_{ISO}, C_{CLVD} and C_{DC} (65%, 34% and 4% respectively) and following Vavryčuk, (2001, 2015) I compute **κ** = 2.05. For a given value of **κ** the proportion of isotropic, CLVD and double couple versus the angle α can be plotted as shown in Figure 72. It is quite surprising that for such a value of **κ**, even for high values of α, the source mechanism could be interpreted with an important shear component. In this case, the
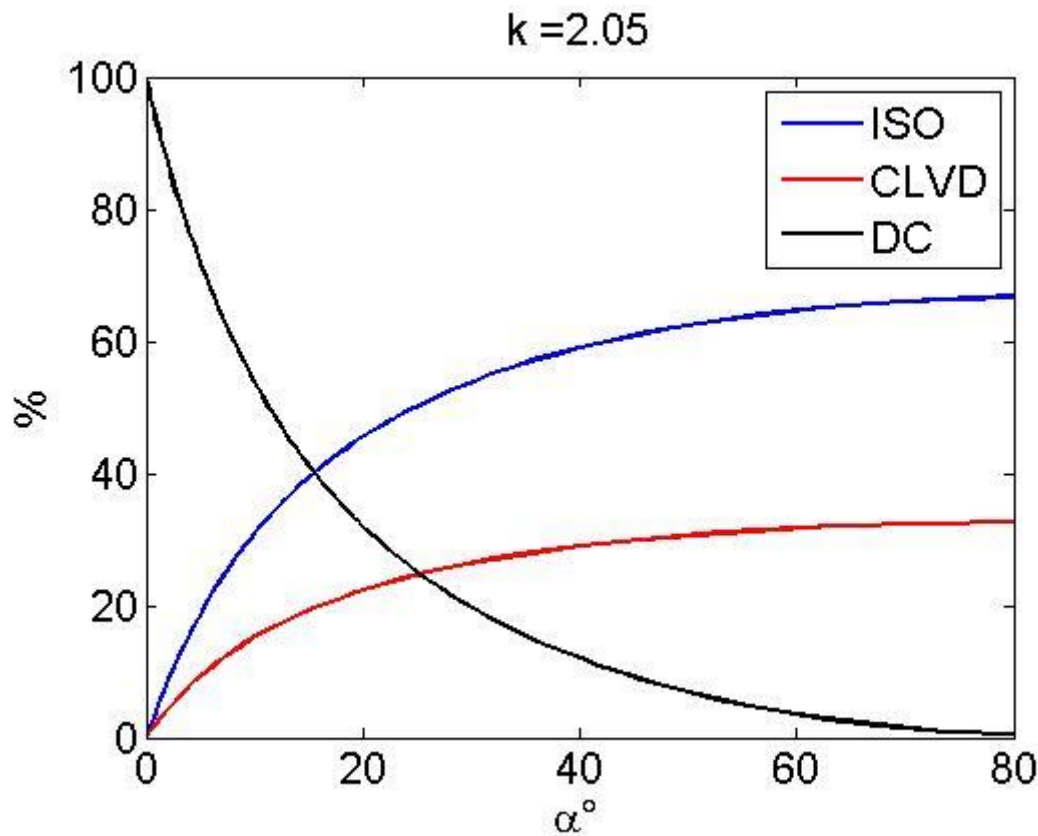
Figure 72 – Relationship between α and the double-couple (DC), isotropic (ISO) and CLVD components for the source mechanism of events with k=2.05 using the relationship of Vavryčuk, (2001).

average values for the mixed ISO/DC mechanism (Equations (64), (65) and (66) for the MT inversion of Table 14) are: α = 90°, β = 90° and ρ = -80° (Figure 18). I exclude *event 03* from the computation because the computed value of **κ** is unrealistic. A value of α = 90° means that the source mechanism is completely shear free. Thus an isotropic source or either a tensile crack should be the most probable source mechanisms.

The moment tensor inversion results for the polychromatic events are coherent between the different decomposition methods used to interpret the source type and

orientation. The decomposition of the solution including forces and the constrained inversion for the MT-only solutions suggest a *quasi*-horizontal tensile crack source mechanism. The PCA points out that the low double-couple components are irrelevant to the solution. Thus, as the events show a high degree of similarity, the tensile crack interpretation should be a reliable source mechanism for the whole set of events. The implication for such source mechanism will be discussed in the next section.

5.4.4 Interpretation of the source mechanism

The MT inversion for the polychromatic set of events points to shallowly dipping tensile cracks located roughly below the BN crater. A shallowly dipping tensile crack was also the retrieved source mechanism for the monochromatic set of events (section 5.3.2), but the volcanic activity context in which occurred the polychromatic events was considerably different. If the monochromatic events were recorded during the so-called "draining phase" this second set of events is more likely related to a "recharging phase" of the volcano. In 2010 the behavior of the volcano became mainly explosive with around 35 major explosions recorded at the summit craters (see section 5.4). On the 25th of August 2010 a powerful phreatomagmatic eruption took place from BN producing an ash plume that rose 1-2 km above the volcano summit (Patanè et al., 2013). In the next two months the volcanic activity became very weak, only some minor explosions, mainly related to ash emissions, took place at BN. During these two months the activity was mainly related to intense degassing from BN. It was at the beginning of November when the explosive activity resumed at BN and since the second half of November that near-continuous ash emissions were recorded. This new reactivation phase led to a new eruptive cycle which took place at the beginning of 2011 from the pit crater of SEC (Patanè et al., 2013). The polychromatic events were recorded on 5th and 6th of October 2010 in a period where CO_2 and SO_2 emissions at the summit craters were increasing and this anticipated the reactivation of BN (Patanè et al., 2013) at the beginning of November. I can presume that, at the time of the recordings, pressure was building up in the shallow plumbing system.

First of all, the locations obtained towards MT inversion and the INGV location are

very coherent: both point to the shallow portion of the summit craters just below BN. Thus, as BN was the most active crater at the time of the recordings, the LP events may be correlated to the BN activity. Contrariwise to the monochromatic set of events, the summit stations for the polychromatic events do not show a "pulse-like" nature, but a more elongated process. A longer process can also be inferred from the retrieved source time functions for *event 14* (Figure 68) with main component M_{zz} showing a ~8 s long source and a decaying coda until ~18 s. The higher frequency content of summit stations (Figure 58 and Figure 60) definitively points to a different source process compared to the monochromatic events, probably involving some fragile response of the rocks surrounding the source region induced by the low frequency source. Moreover, the PCA points to a full tensile mechanism. Taken all together these observations suggest that the events could represent the harmonic oscillation of a magmatic/hydrothermal reservoir repeatedly triggered by pressure steps (Lokmer et al., 2007; Saccorotti et al., 2007). The continuous degassing recorded at BN would suggest that only fluids and gas were actually permeating the shallow plumbing system supporting the hydrothermal origin of the shallow LP signals. Following the resonating fracture hypothesis I can get information about the nature of the fluids/gas involved in the process by computing the quality factor (Q) of the resonator. Q can be estimated from the LPs spectral content as (Saccorotti et al., 2007)

$$Q = \frac{f}{\Delta f}$$
(79)

where f is the frequency corresponding to a given spectral peak and Δf is the width of that peak at half the peak's magnitude. Q can be expressed as: $Q^{-1} = Q_r^{-1} + Q_i^{-1}$ where Q_r^{-1} represents the energy losses at the fluid rock interface and Q_i^{-1} represents the intrinsic attenuation in the fluid. I apply Equation (79) to the dominant frequency peak (~0.6 Hz in average for all the observed events) of the most energetic component (M_{zz}) of the retrieved source time functions. The retrieved Q values (not showed here) show similar results between the whole set of events with average Q = ~5. This value is very similar to the retrieved Q = 1.5 by Saccorotti et al., (2007) who studied thousands of LP events recorded on Mt. Etna in 2004-2005. On the opposite, the retrieved Q is significantly

smaller than those observed at other volcanoes with Q values spanning the 100-500 range (Kumagai and Chouet, 1999; Kumagai et al., 2005). Such a small Q value is of difficult interpretation as it could correspond to many different fluid/gas compositions and combinations of Q_r^{-1} and Q_i^{-1} , (Kumagai and Chouet, 1999, 2000). As found by Saccorotti et al., (2007), such a small value of Q could correspond to a crack filled with a basalt-gas or water-vapour mixtures at very low gas-volume fractions. For instance, at the retrieved LPs hypocentral depth I would expect a lithostatic pressure in the 5-10 MPa range which would correspond to a basalt with a gas-volume fraction close to "0" or to a fracture filled with bubbly water at 1-1.5% of gas volume fraction (Kumagai and Chouet, 2000; Saccorotti et al., 2007). For this computation I do not take in account for more complex fluid/gas mixtures involving other gas phases such as CO_2 or SO_2 which are strong possible candidates for explaining the acoustical properties of the shallow fluid filled cavities. I compute the volume of fluid/gas involved in the source process by means of Equations (70) and (71) as discussed in sections 2.4 and 5.3.4. Averaging the resulting volume variations for the whole set of events I obtain ΔV = 242 – 437 m^3 for the solution including forces. These volume variations are lower than those computed for the monochromatic set of events and comparable to the value obtained by Saccorotti et al., (2007) for VLP events with ΔV = 200 m^3. The retrieved ΔV values would correspond to a normal displacement of 2-4 cm for a 100 m sided square crack which is coherent with the size of the water-vapour filled crack source imagined by Lokmer et al., (2008) for the 2004-2005 Mt. Etna eruption.

The similarity between the Q values and the retrieved ΔV variations computed for the polychromatic set of events and the results obtained by Saccorotti et al., (2007) and Lokmer et al., (2008) suggest that the LPs source mechanism could be related to an oscillating fluid filled crack. The retrieved Q values suggest that the hydrothermal system is the most likely source of LP events. Nakano et al., (2003) proposed a model for the generation of LP seismicity at Kusatsu-Shirane volcano, Japan for a retrieved sub-horizontal tensile crack source mechanism similar to the one encountered here at Mt. Etna. In such a context, a magmatic source located at higher depth could transfer magmatic heat towards the surface by means of hot volcanic gases. This would provide
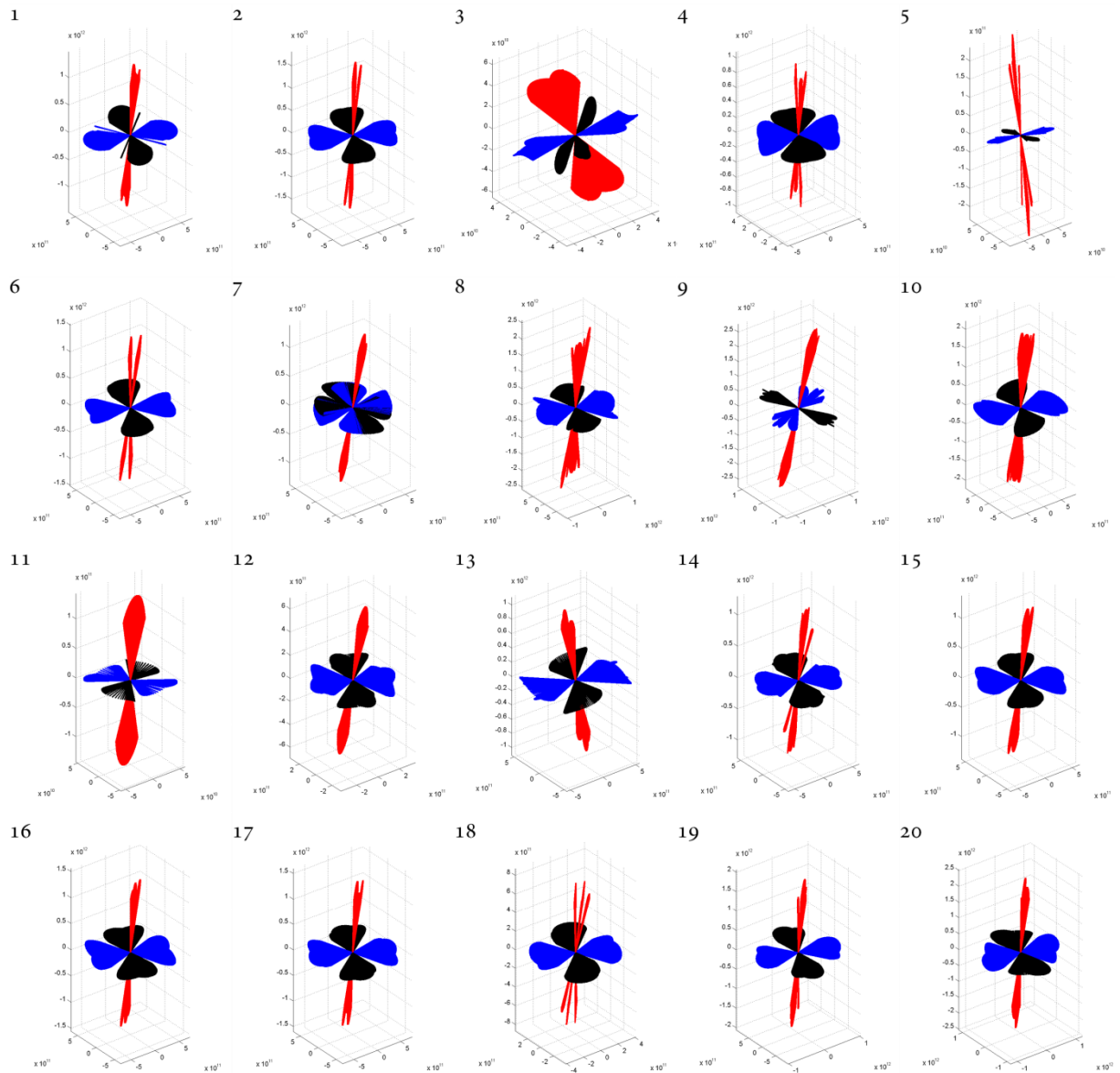
Figure 73 – Eigenvector orientations plot of the MT inversion solutions for each of the considered polychromatic events. The eigenvectors are plotted if at least one MT component was higher than 70% of the maximal absolute peak magnitude. The number of the events is reported on the top left of each sketch. Blue) x-component eigenvector; Black) y-component eigenvector; Red) vertical-component eigenvector.
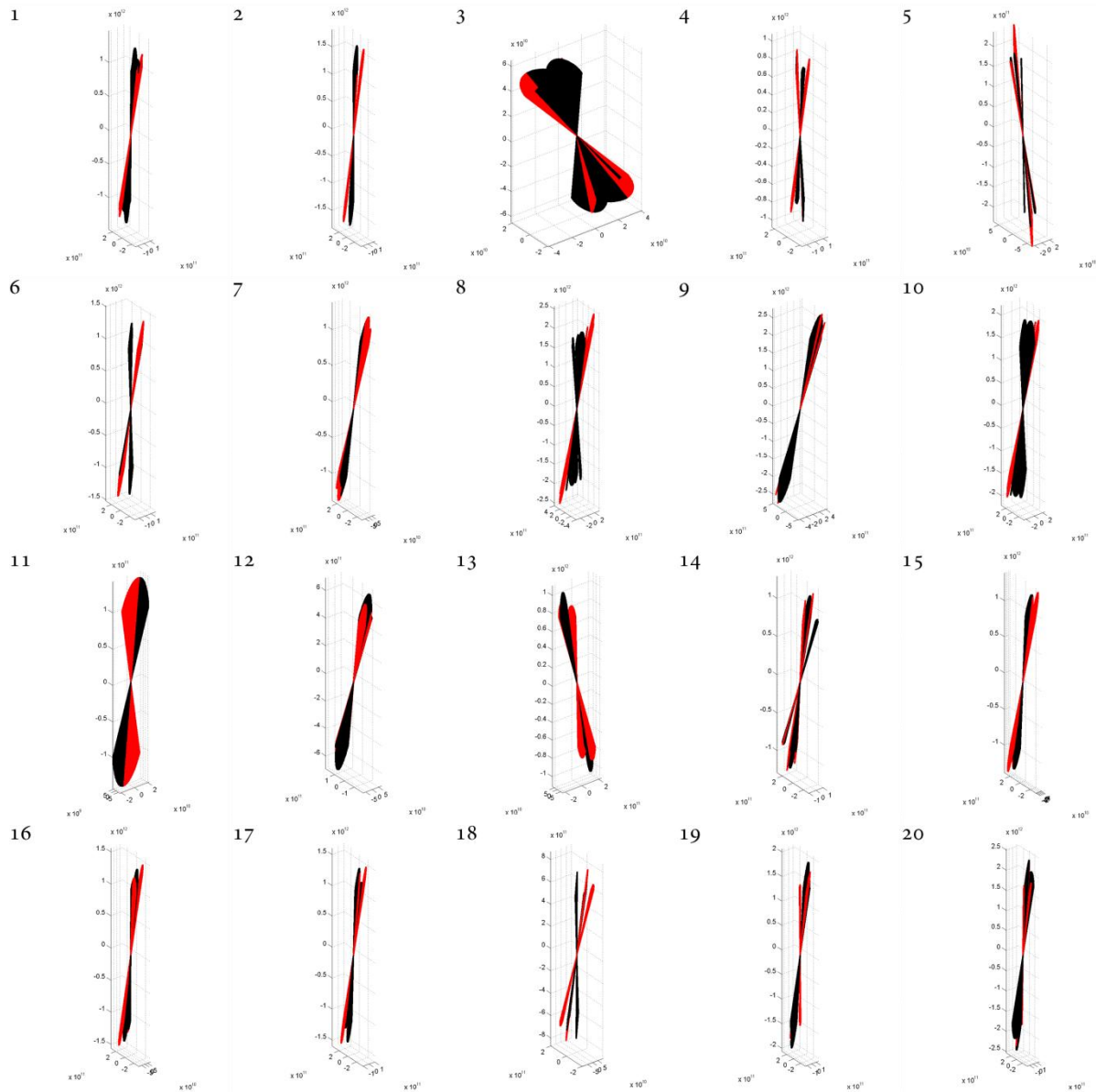
Figure 74 – Same plot as Figure 73, but only for the vertical-component eigenvector. The different colors represent first (red) and second (black) half of the STF solutions. It appears that many events show two roughly similar, but different orientations.

the energy for the generation of steam from hydrothermal water and increase the supply of gas in the resonator causing a gradual building up of steam pressure. Once a certain pressure threshold reached, the fluids would be rapidly discharged from the crack into the conduit causing the collapse of the fracture and the excitation of resonance along the crack walls (Figure 12).

Such a model would fit with the particular state of the activity of Mt. Etna at the time of the recorded LP events, but the oscillations, clearly observed in the decaying coda of the LPs recorded at Kusatsu-Shirane (see Figure 2 in Nakano et al., 2003), are not recognizable here at comparable distance from the source (Figure 58, station *ecpn*). In case of the excitation of a fluid filled crack, I would expect a main source process with a slowly decaying resonating coda. Looking at the retrieved source time functions for the solution including forces for *event 14, M_{zz}* component (Figure 64) it seems that, on the opposite, two sources delayed in time are followed by some resonating features. If I plot the eigenvectors (in time) orientations for all the studied events (Figure 73) it can be clearly seen that the solutions are very similar and point to the same mechanism orientation. It can be recognized that the vertical, and most energetic component, tends to split in two (or three) roughly similar, but distinct, directions. If I focus only on the vertical component and plot with two different colors the eigenvectors for the first (red) and the second (black) portion of the source time functions (Figure 74) it can be seen that the two main directions correspond roughly to two different parts of the source time functions. This is particularly evident for some events (*event 2, event 6, event 11, event 15* and *event 18*). Instead of a resonating source, two "pulse-like" sources delayed in time are acting together. Lokmer et al., (2008), studying the fundamental modes of resonance of a vertical tensile crack, suggested that the oscillating crack could be described by two simultaneously acting, closely spaced sources, but with opposite signs. They argued that different polarizations in the wave train could have been explained by the excitation of perpendicular modes of source resonance. Their considerations were based on the fact that waves with opposite polarization were observed before and after the eruption. It is unlikely that such excitation of perpendicular modes would be produced by two sources closely spaced in time. The hypothesis that a resonant source is at the origin of the recorded polychromatic LPs is supported by the oscillating features observed
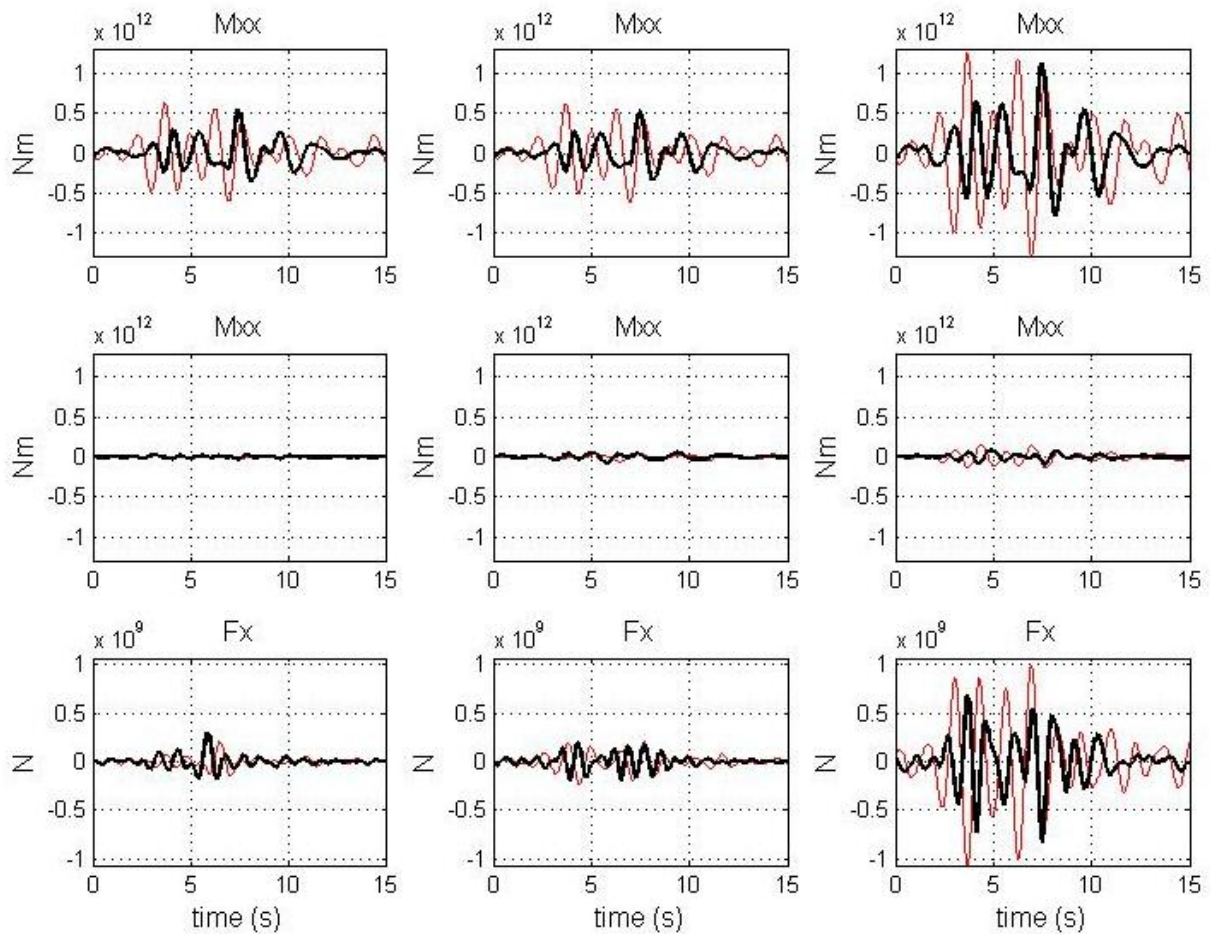
Figure 75 – Comparison between the MT plus single forces inversion solutions of event 14 using four (black) and 13 (red) stations of the INGV permanent seismic network.

for far stations (e.g. station *emcn*, Figure 59 and Figure 61), but it is not recognizable at summit stations. Looking at Figure 65 showing the fit between observed and retrieved data for *event 14*, almost perfect fit is obtained for summit stations *ebel, ecpn* and *eplc*, suggesting that, at the observed frequencies, the velocity model approximates quite well the real geological context in the near-field. For farther stations (e.g. *espc, emfo* etc.) the fit is poor due to accumulated errors in the velocity model and in the topography implementation. Hence it is inferred that the most energetic part of the retrieved MT solutions (Figure 66) comes mainly from summit stations while the oscillating-like coda contribution is mainly due to far stations and path effects or/and errors in the velocity model.

In order to test this interpretation, I perform MT inversion for *event 14* using only four of the summit stations (*eplc, epdn, ecpn* and *ebel*). As expected the misfit value between observed and retrieved data is very low (misfit = 0.130) thus the waveforms recorded at the summit stations are very well reproduced (not showed here). MT decomposition for the MT inversion including only the four summit stations points to the same source mechanism found for the solution including all the available network stations (i.e. a *sub-*horizontal tensile crack with no shear components). I plot the retrieved STF and I compare with the solution obtained including all the available stations (Figure 75). I remark that the solution obtained including only the four summit stations is:

a) similar to the full network solution, but phase and amplitude differences arise due to reduced path effects;

b) shorter compared to the full network solution, further suggesting that any resonating source process is occurring;

c) split in two different "pulse like" waveforms that can be now easily recognized.

These founding are coherent with the model proposed by Bean et al., (2014) who stated that some class of LPs recorded on volcanoes could be referred to slow, quasi-brittle, failure of rocks driven by transient upper-edifice deformation.

At the time of the recordings Mt. Etna was experiencing inflation at medium and low altitudes (Patanè et al., 2013). Close to the surface, due to reduced lithostatic pressure, the minimum principal stress direction would orient normal to the surface itself. The weak-low stiffness materials which compose the shallowest portion of the volcanic edifice would experience a ductile deformation and fractures could open parallel to the surface itself. The retrieved *quasi*-horizontal cracks could be expression of the stress field modification induced by the deformation source at depth. The intense degassing recorded at BN could play an important role and a clear correlation between deformation and seismicity has not been established yet. A simplified model for the inferred source mechanism interpretation is proposed in Figure 76.
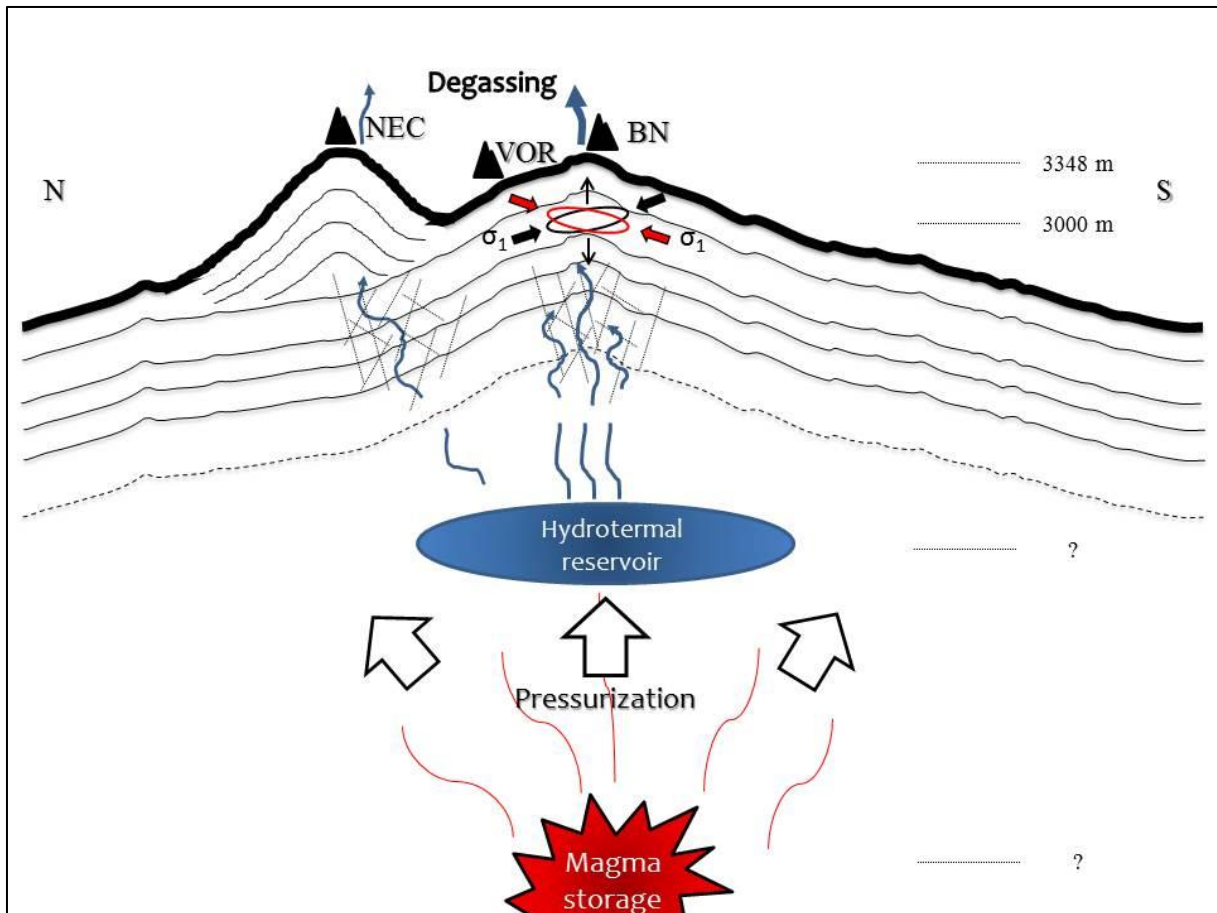
Figure 76 – Sketch of the possible source model for the polychromatic events. Degassin of a magma body or heat/fluid interactions in the hydrotermal system could have triggered pressure building up in the shallow plumbing system. Pressure could cause a modification in the stress field thus inducing the tensile opening of horizonatal cracks in the shallow unconsolidated materials. Intense degassing at the BN crater and the excitiation of shallow fluid filled cavities could also explain the LP events generation. The two sligthly similar crack orientations found for many of the considered events are reported with blac and red ellipses. Note that the sketch is very speculative and the shape of the magma body, the hydrotermal reservoir and the network of fractures below NEC and BN craters are unknown.

5.5 BN explosion (September 5th, 2013)

The last event considered in this study occurred on the 5th of September, 2013. The lava fountain which occurred at the beginning of 2011 (described in the previous section) marked the beginning of a new eruptive cycle which lasted until the end of 2012 leading to the creation of the new cone of NSEC (New South East Crater, April 2012) (Behncke et al., 2014). In 2013 the activity of the volcano continued rather intensely (Spampinato et al., 2015) with episodic lava fountains occurring at NSEC and Strombolian activity at NSEC and BN. A period of quiescence followed this sustained eruptive cycle. In the period from May to September 2013 any eruptive activity was recorded (Cannata et al., 2015; INGV internal reports). On the 5th of September a violent explosion took place at BN. This explosion produced an important morphological modification of the BN crater (Figure 77) and marked a change in the overall activity of the volcano. In the hours and days following the BN explosion an increase in the explosive activity was observed at NSEC which culminated in a paroxysmal episode on the 26th October 2013. The paroxysmal episode marked the beginning of a new eruptive cycle of eight lava fountains which lasted until December 2013 (Cannata et al., 2015; INGV internal reports). I focus my attention here on the 5th September 2013 BN explosion.
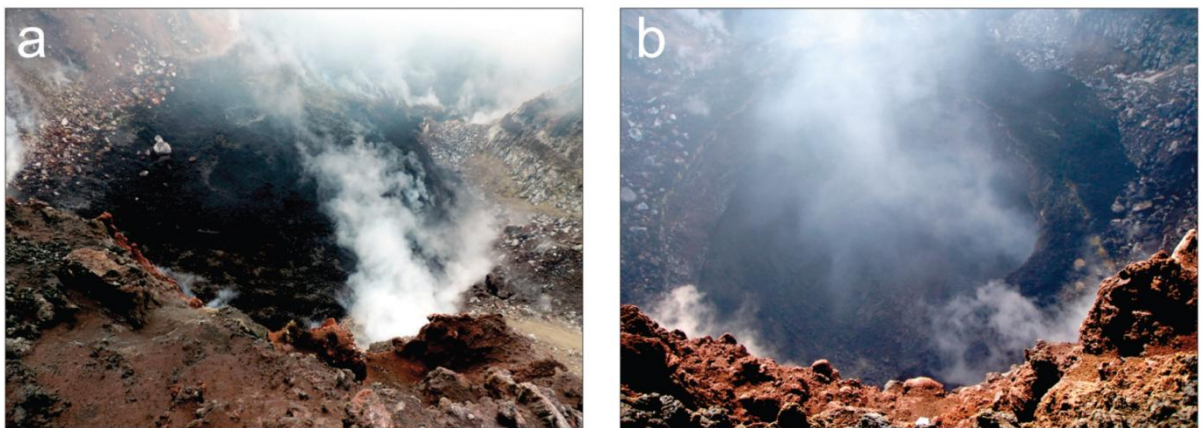
Figure 77 – Pictures taken by (a) Boris Behncke on 23 August and by (b) Biagio Ragonese on 7 September 2013 showing the inner part of BN. The solidified lava flow which covered the NW sector of BN before the explosion was replaced by a depression after the explosion. Figure reproduced after Cannata et al., (2015).
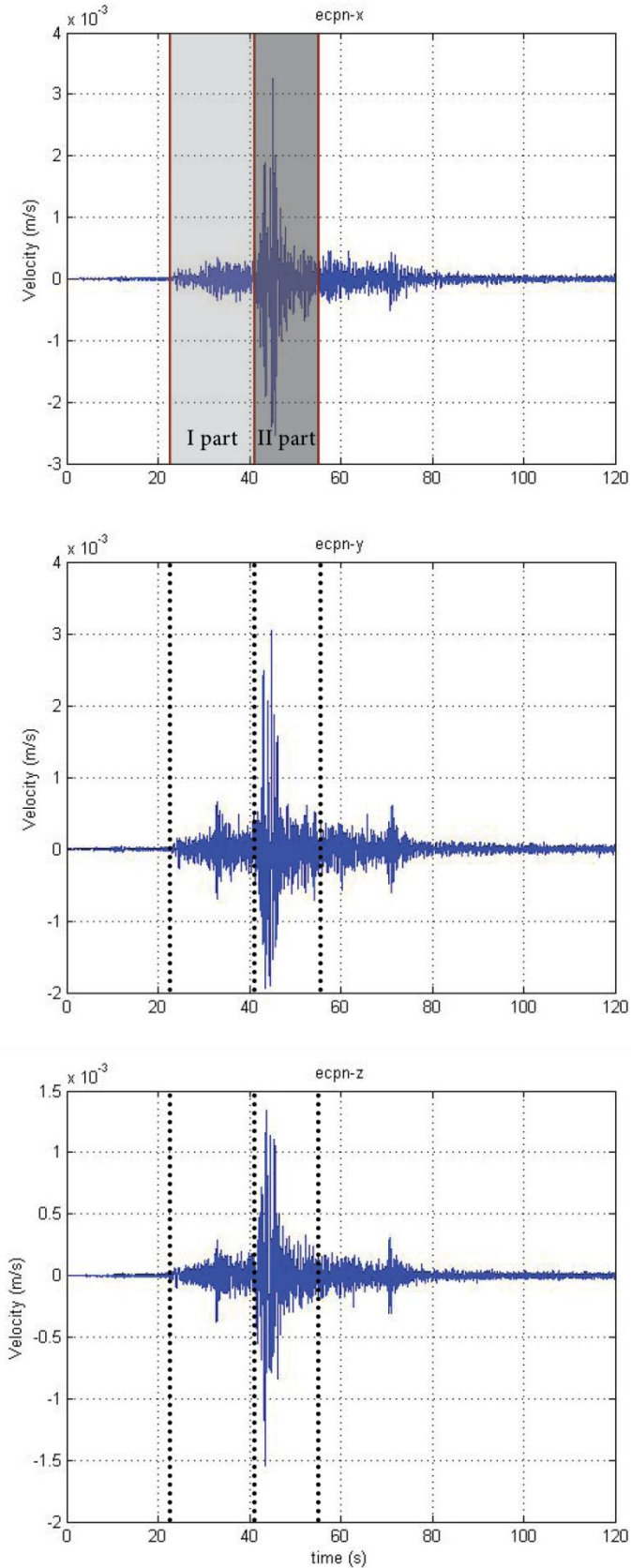
Figure 78 – Raw velocity trace of the BN explosion event recorded at station ecpn. The decomposition in part I and part II is highlighted by the dot lines.

a)

b)

c)
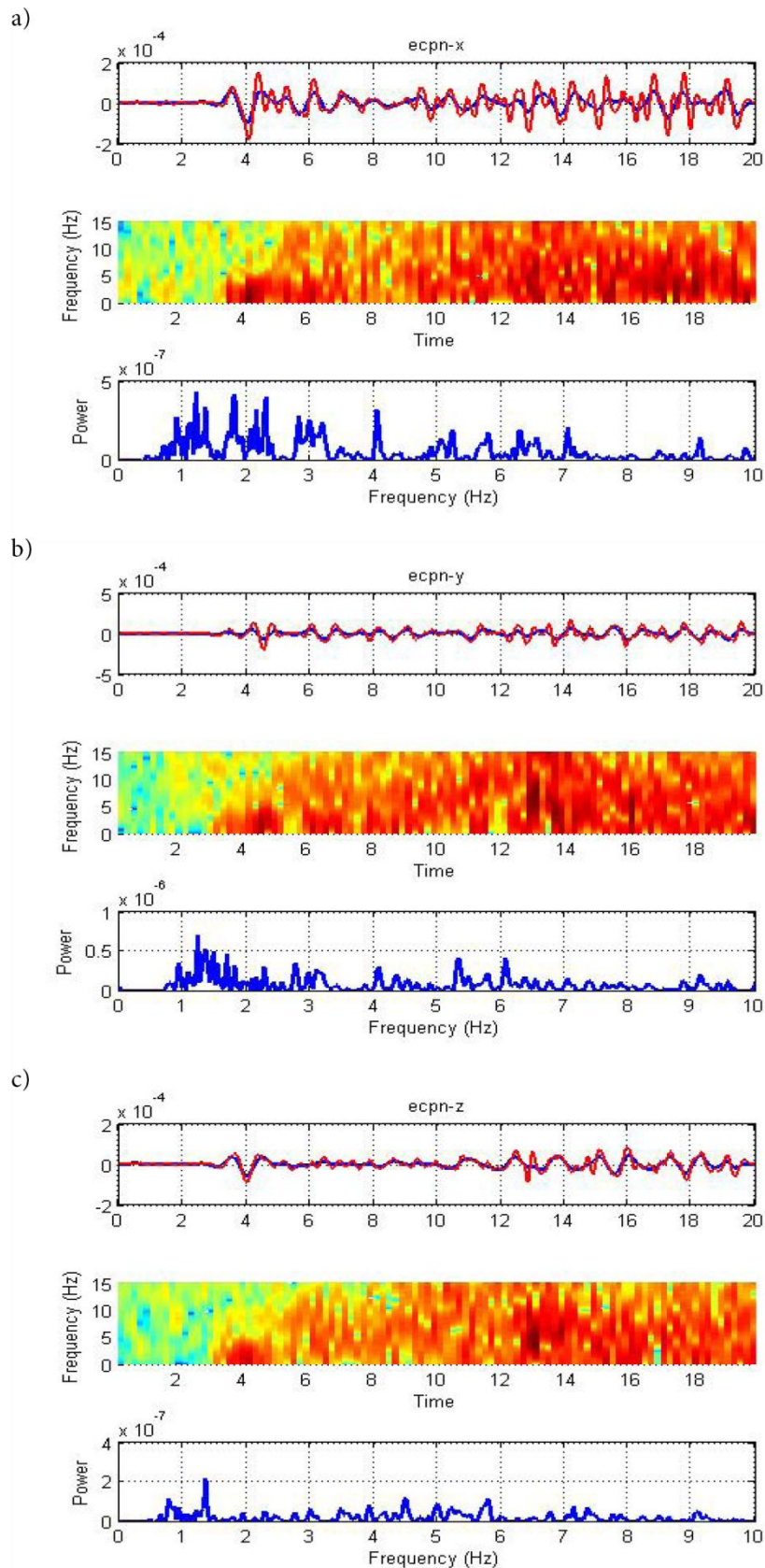
Figure 79 – a) top: x-component of velocity recorded at station ecpn for part I of the BN event. The seismic trace is filtered between 0.2 and 1.3 Hz (blue) and between 0.3 – 3 Hz (red); middle: short time Fourier transform plot of the unfiltered velocity trace, red correspond to high power towards blue lower; bottom: power spectral density of the unfiltered velocity trace. b) and c) same as a), for –y and –z components respectively

a)

b)

c)
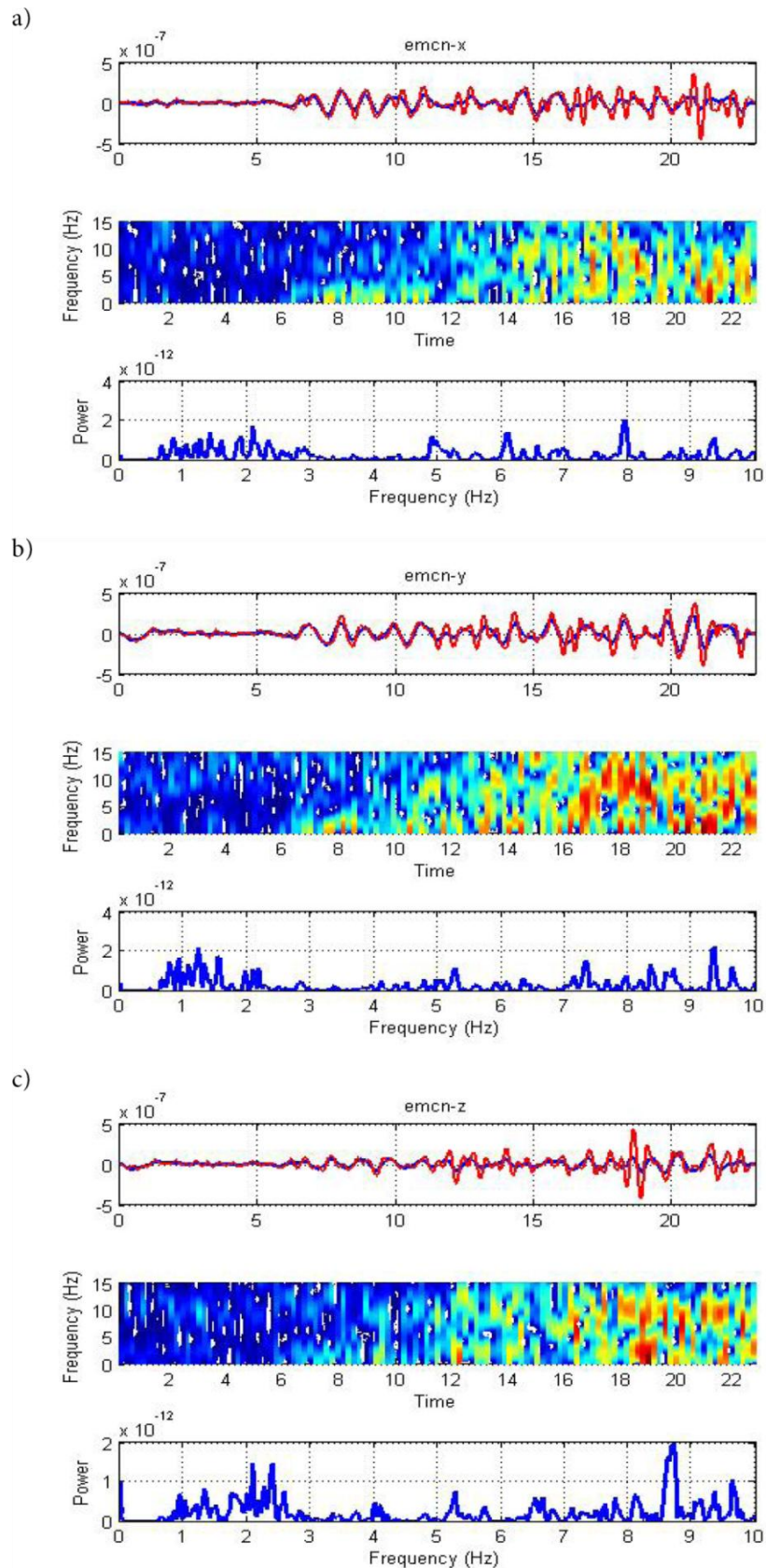
Figure 80 - a) top: x-component of velocity recorded at station emcn for part I of the BN event. The seismic trace is filtered between 0.2 and 1.3 Hz (blue) and between 0.3 – 3 Hz (red); middle: short time Fourier transform plot of the unfiltered velocity trace, red correspond to high power towards blue lower; bottom: power spectral density of the unfiltered velocity trace. b) and c) same as a), for –y and –z components respectively

a)

b)

c)
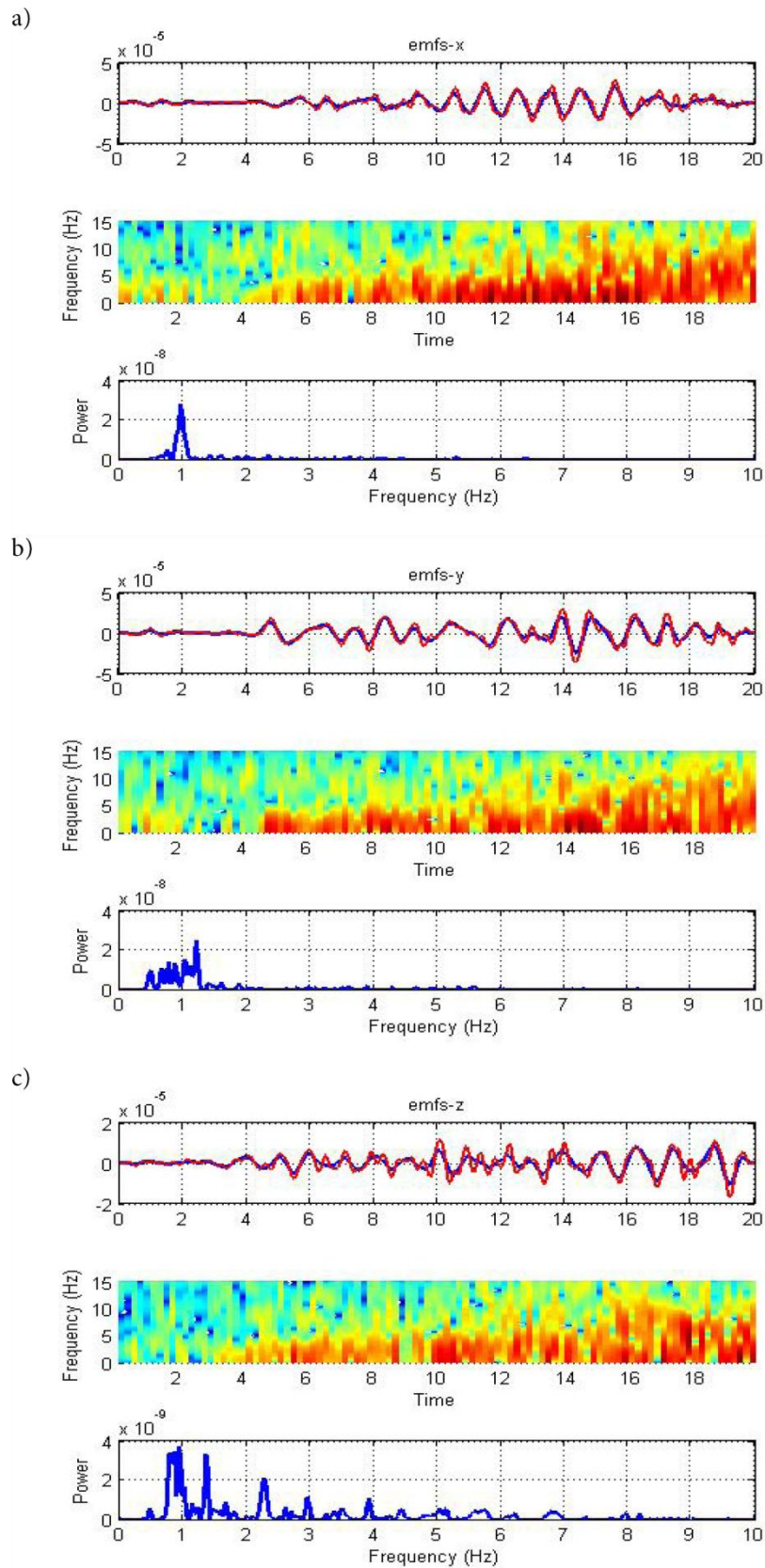
Figure 81 – – a) top: x-component of velocity recorded at station emfs for part I of the BN event. The seismic trace is filtered between 0.2 and 1.3 Hz (blue) and between 0.3 – 3 Hz (red); middle: short time Fourier transform plot of the unfiltered velocity trace, red correspond to high power towards blue lower; bottom: power spectral density of the unfiltered velocity trace. b) and c) same as a), for –y and –z components respectively

a)

b)

c)
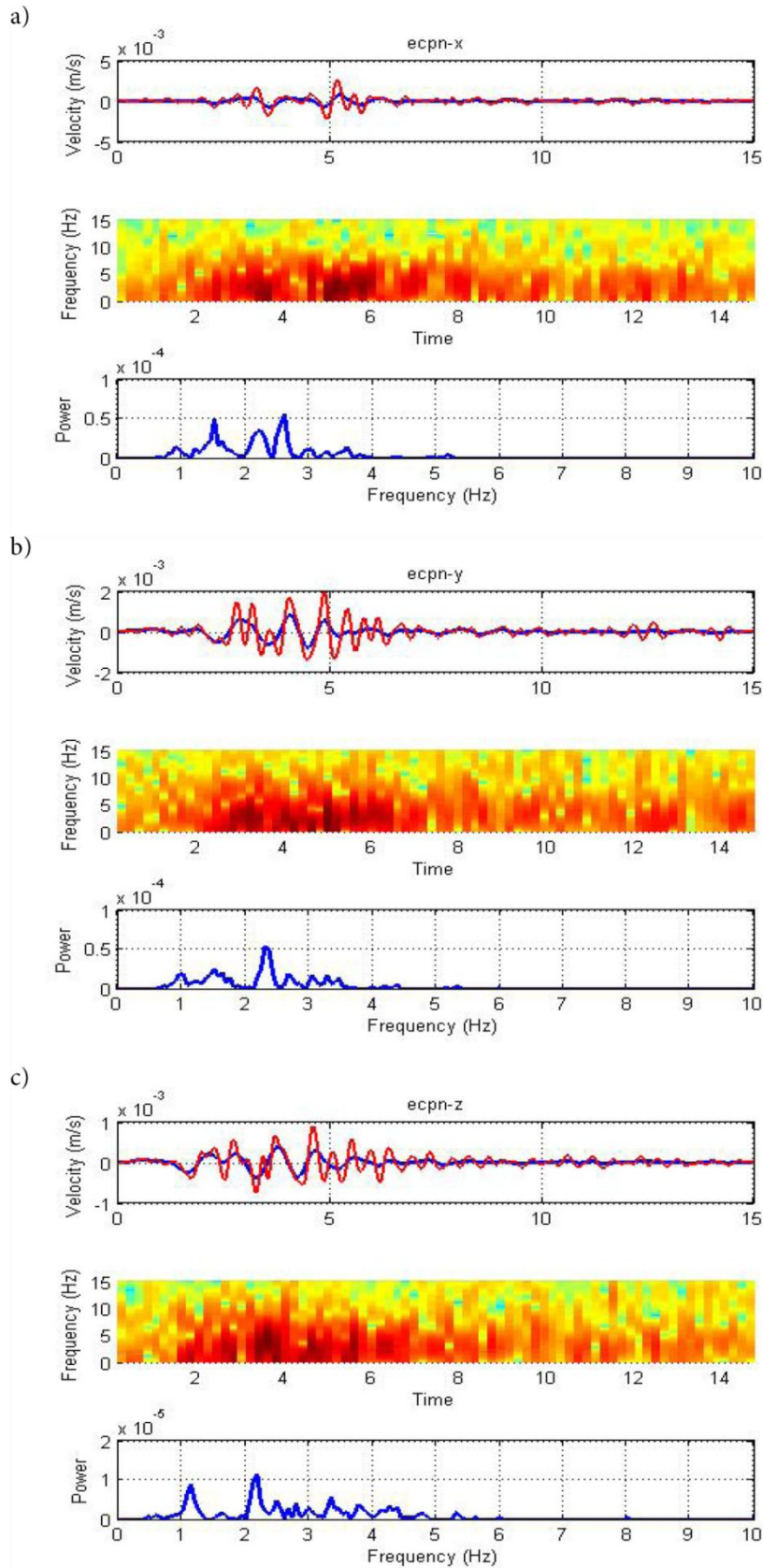
Figure 82 – – a) top: x-component of velocity recorded at station ecpn for part II of the BN event. The seismic trace is filtered between 0.2 and 1.3 Hz (blue) and between 0.3 – 3 Hz (red); middle: short time Fourier transform plot of the unfiltered velocity trace, red correspond to high power towards blue lower; bottom: power spectral density of the unfiltered velocity trace. b) and c) same as a), for –y and –z components respectively

227

a)

b)

c)
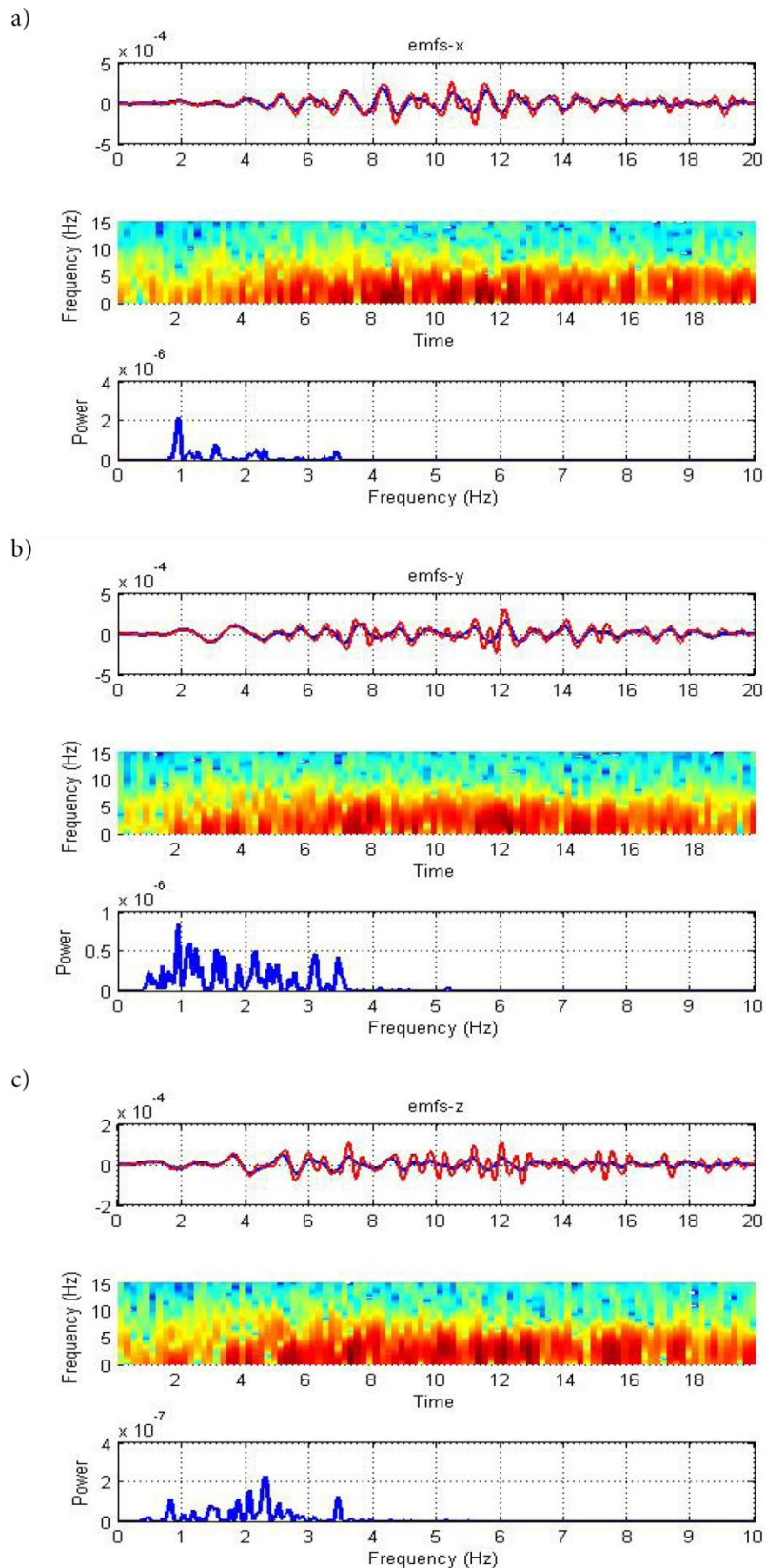
Figure 83 – a) top: x-component of velocity recorded at station emfs for part II of the BN event. The seismic trace is filtered between 0.2 and 1.3 Hz (blue) and between 0.3 – 3 Hz (red); middle: short time Fourier transform plot of the unfiltered velocity trace, red correspond to high power towards blue lower; bottom: power spectral density of the unfiltered velocity trace. b) and c) same as a), for –y and –z components respectively

5.5.1 Data

The BN explosion occurred at 15:39 on the 5th September, 2013. The seismic signal representing the three velocity components of the 120 s trace recorded at station *ecpn* is reported in Figure 78. Cannata et al., (2015) identified two main parts for the recorded signal: a) *part I* showing low amplitude and lasting ~20 s; b) *part II* more energetic with duration of ~15 s and a coda (Figure 78). Cannata et al., (2015) located the two portions of the signal separately and obtained a very shallow source for both solutions with the *part I* slightly deeper (~2500 m.a.s.l) than the one of *part II* (~3100 m.a.s.l.). They interpreted the source mechanism of the *part I* as a sudden modification in the geometry of the shallow plumbing system while *part II* was interpreted as the seismic signature of the expulsion of the BN plug then replaced by a morphological depression. Three examples for *part I* recorded at stations *ecpn, emcn* and *emfs* are plotted in Figure 79, Figure 80 and Figure 81 respectively. The seismic traces have been band-pass filtered in two frequency ranges (0.3 – 1.3 Hz and 0.3 – 3 Hz) and the spectrograms have been computed for the unfiltered signal. The second part of the signal is showed in Figure 82 (*ecpn* station) and Figure 83 (*emfs* station). Station *emcn* (Figure 80), which was used for comparison in the analysis of the previous sets of events, shows very low amplitude (10^{-7} m/s) compared to station *emfs* (Figure 81, 10^{-5} m/s) which is located at a similar distance from the summit craters. The *emcn* signal shows a very low signal-to-noise ratio and many high frequency peaks appear in the spectrogram which are different from the other stations. Hence, *ecpn* station will not be used in the MT inversion.

Both two parts of the signal show an emergent onset at all stations with *part I* showing considerably lower amplitude (~1 order of difference, 10^{-4} to 10^{-3} m/s). *Part I* of the signal shows a pulse-like low frequency onset more evident for station *ecpn* (Figure 79). After the onset the range of frequencies slowly widens. The spectral analysis shows many spectral peaks in the whole band of analyzed frequencies (0-15 Hz) especially for the nearest station *ecpn*. The high frequency peaks disappear for the farther station *emfs* where the main energy is focused in the classical LP range (0.1 – 2 Hz). A weak high frequency process is involved in the source mechanism of *part I* even if the high frequencies are less recognizable for farther stations because of attenuation. Higher

frequencies are hard to interpret toward MT inversion because they are more sensitive to velocity variations. Moreover, the Green's functions have been computed in a velocity model numerically guaranteed until ~3 Hz. Hence, the high frequency contribution to *part I* will be filtered away for the MT inversion. Thus, I will focus my attention on the low frequency part of the signal keeping in mind that while filtering, I'm missing some information about the real source process (Thun et al., 2015). On the opposite, *part II* shows a narrower frequency range (Figure 82 and Figure 83) with two main frequency peaks at ~1 Hz and ~2 Hz. The energy is centered in the classical LP frequency range, thus the source process should mainly be related to a low frequency mechanism. Hence, in order to have the inversion stable I will perform source location and MT inversion for a narrow frequency band (0.3–1.3 Hz) for both *part I* and *part II*.

5.5.2 Location results

I perform MT inversion for all the 14196 point sources in the supposed domain and obtain the best source location corresponding to the lowest residual between observed and retrieved data. The velocity traces are band-pass filtered between 0.3 and 1.3 Hz, integrated, detrended and then convolved with the source time function used for Green's function computation. Results for both the inversions including and without forces are reported in Table 18, Figure 84 (*part I*) and Figure 85 (*part II*). For comparison, I also report the location solution found by INGV obtained towards semblance and R^2 method (Cannata et al., 2013, 2015 for further details).

I start with discussing the location of *part II*. As the signal had a clear surface manifestation (the collapse of BN), I expect to find the location solutions roughly around the BN crater. The INGV solution is exactly located below the BN crater at a very shallow depth (~100 m below the surface, Figure 85). Both solutions for the MT inversions including and without single forces point to a horizontal location slightly far (~50 m) from the BN crater and the INGV location. On the opposite, the locations are very deep (~2300 m.a.s.l.) and not really coherent with the surface evidence of the BN collapse. Comparing the misfit values obtained for the whole Green's functions volume (Figure 85, *b* and *c*) the locations for both the solutions including and without forces are better constrained
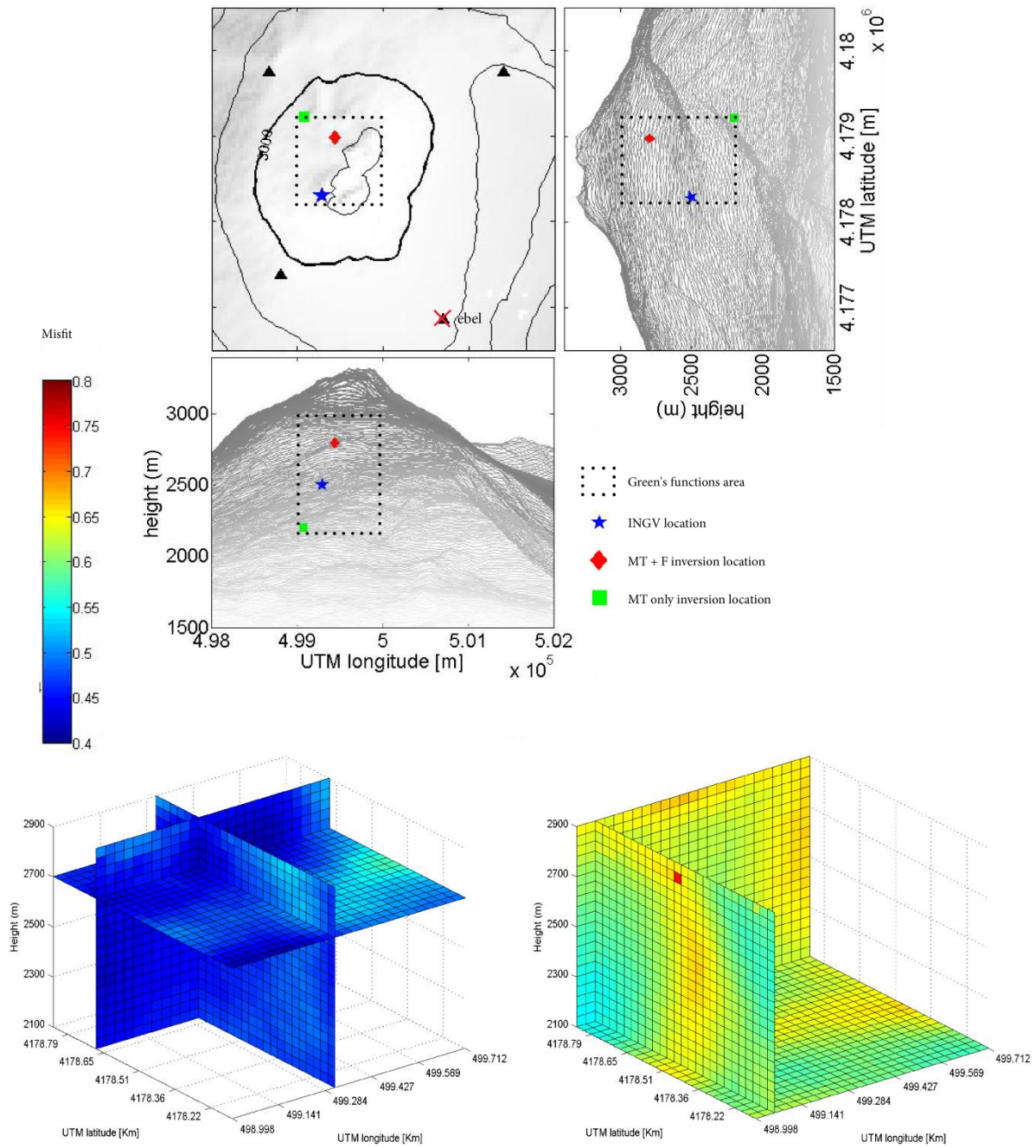
Figure 84 - Graphical representation of the location results for part I of the BN explosion event. a) MT inversion location results. The summit area of Mt. Etna with respective cuts east-west and north-south in UTM coordinates are represented. The dot line square corresponds to the Green's functions area, both solutions including and without single forces are reported. Blue star corresponds to the INGV location. b) slice plot of the residuals for the whole Green's functions volume (left) solution of MT including single forces; (right) solution for MT only.
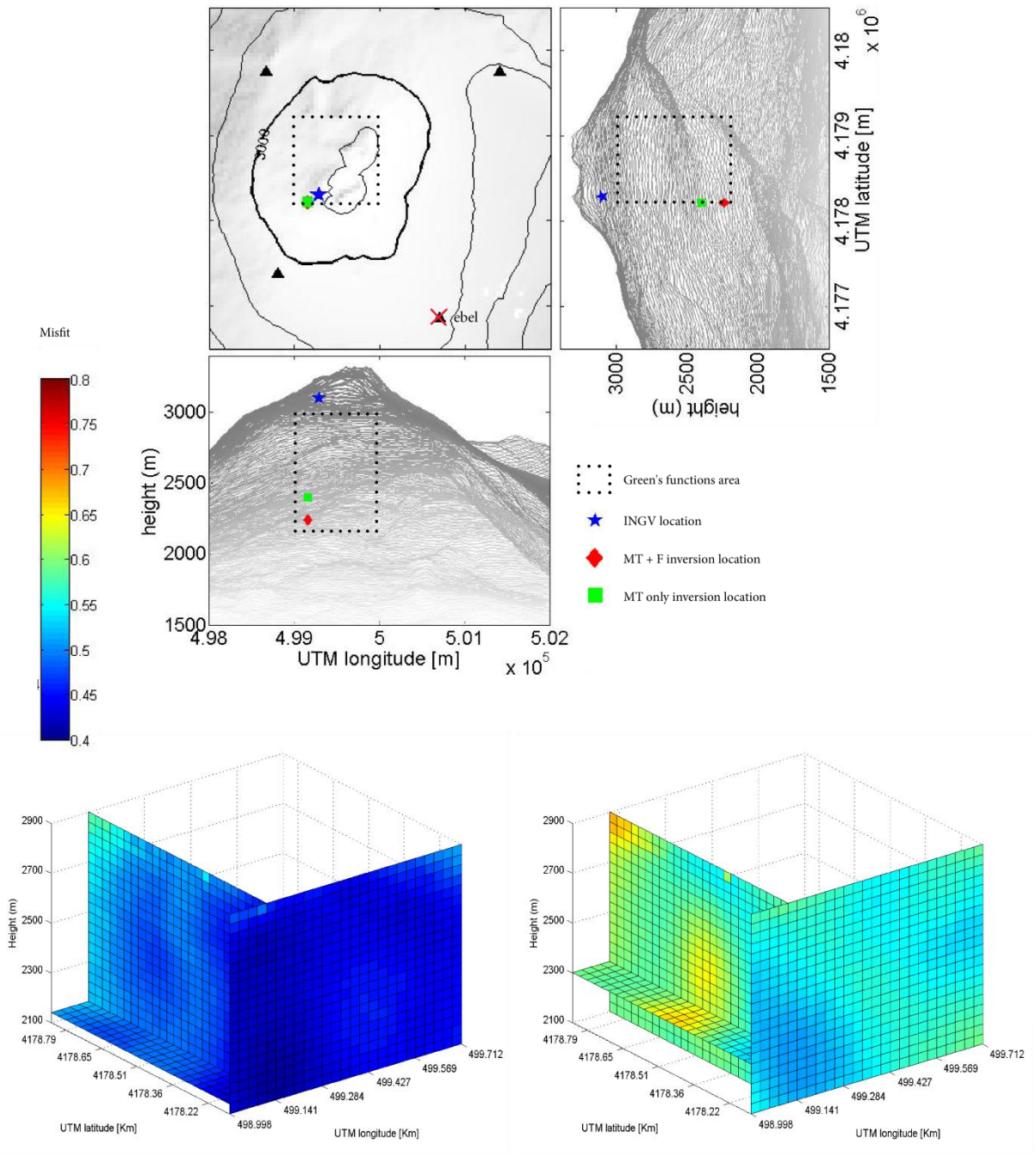
Figure 85 - Graphical representation of the location results for part II of the BN explosion event. a) MT inversion location results. The summit area of Mt. Etna with respective cuts east-west and north-south in UTM coordinates are represented. The dot line square corresponds to the Green's functions area, both solutions including and without single forces are reported. Blue star corresponds to the INGV location. b) slice plot of the residuals for the whole Green's functions volume (left) solution of MT including single forces; (right) solution for MT only.

horizontally than vertically. Especially for the solution including forces, the entire vertical column of point sources shows a little difference in residuals. As stated in the previous chapter the vertical location toward MT inversion lacks of precision. The high vertical difference between the INGV and the MT inversion solutions could come from the lack of near-field stations around the source. The stations available for the inversion (Figure 28) are mainly located far from the summit of Mt. Etna, thus path effects strongly influence the MT inversion. Recall that *emcn* intermediate field station showed low signal to noise data and that *ebel* summit station was destroyed during the paroxysmal episode of 28 February 2013, hence these two stations were not included in MT inversion. The lack of e*bel* station risks to strongly influence the results of the inversion because it was one of the four stations located nearby the summit craters and because it guaranteed good azimuthal coverage (De Barros et al., 2011) towards *Valle del Bove* in a sector poorly covered by seismic stations. The vertical weakly constrained location solution could be directly related to the low coverage of summit stations. As I cannot state *a-priori* which solution better reflects the real location, the source mechanism will be investigated for both the location found towards MT inversion and the location found by INGV.

Location of *part I* points, for both solutions including and without single forces, to the NW side of the summit craters on the opposite side of BN where is located the solution performed by INGV (Figure 84 *a*). In this case the solution including forces is ~300 m shallower than the INGV location while the solution without forces is

Table 18 – MT inversion solution location for both part I and part II of the BN explosion event. The solution is expressed in UTM coordinates (longitude and latitude) and elevation in meters. Left) solution including singles forces; right) solution for MT-only.

	M+F				M only			
	misfit	x (km)	y (km)	z (m)	misfit	x (km)	y (km)	z (m)
Part I	0.404	499438	4178980	2800	0.548	499078	4179220	2200
Part II	0.360	499158	4178220	2240	0.507	499158	4178220	2400

~300 m deeper. The residuals slightly vary between sources located at the opposite sides of the Green's functions domain (Figure 84 *b*). For both solutions with and without single forces the location is not well defined. The evidence of the explosion at the surface

suggests that the realistic location of the seismic signal should be below the BN crater. Due to the lack of stations coverage and to the intrinsic low resolution of the MT inversion location, I cannot discriminate which location is better for investigating the source mechanism. Thus I will perform MT inversion for the two lowest residuals locations and for the INGV solution.

5.5.3 Source mechanism

Moment tensor inversion is performed for both *part I* and *part II* independently. All the results for both *part I* and *part II,* for the lowest residual and for the INGV locations and for both the solutions with and without single forces are reported in Table 19.

5.5.3.1 Part I

MT inversion of *part I* shows misfit values between observed and retrieved data slightly lower than the residuals computed for the second set of events (section 5.4.3) for both the solutions including forces (misfit = 0.404) and MT-only (misfit = 0.548). The eigenvalues ratios for the two solutions are very different pointing to a crack (1 : 1.17 : 2.65) for the solution including forces and to an explosion (1 : 1.1 : 1.16) for the MT-only solution. The PCA shows coherent results with the eigenvalue ratios with C_{ISO} = 61%, C_{CLVD} = 33% and C_{DC} = 6% for the solution including forces corresponding to a quasi-horizontal (θ=11°) crack. On the opposite, the C_{ISO} = 94% for the MT-only solution strongly suggests a full isotropic source mechanism. The retrieved source time functions (Figure 86) show a complex source mechanism. For both solutions with and without single forces the source time functions imply a long source process (~10 s) and it is difficult to interpret them by any simple explication. As expected, a better fit between the observed and the residual data is obtained for the solution including forces (Figure 86). The original amplitudes of the observed signals are better recovered by the M+F solution (Figure 87 and Figure 89).

I perform a constrained inversion for both solutions including and without single forces for an explosion and a crack source mechanism. The results are listed in Table 20 and Figure 90. The explosion solution shows a slightly higher residual than the crack

Figure 86 – a) MT inversion solution including forces for part I of the BN explosion event for the lowest residual source location and 12 stations of the INGV permanent network. b) MT inversion solution excluding forces for the same event.

Figure 87 – Comparison between the observed data and the MT solution convolved with the Green's functions for part I of the BN explosion event. Blue lines correspond to the observed data and red lines to the retrieved solution. Data records for station ebel are missing. Data records for station ebel are missing. Data records for station emcn show a very signal to noise ratio and have been not considered for the MT inversion.

Figure 88 – a) MT inversion solution including forces for part I of the BN explosion event for the INGV source location and 12 stations of the INGV permanent network. b) MT inversion solution excluding forces for the same event.

Figure 89 – Comparison between the observed data and the MT solution convolved with the Green's functions for part I of the BN explosion event for the source loction found by INGV. Blue lines correspond to the observed data and red lines to the retrieved solution. Data records for station ebel are missing. Data records for station emcn show a very signal to noise ratio and have been not considered for the MT inversion.

Table 19 – Results of MT inversion including single forces for BN explosion event for the lowest residuals source location and for the INGV location. Misfit values are computed between observed and retrieved data. Mechanism decomposition and principal component analysis have been performed following the in indications of Vasco, (1989) and (Vavryčuk, 2001, 2015), see section 2.3 for details.

<u>Lowest residual location</u>

M+F	misfit	λ_1	λ_2	λ_3	φ (°)	θ (°)	C_{ISO}	C_{CLVD}	C_{DC}
part I	0.404	1.0	1.17	2.65	-39	11	0.61	0.33	0.06
part II	0.360	1.0	1.14	1.52	59	22	0.80	0.11	0.09

M only	misfit	λ_1	λ_2	λ_3	φ (°)	θ (°)	C_{ISO}	C_{CLVD}	
part I	0.548	1.0	1.1	1.16	-51	142	0.94	0.02	0.04
part II	0.507	1.0	1.21	1.76	-40	94	0.75	0.13	0.12

<u>INGV location</u>

M+F	misfit	λ_1	λ_2	λ_3	φ (°)	θ (°)	C_{ISO}	C_{CLVD}	C_{DC}
part I	0.435	1.0	1.22	1.66	6	8	0.78	0.08	0.14
part II	0.443	1.0	1.02	2.54	75	11	0.60	0.39	0.01

M only	misfit	λ_1	λ_2	λ_3	φ (°)	θ (°)	C_{ISO}	C_{CLVD}	
part I	0.572	1.0	1.42	1.58	-64	44	0.84	0.08	0.08
part II	0.577	1.0	1.89	10.56	-72	6	0.43	0.08	0.49

Figure 90 - - Constrained inversion residuals plot for orientation angles of the MT inversion solution for part I obtained for the MT inversion location. Left) solution including single forces (M+F); right) solution without single forces (M only). Red cross indicates the lowest retrieved minima misfit.

solution. For both the solutions including and without single forces the best orientation angles point to a sub-horizontal crack slightly more inclined for the MT-only solution (θ = 20° and θ = 30° for the solution including and without single forces respectively). The

residuals in both solutions are quite well constrained. I finish by computing κ and α values after the PCA. **K** value for the MT-only solution is unrealistic ($\kappa = 57$). On the opposite, $\kappa = 1.77$ for the solution including forces is similar to the value computed for the second set of events ($\kappa = 2.05$, section 5.4.3) and the corresponding $\alpha = 90°$ infers a full tensile source.

SpurioFor comparison, the MT inversion is performed also for the source location found by INGV. The misfit values are slightly higher than the solution for the lowest residual location. Both M+F and MT-only solutions lead to an eigenvalues ratio which would suggest an isotropic source mechanism. The PCA confirms the predominant isotropic component with CISO = 78% and CISO = 84% for the solutions with

Table 20 – Constrained inversion results for an explosive source and a crack source. For the crack source I also report the best retrieved orientation angles (azimuth and dip). Results are for both solutions including and without single forces.

MT inversion location

	M+F				M only			
	Misfit exp	Misfit crack	φ (∘)	θ (∘)	Misfit exp	Misfit crack	φ (∘)	θ (∘)
part I	0.582	0.531	230	20	0.879	0.757	10	30
part II	0.577	0.546	170	60	0.881	0.797	160	70

INGV location

	M+F				M only			
	Misfit exp	Misfit crack	φ (∘)	θ (∘)	Misfit exp	Misfit crack	φ (∘)	θ (∘)
part I	0.596	0.618	160	80	0.894	0.823	110	30
part II	0.625	0.591	310	60	0.865	0.794	250	20

and without single forces respectively. On the opposite, the double-couple components result in higher values for the INGV location ($C_{DC} = 14\%$ and $C_{DC} = 8\%$ for the solutions with and without single forces respectively). The retrieved source time functions for the solution including forces (Figure 88) show an amplitude almost one order of magnitude smaller than the solution found for the lowest residual location (Figure 86). This difference comes from the different depths of the source and so the different velocity

configuration between the source and the stations. The source time functions show an oscillating behavior, which is different from the pulse-like nature of the other solution. In case of a fluid-filled resonating crack I can get information about the nature of the fluid/gas involved in the process by computing the quality factor (Q, see section 5.4.4 for further details). A computed $Q = 7.5$ is roughly equivalent to the average quality factor obtained for the polychromatic set of events ($Q \sim 5$) which would correspond to a crack filled with a basalt-gas or water-vapor mixtures at very low gas-volume fractions. The solution for MT-only shows again a complex and long source mechanism, but more oscillatory than the solution found for the lowest residual location. If I perform a constrained inversion for an explosion or a tensile crack source (Table 20 and Figure 91) the retrieved misfit values are slightly lower for an explosion source thus supporting the high isotropic component found with the PCA and pointing to a full isotropic source mechanism.
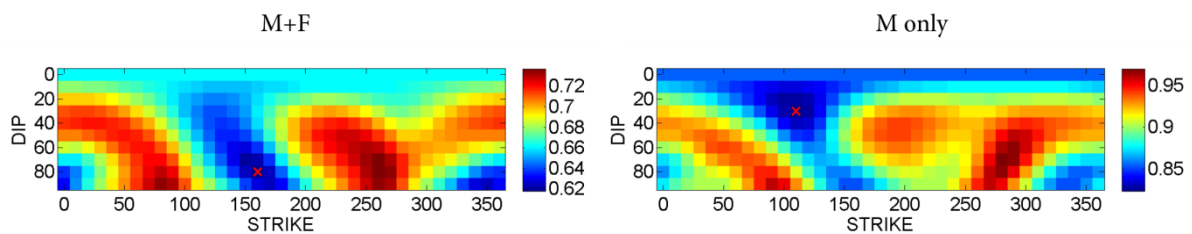
Figure 91 - Constrained inversion residuals plot for orientation angles of the MT inversion solution for part II obtained for the INGV location. Left) solution including single forces (M+F); right) solution without single forces (M only). Red cross indicates the lowest retrieved minima misfit.

5.5.3.2 Part II

MT inversion of *part II* for the lowest residual location shows slightly lower misfit values than *part I* (misfit = 0.360 for the solution including forces and misfit = 0.507 for the MT-only). The eigenvalues decomposition is similar between the two solutions which point to an eigenvalue ratio that can be attributed to an explosive source mechanism. The eigenvalues ratio is (1 : 1.14 : 1.52) including forces while it is (1 : 1.21 : 1.76) for MT-only. The PCA highlights the high isotropic component with $C_{ISO} = 80\%$ for the solution including forces and $C_{ISO} = 75\%$ for the MT-only. The source time functions for both the solutions (Figure 92) show pulse-like waveforms which appear more stable for the
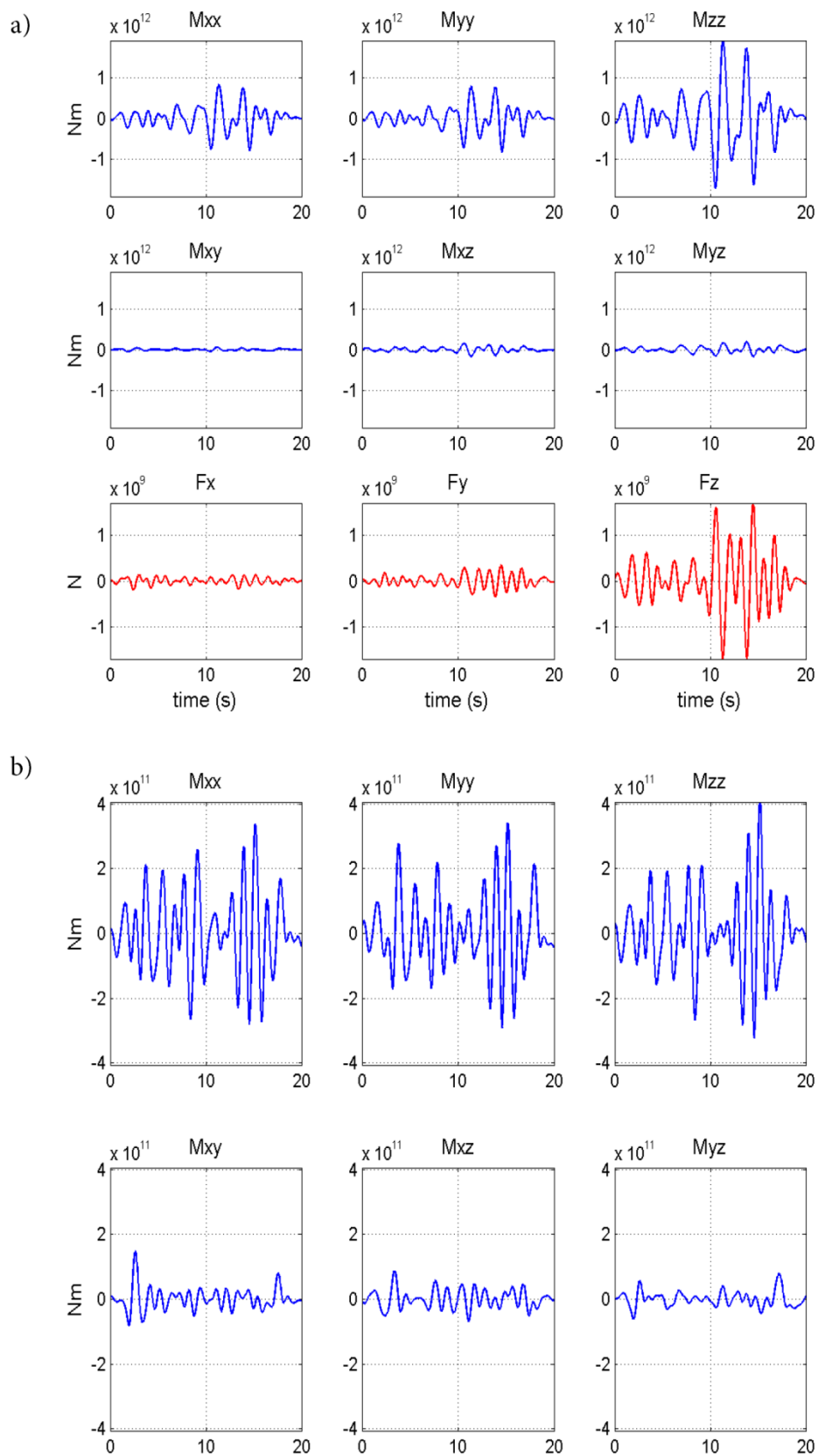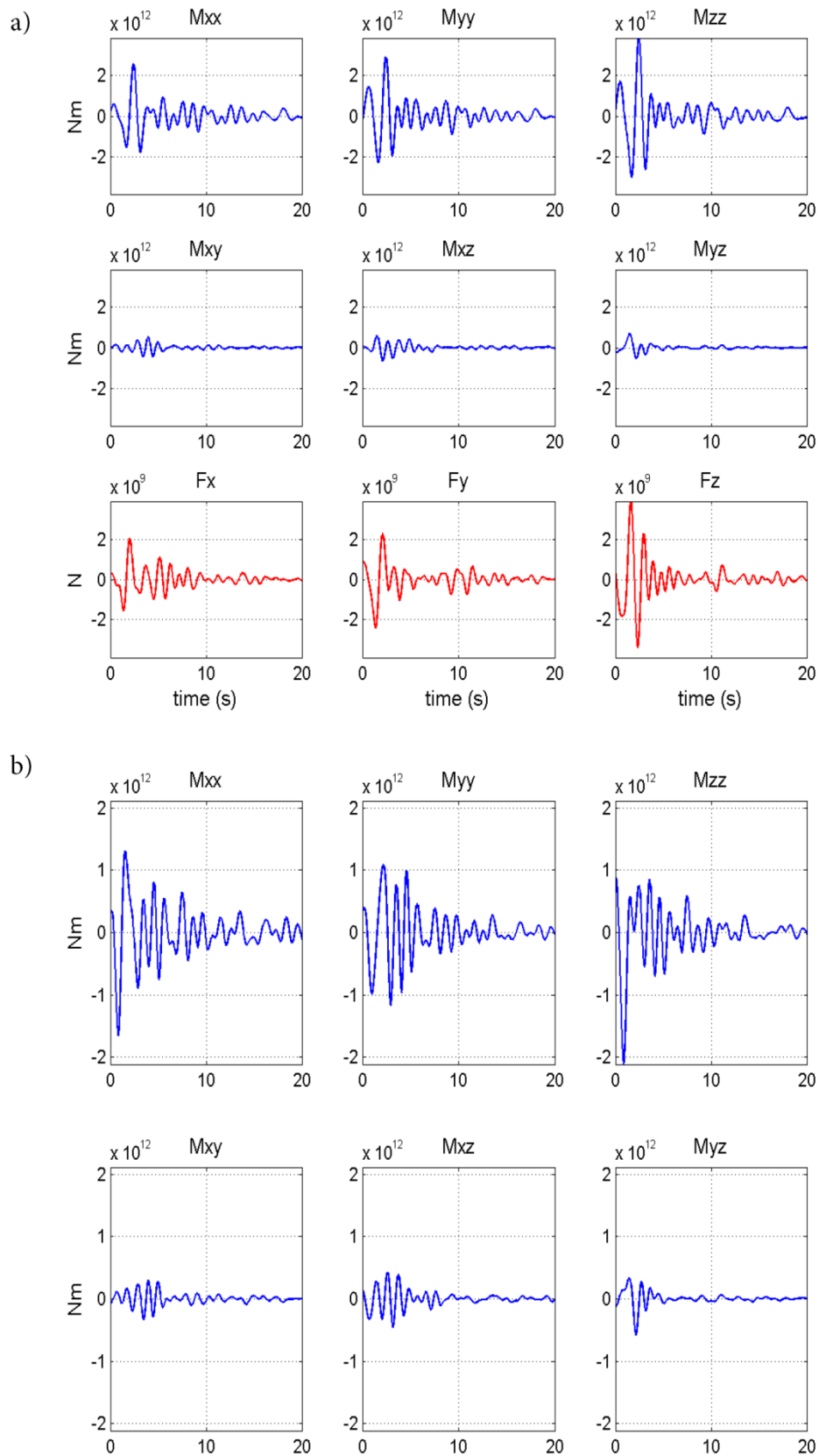
Figure 92 – a) MT inversion solution including forces for part II of the BN explosion event for the lowest residual source location and 12 stations of the INGV permanent network. b) MT inversion solution excluding forces for the same event.
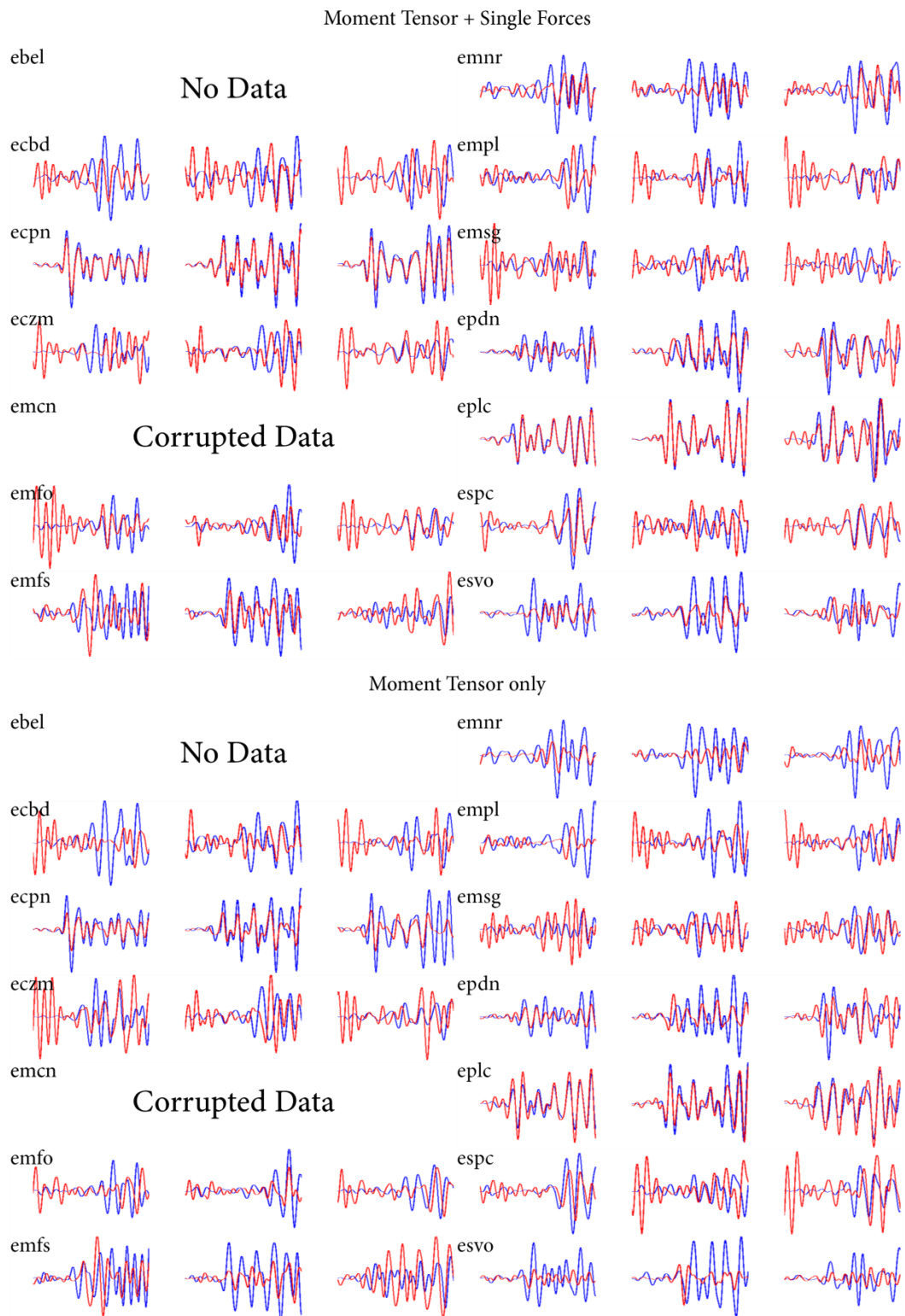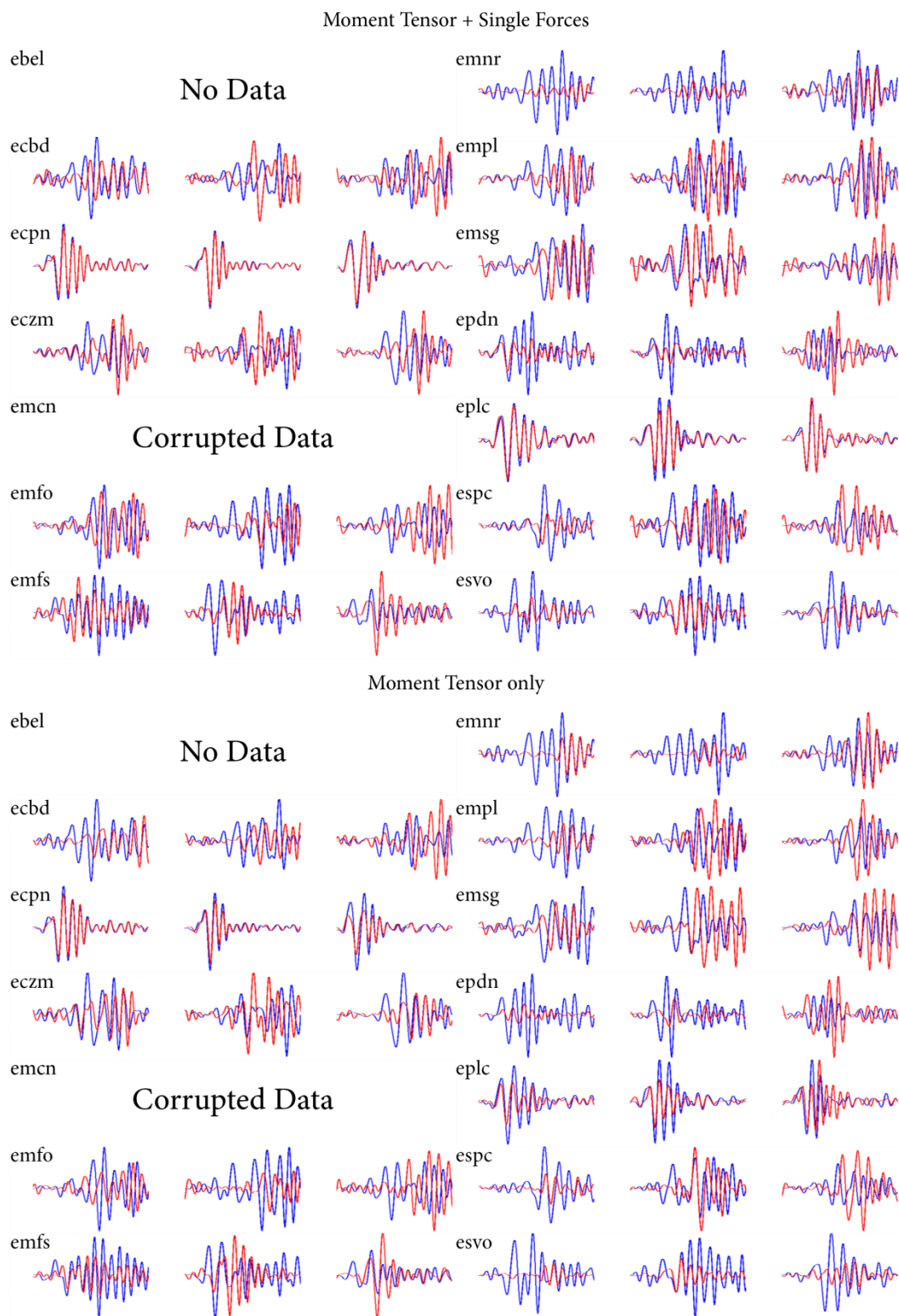
Figure 93 – Comparison between the observed data and the MT solution convolved with the Green's functions for part II of the BN explosion event. Blue lines correspond to the observed data and red lines to the retrieved solution. Data records for station ebel are missing. Data records for station emcn show a very signal to noise ratio and have been not considered for the MT inversion.
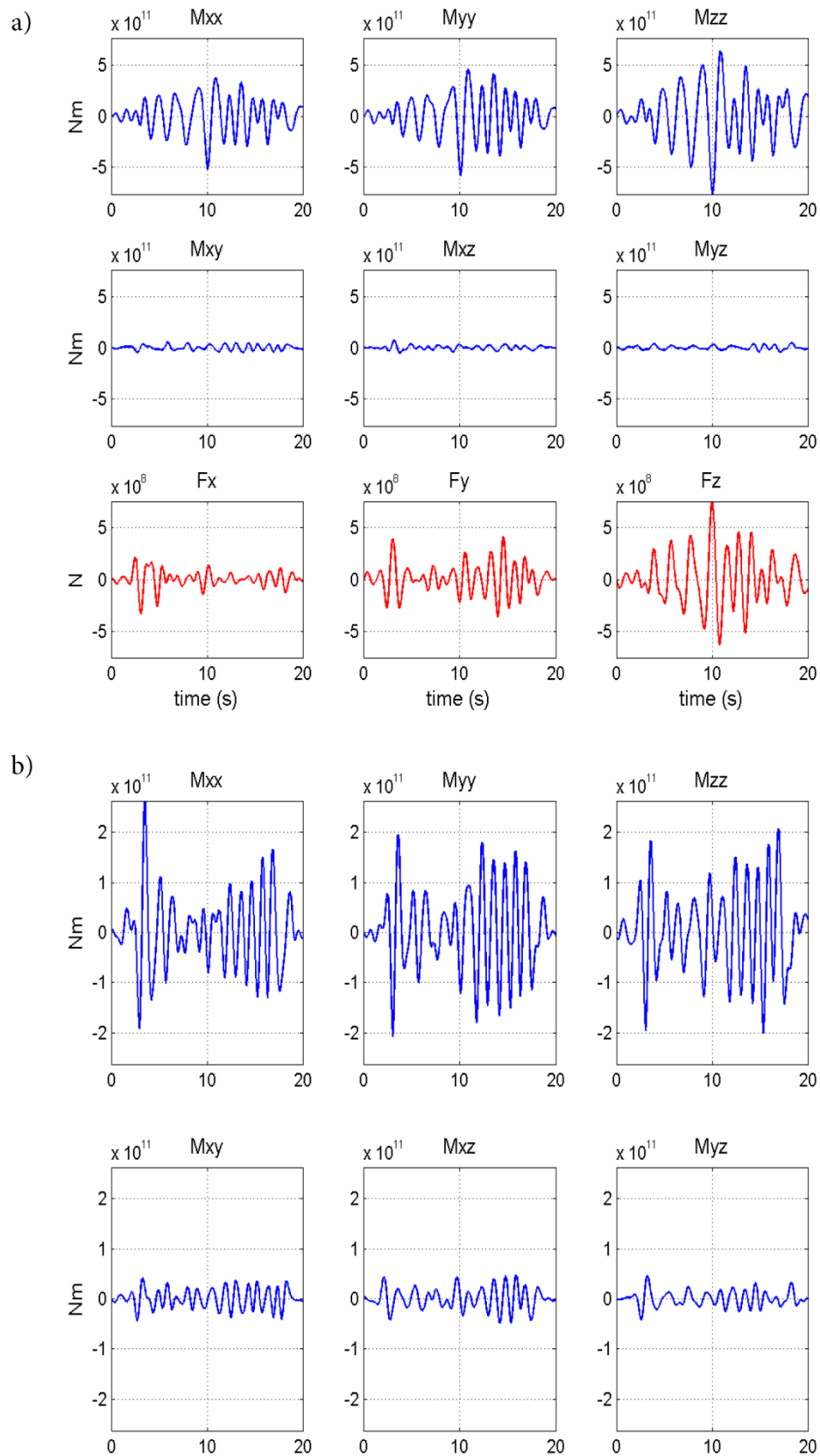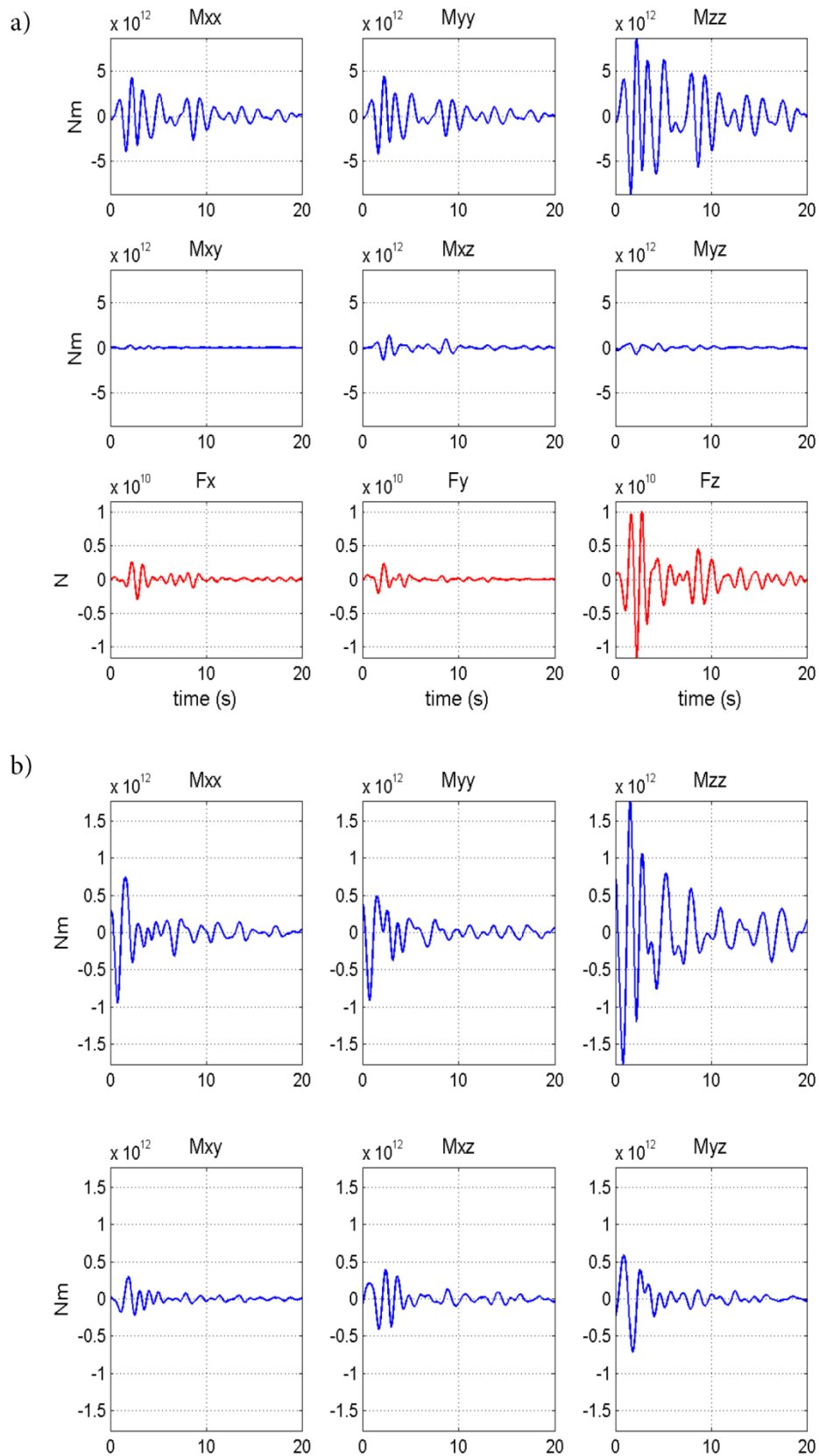
Figure 94 – a) MT inversion solution including forces for part II of the BN explosion event for the INGV source location and 12 stations of the INGV permanent network. b) MT inversion solution excluding forces for the same event.
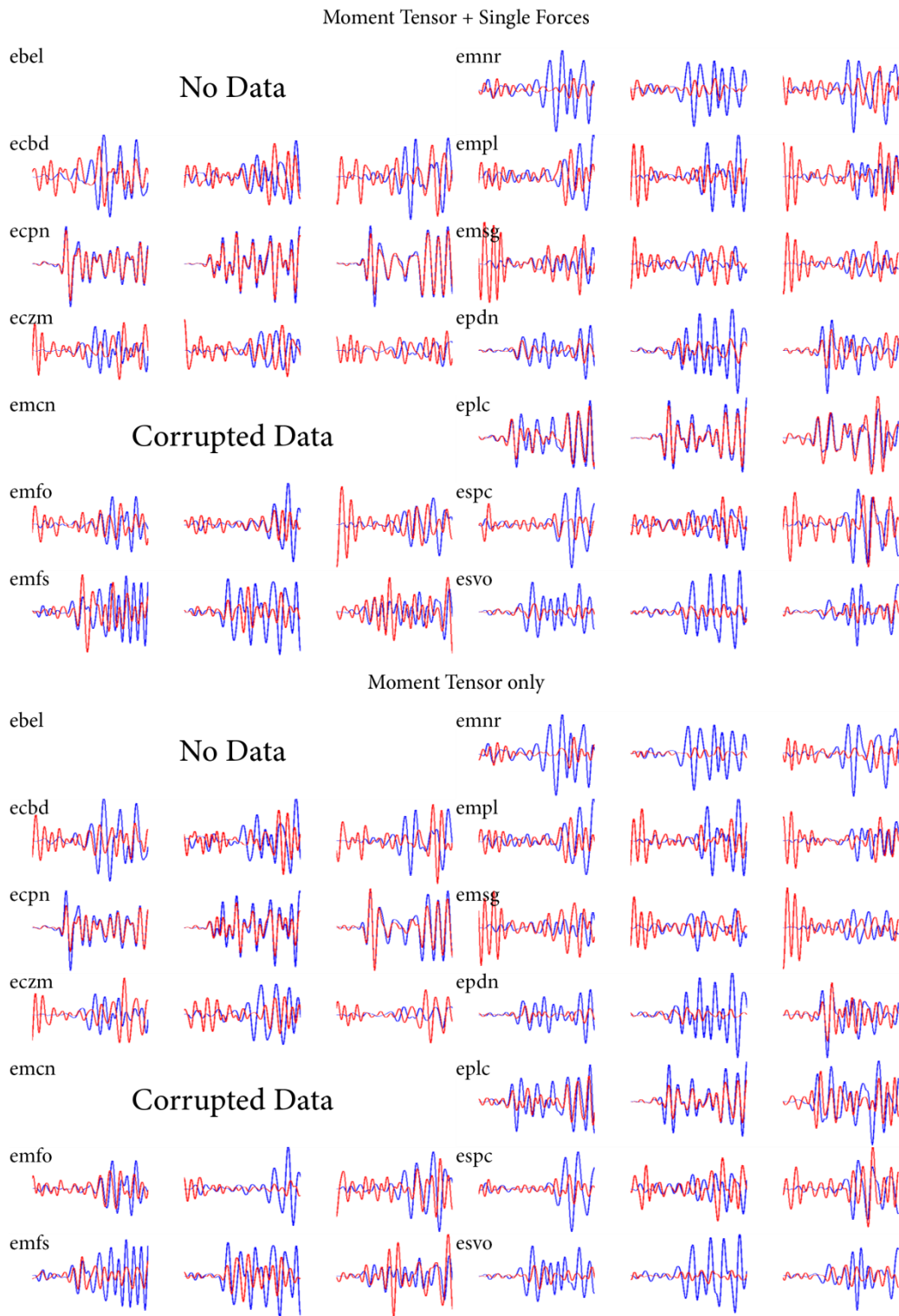
Moment Tensor + Single Forces

Moment Tensor only
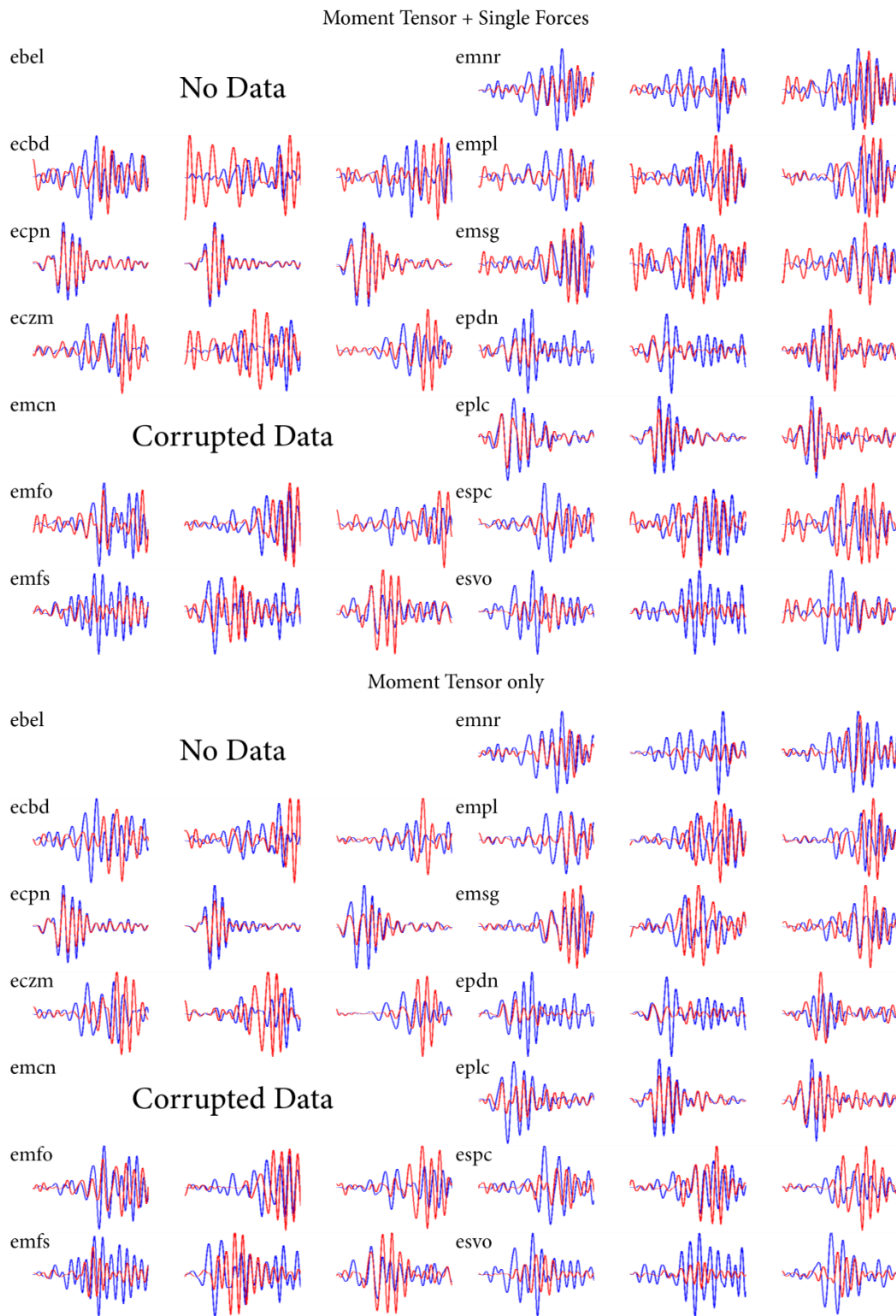
Figure 95 – Comparison between the observed data and the MT solution convolved with the Green's functions for part II of the BN explosion event for the INGV source location. Blue lines correspond to the observed data and red lines to the retrieved solution. Data records for station ebel are missing. Data records for station emcn show a very signal to noise ratio and have been not considered for the MT inversion.
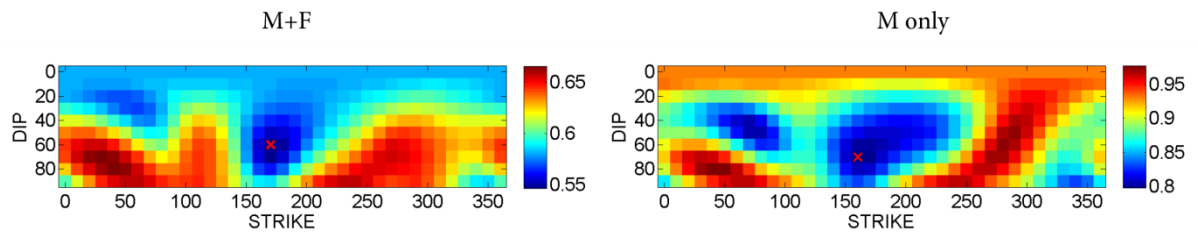
Figure 96 - Constrained inversion residuals plot for orientation angles of the MT inversion solution for part II obtained for the MT inversion location. Left) solution including single forces (M+F); right) solution without single forces (M only). Red cross indicates the lowest retrieved minima misfit.
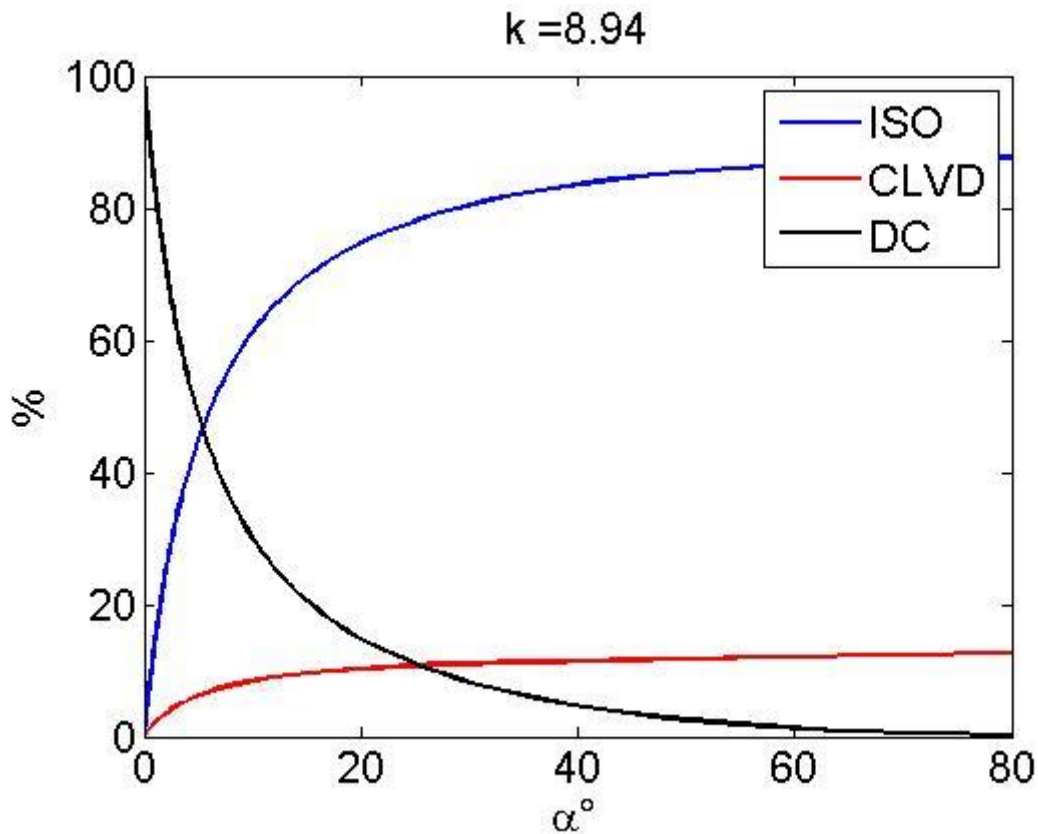
Figure 97 - Relationship between α and the double-couple (DC), isotropic (ISO) and CLVD components for the source mechanism of events with k=8.94 using the relationship of Vavryčuk, (2001).

solution including forces. Source time functions amplitudes are comparable for both solutions (10^{12} Nm) as expected because the locations are very similar. The comparison between the observed and the retrieved data (Figure 93) shows a very good match especially for nearest stations (e.g. *ecpn* and *eplc*). The retrieved synthetic data appear to be more stable than the solution obtained for *part I*. In fact for *part I* some stations (e.g. *eczm, emsg, emfo* etc., Figure 89) show some spurious oscillations at the beginning of the

signals. In *part II* these oscillations do not appear because the more precise source location and the higher signal to noise ratio of the second part of the event.

I perform a constrained inversion with and without single forces for an explosion and a crack source mechanism. The results are listed in Table 20 and Figure 96. The explosion solution show a misfit value (misfit = 0.577) slightly higher than the crack solution (misfit = 0.546) for the inversion including forces. The best orientation angles for the crack mechanism point to a north-south oriented crack inclined ~60° for both solutions. In order to investigate the role of the quite high double-couple component (C_{DC} = 9% and C_{DC} = 12% for the inversions including and without single forces respectively) I compute the values of κ and α after PCA. Both the solutions show a quite high value of κ = 8.9 (inversion including forces) and κ = 7 (inversion for MT-only). The corresponding values of α are very similar with α = 56° for the solution including forces and α = 52° for the MT-only. I plot the angle α in function of the respective percentages of C_{ISO}, C_{CLVD} and C_{DC} for the κ value (Vavryčuk, 2015) of the solution including forces (Figure 97). For the computed values of α the contribution of the double-couple component to the solution is very weak. This supports the hypothesis that the source involves a strong isotropic process.

For comparison I perform MT inversion for the location found by the INGV. The results are listed in Table 19. The misfit values are slightly higher (misfit = 0.443 for the solution including forces). The eigenvalue/eigenvector decomposition points to an

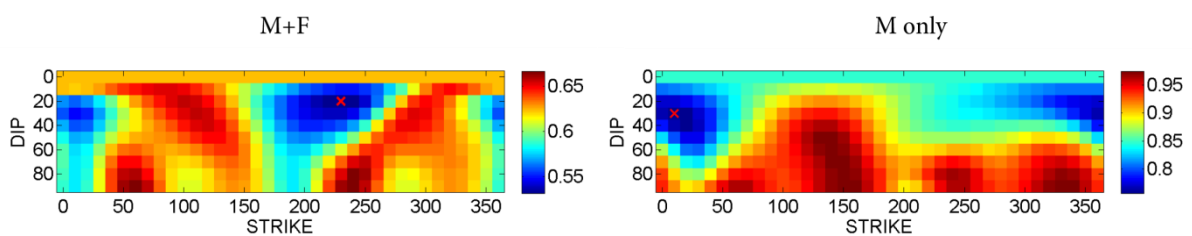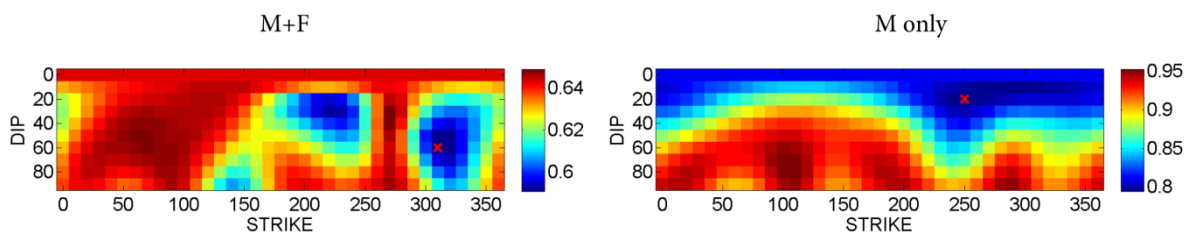*Figure 98 - Constrained inversion residuals plot for orientation angles of the MT inversion solution for part II obtained for the INGV location. Left) solution including single forces (M+F); right) solution without single forces (M only). Red cross indicates the lowest retrieved minima misfit.*

unrealistic eigenvalue ratio for the MT-only solution (1 : 1.89 : 10.56) thus the decomposition appears unstable. The eigenvalues ratio for the solution including forces points to a crack mechanism (1 : 1.02 : 2.54). I perform a constrained inversion for both solutions including and without single forces for an explosion and a crack source

mechanism, the results are listed in Table 20 and Figure 98. Lowest misfit value is obtained for the solution including forces for a tensile crack dipping 60° and oriented roughly NE-SW. The results for all the possible angle couples (Figure 98) show that in the solution including forces appear two sectors with minima residuals, i.e. the solution is not well constrained. The solution for MT-only is more coherent with the retrieved eigenvectors orientation pointing to a shallowly dipping tensile crack. The PCA shows typical values for a crack mechanism with C_{ISO} = 60% and C_{CLVD} = 39%.. The computed **κ** value (**κ = 1.36**) is comparable to the one computed for the polychromatic set of events with angle α = 90° pointing to a full tensile source. Finally, the force components are considerably higher ($F_z \sim 10^{10}$ against $F_z \sim 10^9$) than the solution obtained for the lowest residual source location and most of the energy comes from the force terms.

5.5.4 Interpretation of the source mechanism

The interpretation of the BN explosion event is not straightforward. The locations performed towards MT inversion of *part I* and *part II* are far between them (~ 1 km). On the opposite, the locations performed by INGV are consistent with the surface evidence of the event pointing to two sources located below BN and suggesting an evolution from a deeper (*part I*) to a shallower (*part II*) manifestation. Intuitively the location found by INGV could be correct. Cannata et al., (2015) used an amplitude decay method to locate the two portions of the signal. The amplitude decay method does not need for a fixed velocity model of the volcano, moreover, they used seven summit stations instead of the three used for the MT inversion solution. As stated in the previous chapter, MT inversion location is strongly influenced by the velocity model and the network of stations. If horizontally the MT inversion location of *part II* is coherent with the INGV location, the high vertical difference could come from the wrong velocity model and the lack of *ebel* summit station. On the opposite, location of *part I* is too far away from BN and it is hard to trust the solution. If I take for granted the locations found by the INGV, the MT inversion solutions point to an explosion mechanism for *part I* and to a vertical opening, horizontal tensile crack for *part II.*

Since the end of May the shallow plumbing system of Mt. Etna was becoming

progressively pressurized (Cannata et al., 2015). The authors argued that the BN plug, which formed during effusive eruptions in 2012/2013, could have limited the degassing at BN itself thus creating the conditions for the plumbing system pressurization. *Part I* of the signal could correspond to the response of the system to a fast transient pressure occurred in the main conduit just before the removal of the BN plug. The oscillatory behavior of the STF retrieved for the INGV location (Figure 88) suggests that fuids/gas could be involved in the source process (Chouet, 2003a and references therein). Moreover, the intense and shallow LP and volcanic tremor activity in the months preceding the explosion (Cannata et al., 2015) would be in agreement with a shallow fluid filled pocket containing either hydrothermal fluids or magma. An uprising hydrothermal or magmatic gas slug (Viccaro et al., 2014) could have caused pressure building up at the bottom of the BN plug, thus triggering the retrieved explosive seismic radiation. Cannata et al., (2015) imagined that the second, and most energetic part of the signal, corresponded to the seismic signature of the BN plug expulsion. Once the material failure threshold is reached, the sudden release of pressure at the bottom of the plug would have triggered the sudden removal of the plug itself. The strong vertical force appearing in the MT solution (Figure 94) would be in agreement with the downward directed drag force resulting from the rapid expulsion of the plug. A vertical expansion constrained by the rigid walls of the BN conduit would results in a horizontal crack signature in the MT decomposition.

I compute the volume involved in the process for both sources using equations (70) and (71) as explained in section 5.3.4. For the solutions including forces the computed volumes are $\Delta V = 318 - 572$ m^3 and $\Delta V = 1704 - 3068$ m^3 for *part I* and *part II* respectively. As expected the highest values are found for the most energetic *part II.* The computed volume variations for *part I* (which retrieved source mechanism is an explosion) would correspond to a displacement of the external sphere wall of $D = 25 - 44$ cm for a sphere of radius $r = 10$ m or to $D = 1 - 2$ cm for a sphere of radius $r = 50$ m. For *part II,* the retrieved volume variations would correspond to a normal displacement of $17 - 30$ m for a 10 m sided square crack or to a normal displacement of $0.68 - 1.23$ m for a 50 m sided square crack. The surface evidence of the BN collapse would suggest that the retrieved volume variations are consistent with the energetic nature of the event.
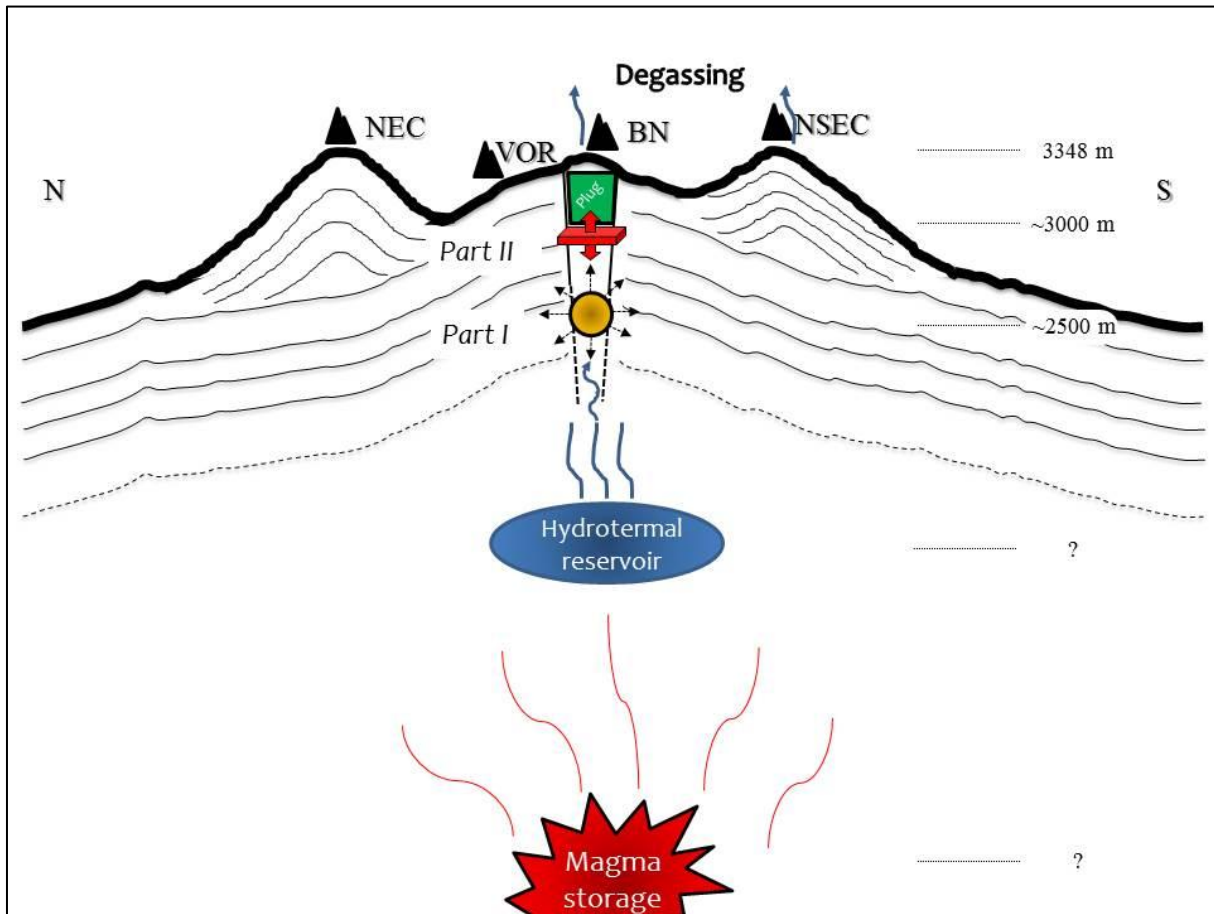
Figure 99 – Sketch of the possible source model for the seismic event accompanying the explosion occurred at the BN crater. The first part of the event could correspond to pressure building up at depth below the BN plug resulting in an explosion signature. The second part of the events, located shallower and just below the BN plug, could correspond to the seismic signature of the removal of the plug itself. Blue arrows indicate degassing. Note that the sketch is speculative and the shape of the magma and hydrotermal reservoirs are not known.

It is noteworthy that the solutions for the lowest residual MT inversion locations point contrariwise to: a) a horizontal tensile crack source for *part I* and b) to an explosive source for *part II.* The comparison between the retrieved and the observed seismic traces for *part I* shows the appearance of many parasite wavelets (Figure 87 and Figure 89) which make me doubting about the reliability of the solutions for both source locations. On the opposite, the solutions for *part II* are more stables. The large vertical difference between the MT inversion and INGV locations could strongly influence the MT inversion and thus the retrieved eigenvalues ratio. The appearance of the strong drag force for the shallower INGV location is consistent with the hypothesized source mechanism and the surface manifestation at the BN crater, thus I lean towards this mechanism interpretation

to explain the origin of the seismic trace accompanying the BN collapse (see sketch for the interpreted source mechanism in Figure 99).

Chapter 6

Conclusions

6.1 General summary

I performed MT inversion for three set of events recorded during different states of activity of Mt. Etna volcano (Chapter 5). I summarize in the following the MT inversion solutions and the corresponding interpretations:

- _Emergent onset:_ all the analyzed LP events show emergent onset and it is impossible to distinguish between _P_-waves and _S_-waves arrivals;

- _Similarity:_ high degree of similarity among then events in the same set. This suggest that, for each considered set of events, a common source process exists;

- _Frequency content_: the first set of events is highly monochromatic with main spectral energy in the typical frequency range for LP events (0.2 – 1.3 Hz). The second and the third set of events are instead polychromatic, i.e. the frequency content is not restricted in a narrow frequency band, but spans a wider frequency range (0.1 - ~5Hz). The higher frequencies are observable at summit stations (e.g. _ecpn, ebel_) while for farther stations (e.g. _empl, emfo_ etc) the higher frequencies attenuate and the spectral content becomes highly monochromatic;

- _"Pulse like" nature_: Summit stations show "pulse like" (Lokmer et al., 2007) waveforms. This feature is clearer for the monochromatic events. I have showed that the polychromatic events show instead two consecutives "pulse like" waveforms. Farther stations show a more oscillatory behavior. This suggests that the oscillating features are more path related (Bean et al., 2013) than generated by resonance phenomena occurring at the source;

- _MT inversion solutions:_ all the MT inversion solutions (except _part I_ of the BN explosion for which solution I'm less confident) point to _quasi_-horizontal tensile cracks. It is noteworthy that the monochromatic set of events seems to be

characterized by a mixed isotropic/shear source. The similarity between the solutions and the fact that no clear resonance phenomena are observed in the MT inversion solutions suggest that the source processes could not directly involve fluids/gas, but could be consequence of slow rupture within the volcanic edifice (Bean et al., 2013).

All these considerations taken together suggest that the LPs on Mt. Etna analyzed in this study cannot be explained by the classic fluid-filled cavity model proposed by Chouet, (1986) and Neuberg et al., (2000).

An alternative model based on brittle failure of melt (section 2.2.5) is proposed by Neuberg et al., (2006) for LP hybrid events recorded at Soufriere Hills, Montserrat. In their model the magma flow transition at a certain depth from a ductile to a friction controlled regime should trigger brittle rupture of magma. The released seismic energy could trigger the resonance of an adjacent resonator filled with low viscous fluids. Conditions for magma ruptures imply high viscosity magma (Tuffen et al., 2003) and that the product of shear strain rate and shear viscosity exceeds a critical value (Dingwell and Webb, 1989). Tuffen and Dingwell, (2005) and Tuffen et al., (2003) found a field evidence for brittle failure of magma in dissected rhyolitic conduits at Torfajokull, Iceland. Giordano and Dingwell, (2003) studied the viscosity of Etna alkali basalts and found that for water contents higher than 1.5 *wt%* their viscosity is comparable to that of the rhyolitic melt. They argued that the crystallinity of Etna basalts is unlikely to shift the viscosity to high enough values to generate strain-rate induced brittle failure, but that external forcing via edifice collapse or rapid cooling of magma due to rock-water interaction could. The polychromatic events could meet some of the conditions for a brittle failure of magma, but the retrieved shallow locations suggest that the high flow rate of magma imposed by Neuberg et al., (2006) would be hardly matched in the shallow plumbing system of Mt. Etna which, at time of the recording, was prevalently showing degassing at the summit craters. Without detailed magma models I cannot speculate further. Brittle failure of magma could explain some of the LPs recorded at Mt. Etna, but the low frequencies are supposed to be triggered by high frequency seismic energy which implies the existence of a resonator and recognizable oscillatory features in the recorded waveforms, also for

near stations. This is in contrast with the "pulse like" nature of the recorded waveforms, thus another source model should be invoked to explain the origin of LP events at Mt. Etna.

The "pulse like" nature of the waveforms recorded at summit stations and the oscillatory behavior recorded at far stations well match with the slow rupture model proposed by Bean et al., (2013). LP events could behave as conventional earthquakes (Eyre et al., 2015) and slow brittle failure at the source could occur, thus a mixed tensile/shear source mechanism (Vavryčuk, 2001, 2011, section 2.3.6) could be invoked. The orientation angles of the mixed source can be retrieved directly from the MT inversion solution (Vavryčuk, 2001) as done in this thesis, or through a non-linear inversion directly from the seismic observations (Vavryčuk, 2011).

The synthetic tests performed in Chapter 4 and section 5.2.2 show that unrealistic double-couple components may be misled in the solution for an original full, tensile source mechanism. On the opposite, further test (section 5.2.2) for a pure double-couple source shows that the MT inversion solution introduces unexpected isotropic components when including single force terms in the MT inversion. The synthetic tests highlight that the choice of an incorrect velocity model, which is anyway a simplification of the real geological context, may produce a fluctuation in the MT inversion solution and may lead to misinterpretation of the results. Thus, full isotropic or full double-couple source mechanisms happened to be misinterpreted as mixed tensile/shear sources. Generally, including single force terms in the MT inversion, even if they are unrealistic, "helps" in stabilizing the solution and the amount of unwanted isotropic or double-couple is reduced compared to MT-only inversion.

Another source of uncertainties comes from the station coverage. De Barros et al., (2011) pointed out that at least ten stations in the very-near field should be included in the MT inversion to obtain a reliable solution. The network available for my MT inversions of the real LP events consisted of only four Mt. Etna summit stations. The synthetic tests of section 5.2.1 highlighted that a vertical tensile crack could be misinterpreted as horizontal one in this particular network configuration. For the polychromatic set of events, the MT-only solution is less stable than the solution including forces, thus I tend to the horizontal crack interpretation. For the monochromatic set of events, both the solutions including

and without single forces are stable, but point to two opposite mechanism orientations. The horizontal crack interpretation is preferable because of the small residual in the solution. Anyway the solution is not perfectly constrained and another source mechanism could be possible.

Synthetic tests comparing the results of MT inversions performed with different velocity models and station network configurations can strongly improve the understanding and the interpretation of the source mechanism, but uncertainties still remain. In the following last section I try to give some suggestions about the designing of a MT inversion for the study of LP events on volcanoes and a brief description of the future trends in volcano seismology.

6.2 Perspectives

If uncertainties related to the structural model can be reduced by performing numerous and targeted synthetic tests, the source model itself must be addressed cautiously. One of the major issues related to the LP events understanding is that many different source models have been proposed to explain their occurrence on volcanoes (Chouet and Matoza, 2013 and references therein). None of these models can be verified or neither falsified because of the lack of direct observations of the physical mechanism at their origin. Nowadays, models are commonly validated by taking the model which shows the best fit between the observed data and the moment tensor solution convolved with the Green's functions. Bean et al., (2008) pointed out that models which give the best fit to the observed data are not necessarily representative of the true source model. The synthetic tests of Chapter 4 support this remark as the best fit is always obtained for the wrong MT solution. Similarly, a vertical crack could be misinterpreted as a horizontal one when taking the lowest misfit solution (section 5.2.2).

In the synthetic tests the source representation is the same in the direct and in the inverse problem. Thus, it is not the source model which is tackled itself, but the ability of the inverse problem in retrieving the original known solution. The new source models proposed in the last decades (e.g. Bean et al., 2014; Iverson, 2008; Neuberg et al., 2006) are counterpoised or complementary to the most accepted resonating crack LP source

model (Chouet, 1986; Neuberg et al., 2000). At present, LP events show similar frequency content with different, but very common features everywhere. Hence, the question is whether any of the source models mentioned above is applicable and adjustable for each context. However, the observations may contain additional information about the physical source processes which have not been investigated yet.

One example of new implications for LP seismicity was investigated recently by Thun et al., (2015). The authors were able to uncover a step-like displacement component from LP signals, outside the common spectral range of analysis for this kind of events. LP events could contain information about both translational and rotational motion when analyzed in a broader frequency band. At present, rotational motion is measured with tilt meters or GPS while translational motion through seismometers. It is well known that horizontal components of seismometers are also sensitive not only to translational motion but also to tilts (Graizer, 2005; Rodgers, 1968) which is normally interpreted as very long period noise in the recorded signal. Fournier et al., (2011) suggested that translational motion and ground tilt contribution to tilt meters and seismometers could be quantified by comparing with high-rate GPS measurements, but only in case the deformation amplitude is large enough (> 1 mm, due to the low signal to noise ratio of GPS data). Van Driel et al., (2015) and Maeda et al., (2011) proposed to compute directly the Green's functions including both the seismometer's response to translational motion and the tilt contribution. Chouet and Dawson, (2015) successfully applied this approach to some VLP (very long period) events recorded at Kilauea Volcano, Hawaii and were able to recognize one cycle of inflation/deflation of a volumetric source.

The tilt contribution to the signal should be relevant only when considering VLP events, but if in general events are to be analyzed in a broad frequency band, such an approach can be useful. For example, Thun et al., (2015) investigated the step-like displacement component associated to LP seismicity. An issue is that displacement steps have a broad spectrum, including static (or zero) frequencies. The authors suggested the implementation of a moving median filter to overcome this problem and successfully applied their method to displacement steps obtained in laboratory controlled experiments. The median filter was applied to some LP events recorded on Turrialba volcano, Costarica and Mt. Etna and they found that numerous "pulse like" LP events

included step-like displacement. If LP events are expression of both translational motion and ground deformation, two main issues arise concerning MT inversion:

1. *Frequency content*: in order to get stability, MT inversion is performed for filtered signals. In my case the signals have been band-pass filtered between 0.3-1.3 Hz. Thus any information relative to any possible static displacement (0 Hz) is lost during filtering;

2. *Green's functions*: Green's functions for the seismic response of the Earth's medium are usually not designed to take in account for static displacement.

One recent approach to get more insights into volcano seismicity is the multiparametric study of different monitoring parameters (e.g. Cannata et al., 2015; Jousset et al., 2012, 2013; Patanè et al., 2013; Rivet et al., 2014; Spampinato et al., 2015; Takeo et al., 2006). By comparing volcano seismicity with other monitoring techniques, the seismic source can be constrained to a certain range of possible physical processes and uncertainties accompanying the interpretation of the solution in MT inversion can be reduced. If LP events are suspected to contain static ground displacement, joint-analysis with InSar, tilt or GPS techniques would help in minimizing the intrinsic error of the MT inversion.

In conclusion many lessons have been learned through the synthetic tests and the MT inversions of real Mt. Etna LP events recorded during different states of the volcanic activity. Hopefully these will contribute to design future analysis of LP events in volcanic contexts with a special regard to Mt. Etna volcano. Many of the points highlighted in this thesis are consistent with the other recent works (e.g. Bean et al., 2008; Cesca et al., 2008; De Barros et al., 2011; Eyre et al., 2015; Lokmer et al., 2007, 2008). Recommendations include:

- *Synthetic tests:* synthetics tests should always be performed in order to better design the MT inversion and help in constraining and interpreting the solution.

Three main points should be addressed when designing a synthetic test:

1. *Velocity model:* if possible, different velocity models should be compared. Computing the Green's functions for different velocity models is computationally expensive, but the results can help in constraining the solution when dealing with real data;

2. *Number of stations and distribution:* use a dense network of stations especially in the summit region (close to the source). At least one station should be located as close as possible nearby the source in order to accurately extract the source signature;

3. *Source models:* different source mechanism and orientations should be simulated in order to test the sensitivity of the MT inversion to the velocity model and the network of stations.

- *Source location from different methods:* source location from MT inversion lead sometimes to rough locations (especially vertical location). Other location methods such as amplitude decay, cross-correlation coefficient and semblance (e.g. Cannata et al., 2013 and references therein) should instead be used;

- *Multiparametric approach:* comparing volcano seismicity with other monitoring techniques such as fluid/gas geochemistry, acoustic and deformation will strongly improve the understanding of the source mechanism of LP events;

- *Green's function including ground tilt contribution:* if tilt is recognized to play an important role in the observed LP events, implementation of ground tilt in the Green's functions will help in getting a wider picture of the source process and its link to the volcanic activity;

- _Filtered signals:_ Careful attention should be paid when filtering the LP events. Important information relatives to the source may be lost during the filtering process.

All these considerations taken together should lead to a better understanding and interpretation of LP activity and could help in clarifying its significance in terms of an eruption forecasting tool.

References

Aiuppa, A., Cannata, A., Cannavò, F., Di Grazia, G., Ferrari, F., Giudice, G., Gurrieri, S., Liuzzo, M., Mattia, M., Montalto, P., et al. (2010). Patterns in the recent 2007–2008 activity of Mount Etna volcano investigated by integrated geophysical and geochemical observations. Geochem. Geophys. Geosystems *11*, n/a – n/a.

Aki, S., K., Fehler, M., and Das, I. (1977). Source mechanism of volcanic tremor: fluid-driven crack models and their application to Kilauea eruption. *2*.

Aki and Richards (2002). Quantitative Seismology, Second Edition. (University Science Books.).

Alidibirov, M., and Dingwell, D.B. (1996). Magma fragmentation by rapid decompression. Nature *380*, 146–148.

Allard, P., Behncke, B., D'Amico, S., Neri, M., and Gambino, S. (2006). Mount Etna 1993–2005: Anatomy of an evolving eruptive cycle. Earth-Sci. Rev. *78*, 85–114.

Almendros, J., Chouet, B., Dawson, P., and Bond, T. (2002). Identifying elements of the plumbing system beneath Kilauea Volcano, Hawaii, from the source locations of very-long-period signals. Geophys. J. Int. *148*, 303–312.

Alparone, S., Andronico, D., Lodato, L., and Sgroi, T. (2003). Relationship between tremor and volcanic activity during the Southeast Crater eruption on Mount Etna in early 2000. J. Geophys. Res. Solid Earth *108*, n/a – n/a.

Alparone, S., Cannata, A., Gambino, S., Gresta, S., Milluzzo, V., and Montalto, P. (2010). Time-space variation of volcano-seismic events at La Fossa (Vulcano, Aeolian Islands, Italy): new insights into seismic sources in a hydrothermal system. Bull. Volcanol. *72*, 803–816.

Alparone, S., Cocina, O., Gambino, S., Mostaccio, A., Spampinato, S., Tuvè, T., and Ursino, A. (2013). Seismological features of the Pernicana–Provenzana Fault System (Mt. Etna, Italy) and implications for the dynamics of northeastern flank of the volcano. J. Volcanol. Geotherm. Res. *251*, 16–26.

Anderson, E.M. (1937). IX.—The Dynamics of the Formation of Cone-sheets, Ring-dykes, and Caldron-subsidences. Proc. R. Soc. Edinb. *56*, 128–157.

Andronico, D., Cristaldi, A., and Scollo, S. (2008). The 4–5 September 2007 lava fountain at South-East Crater of Mt Etna, Italy. J. Volcanol. Geotherm. Res. *173*, 325–328.

Andronico, D., Lo Castro, M.D., Sciotto, M., and Spina, L. (2013). The 2010 ash emissions at the summit craters of Mt Etna: Relationship with seismo-acoustic signals. J. Geophys. Res. Solid Earth *118*, 51–70.

Arciniega-Ceballos, A., Dawson, P., and Chouet, B.A. (2012). Long period seismic source characterization at Popocatépetl volcano, Mexico. Geophys. Res. Lett. *39*, n/a – n/a.

Auger, E., D'Auria, L., Martini, M., Chouet, B., and Dawson, P. (2006). Real-time monitoring and massive inversion of source parameters of very long period seismic signals: An application to Stromboli Volcano, Italy. Geophys. Res. Lett. *33*, n/a – n/a.

Azaïez, M., Dauge, M., and Maday, Y. (1993). Méthodes spectrales et des éléments spectraux.

Azzaro, R., Bonforte, A., Branca, S., and Guglielmino, F. (2013). Geometry and kinematics of the fault systems controlling the unstable flank of Etna volcano (Sicily). J. Volcanol. Geotherm. Res. *251*, 5–15.

Balmforth, N.J., Craster, R.V., and Rust, A.C. (2005). Instability in flow through elastic conduits and volcanic tremor. J. Fluid Mech. *527*, 353–377.

Battaglia, M., Segall, P., Murray, J., Cervelli, P., and Langbein, J. (2003). The mechanics of unrest at Long Valley caldera, California: 1. Modeling the geometry of the source using GPS, leveling and two-color {EDM} data. J. Volcanol. Geotherm. Res. *127*, 195–217.

Bean, C., Lokmer, I., and O'Brien, G. (2008). Influence of near-surface volcanic structure on long-period seismic signals and on moment tensor inversions: Simulated examples from Mount Etna. J. Geophys. Res. *113*.

Bean, C.J., De Barros, L., Lokmer, I., Métaxian, J.-P., O' Brien, G., and Murphy, S. (2013). Long-period seismicity in the shallow volcanic edifice formed from slow-rupture earthquakes. Nat. Geosci. *7*, 71–75.

Bean, C.J., De Barros, L., Lokmer, I., Metaxian, J.-P., O/' Brien, G., and Murphy, S. (2014). Long-period seismicity in the shallow volcanic edifice formed from slow-rupture earthquakes. Nat. Geosci *7*, 71–75.

Behncke, B., Neri, M., and Sturiale, G. (2004). Rapid morphological changes at the summit of an active volcano: reappraisal of the poorly documented 1964 eruption of Mount Etna (Italy). Geomorphology *63*, 203–218.

Behncke, B., Neri, M., Pecora, E., and Zanon, V. (2006). The exceptional activity and growth of the Southeast Crater, Mount Etna (Italy), between 1996 and 2001. Bull. Volcanol. *69*, 149–173.

Behncke, B., Calvari, S., Giammanco, S., Neri, M., and Pinkerton, H. (2008). Pyroclastic density currents resulting from the interaction of basaltic magma with hydrothermally altered rock: an example from the 2006 summit eruptions of Mount Etna, Italy. Bull. Volcanol. *70*, 1249–1268.

Behncke, B., Branca, S., Corsaro, R.A., Beni, E.D., Miraglia, L., and Proietti, C. (2014). The 2011–2012 summit activity of Mount Etna: Birth, growth and products of the new {SE} crater. J. Volcanol. Geotherm. Res. *270*, 10–21.

Benson, P.M., Vinciguerra, S., Meredith, P.G., and Young, R.P. (2008). Laboratory simulation of volcano seismicity. Science *322*, 249–252.

Bonaccorso, A., and Patanè, D. (2001). Shear response to an intrusive episode at Mt. Etna volcano (January 1998) inferred through seismic and tilt data. Tectonophysics *334*, 61–75.

Bonaccorso, A., Bonforte, A., Guglielmino, F., Palano, M., and Puglisi, G. (2006). Composite ground deformation pattern forerunning the 2004–2005 Mount Etna eruption. J. Geophys. Res. Solid Earth *111*, n/a – n/a.

Bonaccorso, A., Bonforte, A., Currenti, G., Negro, C.D., Stefano, A.D., and Greco, F. (2011a). Magma storage, eruptive activity and flank instability: Inferences from ground deformation and gravity changes during the 1993–2000 recharging of Mt. Etna volcano. J. Volcanol. Geotherm. Res. *200*, 245–254.

Bonaccorso, A., Cannata, A., Corsaro, R.A., Di Grazia, G., Gambino, S., Greco, F., Miraglia, L., and Pistorio, A. (2011b). Multidisciplinary investigation on a lava fountain preceding a flank eruption: The 10 May 2008 Etna case. Geochem. Geophys. Geosystems *12*, n/a – n/a.

Bonafede, M., Dragoni, M., and Quareni, F. (1986). Displacement and stress fields produced by a centre of dilation and by a pressure source in a viscoelastic half-space: application to the study of ground deformation and seismic activity at Campi Flegrei, Italy. Geophys. J. R. Astron. Soc. *87*, 455–485.

Bonforte, A., Guglielmino, F., Coltelli, M., Ferretti, A., and Puglisi, G. (2011). Structural assessment of Mount Etna volcano from Permanent Scatterers analysis. Geochem. Geophys. Geosystems *12*, n/a – n/a.

Borgia, A., Ferrari, L., and Pasquare, G. (1992). Importance of gravitational spreading in the tectonic and volcanic evolution of Mount Etna. Nature *357*, 231–235.

Bousquet, G. J.C.and Lanzafame (2004). The tectonics and geodynamics of Mt Etna: synthesis and interpretation of geological and geophysical data. In Mt.Etna: Volcano LAboratory, (American Geophysical Union),.

Bousquet, J.C., and Lanzafame, G. (2013). The Tectonics and Geodynamics of Mt. Etna: Synthesis and Interpretation of Geological and Geophysical Data. In Mt. Etna: Volcano Laboratory, (American Geophysical Union), pp. 29–47.

Branca, S., and Carlo, P. (2005). Types of eruptions of Etna volcano AD 1670–2003: implications for short-term eruptive behaviour. Bull. Volcanol. *67*, 732–742.

Branca, F., S., Coltelli, M., Groppelli, G., and Pasquarè, G. (2009). Note illustrative alla carta geologica d'Italia alla scala 1:50.000. Foglio 625 Acireale.

Branca, F., S., Coltelli, M., Groppelli, G., and Lentini, F. (2011a). Geological map of Etna volcano, 1:50,000 scale. *130*.

Branca, S., Coltelli, M., and Groppelli, G. (2004). Geological Evolution of Etna volcano. In Etna Volcano Laboratory, (American Geophysical Union), pp. 49–63.

Branca, S., Coltelli, M., De Beni, E., and Wijbrans, J. (2008). Geological evolution of Mount Etna volcano (Italy) from earliest products until the first central volcanism (between 500 and 100 ka ago) inferred from geochronological and stratigraphic data. Int. J. Earth Sci. *97*, 135–152.

Branca, S., Coltelli, M., Groppelli, G., and Lentini, F. (2011b). Geological map of Etna volcano, 1:50,000 scale. Ital. J. Geosci. *130*, 265–291.

Budi-Santoso, A., Lesage, P., Dwiyono, S., Sumarti, S., Subandriyo, Surono, Jousset, P., and Metaxian, J.-P. (2013). Analysis of the seismic activity associated with the 2010 eruption of Merapi Volcano, Java. J. Volcanol. Geotherm. Res. *261*, 153–170.

Calvari, S., Groppelli, G., and Pasquarè, G. (1994). Preliminary geological data on the south-western wall of the Valle del Bove, Mt Etna, Sicily. Acta Volcanol. *5*, 15–30.

Cannata, A., Hellweg, M., Grazia, G.D., Ford, S., Alparone, S., Gresta, S., Montalto, P., and Patanè, D. (2009a). Long period and very long period events at Mt. Etna volcano: Characteristics, variability and causality, and implications for their sources. J. Volcanol. Geotherm. Res. *187*, 227–249.

Cannata, A., Montalto, P., Privitera, E., Russo, G., and Gresta, S. (2009b). Tracking eruptive phenomena by infrasound: May 13, 2008 eruption at Mt. Etna. Geophys. Res. Lett. *36*.

Cannata, A., Sciotto, M., Spampinato, L., and Spina, L. (2011). Insights into explosive activity at closely-spaced eruptive vents using infrasound signals: Example of Mt. Etna 2008 eruption. J. Volcanol. Geotherm. Res. *208*, 1–11.

Cannata, A., Di Grazia, G., Aliotta, M., Cassisi, C., Montalto, P., and Patanè, D. (2013). Monitoring Seismo-volcanic and Infrasonic Signals at Volcanoes: Mt. Etna Case Study. Pure Appl. Geophys. *170*, 1751–1771.

Cannata, A., Spedalieri, G., Behncke, B., Cannavò, F., Di Grazia, G., Gambino, S., Gresta, S., Gurrieri, S., Liuzzo, M., and Palano, M. (2015). Pressurization and depressurization phases inside the plumbing system of Mt. Etna volcano: evidence from a multiparametric approach. J. Geophys. Res. Solid Earth n/a – n/a.

Carcione, J.M., and Wang, J.P. (1993). A Chebyshev collocation method for the wave equation in generalazid coordinates. (Comp. Fluid Dyn. J. 2 269–290.).

Cardaci, C., Coviello, M., Lombardo, G., Patané, G., and Scarpa, R. (1993). Seismic tomography of Etna volcano. J. Volcanol. Geotherm. Res. *56*, 357–368.

Cauchie, L., and Saccorotti, G. (2013). Probabilistic inversion of Rayleigh-wave dispersion data: an application to Mt. Etna, Italy. J. Seismol. *17*, 335–346.

Cauchie, L., Saccorotti, G., and Bean, C.J. (2015). Amplitude and recurrence time analysis of LP activity at Mt. Etna, Italy. J. Geophys. Res. Solid Earth n/a – n/a.

Cesca, S., Battaglia, J., Dahm, T., Tessmer, E., Heimann, S., and Okubo, P. (2008). Effects of topography and crustal heterogeneity on the source estimation of LP events at Kilauea volcano. Geophys J Int *172*, 1219–1236.

Chiarabba, F. C.andAmato, A.andBoschi, E.andBarberi (2000). Recent seismicity and tomographic modeling of the Mount Etna plumbing system. *105*.

Chiarabba, C., Amato, A., Boschi, E., and Barberi, F. (2000). Recent seismicity and tomographic modeling of the Mount Etna plumbing system. J. Geophys. Res. Solid Earth *105*, 10923–10938.

Chouet, B. (1985). Excitation of a buried magmatic pipe: a seismic source model for volcanic tremor. (Journal of Geophysical Research).

Chouet, B. (1986). Dynamics of a fluid-driven crack in three dimensions by the finite difference method. (Journal of Geophysical Research).

Chouet, B. (1988). Resonance of a fluid-driven crack: radiation properties and implications for the source of long-period events and harmonic tremor (ournal of Geophysical Research).

Chouet, B. (1992). A seismic model for the source of long-period events and harmonic tremor. (In: Gasparini, P., Scarpa, R., Aki, K. (Eds.), Volcanic Seismology).

Chouet, B. (1996). New methods and future trends in seismological volcano monitoring (Monitoring and mitigation of volcanic hazards Scarpa/Tilling (eds). Springer-Verlag Berlin Hieldelberg).

Chouet, B. (2003a). Volcano seismology. Pure Appl. Geophys. *160*, 739–788.

Chouet, B. (2003b). Source mechanisms of explosions at Stromboli Volcano, Italy, determined from moment-tensor inversions of very-long-period data. J. Geophys. Res. *108*.

Chouet, B.A., and Matoza, R.S. (2013). A multi-decadal view of seismic methods for detecting precursors of magma movement and eruption. J. Volcanol. Geotherm. Res. *252*, 108–175.

Chouet, B., and Dawson, P. (2011). Shallow conduit system at Kilauea Volcano, Hawaii, revealed by seismic signals associated with degassing bursts. J. Geophys. Res. *116*.

Chouet, B., and Dawson, P. (2015). Seismic source dynamics of gas-piston activity at Kīlauea Volcano, Hawai'i: CHOUET AND DAWSON. J. Geophys. Res. Solid Earth *120*, 2525–2560.

Chouet, B., Dawson, P., and Arciniega-Ceballos, A. (2005). Source mechanism of Vulcanian degassing at Popocatépetl Volcano, Mexico, determined from waveform inversions of very long period signals. J. Geophys. Res. Solid Earth *110*, n/a – n/a.

Chouet, B.A., Page, R.A., Stephens, C.D., Lahr, J.C., and Power, J.A. (1994). The 1989-1990 Eruptions of Redoubt Volcano, Alaska Precursory swarms of long-period events at Redoubt Volcano (1989–1990), Alaska: Their origin and use as a forecasting tool. J. Volcanol. Geotherm. Res. *62*, 95–135.

Collier, L., and Neuberg, J. (2006). Incorporating seismic observations into 2D conduit flow modeling. J. Volcanol. Geotherm. Res. *152*, 331–346.

Coltelli, M. M.andGarduno, V.H.andNeri, M.andPasquaré, G.andPompillo (1994). Geology of the northern wall of Valle del Bove, Mt Etna (Sicily). *5*.

Coltelli, M., Del Carlo, P., and Vezzoli, L. (1998). Discovery of a Plinian basaltic eruption of Roman age at Etna volcano, Italy. Geology *26*, 1095–1098.

Coltelli, M., Del Carlo, P., and Vezzoli, L. (2000). Stratigraphic constraints for explosive activity in the past 100 ka at Etna Volcano, Italy. Int. J. Earth Sci. *89*, 665–677.

Corsaro, R.A., and Cristofolini, R. (2000). Subaqueous volcanism in the Etnean area : evidence for hydromagmatic activity and regional uplift inferred from the Castle Rock of Acicastello. Elsevier Oxf. Roy.-UNI 1976 Rev. *95*, 209–225.

Corsaro, R.A., and Pompilio, M. (2004). Buoyancy-controlled eruption of magmas at Mt Etna: Buoyancy-controlled eruption of magmas at Mt Etna. Terra Nova *16*, 16–22.

Cristiano, L., Petrosino, S., Saccorotti, G., Ohrnberger, M., and Scarpa, R. (2010). Shear-wave velocity structure at Mt. Etna from inversion of Rayleigh-wave dispersion patterns (2 s < T < 20 s). Ann. Geophys. *53*.

Crosson, D.A. R.S.andBame (1985). A spherical source model for low frequency volcanic earthquakes. (Journal of Geophysical Research).

Cruz, F.G., and Chouet, A.B. (1997). Long-period events, the most characteristic seismicity accompanying the emplacement and extrusion of a lava dome in Galeras Volcano, Colombia, in 1991. J. Volcanol. Geotherm. Res. *77*, 121–158.

Dahm, F. T.andKruger (2014). Moment tensor inversion and moment tensor interpretation. In New Manual of Seismological Observatory Practice (NMSOP), P. Bormann, ed. (Postadm: Deutsches GeoForschungsZentrum GFZ),.

Das, I., and Zoback, M.D. (2011). Long-period, long-duration seismic events during hydraulic fracture stimulation of a shale gas reservoir. Lead. Edge *30*, 778–786.

D'Auria, L., Giudicepietro, F., Aquino, I., Borriello, G., Del Gaudio, C., Lo Bascio, D., Martini, M., Ricciardi, G., Ricciolino, P., and Ricco, C. (2011). Repeated fluid-transfer episodes as a mechanism for the recent dynamics of Campi Flegrei caldera (1989–2010). J. Geophys. Res. Solid Earth 1978–2012 *116*.

Davi, R., O'Brien, G.S., Lokmer, I., Bean, C.J., Lesage, P., and Mora, M.M. (2010). Moment tensor inversion of explosive long period events recorded on Arenal volcano, Costa Rica, constrained by synthetic tests. J. Volcanol. Geotherm. Res. *194*, 189–200.

Davi, R., O'Brien, G.S., Barros, L.D., Lokmer, I., Bean, C.J., Lesage, P., Mora, M.M., and Soto, G.J. (2012). Seismic source mechanisms of tremor recorded on Arenal volcano, Costa Rica, retrieved by waveform inversion. J. Volcanol. Geotherm. Res. *213–214*, 1–13.

Dawson, J. P.B.andChouet, B.andPower (2011). Determining the seismic source mechanism and location for an explosive eruption with limited observational data: Augustine Volcano, Alaska. (Geophysical Research Letters).

De Barros, L., Bean, C.J., Lokmer, I., Saccorotti, G., Zuccarello, L., O'Brien, G.S., Métaxian, J.-P., and Patanè, D. (2009). Source geometry from exceptionally high resolution long period event observations at Mt Etna during the 2008 eruption. Geophys. Res. Lett. *36*.

De Barros, L., Lokmer, I., Bean, C.J., O'Brien, G.S., Saccorotti, G., Métaxian, J.-P., Zuccarello, L., and Patanè, D. (2011). Source mechanism of long-period events recorded by a high-density seismic network during the 2008 eruption on Mount Etna. J. Geophys. Res. *116*.

De Barros, L., Lokmer, I., and Bean, C.J. (2013). Origin of spurious single forces in the source mechanism of volcanic seismicity. J. Volcanol. Geotherm. Res. *262*, 1–6.

De Beaumont, E. (1836). Recherche sur la structure et l'origine du Mount Etna. *ser. 3, 9*.

De Beni, E., Branca, S., Coltelli, M., Groppelli, G., and Wijbrans, J.R. (2011). 40Ar/39Ar isotopic dating of Etna volcanic succession. Ital. J. Geosci. *130*, 292–305.

Delaney, P.T., and McTigue, D.F. (1994). Volume of magma accumulation or withdrawal estimated from surface uplift or subsidence, with application to the 1960 collapse of Kilauea volcano. Bull. Volcanol. *56*, 417–424.

De Martin, F. (2010). Influence of the nonlinear behavior of soft soils on strong ground motions. Ecole Centrale Paris.

De Martin, F. (2011). Verification of a Spectral-Element Method Code for the Southern California Earthquake Center LOH.3 Viscoelastic Case. Bull. Seismol. Soc. Am. *101*, 2855–2865.

Dingwell, D.B. (1996). Volcanic Dilemma–Flow or Blow? Science *273*, 1054–1055.

Dingwell, D., and Webb, S. (1989). Structural relaxation in silicate melts and non-Newtonian melt rheology in geologic processes. Phys. Chem. Miner. *16*, 508–516.

Di Stefano, A., and Branca, S. (2002). Long-term uplift rate of the Etna volcano basement (southern Italy) based on biochronological data from Pleistocene sediments. Terra Nova *14*, 61–68.

van Driel, M., Wassermann, J., Pelties, C., Schiemenz, A., and Igel, H. (2015). Tilt effects on moment tensor inversion in the near field of active volcanoes. Geophys. J. Int. *202*, 1711–1721.

Dufumier, H., and Rivera, L. (1997). On the resolution of the isotropic component in moment tensor inversion. Geophys. J. Int. *131*, 595–606.

Eaton, D., and Forouhideh, F. (2011). Solid angles and the impact of receiver-array geometry on microseismic moment-tensor inversion. GEOPHYSICS *76*, WC77–WC85.

Eshelby, J.D. (1957). The determination of an ellipsoidal inclusion, and related problems. (Department of Physical Metallurgy, University of Birmingham.).

Eyre, T.S., Bean, C.J., De Barros, L., O'Brien, G.S., Martini, F., Lokmer, I., Mora, M.M., Pacheco, J.F., and Soto, G.J. (2013). Moment tensor inversion for the source location and mechanism of long period (LP) seismic events from 2009 at Turrialba volcano, Costa Rica. J. Volcanol. Geotherm. Res. *258*, 215–223.

Eyre, T.S., Bean, C.J., De Barros, L., Martini, F., Lokmer, I., Mora, M.M., Pacheco, J.F., and Soto, G.J. (2015). A brittle failure model for long-period seismic events recorded at Turrialba Volcano, Costa Rica. J. Geophys. Res. Solid Earth *120*, 1452–1472.

Falsaperla, S., Privitera, E., Chouet, B., and Dawson, P. (2002). Analysis of long-period events recorded at Mount Etna (Italy) in 1992, and their relationship to eruptive activity. J. Volcanol. Geotherm. Res. *114*, 419–440.

Fehler, B. M.andChouet (1982). Operation of a digital seismic network on Mount St. Helens volcano and observations of long period seismic events that originate under the volcano. (Geophysical Research Letters).

Ferrazzini and Aki (1987). Slow waves trapped in a fluid-filled infinite crack: implication for volcanic tremor. 92 (B9), 9215–9223. (Journal of Geophysical Research).

Festa, G. (2004). Slip imagin by isochron back projection and source dynamics with spectral element methods (PhD Thesis).

Fournier, N., Jolly, A.D., and Miller, C. (2011). Ghost tilt signal during transient ground surface deformation events: Insights from the September 3, 2010 Mw7.1 Darfield earthquake, New Zealand. Geophys. Res. Lett. *38*, n/a – n/a.

Fujita, E., Ida, Y., and Oikawa, J. (1995). Eigen oscillation of a fluid sphere and source mechanism of harmonic volcanic tremor. J. Volcanol. Geotherm. Res. *69*, 365–378.

Gilbert, J.S., and Lane, S.J. (2008). The consequences of fluid motion in volcanic conduits. Geol. Soc. Lond. Spec. Publ. *307*, 1–10.

Giordano, D., and Dingwell, D. (2003). Viscosity of hydrous Etna basalt: implications for Plinian-style basaltic eruptions. Bull. Volcanol. *65*, 8–14.

Gonnermann, H.M., and Manga, M. (2007). The Fluid Mechanics Inside a Volcano. Annu. Rev. Fluid Mech. *39*, 321–356.

Goto, A. (1999). A new model for volcanic earthquake at Unzen Volcano: melt rupture. (Geophysical Research Letters).

Gottsmann, G. J.andRymer, H.andBerrino (2006). Unrest at the Campi Flegrei caldera (italy): a critical evaluation of source parameters from geodetic data inversion (Journal of Volcanology and Geothermal Research, 132-145).

Graizer, V.M. (2005). Effect of tilt on strong motion data processing. Soil Dyn. Earthq. Eng. *25*, 197–204.

Green, D.N., and Neuberg, J. (2006). Waveform classification of volcanic low-frequency earthquake swarms and its implication at Soufrière Hills Volcano, Montserrat. J. Volcanol. Geotherm. Res. *153*, 51–63.

Gudmundsson, A. (2006). How local stresses control magma-chamber ruptures, dyke injections, and eruptions in composite volcanoes. Earth-Sci. Rev. *79*, 1–31.

Guest, J.E. (1973). The Summit of Mount Etna Prior to the 1971 Eruptions [and Discussion]. Philos. Trans. R. Soc. Lond. Math. Phys. Eng. Sci. *274*, 63–78.

Gvirtzman, Z., and Nur, A. (1999). The formation of Mount Etna as the consequence of slab rollback. Nature *401*, 782–785.

Hale, A.J. (2007). Magma flow instabilities in a volcanic conduit: Implications for long-period seismicity. Phys. Earth Planet. Inter. *163*, 163–178.

Hamada, N., Jingu, H., and Ikumoto, K. (1976). On the volcanic earthquake with slowly decaying coda wave (in Japanesewith English abstract). 167–183.

Haney, M.M., Chouet, B.A., Dawson, P.B., and Power, J.A. (2013). Source characterization for an explosion during the 2009 eruption of Redoubt Volcano from very-long-period seismic waves. J. Volcanol. Geotherm. Res. *259*, 77–88.

Harrington, R.M., and Brodsky, E.E. (2007). Volcanic hybrid earthquakes that are brittle-failure events. Geophys. Res. Lett. *34*, n/a – n/a.

Haskell, N.A. (1953). The dispersion of surface waves on multilayered media. Bull. Seismol. Soc. Am. *43*, 17–34.

Hidayat, D., Chouet, B., Voight, B., Dawson, P., and Ratdomopurbo, A. (2002). Source mechanism of very-long-period signals accompanying dome growth activity at Merapi volcano, Indonesia. Geophys. Res. Lett. *29*, 33–1 – 33–34.

Hirn, A., Nercessian, A., Sapin, M., Ferrucci, F., and Wittlinger, G. (1991). Seismic heterogeneity of Mt Etna: structure and activity. Geophys. J. Int. *105*, 139–153.

Hori, S., Fukao, Y., Kumazawa, M., Furumoto, M., and Yamamoto, A. (1989). A new method of spectral analysis and its application to the Earth's free oscillations: The "Sompi" method. J. Geophys. Res. Solid Earth *94*, 7535–7553.

Ichihara, M., and Rubin, M.B. (2010). Brittleness of fracture in flowing magma. J. Geophys. Res. Solid Earth *115*, n/a – n/a.

INGV internal reports http://www.ct.ingv.it/it/rapporti/multidisciplinari.html?view=docman.

Iverson, R.M. (2008). Dynamics of seismogenic volcanic extrusion resisted by a solid surface plug, Mount St. Helens, 2004-2005: Chapter 21 in A volcano rekindled: the renewed eruption of Mount St. Helens, 2004-2006 (Reston, VA).

Iverson, R.M., Dzurisin, D., Gardner, C.A., Gerlach, T.M., LaHusen, R.G., Lisowski, M., Major, J.J., Malone, S.D., Messerich, J.A., Moran, S.C., et al. (2006). Dynamics of seismogenic volcanic extrusion at Mount St Helens in 2004-05. Nature *444*, 439–443.

James, M.R., Lane, S.J., Chouet, B., and Gilbert, J.S. (2004). Pressure changes associated with the ascent and bursting of gas slugs in liquid-filled vertical and inclined conduits. J. Volcanol. Geotherm. Res. *129*, 61–82.

Joreskog, K.G., Klovan, J.E., and Reyment, R.A. (1976). Geological Factor Analysis. Elsevier Amst.

Jost, M.L., and Herrmann, R.B. (1989). A Student's Guide to and Review of Moment Tensors. Seismol. Res. Lett. *60*, 37–57.

Jousset, P., Neuberg, J., and Jolly, A. (2004). Modelling low-frequency volcanic earthquakes in a viscoelastic medium with topography. Geophys. J. Int. *159*, 776–802.

Jousset, P., Pallister, J., Boichu, M., Buongiorno, M.F., Budisantoso, A., Costa, F., Andreastuti, S., Prata, F., Schneider, D., Clarisse, L., et al. (2012). The 2010 explosive eruption of Java's Merapi volcano—a "100-year"event. J. Volcanol. Geotherm. Res. *241*, 121–135.

Jousset, P., Budi-Santoso, A., Jolly, A.D., Boichu, M., Surono, Dwiyono, S., Sumarti, S., Hidayati, S., and Thierry, P. (2013). Signs of magma ascent in {LP} and {VLP} seismic events and link to degassing: An example from the 2010 explosive eruption at Merapi volcano, Indonesia. J. Volcanol. Geotherm. Res. *261*, 171–192.

Julian, B.R. (1994). Volcanic tremor: nonlinear excitation by fluid flow. (Journal of Geophysical Research).

Julian, B.R., Miller, A.D., and Foulger, G.R. (1998). Non-double-couple earthquakes 1. Theory. Rev. Geophys. *36*, 525–549.

Kaneshima, S., Kawakatsu, H., Matsubayashi, H., Sudo, Y., Tsutsui, T., Ohminato, T., Ito, H., Uhira, K., Yamasato, H., Oikawa, J., et al. (1996). Mechanism of Phreatic Eruptions at Aso Volcano Inferred from Near-Field Broadband Seismic Observations. Science *273*, 643–645.

Kawakatsu, H., Kaneshima, S., Matsubayashi, H., Ohminato, T., Sudo, Y., Tsutsui, T., Uhira, K., Yamasato, H., Ito, H., and Legrand, D. (2000). Aso94: Aso seismic observation with broadband instruments. J. Volcanol. Geotherm. Res. *101*, 129–154.

Knopoff, L., and Randall, M.J. (1970). The compensated linear-vector dipole: A possible mechanism for deep earthquakes. J. Geophys. Res. *75*, 4957–4963.

Komatisch, F.J. D.andVilotte, J.P.andVai, R.andCastillo-Covarrubias, J.M.andSanchez-Sesma (1999). The spectral element method for elastic wave equations - application to 2-D and 3-D seismic problems. (nt. J. Numer. Meth. Engng. 45 1139–1164.).

Komatisch, R. D.andMartin (2007). An unsplit convolutional Perfectly Matched Layer improved at grazing incidence for the seismic wave equation (Geophysics 72 SM155–SM167.).

Komatitsch, D. (1997). Méthodes spectrale et éléments spectraux pour l'equation de l'elastodynamique 2D et 3D en milieu hétérogène (PhD Manuscript).

Komatitsch, P. D.andCoutel, F.andMora (1996). Tensorial formulation of the wave equation for modelling curved interfaces. (Geophys. J. Int. 127).

Konstantinou, V. K.I.andSchlindwein (2003). Nature, wavefield properties and source mechanism of volcanic tremor: a review. (Journal of volcanology and geothermal research).

Krieger, L.U. (2011). Automated inversion of long period signals from shallo volcanic and induced seismic events. (PhD Thesis, University of Hamburg).

Kumagai, H. (2002a). Temporal evolution of a hydrothermal system in Kusatsu-Shirane Volcano, Japan, inferred from the complex frequencies of long-period events. J. Geophys. Res. *107*.

Kumagai, H. (2002b). Waveform inversion of oscillatory signatures in long-period events beneath volcanoes. J. Geophys. Res. *107*.

Kumagai, H., and Chouet, B.A. (1999). The complex frequencies of long-period seismic events as probes of fluid composition beneath volcanoes. Geophys. J. Int. *138*.

Kumagai, H., and Chouet, B.A. (2000). Acoustic properties of a crack containing magmatic or hydrothermal fluids. J. Geophys. Res. Solid Earth *105*, 25493–25512.

Kumagai, H., Chouet, B.A., and Dawson, P.B. (2005). Source process of a long-period event at Kilauea volcano, Hawaii. Geophys. J. Int. *161*, 243–254.

Kumagai, H., Nakano, M., Maeda, T., Yepes, H., Palacios, P., Ruiz, M., Arrais, S., Vaca, M., Molina, I., and Yamashima, T. (2010). Broadband seismic monitoring of active volcanoes using deterministic and stochastic approaches. J. Geophys. Res. *115*.

Kumazawa, M., Imanishi, Y., Fukao, Y., Furumoto, M., and Yamamoto, A. (1990). A theory of spectral analysis based on the characteristic property of a linear dynamic system. Geophys. J. Int. *101*, 613–630.

Laigle, M., Hirn, A., Sapin, M., Lépine, J.-C., Diaz, J., Gallart, J., and Nicolich, R. (2000). Mount Etna dense array local earthquake P and S tomography and implications for volcanic plumbing. J. Geophys. Res. Solid Earth *105*, 21633–21646.

Lamb, H. (1904). On the propagation of tremors over the surface of an elastic solid (Philosophical Transactions of the Royal Society of London A203 1–42.).

Lay, T., and Wallace, T.C. (1995). Modern global seismology (Academic press).

Leet, R.C. (1988). Saturated and subcooled hydrothermal boiling in groundwater flow channels as a source of harmonic tremor. J. Geophys. Res. Solid Earth *93*, 4835–4849.

Legrand, D., Kaneshima, S., and Kawakatsu, H. (2000). Moment tensor analysis of near-field broadband waveforms observed at Aso Volcano, Japan. J. Volcanol. Geotherm. Res. *101*, 155–169.

Lokmer, I., Bean, C.J., Saccorotti, G., and Patanè, D. (2007). Moment-tensor inversion of LP events recorded on Etna in 2004 using constraints obtained from wave simulation tests. Geophys. Res. Lett. *34*.

Lokmer, I., Saccorotti, G., Di Lieto, B., and Bean, C.J. (2008). Temporal evolution of long-period seismicity at Etna Volcano, Italy, and its relationships with the 2004–2005 eruption. Earth Planet. Sci. Lett. *266*, 205–220.

Luca, G.D., Filippi, L., Patanè, G., Scarpa, R., and Vinciguerra, S. (1997). Three-dimensional velocity structure and seismicity of Mt. Etna Volcano, Italy. J. Volcanol. Geotherm. Res. *79*, 123–138.

Madariaga, R. (2007). Seismic source theory (Elsevier).

Maeda, Y., Takeo, M., and Ohminato, T. (2011). A waveform inversion including tilt: method and simple tests: A waveform inversion including tilt. Geophys. J. Int. *184*, 907–918.

Masterlark, T. (2007). magma intrusion and deformation predictions: sensitivities to the Mogi assumptions (Jour. of. Geoph. Res., B06419, doi: 10.1029/2006JB004860).

Matoza, R.S., and Chouet, B.A. (2010). Subevents of long-period seismicity: Implications for hydrothermal dynamics during the 2004–2008 eruption of Mount St. Helens. J. Geophys. Res. Solid Earth *115*, n/a – n/a.

Matoza, R.S., Garcés, M.A., Chouet, B.A., D'Auria, L., Hedlin, M.A.H., De Groot-Hedlin, C., and Waite, G.P. (2009). The source of infrasound associated with long-period events at Mount St. Helens. J. Geophys. Res. *114*.

McGuire, W.J., and Pullen, A.D. (1989). Location and orientation of eruptive fissures and feederdykes at Mount Etna; influence of gravitational and regional tectonic stress regimes. J. Volcanol. Geotherm. Res. *38*, 325–344.

McNutt, S.R. (2005). VOLCANIC SEISMOLOGY. Annu. Rev. Earth Planet. Sci. *33*, 461–491.

McTigue, D.F. (1987). Elastic stress and deformation near a finite spherical magma body: Resolution of the point source paradox. J. Geophys. Res. Solid Earth *92*, 12931–12940.

Menke, 1989 (1989). Geophysical data analysis: discrete inverse theory, revised edition.

Mogi, K. (1958). Relations between the Eruptions of various volcanoes and the deformation of the ground surfaces around them. (Bulletin of the earthquake research institute, Vol. 36, pp. 99-134).

Molina, I., Kumagai, H., García-Aristizábal, A., Nakano, M., and Mothes, P. (2008). Source process of very-long-period events accompanying long-period signals at Cotopaxi Volcano, Ecuador. J. Volcanol. Geotherm. Res. *176*, 119–133.

Morgan, S.C., Malone, S.D., Qamar, A.I., Thelen, W.A., Wright, A.K., and Caplan-Auerbach, J. (2008). Seismicity associated with renewed dome building at Mount St. Helens, 2004-2005: Chapter 2 in A volcano rekindled: the renewed eruption of Mount St. Helens, 2004-2006 (Reston, VA).

Morrissey, M.M., and Chouet, B.A. (1997). A numerical investigation of choked flow dynamics and its application to the triggering mechanism of long-period events at Redoubt Volcano, Alaska. J. Geophys. Res. Solid Earth *102*, 7965–7983.

Muller, G. (1973). Seismic moment and long period radiation of underground nuclear explosions (Bull. Seism. Soc. Am. 63, 847-857).

Muller, G. (2001). Volume change of seismic sources from moment tensor (Bull. Seism. Soc. of America, 880-884).

Nakamichi, H., Kumagai, H., Nakano, M., Okubo, M., Kimata, F., Ito, Y., and Obara, K. (2009). Source mechanism of a very-long-period event at Mt Ontake, central Japan: Response of a hydrothermal system to magma intrusion beneath the summit. J. Volcanol. Geotherm. Res. *187*, 167–177.

Nakano, M. (2005). Waveform inversion of volcano-seismic signals assuming possible source geometries. Geophys. Res. Lett. *32*.

Nakano, M., Kumagai, H., Kumazawa, M., Yamaoka, K., and Chouet, B.A. (1998). The excitation and characteristic frequency of the long-period volcanic event: An approach based on an inhomogeneous autoregressive model of a linear dynamic system. J. Geophys. Res. Solid Earth *103*, 10031–10046.

Nakano, M., Kumagai, H., and Chouet, B.A. (2003). Source mechanism of long-period events at Kusatsu–Shirane Volcano, Japan, inferred from waveform inversion of the effective excitation functions. J. Volcanol. Geotherm. Res. *122*, 149–164.

Neri, M., Mazzarini, F., Tarquini, S., Bisson, M., Isola, I., Behncke, B., and Pareschi, M.T. (2008). The changing face of Mount Etna's summit area documented with Lidar technology. Geophys. Res. Lett. *35*, n/a – n/a.

Neuberg, J., Luckett, R., Baptie, B., and Olsen, K. (2000). Models of tremor and low-frequency earthquake swarms on Montserrat. J. Volcanol. Geotherm. Res. *101*, 83–104.

Neuberg, J.W., Tuffen, H., Collier, L., Green, D., Powell, T., and Dingwell, D. (2006). The trigger mechanism of low-frequency earthquakes on Montserrat. J. Volcanol. Geotherm. Res. *153*, 37–50.

Nolen-Hoeksema, R.C., and Ruff, L.J. (2001). Moment tensor inversion of microseisms from the B-sand propped hydrofracture, M-site, Colorado. Tectonophysics *336*, 163–181.

Norini, G., and Acocella, V. (2011). Analogue modeling of flank instability at Mount Etna: Understanding the driving factors. J. Geophys. Res. Solid Earth *116*, n/a – n/a.

Ohminato, T. (2006). Characteristics and source modeling of broadband seismic signals associated with the hydrothermal system at Satsuma–Iwojima volcano, Japan. J. Volcanol. Geotherm. Res. *158*, 467–490.

Ohminato, T., and Chouet, B.A. (1997). A free-surface boundary condition for including 3D topography in the finite-difference method. Bull. Seismol. Soc. Am. *87*, 494–515.

Ohminato, T., Chouet, B.A., Dawson, P., and Kedar, S. (1998). Waveform inversion of very long period impulsive signals associated with magmatic injection beneath Kilauea volcano, Hawaii. J. Geophys. Res. Solid Earth *103*, 23839–23862.

Ohminato, T., Takeo, M., Kumagai, H., Yamashina, T., Oikawa, J., Koyama, E., Tsuji, H., and Urabe, T. (2006). Vulcanian eruptions with dominant single force components observed during the Asama 2004 volcanic activity in Japan. Earth Planets Space *58*, 583–593.

Palo, M., Ibáñez, J.M., Cisneros, M., Bretón, M., Del Pezzo, E., Ocaña, E., Orozco-Rojas, J., and Posadas, A.M. (2009). Analysis of the seismic wavefield properties of volcanic explosions at Volcán de Colima, México: insights into the source mechanism. Geophys. J. Int. *177*, 1383–1398.

Papale, P. (1999). Strain-induced magma fragmentation in explosive eruptions. Nature *397*, 425–428.

Pasquare, G., Servizio geologico., Italy., Consiglio Nazionale delle Ricerche., and Commissione per la Cartopgrafia Geologica e Geomorfologica. (1992). Carta geologica d'Italia, 1: 50.000 : guida al rilevamento (Rome: Servizio Geologico Nazionale).

Patane, D., Chiarabba, C., Cocina, O., De Gori, P., Moretti, M., and Boschi, E. (2002). Tomographic images and 3D earthquake locations of the seismic swarm preceding the 2001 Mt. Etna eruption: Evidence for a dyke intrusion. Geophys. Res. Lett. *29*, 135–1 – 135–4.

Patanè, D., Aliotta, M., Cannata, A., Cassisi, C., Coltelli, M., and Di Grazia, G. (2011). Interplay between Tectonics and Mount Etna's Volcanism: Insights into the Geometry of the Plumbing System. New Front. Tecton. Res. - Midst Plate Converg. Dr Uri Schattner Ed.

Patanè, D., Aiuppa, A., Aloisi, M., Behncke, B., Cannata, A., Coltelli, M., Di Grazia, G., Gambino, S., Gurrieri, S., Mattia, M., et al. (2013). Insights into magma and fluid transfer at Mount Etna by a multiparametric approach: A model of the events leading to the 2011 eruptive cycle. J. Geophys. Res. Solid Earth *118*, 3519–3539.

Patera, A.T. (1984). A spectral element method for fluid dynamics : laminar flow in a channel expansion (J. Comput. Phys. 54, 468–488.).

Ponte, G. (1920). Il cratere centrale dell'Etna. Suoi cambiamenti e sue eruzioni. Atti Accad. Gioenia Sci. Nat. Catania *ser V 12*, 1–12.

Potter, R.R. C.C.andStewart (1998). Density predictions using Vp and Vs sonic logs. *10*.

Power, J.A., and Lalla, D.J. (2010). Seismic observations of Augustine Volcano, 1970-2007.

Priolo, G. EandCarcione, J.M.andSeriani (1994). Numerical simulation of interface waves by high-order spectral modeling techniques. (The Journal the Acoustical Society of America 95 681–693.).

Privitera, E., Bonanno, A., Gresta, S., Nunnari, G., and Puglisi, G. (2012). Triggering mechanisms of static stress on Mount Etna volcano. An application of the boundary element method. J. Volcanol. Geotherm. Res. *245–246*, 149–158.

Rasà, R., Azzaro, R., and Leonardi, O. (1996). Aseismic creep on faults and flank instability at Mount Etna volcano, Sicily. Geol. Soc. Lond. Spec. Publ. *110*, 179–192.

Richards, P.G. (2005). Equivalent Volume Sources for Explosions at Depth: Theory and Observations. Bull. Seismol. Soc. Am. *95*, 401–407.

Rivet, D., Brenguier, F., Clarke, D., Shapiro, N.M., and Peltier, A. (2014). Long-term dynamics of Piton de la Fournaise volcano from 13 years of seismic velocity change measurements and GPS observations. J. Geophys. Res. Solid Earth *119*, 7654–7666.

Rodgers, P.W. (1968). The response of the horizontal pendulum seismometer to Rayleigh and Love waves, tilt, and free oscillations of the earth. Bull. Seismol. Soc. Am. *58*, 1385–1406.

Romano, R., Lentini, F., and Sturiale, C. (1979). Carta geologica del Monte Etna, scala 1:50.000 (Mem. Soc. Geo. Italiana).

Rowe, C.A., Thurber, C.H., and White, R.A. (2004). Dome growth behavior at Soufriere Hills Volcano, Montserrat, revealed by relocation of volcanic event swarms, 1995–1996. J. Volcanol. Geotherm. Res. *134*, 199–221.

Rust, A.C., Balmforth, N.J., and Mandre, S. (2008). The feasibility of generating low-frequency volcano seismicity by flow through a deformable channel. Geol. Soc. Lond. Spec. Publ. *307*, 45–56.

Rust, D., Behncke, B., Neri, M., and Ciocanel, A. (2005). Nested zones of instability in the Mount Etna volcanic edifice, Italy. J. Volcanol. Geotherm. Res. *144*, 137–153.

Saccorotti, G., Chouet, B., and Dawson, P. (2001). Wavefield properties of a shallow long-period event and tremor at Kilauea Volcano, Hawaii. J. Volcanol. Geotherm. Res. *109*, 163–189.

Saccorotti, G., Zuccarello, L., Del Pezzo, E., Ibanez, J., and Gresta, S. (2004). Quantitative analysis of the tremor wavefield at Etna Volcano, Italy. J. Volcanol. Geotherm. Res. *136*, 223–245.

Saccorotti, G., Lokmer, I., Bean, C.J., Di Grazia, G., and Patanè, D. (2007). Analysis of sustained long-period activity at Etna Volcano, Italy. J. Volcanol. Geotherm. Res. *160*, 340–354.

Savage, J.C. (1988). Principal Component Analysis of Geodetically Measured Deformation in Long Valley Caldera, Eastern California, 1983–1987. J. Geophys. Res. Solid Earth *93*, 13297–13305.

Schellart, W.P. (2010). Mount Etna–Iblean volcanism caused by rollback-induced upper mantle upwelling around the Ionian slab edge: An alternative to the plume model. Geology *38*, 691–694.

Schuberth, B. (2003). The Spectral Element Method for seismic wave propagation. (PhD Thesis, Munchen.).

Small, C., and Naumann, T. (2001). The global distribution of human population and recent volcanism. Glob. Environ. Change Part B Environ. Hazards *3*, 93–109.

Spampinato, L., Sciotto, M., Cannata, A., Cannavò, F., La Spina, A., Palano, M., Salerno, G.G., Privitera, E., and Caltabiano, T. (2015). Multiparametric study of the February–April 2013 paroxysmal phase of Mt. Etna New South-East crater. Geochem. Geophys. Geosystems *16*, 1932–1949.

Stacey, R. (1988). Improved transparent boundary formulations for the elastic-wave equation. *78*.

Stephens, C.D., and Chouet, B. (2001). Evolution of the December 14, 1989 precursory long-period event swarm at Redoubt Volcano, Alaska. J. Volcanol. Geotherm. Res.

Syahbana, D.K., Caudron, C., Jousset, P., Lecocq, T., Camelbeeck, T., Bernard, A., and Surono (2014). Fluid dynamics inside a "wet" volcano inferred from the complex frequencies of long-period (LP) events: An example from Papandayan volcano, West Java, Indonesia, during the 2011 seismic unrest. J. Volcanol. Geotherm. Res. *280*, 76–89.

Takei, Y., and Kumazawa, M. (1994). Why have the single force and torque been excluded from seismic source models? Geophys. J. Int. *118*, 20–30.

Takeo, M., Aoki, Y., Ohminato, T., and Yamamoto, M. (2006). Magma supply path beneath Mt. Asama volcano, Japan. Geophys. Res. Lett. *33*.

Tanguy, J.C., and Patané, G. (1984). Activity of mount Etna, 1977–1983: Volcanic phenomena and accompanying seismic tremor. Bull. Volcanol. *47*, 965–976.

Thomas, M.E., and Neuberg, J. (2012). What makes a volcano tick—A first explanation of deep multiple seismic sources in ascending magma. Geology *40*, 351–354.

Thomson, W.T. (1950). Transmission of Elastic Waves through a Stratified Solid Medium. J. Appl. Phys. *21*, 89–93.

Thun, J., Lokmer, I., and Bean, C.J. (2015). New observations of displacement steps associated with volcano seismic long-period events, constrained by step table experiments. Geophys. Res. Lett. *42*, 3855–3862.

Tuffen, H., and Dingwell, D. (2005). Fault textures in volcanic conduits: evidence for seismic trigger mechanisms during silicic eruptions. Bull. Volcanol. *67*, 370–387.

Tuffen, H., Dingwell, D.B., and Pinkerton, H. (2003). Repeated fracture and healing of silicic magma generate flow banding and earthquakes? Geology *31*, 1089–1092.

Varley, N.R., Arámbula-Mendoza, R., Reyes-Dávila, G., Stevenson, J., and Harwood, R. (2010). Long-period seismicity during magma movement at Volcán de Colima. Bull. Volcanol. *72*, 1093–1107.

Vasco, D.W. (1989). Deriving source-time functions using principal component analysis. Bull. Seismol. Soc. Am. *79*, 711–730.

Vavryčuk, V. (2001). Inversion for parameters of tensile earthquakes. *106*.

Vavryčuk, V. (2011). Tensile earthquakes: Theory, modeling, and inversion. J. Geophys. Res. *116*.

Vavryčuk, V. (2015). Moment tensor decompositions revisited. J. Seismol. *19*, 231–252.

Viccaro, M., Garozzo, I., Cannata, A., Grazia, G.D., and Gresta, S. (2014). Gas burst vs. gas-rich magma recharge: A multidisciplinary study to reveal factors controlling triggering of the recent paroxysmal eruptions at Mt. Etna. J. Volcanol. Geotherm. Res. *278–279*, 1–13.

Villaseñor, A., Benz, H.M., Filippi, L., De Luca, G., Scarpa, R., Patanè, G., and Vinciguerra, S. (1998). Three-dimensional P-wave velocity structure of Mt. Etna, Italy. Geophys. Res. Lett. *25*, 1975–1978.

Virieux, J. (1986). P-SV wave propagation in heterogeneous media velocity-stress finite-difference method. (Geophysics 51 889–901.).

Voight, B., Sparks, R.S.J., Miller, A.D., Stewart, R.C., Hoblitt, R.P., Clarke, A., Ewart, J., Aspinall, W.P., Baptie, B., Calder, E.S., et al. (1999). Magma Flow Instability and Cyclic Activity at Soufriere Hills Volcano, Montserrat, British West Indies. Science *283*, 1138–1142.

Waite, G.P., Chouet, B.A., and Dawson, P.B. (2008). Eruption dynamics at Mount St. Helens imaged from broadband seismic waveforms: Interaction of the shallow magmatic and hydrothermal systems. J. Geophys. Res. *113*.

Waltershausen, W.S. (1844). Atlas des Aetna (Berlin: Gottingen, Weimar).

Waltershausen, W.S. (1880). Der Aetna (Engelman, Leipzig).

Wassermann (2011). Volcano Seismology.

Webb, S.L., and Dingwell, D.B. (1990). Non-Newtonian rheology of igneous melts at high stresses and strain rates: Experimental results for rhyolite, andesite, basalt, and nephelinite. J. Geophys. Res. Solid Earth *95*, 15695–15701.

Wielandt, E. (2001). Basics of the volume-source model and its application in volcano seismology (Institute of Geophysics, University of Stuttgart).

Yoon, T.J. K.T.andChung (1996). Three-dimensional mixed explicit-implicit generalized Galerkin spectral element methods for high-speed turbulent compressible flows. (Comp. Meth. Appl. Mech. Eng. 135, 343–367.).

Zecevic, M., De Barros, L., Bean, C.J., O'Brien, G.S., and Brenguier, F. (2013). Investigating the source characteristics of long-period (LP) seismic events recorded on Piton de la Fournaise volcano, La Réunion. J. Volcanol. Geotherm. Res. *258*, 1–11.

Zienkiewicz, O.Z. (1989a). The Finite Element Method, Fourth Edition, Volume 1: Basic Formulation and Linear Problems. (McGraw-Hill Book Company.).

Zienkiewicz, R.L. O.Z.andTaylor (1989b). The Finite Element Method, Fourth Edition, Volume 2: Solid and Fluid Mechanics Dynamics and Non-Linearity. (McGraw-Hill Book Company.).

Zobin, V.M. (2012). Introduction to volcanic seismology (Oxford: Elsevier).

Zobin, V.M., Reyes, G.A., Guevara, E., and Bretón, M. (2008). Seismological constraints on the position of the fragmentation surfaces in the volcano conduit. Earth Planet. Sci. Lett. *275*, 337–341.